UNIVERSITÉ DE STRASBOURG

ÉCOLE DOCTORALE de PHYSIQUE et CHIMIE-PHYSIQUE (ED182)

Institut de Physique et Chimie des Matériaux de Strasbourg

THÈSE présentée par :

Georgian MELINTE

soutenue le : **18 septembre 2015**

pour obtenir le grade de : **Docteur de l'université de Strasbourg**

Discipline/ Spécialité : Physique

Advanced 3D and *in-situ* TEM approaches applied to carbon-based and zeolitic nanomaterials

THÈSE dirigée par :
M. ERSEN Ovidiu — Professeur, Université de Strasbourg, France

THÈSE co-dirigée par :
M. PHAM-HUU Cuong — Directeur de recherche, ICPEES, Strasbourg, France

RAPPORTEURS :
M. BOTTON Gianluigi — Professeur, McMaster University, Hamilton, Canada
M. RØNNING Magnus — Professeur, Norwegian University of Science and Technology, Trondheim, Norvège

---

AUTRES MEMBRES DU JURY :
M. EBBESEN Thomas — Professeur, Université de Strasbourg, France
M. RICOLLEAU Christian — Professeur, Université Paris 7 Denis Diderot, France
M. VALTCHEV Valentin — Directeur de Recherche, ENSICAEN, Caen, France
Mme MOLDOVAN Simona — Chercheur, IPCMS, Strasbourg, France

Georgian MELINTE

Advanced 3D and *in-situ* TEM approaches applied to carbon-based and zeolitic nanomaterials

Résumé

Dans le cadre de cette thèse, des techniques avancées de Microscopie électronique à transmission (MET) ont été utilisées dans le but de caractériser et de fabriquer de nouveaux nanomatériaux pour des applications dans les domaines de la nanoélectronique et de la catalyse. Trois types de matériaux fonctionnalisés sont étudiés: le graphène multifeuillets (FLG– Few-Layer Graphene) avec des nanomotifs, des nanotubes de carbone (CNTs - Carbon Nanotubes en anglais) et des zéolithes mésoporeux. La formation de nanomotifs de tranchées et de tunnels sur des flocons de FLG à l'aide de nanoparticules (NPs) de fer est étudiée dans une approche qui combine la tomographie électronique et la MET environnementale. Le rôle des facettes de la nanoparticule et des paramètres topographiques de FLG a été déterminé du point de vue quantitatif, ce qui a mené à la mise en évidence du mécanisme de formation des nanomotifs de tranchées et de tunnels. Le transfert de nanoparticules à base de métal entre deux nanostructures de carbone a été également étudié, en temps réel, en employant un porte-échantillon MET couplé avec un dispositif STM (Scanning Tunneling Microscope en anglais). Le protocole de contrôle du transfert des nanoparticules, les transformations chimiques et structurales subies par celles-ci, le mécanisme de croissance de nouvelles nanoparticules et d'autres phénomènes liés à ces effets ont été étudiés avec attention. La dernière partie de la thèse est centrée sur l'étude de la tomographie électronique à faible dose de la porosité induite dans deux classes de zéolithes, ZSM-5 et zéolithe Y, en utilisant un traitement chimique novateur à base de fluor.

Abstract

In this thesis, advanced Transmission Electron Microscopy (TEM) techniques are used to characterize and fabricate new nanomaterials with applications in nanoelectronics and catalysis. Three types of functionalized materials are investigated: nanopatterned few-layer graphene (FLG), carbon nanotubes (CNTs) and mesoporous zeolites. The nanopatterning process of FLG flakes by iron nanoparticles (NPs) is studied using an approach combining electron tomography (ET) and environmental TEM. The role of the nanoparticle faceting and of the FLG topographic parameters has been quantitatively determined leading to the first determination of the operating mechanism of the patterning process. The mass transfer of metallic-based NPs between two carbon nanostructures was studied as well in real-time by using a TEM-STM holder. The protocol of controlling the mass transfer, the chemical and structural transformations of the NPs, the growth mechanism of the new NPs and other related phenomena were carefully investigated. The last part deals with the low-dose ET investigation of the porosity induced in two classes of zeolites, ZSM-5 and zeolite Y, by an innovative fluoride-based chemical treatment.

Acknowledgments

These studies were performed at the Institute of Physics and Chemistry of Strasbourg (IPCMS) in the Department of Surfaces and Interfaces under the coordination of Prof. Ovidiu Ersen and under the co-supervision of Dr. Cuong Pham-Huu from the Institute of Chemistry and Processes for Energy, Environment and Health Strasbourg (ICPEES).

First and foremost, I would like to thank my supervisors, Prof. Ovidiu Ersen and Dr. Cuong Pham-Huu, for the immense opportunity of being part of their research groups and the constant advising and support offered during the last three years. My deepest gratitude to Prof. Ersen who included me in many exciting projects and offered me great career opportunities.

It gives me a great pleasure to thank Prof. Gianluigi Botton and Prof. Magnus Rønning for dedicating some of their time to review my work. I am also very thankful to Prof. Thomas Ebbesen, Prof. Christian Ricolleau, Dr. Valentin Valtchev and Dr. Simona Moldovan for accepting to be part of my thesis jury.

I spent three amazing years at IPCMS, so I would like to address particular thanks for this to all members of the electron microscopy team and especially to Dr. Maria Girleanu, Dris Ihiawakrim, Dr. Corinne Ulhaq-Bouillet and Kassiogé Dembele. Special thanks to Dr. Lucian Roiban, Dr. Ileana Florea and Dr. Andrea Porto Carreiro for their very helpful pieces of advice and training.

I share the credit of my work with many great chemists who introduced me to world of functionalized nanomaterials. Special acknowledgments to Dr. Walid Baaziz, Dr. Izabela Janowska, Prof. Sylvie Bégin-Colin and Dr. Xiaojie Liu for their continuous support of the projects involving carbon nanostructures and oxide nanoparticles. It was also a great pleasure to collaborate with Dr. Valentin Valtchev and Dr. Zhengxing Qin from the Laboratory of Catalysis and Spectrochemistry (LCS) Caen in the investigation of zeolitic materials.

I would like to express my appreciation to Dr. Charles Hirlimann for his patient advising during the writing of this thesis.

My deepest gratitude to Prof. Lucian Baia and Prof. Monica Baia for their precious help during my Master's years.

A special kind of thank you to Raluca for her patient support during these beautiful but difficult years. Also, many thanks to all my friends especially to Robert, Aline, Codrin and Adela.

La final, dar nu in ultimul rand, le multumesc parintilor mei Ilenuta si Petru pentru sprijinul si numeroasele sacrificii pe care le-au facut pentru ca eu sa pot ajunge aici. Le multumesc de-asemenea fratilor si surorilor mele Cristian, Catalina, Daniel, Eliza si Emanuela.

Contents

Résumé de thèse *1*

Introduction *1*

Chapter I

State-of-the-art in electron microscopy applied to materials science *24*

1.1. A brief history of electron microscopy 24

1.2. The electron microscope: a multifunctional tool 26

1.3 References 31

Chapter II

A 3D insight on the catalytic nanopatterning of few-layer graphene *33*

2.1. State-of-the-art 33

2.2. Methods 39

2.2.1. Sample preparation 39

2.2.2. Techniques 40

2.3. Advanced 2D characterization: HR-TEM and STEM-EELS 41

2.4. Electron Tomography 46

2.4.1. A 3D overview of the nanopatterned FLG by tomography 46

2.4.2. The topographic influence on the nanoparticle motion 51

2.5. Discussion 61

2.6. Subsequent applications of the catalytic nanopatterning 64

2.6.1. From pencil leads to monolayer graphene nanoribbons 64

2.6.2. Nanopatterned FLG flakes as support for nanoparticle catalyst 68

2.7. Conclusions 70

2.8. Perspective 70

2.9. References 71

Chapter III

In-situ observation of catalytic nanopatterning of few-layer graphene 74

3.1 Environmental electron microscopy 74

3.1.1 State-of-the-art 74

3.1.2 “Imaging” chemical reactions under electron beams 78

3.2 Methods 82

3.2.1. Atmosphere Protochips™ windows-type E-cell 82

3.2.2. Synthesis of FLG flakes decorated with $Fe_{3-x}O_4$ nanoparticles 86

3.2.3. Preparation of the experiment 86

3.3 The reduction of $Fe_{3-x}O_4$ nanoparticles 88

3.4 Real-time observation and analysis of the catalytic channeling 94

3.4.1 Preparation of the channeling experiment 94

3.4.2 Initiation of the channeling process 96

3.4.3 Catalytically active nanoparticles: unstable structures 97

3.4.4 Experimental insight in the channeling mechanism 99

3.4.5 From edge recession to channel formation 100

3.4.6 Splitting of active nanoparticles 102

3.4.7 Channeling rates 104

3.4.8 The faceting influence on the channeling activity 105

3.5 Discussion 108

3.6. Conclusions 111

3.7 Perspective 111

3.8 References 112

Chapter IV

Carbon nanotubes as nanodispensers for metal particles onto graphene 114

4.1. State-of-the-art 114

4.2 Methods 117

4.2.1 Synthesis of Fe_3O_4-filled CNTs and FLG sheets 117

4.2.2 Experimental TEM-STM setup 117

4.3 Joule activation of carbon nanotubes conductivity 118

4.4 Nanoparticle deposition using raw nanotubes 122

4.5 CNT to FLG nanoparticle transfer by electromigration 124

4.6 Nanoparticles transfer under a high current 128
4.7 Nanoparticles transfer under inversed voltage polarity 129
4.8 Discussion 131
4.9 Conclusions 134
4.10 Perspective 134
4.11 References 135

Chapter V

A 3D TEM insight in the hierarchical porosity of ZSM-5 and Y zeolites 137

5.1. State of the art 137
5.1.1. Post-synthesis induced mesoporosity in zeolitic materials 137
5.1.2. New approach: simultaneous Si/Al demetallation by fluoride etching 139
5.2. Hierarchical porosity induced by fluoride etching in ZSM-5 zeolites 140
5.2.1. Methods 141
5.2.2. Classical TEM characterization 146
5.2.3. Electron Tomography 148
5.2.4. Conclusion and perspective 167
5.3. Hierarchical porosity induced by fluoride etching in zeolite Y 170
5.3.2. Classical TEM characterization 172
5.3.3. Electron Tomography 173
5.3.4. Conclusion and perspective 185
5.4. General conclusions and perspectives of the Chapter V 187
5.5. References 188

Conclusions and perspectives 190

Annex A 192

Annex B 193

Résumé de thèse

Microscopie électronique 3D et environnementale de nanomatériaux carbonés et zéolitiques

Introduction

La microscopie électronique est une technique de caractérisation versatile qui permet la réalisation d'une vaste gamme d'études dans les modes *in-situ* et *ex-situ*. Aujourd'hui, un microscope électronique est plus qu'un outil d'imagerie ; il s'agit d'un équipement complexe entièrement équipé pour l'étude de nano-objets et des processus physico-chimiques d'intérêt dans le domaine des nanosciences et nanotechnologies. Il permet également d'analyser des échantillons en temps réel dans des conditions de travail variées : atmosphère gazeuse, milieu liquide, tension de polarisation, températures élevées etc., et d'accéder à une vaste gamme de propriétés et caractéristiques structurales, morphologiques et chimiques.

Dans le cadre de cette thèse, des techniques avancées de microscopie électronique en transmission (MET) ont été utilisées dans le but de caractériser et de fabriquer de nouveaux nanomatériaux ayant des applications potentielles dans les domaines de la nanoélectronique et de la catalyse. Trois types de matériaux sont étudiés : graphène multifeuillets (FLG – Few-Layer Graphene en anglais) avec des nanomotifs ou nanostructurées, nanotubes de carbone (CNTs – Carbon Nanotubes en anglais) et zéolithes mésoporeux. Dans la première partie de la thèse, la formation de nanomotifs de tranchées et de tunnels sur des feuilles de FLG en exploitant l'activité catalytique des nanoparticules de fer est étudiée à travers une approche qui combine la tomographie électronique et le mode environnemental. La tomographie électronique montre une forte influence à la fois de la topographie du substrat du FLG et de la morphologie des nanoparticules actives, en permettant une description complète des caractéristiques du processus de découpe des motifs. L'observation en temps réel du processus à l'intérieur d'une cellule de gaz environnementale (Protochips™ Atmosphere) a mise en évidence un mécanisme complexe de découpe, c'est à dire des rendements irréguliers de coupure des feuillets FLG et des restructurations constantes des nanoparticules actives. Le changement permanent entre les deux

mécanismes catalytiques identifiés (récession de bord et découpe droite) est associé à l'existence d'une affinité entre les facettes de certaines nanoparticules et certaines orientations cristallographiques du substrat du FLG. La deuxième partie de la thèse présente une procédure simple pour la réalisation de la nano-impression contrôlée de nanoparticules de fer sur des multifeuillets de graphène, en utilisant des nanotubes de carbone (CNT) comme « nano-réservoirs » du métal. Les transformations structurales et chimiques subies par les CNTs et les nanoparticules encapsulées pendant la procédure de transfert sur les FLG, le mécanisme de nucléation des nouvelles nanoparticules et d'autres phénomènes reliés à ces effets sont étudiés en temps réel à l'aide d'un porte-échantillon MET-STM (Nanofactory™). La partie finale est dédiée à l'étude en utilisant la MET 3D (ou tomographie électronique) à faible dose d'irradiation de la porosité secondaire induite dans deux classes de zéolithes, ZSM-5 et zéolithes Y par un traitement chimique novateur à base de fluor. La quantification des paramètres les plus importants qui caractérisent cette mésoporosité induite offre des informations directes sur le mécanisme d'attaque chimique. En plus, elle aide à la prédiction des propriétés de ces zéolithes de structure hiérarchisée.

L'approche proposée ici qui utilise conjointement des techniques avancées de microscopie électronique à l'échelle subnanométrique, à trois dimensions et en temps réel, appliquées à l'étude de nanostructures à base de carbone et de zéolithes mésoporeux, nous a permis de comprendre les propriétés et le comportement de ces matériaux. Les résultats obtenus représentent un pas en avant dans le but de contrôler et de prédire l'évolution des processus d'intérêt à échelle nanométrique.

La thèse se divise en cinq chapitres. Un résumé de leur contenu est présenté ci-dessous.

Le premier chapitre présente une courte histoire de la microscopie électronique dans le contexte de son évolution d'une simple technique d'imagerie à une technique capable d'analyses à la résolution atomique dans des conditions de travail dynamiques et hors-équilibre. L'importance des correcteurs d'aberration est soulignée, ainsi que l'avancement technologique qui a permis le développement de nombreuses techniques *in-situ*.

Le deuxième chapitre introduit, dans sa première partie, les propriétés fondamentales du processus catalytique de découpe réalisé par des nanoparticules métalliques sur des substrats de FLG. La deuxième partie présente une caractérisation générale des feuillets de FLG initiaux et nanostructurés. Une troisième section se base sur l'étude de la tomographie électronique des

tranchées à la surface ouverte et des tunnels créés pendant l'hydrogénation catalytique du carbone, processus induits par les nanoparticules métalliques en fer. La résolution nanométrique de la tomographie électronique permet la corrélation des caractéristiques des tranchées avec la topographie de la surface des feuillets de FLG. Une discussion détaillée qui traite l'influence de chaque type de caractéristique topographique sur le mouvement de la nanoparticule est présentée. Dans la dernière partie de ce chapitre, quelques applications potentielles de la découpe catalytique sont discutées, en mettant l'accent sur nos résultats préliminaires sur ce thème complexe.

Le troisième chapitre continue avec l'étude de la découpe catalytique des feuillets de FLG avec des nanoparticules de fer dans une cellule de gaz environnementale. Dans la première partie, les particularités techniques et fondamentales de la microscopie électronique environnementale sont discutées. L'influence du faisceau électronique sur l'environnement réactionnel à l'intérieur d'une cellule de gaz est discutée. La deuxième section montre la réduction des nanoparticules de $Fe_{3-x}O_4$, présentée comme un exemple de l'influence du faisceau électronique dans des cinétiques de réaction normales. Dans la troisième partie du chapitre, l'observation en temps réel du comportement catalytique de découpe des nanoparticules est présentée et discutée. Les particularités des processus de récession du bord et de découpe droite sont corrélées avec les propriétés morphologiques et structurales des nanoparticules actives.

Le quatrième chapitre présente le concept de « nano-impression ». En utilisant une technique combinée MET-STM, un transfert contrôlé de nanoparticules en utilisant le phénomène d'électromigration du canal interne d'un CNT sur une feuille de FLG est présenté. L'étude propose quatre étapes consécutives pour contrôler le transfert de masse : le recuit du tube, la transformation chimique ou la réduction des particules originales, la migration des particules à travers le tube sous l'impulse de la force électrique et le transfert des atomes de métal sur la feuille de graphène. Le mécanisme de la migration des atomes, la formation de nouvelles nanoparticules et la possibilité de mieux contrôler le processus de dépôt sont discutées en détail.

Le cinquième et dernier chapitre introduit une étude de tomographie électronique de la porosité secondaire créée dans les zéolithes ZSM-5 et zéolithe Y à l'aide d'un traitement chimique à base de fluor. La première partie se concentre sur les enchantions de ZSM-5. L'évolution du réseau mésoporeaux en fonction du temps d'attaque du fluor est quantifiée en utilisant un des paramètres extraits des informations tomographiques : le volume poreux, la taille

des pores, leur distribution spatiale et leur l'interconnectivité. La possibilité de reconstruire et caractériser les cages microporeuses est discutée en relation avec nos résultats préliminaires sur ce sujet. La deuxième partie présente le même type d'analyse sur la porosité secondaire induite dans des échantillons de la zéolithe Y. Les particularités du mécanisme d'attaque chimique et l'évolution du réseau mésoporeaux sont alors présentés de manière très détaillée.

Chapitre I

État de l'art de la microscopie électronique appliquée à la science des matériaux

A la fin du XIX^{ème} siècle, les scientifiques se sont rendus compte que la résolution des microscopes optiques est limitée à environs 300 nm par la longueur d'onde de la lumière. La solution pour obtenir une meilleure résolution est venue de la fameuse interprétation de L. de Broglie de la dualité onde-particule. Il a affirmé qu'une onde peut être associée à toutes les particules ayant une masse dont la longueur d'onde dépend du moment de la particule[1]. Comme la longueur d'onde d'un faisceau d'électrons accéléré dans une différence de potentiel de 100 kV est d'environ 4 pm, beaucoup plus réduite que le diamètre d'un atome, il est devenu clair que la microscopie électronique représente la meilleure solution pour réaliser une imagerie à résolution atomique[2]. Peu de temps après, en 1932, le premier Microscope Electrique en Transmission (MET) a été construit à Berlin par M. Knoll et E. Ruska[3,4]. Ils ont reporté une résolution de 50 nm seulement un an après la construction du premier prototype, dépassant ainsi la résolution des microscopes optiques. Quelques années après, Knoll et son équipe ont construit le premier Microscope Electronique à Balayage par Transmission (MEBT)[5].

Dans les premières années après l'invention de la microscopie électronique, les scientifiques l'ont employée exclusivement dans des buts d'imagerie. Néanmoins, ils se sont vite rendu compte qu'elle pouvait potentiellement être bien plus utile pour la science des matériaux. Cela est dû à la multitude de signaux qui se forment lorsque le faisceau d'électrons à haute énergie traverse le spécimen (des électrons dispersés élastiquement et inélastiquement, des rayons X caractéristiques, des électrons secondaires etc.). En raison de cette grande quantité d'interactions et basé sur les optiques d'un microscope électronique, un grand nombre d'analyses

sont possibles[6]. À part l'imagerie avec un contraste de densité moyenne (MET conventionnelle) ou un contraste de phase (MET à haute résolution), les analyses les plus courantes réalisées en utilisant un microscope électronique sont l'Analyse Dispersive en Energie (EDX – Energy Dispersive X-Ray Spectroscopy en anglais) et la Spectroscopie de Pertes d'Energie des Electrons (EELS – Electron Energy Loss Spectroscopy en anglais). Ces deux techniques sont intégrées dans ce qui s'appelle la Microscopie Electronique Analytique (AEM – Analytical Electron Microscopy en anglais). Bien que la microscopie électronique soit associée habituellement à l'imagerie, la diffraction des électrons (ED – Electron Diffraction en anglais) a toujours été une partie de la microscopie électronique.

La contribution de la microscopie électronique au développement de la science des matériaux est inestimable. Traditionnellement, son rôle était de mesurer les propriétés morphologiques, structurales et chimiques d'un matériau et de corréler ces propriétés avec les fonctionnalités du matériau dans des conditions de travail réalistes. Par conséquent, la microscopie électronique est par définition une technique ex-situ dans laquelle seulement des échantillons post-réaction ont été analysés. Néanmoins, un besoin d'observer les transformations subies par un matériau dans son environnement de réaction et dans de vraies conditions de son utilisation a toujours existé. D'autre part, parfois, pour comprendre complètement la performance d'un matériau sous certaines conditions de travail (réactions en phase solide-gaz/liquide, réponse optique etc.), il est nécessaire d'obtenir la structure 3D du matériau. Un tel accès mène à une interprétation sans ambigüités des résultats et construit une relation entre la structure et la réactivité ou la performance catalytique des matériaux. Des images STEM et MET conventionnelles et de haute résolution et des cartographies chimiques sont toutes des projections en 2D d'objets en 3D. La technique capable de reconstruire l'image 3D de l'objet, basée sur des projections 2D STEM et MET est la Tomographie Electronique (ET – Electron Tomography en anglais)[7].

En conclusion, la microscopie électronique a beaucoup progressé, en passant d'une simple technique d'imagerie à un équipement complexe parfaitement adapté pour la nanoscience et la nanotechnologie. Maintenant, en utilisant le même microscope électronique, un nombre conséquent d'analyses peuvent être réalisées consécutivement sans aucun changement dans les optiques du microscope. Le même spécimen peut être analysé dans des conditions

atmosphériques variées à des pressions allant jusqu'à 4 atm et à des températures d'à peu près 1000°C ou sous contrainte électrique et mécanique.

Chapitre II

Aperçu 3D de la nanostructuration catalytique du graphène multifeuillets

Le graphène, un cristal bidimensionnel constitué par des atomes de carbone avec l'hybridation sp^2, est l'unité structurale et fonctionnelle de tous les matériaux graphitiques[8]. L'arrangement des atomes de C avec des liens de type sp^2 dans un réseau hexagonal d'une épaisseur monoatomique mène à des propriétés physiques[9,10] et chimiques[11] uniques. Malgré ses propriétés exceptionnelles, l'implémentation généralisée du graphène à la fois dans les secteurs de l'électronique et de la catalyse reste un défi. Pour faire progresser cette problématique, une stratégie proposée est la nanostructuration catalytique du graphène multifeuillets (FLG – Few Layer Graphene en anglais) en employant des nanoparticules métalliques pour créer des nanotranchées hautement accessibles sur la surface du FLG[12]. Il y a deux types de réactions qui peuvent conduire à la nanostructuration du graphite, en fonction du gaz utilisé : l'hydrogénation[13,14] (H_2) et l'oxygénation[15,16] (O_2).

La morphologie des feuillets de FLG après traitement thermique dans une atmosphère d'hydrogène est présentée dans la Fig. 2.1a. La surface de FLG a été complétement transformée pendant l'hydrogénation catalytique et montre des tranchées avec des longueurs qui varient entre 30 nm et 1 µm et des largeurs variant entre 10 et 100 nm. À grande échelle, l'observation de la découpe semble un processus chaotique, tandis qu'à une échelle plus réduite (Fig. 2.1b), elle semble un processus complétement ordonné. Toutes les tranchées qui apparaissent dans la Fig. 2.1b sont parallèles à la direction <11-20>, en laissant les bords des tranchées avec une morphologie en zig-zag (Fig. 2.1c). Dans notre expérience, des tranchées orientées dans la direction <10-10> (Fig. 2.1d) apparaissent très rarement.

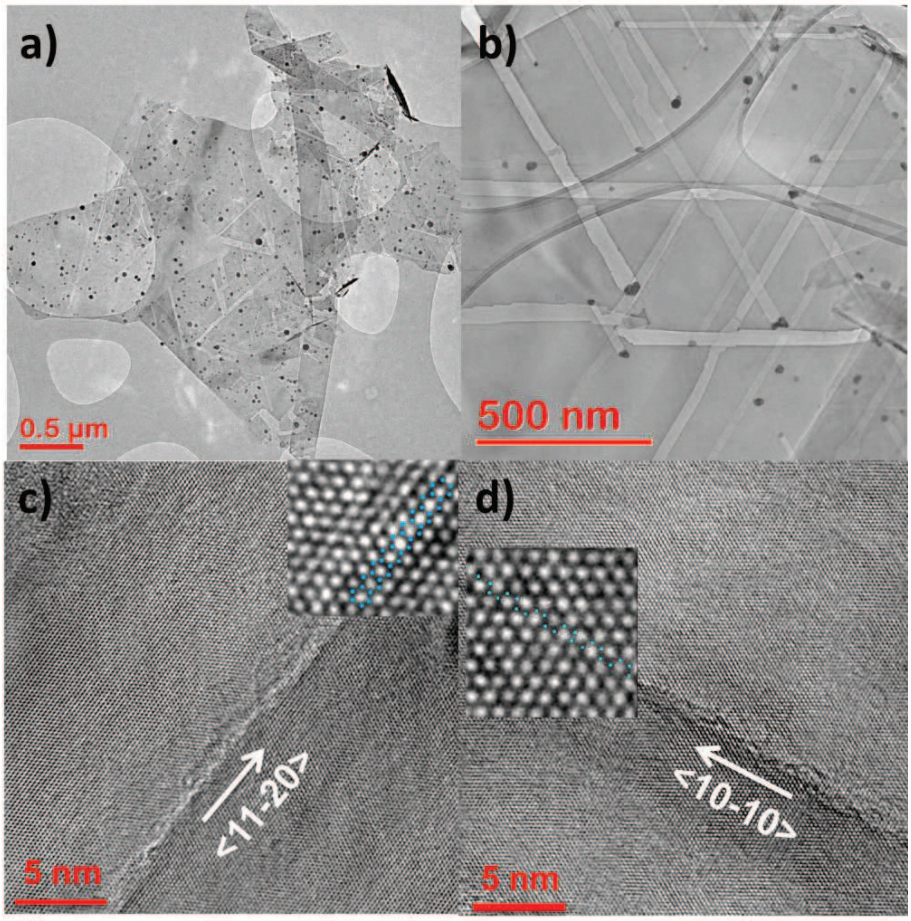

Figure 2.1. a) Image MET d'un feuillet de FLG classique après l'hydrogénation catalytique ; b) Image MET montrant l'orientation préférentielle des tranchées parallèles à la direction <11-20> ; images HR-MET illustrant les types de bords des tranchées : morphologie c) en zigzag et d) en « fauteuil ».

En se basant sur la tomographie électronique, nous avons pu accéder à des informations cruciales qui concernent la topographie d'une feuille de FLG à l'échelle nanométrique. Les analyses ont été donc réalisées dans plusieurs régions du système structuré par voie catalytique pour mieux comprendre le processus de nanostructuration. Une des situations rencontrées se produit lorsque la nanoparticule active a traversé un défaut ou le bord d'une seconde feuille de FLG superposée (Fig. 2.2a). La projection MET (acquise à 0^{o}) de la tranchée sélectionnée pour l'analyse tomographique est présentée dans la Fig. 2.2b, tandis qu'une tranche *xy* à travers la reconstruction de la tranchée est montrée dans la Fig. 2.2c. L'image du haut de la Fig. 2.2d montre une coupe *yz* extraite du côté du bord droit de la tranchée (ligne jaune dans 2.2c). Cela

montre directement le profil géométrique du défaut avec une hauteur d'environ 10 nm. La coupe du bas *yz* de la Fig. 2.2d a été extraite du centre de la tranchée.

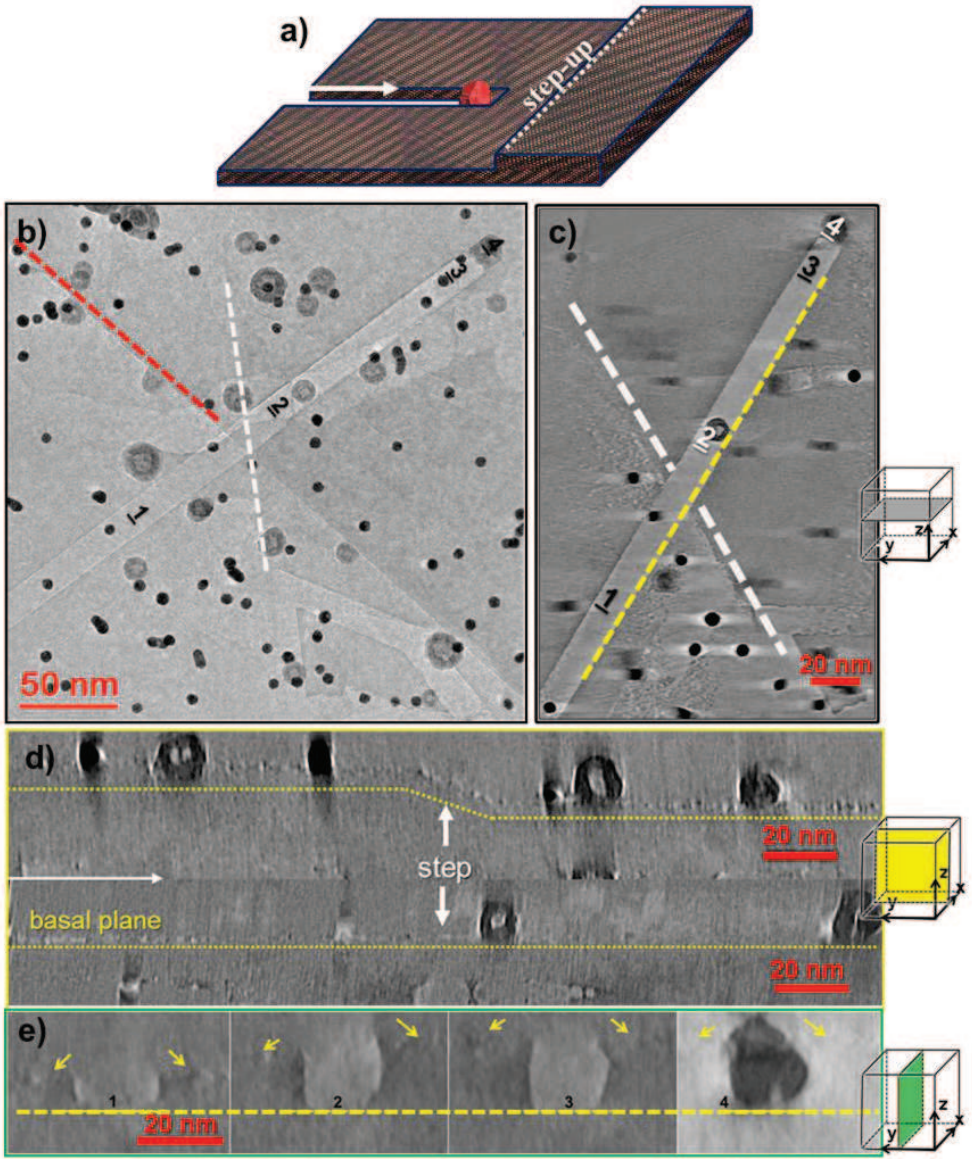

Figure 2.2. a) Représentation schématique de l'interaction d'une particule avec une marche graphitique « ascendante » sur le plan initial de la feuille de FLG ; b) Image MET de la tranchée coupée dans une zone de la FLG non-uniforme ; c) Coupe *xy* à travers le volume reconstruit de la tranchée présentée en 2.2b. La ligne blanche souligne la position du défaut vers la partie supérieure. Les chiffres de 1 à 4 montrent la position des coupes *xz* présentées en 2.2e ; d) Coupes *yz* à travers le bord droit (en haut) (ligne jaune dans 2.2c) et à travers le centre de la tranchée (en bas) ; e) Coupes *xz* montrant l'évolution de la hauteur des parois de la tranchée.

Cela montre que le plan basal initial reste inchangé même quand la particule traverse le défaut. Après ce moment, seule la hauteur des parois de la tranchée change, comme il est montré

dans la Fig. 2.2e. Si on prend en considération la relation entre le profil des tranchées et la forme de la nanoparticule, on observe que la géométrie de la tranchée correspond parfaitement aux caractéristiques géométriques de la nanoparticule à l'origine de la tranchée. Cette corrélation confirme le fait que, même sur des surfaces qui ne sont pas plates, les nanoparticules restent en contact avec le plan basal initial pendant tout le processus de découpe et que la partie active de la surface de la nanoparticule dépend de la hauteur du défaut. Le plan basal graphitique sur lequel la nanoparticule se fixe initialement définit le mouvement de la nanoparticule pendant la découpe. Le plan basal et la direction de découpe ne changent pas lorsque la nanoparticule traverse des obstacles définis par des défauts topographiques « ascendants ». Si la hauteur de ces obstacles est plus grande que la taille des nanoparticules, on assiste à la création de tranchées sous la surface, des tunnels.

Chapitre III

Observation *in-situ* de la nanostructuration catalytique du graphène multifeuillets

Dans certains cas, une restructuration des particules actives pendant le processus de découpe a été clairement observée. Le comportement de la nanoparticule au moment où sa direction de découpe change est particulièrement intéressant. En utilisant les informations de la tomographie électronique, nous étions incapables de prédire le vrai comportement de la nanoparticule active dans des telles conditions. Par conséquent, l'observation en temps réel de la nanostructuration du substrat de FLG est essentielle. La microscopie électronique environnementale (ETEM – Environmental Electron Microscopy en anglais) représente la technique la plus adéquate pour l'investigation des processus dynamiques, offrant accès à une imagerie et à des analyses chimiques à une résolution quasi-atomique en temps réel. Néanmoins, la compréhension des processus physiques et chimiques qui interviennent lors de l'exposition directe au faisceau d'électrons hautement accéléré n'est pas simple. Puisque le faisceau d'électrons peut changer la composition du gaz de réaction du point de vue de charges électriques, modifier la température locale autour de l'échantillon ou induire des changements

structuraux à l'échantillon, tous ces aspects doivent être pris en considération lors de l'analyse des résultats.

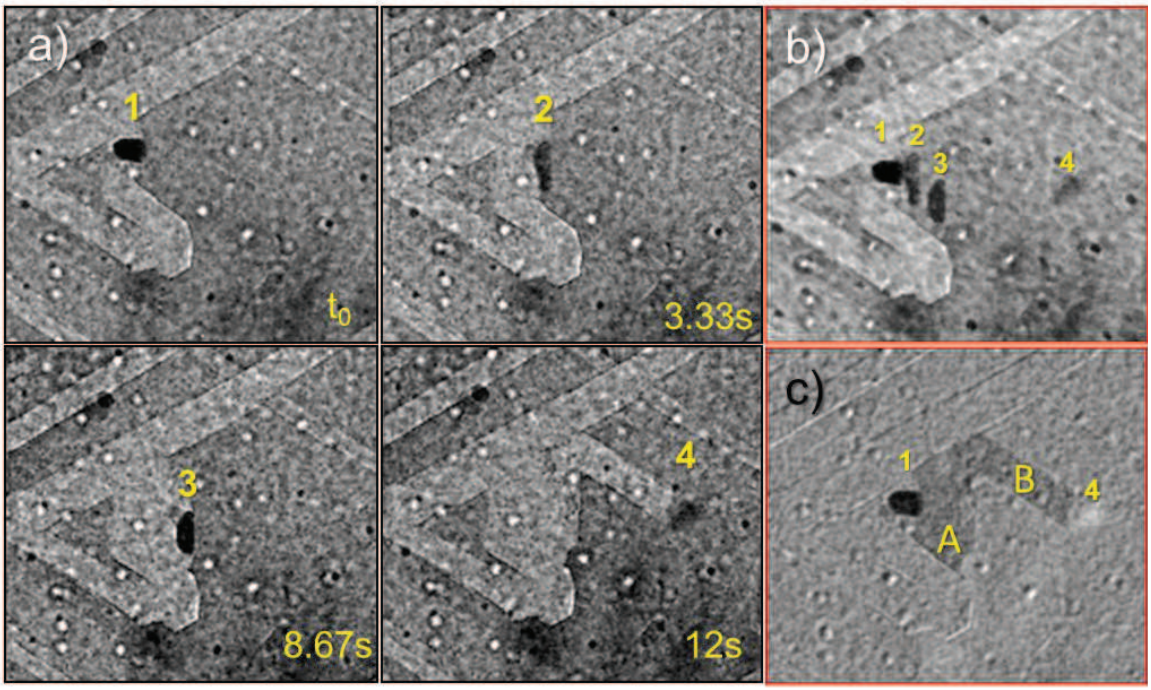

Figure 3.1. a) Série d'images consécutives à faible grandissement d'une nanoparticule qui enlève les atomes de carbone d'un bord de FLG parallèle avec celui-ci; b) Projection Z de la série d'images successives alignées du 3.1a ; c) Image calculée à l'aide de la première et de la dernière image dans 3.1a surlignant les régions de carbone qui ont réagi (zone A – récession des bords et zone B – découpe).

La première observation est liée à la morphologie instable des nanoparticules actives. Pendant la période de prédécoupe, lorsque la nanoparticule est en contact seulement avec le bord de FLG et elle n'est pas clôturée entre les parois restrictifs de la tranchée, la nanoparticule bascule en avant et en arrière sur le bord, en enlevant des atomes de carbone à travers une dissolution de type « récession de bords » (voir Fig. 3.1). Pendant la récession de bords, les nanoparticules subissent une réorganisation continuelle pour maximiser leur interface avec le carbone. En dépit du comportement très dynamique de la particule lors de sa restructuration, du point de vue des rendements de l'enlèvement de carbone, la récession des bords n'est pas très efficace. Le taux de dissolution de carbone pendant la récession des bords est d'au moins 10 fois plus faible que pendant l'activité de découpe. En ce qui concerne le mécanisme de découpe, la récession des bords est causée par l'état proche de la fusion des nanoparticules à ces températures (775-825°C), effet qui est augmenté par la concentration haute de carbone dissoute à l'intérieur

de la nanoparticule de fer. En raison des forces d'adhésion fortes qui apparaissent à l'interface nanoparticule/bord de FLG, ces structures proches de la fusion subissent un processus de refacettage constant. Le refacettage continue jusqu'au moment où une position d'équilibre entre l'orientation des facettes et l'orientation cristallographique des feuillets de FLG est atteinte.

De l'observation préliminaire des échantillons *ex-situ* nanostructurés, nous avons considéré que, lorsque la direction de la découpe est changée, la facette frontale de la nanoparticule perd son rôle actif, rôle pris alors par l'une des facettes latérales. Aucun autre processus de refacettage n'a été pris en considération. Néanmoins, l'observation en temps réel montre que, pendant le changement de la direction de découpe, à la fois sur une surface uniforme de FLG ou lorsqu'elle rencontre un bord du FLG, la nanoparticule subit un processus de refacettage lent et complexe (Fig. 3.2). Ce processus est très dynamique puisque toute la structure et la morphologie de la nanoparticule est changée.

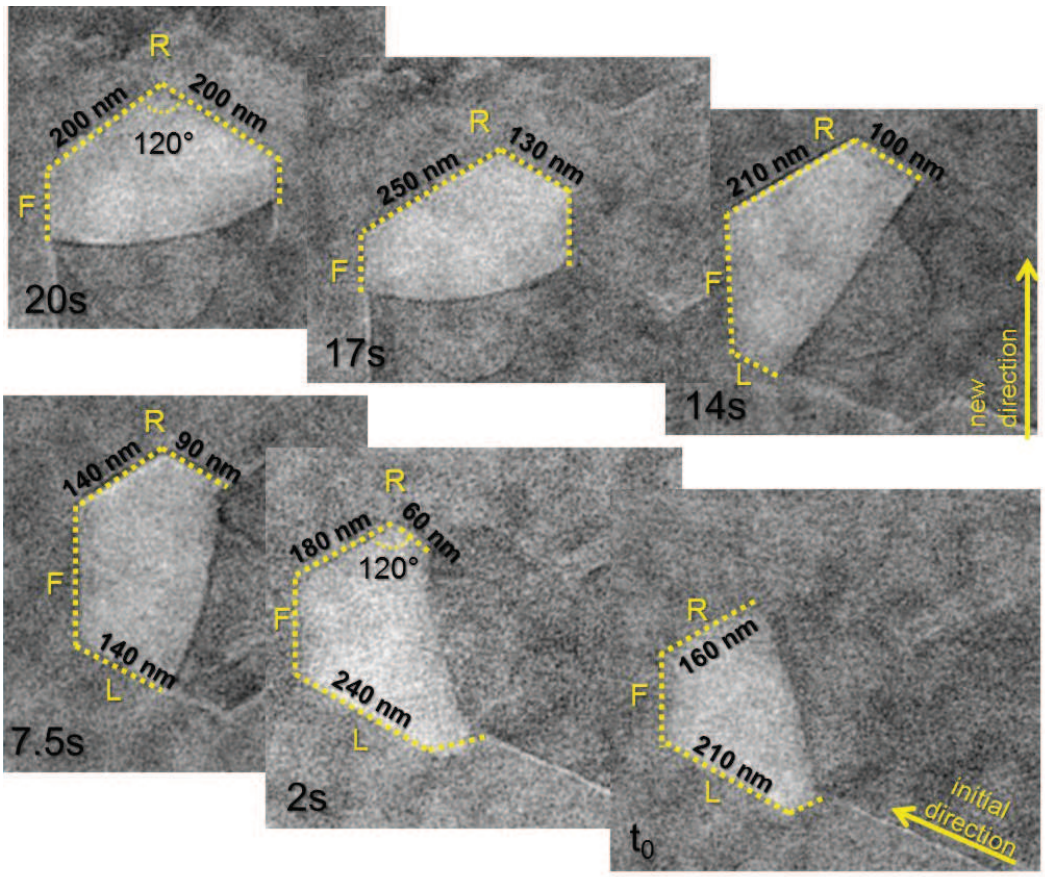

Figure 3.17. Série d'images consécutives montrant des fluctuations dans le facettage d'une nanoparticule pendant le changement de la direction de découpe sur une zone uniforme de FLG. Les images ont été extraites d'un film enregistré à un grandissement de 250kX. La résolution temporelle a été 0,33s.

Chapitre IV

Nanotubes de carbone comme nanopipettes pour déposer des nanoparticules métalliques sur le graphène

Les nouveaux concepts de transfert de nano- ou femtomasse à des endroits bien précises à l'échelle du nanomètre [17] ou de génération de nanofils[18] dans un nanotube ont conduit au développement des approches à façon basées sur un transport orienté de la masse correspondante à l'intérieur ou à l'extérieur des nanotubes de carbone. Durant ces dernières années, des progrès considérables ont été réalisé dans la compréhension de ces phénomènes de diffusion et de transport de « nano-masse » sur les surfaces intérieures[19] et/ou extérieures[20] des CNTs. Plusieurs phénomènes ont été suggérés comme étant susceptibles d'induire la diffusion contrôlée du métal. La force basée sur l'électromigration ($\overrightarrow{F_e}$) a été proposée comme étant l'une de possibilités pour induire la diffusion du métal à l'intérieur des CNTs.[18,19,21] Dans ce contexte, l'étude réalisée dans cette thèse montre que les CNTs peuvent être utilisés comme des nanopipettes pour permettre un transfert nanométrique contrôlé de masse entre deux nanostructures conductrices, c'est-à-dire dans ce cas d'un CNT vers un substrat de graphène et vice-versa. En appliquant une différence de potentiel électrique pour que le flux d'électrons dans le nanotube soit orienté dans la direction de son point de contact avec le FLG, le transfert se réalise entre la partie intérieure du CNT et les feuillets de FLG. Du point de vue phénoménologique, la force d'électromigration ($\overrightarrow{F_e}$) peut agir sur les atomes métalliques le long de l'axe principale du CNT sous l'application du champ électrique à ses extrémités ; cette force est donc responsable du déplacement des nanoparticules de fer du centre du nanotube vers sa sortie. En revanche, un processus « soutenu » par la force d'électromigration est très sensible aux moindres variations électriques qui déterminent des transferts mal contrôlés. Le principal facteur responsable pour les variations non-contrôlées de courant est la structure brute du point de vue électrique du CNT et la présence du carbone résiduel amorphe qui couvre parfois ses parois. Dans ce cadre, l'évolution d'une structure mal conductrice de courant à une structure très conductrice, avec peu de défauts dans les parois des CNTs, peut se faire par chauffage Joule lors du passage de courant. De cette manière, le système NPs de Fe @ CNT peut devenir un dispositif Ohmique après une courte exposition à des impulsions de courant (au moins deux impulsions). Par la suite, en ce qui concerne le processus

de transfert proprement dit, il faut mentionner que les atomes de métal sont liés faiblement au substrat graphitique de la surface intérieure du tube, ce qui facilite leur diffusion sur la surface interne dans la direction imposée par la force d'électromigration.

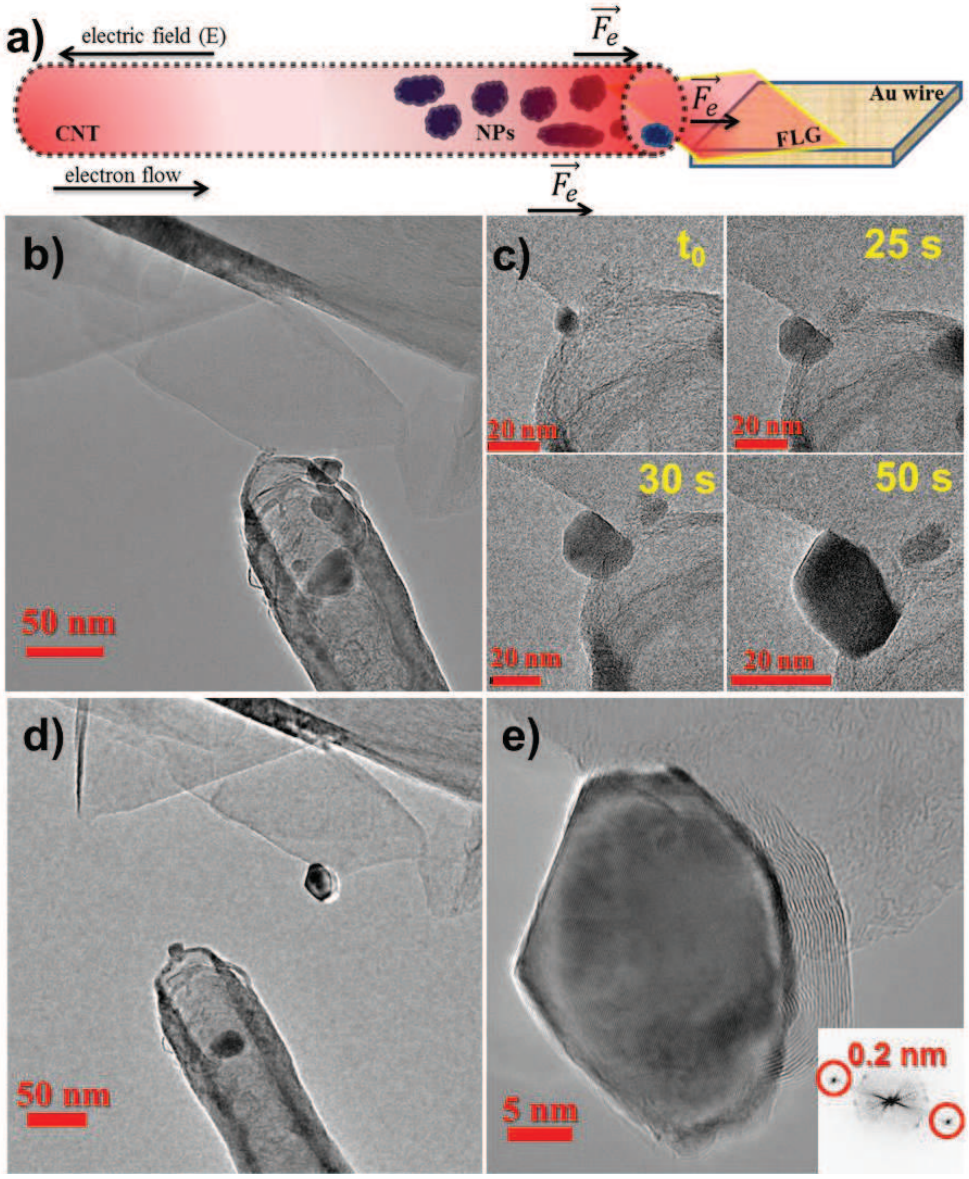

Figure 4.1. Dépôt contrôlé d'une nanoparticule métallique de Fe au bord d'une feuille de FLG. a) Représentation schématique de l'expérience montrant les forces qui interviennent, une fois la différence de potentiel électrique appliquée. b) Le système CNT/FLG avant la déposition de la nanoparticule. c) Série d'images consécutives montrant la croissance de la nanoparticule au bord de la feuille de graphène (résolution temporelle 0,33s). d) Le système CNT/FLG après la déposition de la nanoparticule au bord du FLG. e) Image HR-TEM de la nanoparticule finale attachée au bord du FLG. L'analyse FFT (Fast Fourier Transform en anglais) permet de déduire un paramètre de réseau d'environ ~0.2 nm, caractéristique du Fe métallique dans les structures de type ϕ et γ.

La nanoparticule commence à croître au voisinage du premier site riche en défauts structuraux que les atomes diffusants rencontrent. La manière dans laquelle la croissance de la nanoparticule se déroule dépend également de la position du germe initial sur le feuillet de FLG, c'est-à-dire sur la surface plane ou au niveau du bord. Le facettage de la nanoparticule est en changement continu tout au long de la croissance de la particule, mais en maintenant en général une forme hexagonale. L'aspect facetté et le contraste de phase et de diffraction observée par imagerie HR-TEM au niveau de la particule pendant le processus de croissance montrent que sa température décroît dans la direction perpendiculaire au substrat de graphène, ce que facilite sa cristallisation au fur et à mesure du processus. Le fait que les germes initiaux des nanoparticules peuvent être interprétés comme des pièges « froides » pour les atomes diffusants explique également pourquoi une seule nanoparticule se forme à la fois.

Chapitre V

Aperçu MET 3D de la porosité hiérarchique des zéolithes ZSM-5 et Y

Ce chapitre présente une étude de MET-3D de la porosité secondaire induite par un attaque chimique en utilisant une solution à base de fluor sur deux familles de zéolithes, ZSM-5 et zéolithe Y. Une description complète de la méthodologie de travail en tomographie électronique (conditions d'acquisition, procédure de segmentation, quantification etc.) est présentée. En définissant des protocoles spécifiques en fonction de propriétés et du comportement des échantillons, des représentations 3D pertinentes qui traduisent les caractéristiques morphologiques des échantillons de zéolithes ont été obtenues. De plus, ce type de méthodologie, une fois mise au point, a permis l'analyse d'un grand nombre d'échantillons, en permettant à la tomographie électronique de franchir une étape essentielle dans son développement, afin de devenir une technique plus accessible et applicable sur un nombre de grains significatif de l'échantillon. L'approche 3D-MET a fourni des informations précises sur la taille de pores et sur leur distribution spatiale, ainsi que de manière plus générale sur leur volume poreux et connectivités. Du point de vue phénoménologie, des informations directes sur le mécanisme de

dissolution de réseaux mixtes aluminosilicates ont été extraites à partir des reconstructions obtenues. En contrôlant avec attention les conditions d'acquisition, une image 3D du réseau microporeux de zéolithes ZSM-5 a été également obtenue. Ces résultats ouvrent la voie d'obtention d'une vraie image 3D des micropores, image qui est d'une importance colossale après les traitements post-synthèse des zéolithes, dans le but général de la compréhension et de la prédiction des propriétés de ces matériaux.

Conclusions et perspectives

Dans le cadre de cette thèse, des techniques avancées de microscopie électronique en transmission (MET) ont été utilisées avec le but d'étudier les propriétés de trois types de nanomatériaux et nanostructures: graphène multifeuillets (FLG) avec des nanomotifs, nanotubes de carbone (CNTs) et zéolithes mésoporeux.

Des réactions catalytiques hydrogène-carbone ont été employées dans la nanostructuration des feuillets de FLG à l'aide de nanoparticules de fer avec un réseau de tranchées multi-orientées. Tout d'abord, les propriétés du mouvement des nanoparticules pendant l'action de découpe ont été étudiées ex-situ en utilisant la tomographie électronique. Les résultats ont montré la grande influence à la fois de la topographie du substrat de FLG et de la morphologie des nanoparticules actives dans la définition des caractéristiques du processus de coupure. Les nanoparticules localisées initialement aux bords ou attachées aux défauts sur les feuillets de FLG créent des tranchées à la surface ouverte ou des tunnels avec des orientations, des longueurs et des morphologies définies par la cristallographie et la topographie du substrat de carbone. L'analyse en coupe transverse des volumes 3D souligne le rôle du profil géométrique des nanoparticules actives sur la taille et la forme de la tranchée, en mettant l'accent sur l'évolution du plan basal dans les tranchées qui résultent du processus de découpe. L'observation en temps réel du processus de découpe dans une cellule environnementale de gaz s'est concentrée sur la compréhension de l'influence de la morphologie des nanoparticules sur le processus dynamique de nanostructuration. Elle a montré un mécanisme de création de tranchées plus complexe que la prédiction effectuée par les recherches ex-situ. Les taux de création de tranchées n'ont pas été constantes puisque la vitesse des nanoparticules a varié de quelques $nm \bullet s^{-1}$ à quelques centaines de $nm \bullet s^{-1}$. Une restructuration continue des nanoparticules de fer proches de la fusion a été

proposée comme étant l'origine principale de la variation du taux de création des tranchées. L'existence de deux mécanismes de découpe, la récession des bords et la découpe droite, ainsi que la fluctuation permanente d'une nanoparticule active entre les deux, ont été associées à l'existence d'une affinité entre certaines facettes des nanoparticules et certaines orientations cristallographiques du substrat de FLG. Comme l'observation directe des nanoparticules pendant le changement de la direction de découpe l'a montrée, cette affinité peut également être responsable pour le fait que les nanoparticules tournent sur des surfaces uniformes de feuillets de FLG.

Le transfert contrôlé de nanoparticules de fer sur des feuillets de graphène suspendues a été réalisé et observé en temps réel en utilisant un porte-échantillon MET-STM (Nanofactory™). De manière générale, en utilisant le processus d'électromigration de nanoparticules à base de fer dans des nanotubes de carbone comme force motrice pour le déplacement de la matière, nous avons montré la disponibilité de tous les ingrédients nécessaires pour l'impression de séries binaires de « zéro » et de « un » à l'échelle nanométrique. Une procédure de recuit de type Joule a été conçue pour assurer un comportement reproductible du tube qui agit finalement comme un « stylo » nanométrique dans le processus d'écriture. En effet, le tube rempli de métal peut déposer, par un mécanisme de type mûrissement d'Ostwald, des nanoparticules de métal sur la surface de la feuille de graphène, très important, d'une façon contrôlée. Inverser le voltage assure le transfert des nanoparticules de la surface du graphène dans les nanotubes, démontrant la possibilité d'effacement du « stylo » associé au nanotube de carbone, ouvrant ainsi la voie à la correction des « erreurs d'écriture ». De manière plus précise, le protocole pour arriver au contrôle du transfert, les transformations chimiques et structurales subies par les nanoparticules de $Fe_{3-x}O_4$ et par le CNT, le mécanisme de croissance des nanoparticules à peine formées et d'autres phénomènes en relation avec ces processus ont été étudiés.

Dans la dernière partie de la thèse, l'évolution de la mésoporosité secondaire dans des zéolithes traitées avec une solution à base de fluor a été étudiée en employant la tomographie électronique à faible dose d'irradiation. En plus de la compréhension du mécanisme de dissolution de la structure Si/Al dans les zéolithes ZSM-5 et Y, l'approche a permis à mieux mettre en évidence l'apport de la tomographie électronique pour l'obtention d'informations 3D quantitatives telles que la taille et la distribution spatiale des pores, la porosité d'ensemble et la connectivité du réseau poreaux. Ces paramètres ont été employés pour créer une cinématique

d'évolution du réseau poreaux secondaire en fonction de la durée de l'attaque chimique au fluor. Une résolution supérieure à 1,1 nm a été reportée, permettant ainsi la visualisation directe des cages des micropores dans les zéolithes ZSM-5 et l'interface entre les différents domaines cristallins de la zéolithe Y.

Les études présentées dans le cadre de cette thèse ouvrent de nouvelles perspectives pour l'optimisation des propriétés des nanostructures de carbone et des matériaux zéolitiques, ainsi que pour le développement de nouvelles approches d'analyse autour de la tomographie électronique. En combinant les techniques de microscopie électronique in-situ avec la tomographie électronique, à la fois en temps réel ou post-réaction, il sera possible d'obtenir une quantification précise de la dynamique des réactions chimiques ou catalytiques et plus généralement de l'évolution de nanomatériaux et de nano-objets 3D dans des conditions environnementales particulières. .

Références

1. Reimer, L. & Kohl, H. in *Transmission Electron Microscopy* 45 (W. T. Rhodes, 2008).
2. Krumeich, F. Properties of Electrons, their Interactions with Matter and Applications in Electron Microscopy. at <http://www.microscopy.ethz.ch/downloads/Interactions.pdf>
3. Ruska, E. The Development of the Electron Microscope and of Electron Microscopy. (1986). at <www.nobelprize.org>
4. Knoll, M. & Ruska, E. *Z Phys.* **78,** 318 (1932).
5. Knoll, M. *Z. Tech. Phys.* **16,** 467–475 (1935).
6. Williams, D. B. & Carter, C. B. in *Transmission Electron Microscopy* 3–22 (Springer US, 2009). at <http://link.springer.com.scd-rproxy.u-strasbg.fr/chapter/10.1007/978-0-387-76501-3_1>
7. Ersen, O., Florea, I., Hirlimann, C. & Pham-Huu, C. Exploring nanomaterials with 3D electron microscopy. *Mater. Today* doi:10.1016/j.mattod.2015.04.004
8. Geim, A. K. & Novoselov, K. S. The rise of graphene. *Nat. Mater.* **6,** 183–191 (2007).
9. Novoselov, K. S. *et al.* Electric Field Effect in Atomically Thin Carbon Films. *Science* **306,** 666–669 (2004).
10. Castro Neto, A. H., Guinea, F., Peres, N. M. R., Novoselov, K. S. & Geim, A. K. The electronic properties of graphene. *Rev. Mod. Phys.* **81,** 109–162 (2009).
11. Geim, A. K. Graphene: Status and Prospects. *Science* **324,** 1530–1534 (2009).
12. Wang, M. *et al.* Structural Modification of Graphene Sheets to Create a Dense Network of Defect Sites. *J. Phys. Chem. Lett.* **4,** 1484–1488 (2013).
13. Tomita, A., Sato, N. & Tamai, Y. Hydrogenation of carbons catalyzed by nickel, platinum and rhodium. *Carbon* **12,** 143–149 (1974).
14. Tomita, A. & Tamai, Y. Hydrogenation of carbons catalyzed by transition metals. *J. Catal.* **27,** 293–300 (1972).
15. Goethel, P. J. & Yang, R. T. Mechanism of catalyzed graphite oxidation by monolayer channeling and monolayer edge recession. *J. Catal.* **119,** 201–214 (1989).

16. Baker, R. T. K., France, J. A., Rouse, L. & Waite, R. J. Catalytic oxidation of graphite by platinum and palladium. *J. Catal.* **41,** 22–29 (1976).
17. Dong, Tao, Zhang, L., Zhang & Nelson, B. J. Nanorobotic Spot Welding: Controlled Metal Deposition with Attogram Precision from Copper-Filled Carbon Nanotubes. *Nano Lett.* **7,** 58–63 (2007).
18. Zou, R. *et al.* Melting of metallic electrodes and their flowing through a carbon nanotube channel within a device. *Adv. Mater. Deerfield Beach Fla* **25,** 2693–2699 (2013).
19. Král, P. & Wang, B. Material Drag Phenomena in Nanotubes. *Chem. Rev.* **113,** 3372–3390 (2013).
20. Regan, B. C., Aloni, S., Ritchie, R. O., Dahmen, U. & Zettl, A. Carbon nanotubes as nanoscale mass conveyors. *Nature* **428,** 924–927 (2004).
21. Suzuki, M. *et al.* Current-induced breakdown of carbon nanofibers. *J. Appl. Phys.* **101,** 114307 (2007).

Introduction

Electron microscopy is a versatile characterization technique allowing a large range of investigations to be performed in both *ex-situ* and *in-situ* modes. Today, an electron microscope is more than an imaging tool, it is a fully equipped work-station for nanoscience and nanotechnology. It allows samples to be analyzed in real-time under different working conditions (gas atmosphere, liquid medium, bias voltage, high temperatures, etc.) and reveals a wide range of structural, morphological and chemical properties.

In this thesis, advanced Transmission Electron Microscopy (TEM) techniques are used to characterize and fabricate new nanomaterials with applications in nanoelectronics and catalysis. Three types of functionalized materials are investigated: nanopatterned few-layer graphene (FLG), carbon nanotubes (CNTs) and mesoporous zeolites. In the first part of the thesis, the nanopatterning process of FLG flakes by iron nanoparticles is studied using an approach combining electron tomography and environmental TEM. Electron tomography reveals a strong influence of both the topography of the FLG substrate and the morphology of the active nanoparticles in defining the characteristics of the channeling process. The real-time observation of the process inside an environmental gas cell (Protochips™ Atmosphere) reveals a complex channeling mechanism, i.e. irregular channeling rates and constant restructuring of the active nanoparticles. The permanent changing between the two cutting mechanism identified (edge recession and straight channeling) is associated with the existence of an affinity between some facets of the nanoparticles and certain crystallographic orientations of the FLG substrate. The second part of the thesis presents a simple procedure for achieving the controlled nano-printing of iron nanoparticles on suspended graphene flakes, using carbon nanotubes as metal "nano-reservoirs". The structural and chemical transformations undergone by the CNTs and the encapsulated nanoparticles during the transfer procedure, the nucleation mechanism of the newly formed nanoparticles and other related phenomena are investigated in real-time using a TEM-STM holder (Nanofactory™). The last part deals with the low-dose 3D TEM investigation of the secondary porosity induced in two classes of zeolites, ZSM-5 and zeolite Y, by an innovative fluoride-based chemical treatment. The quantification of the most important parameters characterizing the induced mesoporosity offers an insight in the etching mechanism and also helps predict the properties of these hierarchical zeolites.

The above presented investigations using advanced *ex-situ* and *in-situ* TEM techniques of carbon-based nanostructures and mesoporous zeolites help us understand the properties and the behaviors of these materials. The results obtained represent a step-forward in the attempt to control and predict the evolution of nanoscale processes.

The thesis is divided in five chapters. A summary of their content is presented below.

Chapter I presents a brief history of electron microscopy in the context of its evolution from a simple imaging technique to one capable of atomic resolution analyses under dynamic working conditions. The importance of the aberration correctors is highlighted together with the technological advancement which allowed the development of numerous *in-situ* techniques.

Chapter II introduces in the first part the fundamental properties of the catalytic channeling process carried out by metallic nanoparticles in FLG substrates. The second part presents a general characterization of the initial and the nanopatterned FLG flakes. The third section is based on the electron tomography investigation of the open-surface channels and the tunnels created during the catalytic hydrogenation of carbon, process sustained by the metallic iron nanoparticles. The nanometric resolution of the electron tomography allows the correlation of the channels characteristics and the surface topography of the FLG flakes. A detailed discussion about the influence of each type of topographical feature on the nanoparticle motion is presented. In the last part of this chapter, some potential applications of the catalytic channeling are discussed with emphasis on our preliminary results on this topic.

Chapter III continues the investigation of the catalytic channeling of FLG flakes with iron nanoparticles in an environmental gas cell. In the first part, the technical and fundamental particularities of the environmental electron microscopy are discusses. The influence of the electron beam on the reaction environment inside a gas E-cell is highlighted. The second section shows the reduction of the $Fe_{3-x}O_4$ nanoparticles, presented as an example on the electron beam "interference" in the normal reaction kinetics. In the third part of the chapter, the real-time observation of the channeling behavior of the nanoparticles is presented and discussed. The particularities of the edge recession and the straight channeling cutting mechanism are correlated with the morphological and the structural properties of the active nanoparticles.

Chapter IV presents the concept of "nano-printing". Using a combined TEM-STM technique a reliable electrically controlled transfer of nanoparticles from the inner part of a CNT onto a FLG sheet is presented. The study proposes four consecutive steps in order to control the

mass transfer: the annealing of the tube, the chemical transformation or the reduction of the original particles, the particle transfer through the tube under the impulse of the electromigration force, and the dispensing of the metal atoms on the graphene sheet. The mechanism of the atom migration, the formation of new nanoparticles and the possibility of correcting the error in the deposition process are discussed in detailed.

Chapter V introduces an electron tomography study of the secondary porosity created in ZSM-5 and Y zeolites by a fluoride-based chemical treatment. The first part tackles the ZSM-5 samples. The evolution of the mesoporous network as a function of the fluoride etching time is followed using a number of parameters extracted from the tomography data: porosity, pore size and spatial distributions and pores interconnectivity). The possibility of achieving a 3D reconstruction of the microporous cages is discussed in relation with our preliminary results on this topic. The second part presents the same type of analysis on the secondary porosity induced in zeolite Y samples. The particularities of the etching mechanism and the evolution of the mesoporous network are then deepened.

Chapter I

State-of-the-art in electron microscopy applied to materials science

1.1. A brief history of electron microscopy

At the end of the nineteenth century scientists realized that the resolution of the visible-light microscopes is limited to about 300 nm by the wavelength of light. As it was a fundamental limitation and not a technological one, their frustration was immense[1]. The solution came from L. de Broglie's famous interpretation of the wave-particle duality. In 1905, A. Einstein introduced the concept of photons in order to explain the photoelectric effect, thus creating the concept of wave-particle duality for light[2]. L.de Broglie assumed that a wavelength can be associated for all particles with a finite mass and this wavelength depends on the momentum carried out by the particle[3]. The de Broglie's theory was demonstrated by an experiment involving beams of electrons shot in crystalline metal targets[4]. As the electrons diffracted in the same way were X-rays do, the wave character of particles was proven and the way towards electron microscopy was opened. As the wavelength of an electron beam accelerated in a 100 kV potential drop is around 4 pm, much smaller than the diameter of an atom, it was soon clear that electron microscopy represents the best solution for achieving atomic resolution imaging[5]. It was not long (1932) until the first Transmission Electron Microscope (TEM) was built in Berlin by M. Knoll and E. Ruska[6,7]. They reported a 50 nm resolution only one year after the first prototype was built, undoubtedly overcoming the resolution of the visible-light microscopes. A few years later, Knoll and his team built the first Scanning Transmission Electron Microscope (STEM)[8].

The overall designs of the first electron microscopes (EM) are generally still used in modern ones. At the top of the microscope stays the electron source. The electrons emitted are accelerated in a potential drop at acceleration voltages ranging from 60 to a few hundred kV.

Above the sample position, a system of electromagnetic lenses (condenser lenses) is converting the electron beam in a parallel (TEM) or condensed (STEM) one. In TEM microscopes the image of the sample is created by another lens, called the objective lens, and a system of intermediate lenses magnifies this image which is further projected onto the detector.

Modern microscopes contain many more additional components, allowing them to be highly versatile tools. However, throughout the evolution of electron microscopy understanding and designing the proper electromagnetic lenses represented the main struggle for microscopiests. A few years after the invention of the EM, O. Scherzer demonstrated that spherical and chromatic aberrations, which drastically distorts the electron beam passing through an electromagnetic lens, could not be eliminated by any technological advance[9,10]. Therefore, the perspective of imaging matter with atomic resolution faded away very quickly. This limitation can be explained in a very simplified way by comparing the electromagnetic lenses with their optical counterparts. The aberration of optical lenses can be neutralized in a dual converging-diverging lens system, where both lenses generates equal aberrations but with an opposite sign that add to zero. However, all electromagnetic lenses are converging ones and at that time Scherzer had no solution for this problem. Ten years later, in one of the most important paper for the electron microscopy field, he proposed a lens design capable of correcting spherical aberrations (Cs)[11]. However, for the next half-century all attempts to build a functional aberration corrected EM had failed, mostly due to technological limitations. An aberration corrector is a multi-lens system that requires a very precise alignment adjustable in real-time. The hardware and software technologies capable of controlling such systems had become available only in the mid-1990s. Very soon, H. Rose, M. Haider and K. Urban built up the first stable Cs-corrected TEM, and in 1998 they reported the first Cs-corrected high resolution TEM image recorded with a corrected commercial microscope[12]. Their corrector design was based on hexapoles lenses and nowadays this design is the most common one in corrected EM, for both TEMs and STEMs. Almost at the same time as Rose's group, O. Krivanek and N. Dellby constructed the first stable Cs probe-corrected STEM microscope, equipped with a corrector based on a quadrupole–octopole design[13].

Nowadays, corrected EMs capable of resolving structures with atomic resolution even for the most complex alloys[14], or identifying single atom dopants in two-dimensional materials are largely available[15,16]. The aberration corrected S/TEM microscopes opened a new era in the material science, and especially in those linked with nanoscience where more and more

researches are focused in nowadays. Indeed, the most important developments during the last decades are reinforced by the extensive use of electron microscopy to uncover the microscopic structure, as well as the chemical composition of the materials, which allow one to build up theoretical models and optimize the industrial processes.

1.2. The electron microscope: a multifunctional tool

In the first years of electron microscopy scientists used it exclusively for imaging. However, they soon realized that the contribution of an EM to the material science can go well beyond imaging. This is due to the multitude of signals formed when the high-energy electron beam passes through the specimen (elastically and inelastically scattered electrons, characteristic X-rays, secondary electrons, etc.). Due to this large amount of interactions and based on the optics of an EM, a large number of analyses are possible[1]. Beside imaging with mass contrast (conventional TEM) or phase contrast (high resolution TEM), the most common analysis performed using an EM are the Energy Dispersive X-ray Spectroscopy (EDX) and Electron Energy Loss Spectroscopy (EELS). These two techniques are integrated in what is called Analytical Electron Microscopy (AEM). Although, electron microscopy is mostly associated with images, electron diffraction had always been a part of EM. The optics of an EM allows a direct switch between imaging and diffraction modes. Nowadays, various electron diffraction techniques are incorporated in S/TEM microscope (selected area, nanobeam, and convergent beam electron diffraction) revealing diverse and complementary structural information at nanoscale[17,18].

Probably the most common TEM analysis is the mass-thickness contrast imaging (conventional TEM). The mass-thickness contrast is based on the number of electrons scattered by the specimen at angles larger than the objective aperture (not reaching the detector). Thicker regions of the specimen will scatter more electrons then the thinner ones and also the electrons will be more scattered by heavier elements than by lighter ones[19,20]. The scale range of conventional TEM is between a few μm to a few nm. It is revealing information related to the sample size and shape (i.e. for metallic nanoparticles and zeolite crystals), the morphology of the sample (i.e. porous materials, carbon nanotubes, nanostructured few-layer graphene) or the dispersion of catalytic phases on substrates (i.e. metallic nanoparticles dispersed on Al_2O_3). For

crystalline samples the conventional imaging can be directly combined with the electron diffraction mode (diffraction contrast) offering a complete morpho-structural characterization of the sample. Moreover, electron diffraction combined with advanced mathematical models can be applied even for amorphous materials (i.e. polymers, glasses) in order to investigate their short-range structural order[21].

High resolution TEM imaging (HR-TEM) is one of the most important and at the same time one of the most complex TEM technique. This is because HR-TEM imaging is based on the phase contrast. The nature of the phase contrast is the interference of the scattered wave and the incident wave at the image point. The complexity of the phase contrast arises from its dependency on multiple factors: the aberrations of the lenses, the spatial and temporal coherencies of the electron beam and the thickness of the analyzed specimens[22]. The motivation behind the construction of the aberration correctors was the need to eliminate the influence of spherical and chromatic (Cc) aberrations from the HR-TEM imaging. These aberrations were the main factor limiting the resolution of an electron microscope. With today's microscopes the atomic resolution imaging has become almost a routine analysis. However, interpreting the HR-TEM images is not really straightforward. When the HR-TEM is used for distinguishing different phases of catalytic nanoparticles, to study metal/oxide core-shell structures, or to identify structural defects in zeolitic materials, the image interpretation can be relatively simple. Nevertheless, the complexity of the nanomaterials used today in nanoelectronics, catalysis or even metallurgy, and the difficulty of interpreting the HR-TEM images of such structures, lead to parallel development of software capable of simulating the HR-TEM images in order to assist the image interpretation[23].

After the successful implementation of aberration probe correctors, the High-Angle Annular Dark-Field (HAADF) working mode in STEM microscopes became one of the most important microscopy techniques. HAADF imaging is also referred as Z-contrast imaging. This is due to the fact that HAADF images are created mostly with high angle incoherently scattered electrons, and this "Rutherford" scattering depends strongly on the atomic number ($\sim Z^2$)[24]. As the diffraction contrast effects are smoothed out, HAADF imaging is unaffected by contrast inversions created by small changes in lens focus or variations of the specimen thickness[25]. The interpretation of HAADF images at atomic resolution is significantly more accessible than the

one of HR-TEM images. Nowadays, the STEM-HAADF is used to analyze all sorts of materials, from metallic nanoparticles to two-dimensional structures and complex superconductors[15,26–28].

As already discussed, one of the advantages of EM is the great variety of signals created by the interaction of the electrons with the specimen, which can be analyzed. Analytical signals, the characteristic X-rays and inelastically scattered electrons, are two of the most important additional signals used in EM. They are both created when the ionization of the specimen's atoms occurs due to their interaction with the electron beam[29,30]. Characteristic X-rays are studied by the EDX spectroscopy. The energy of the X-rays emitted by a chemical element is characteristic of that element. Therefore, the first information offered by EDX spectroscopy is related to the chemical composition of the samples and by integrating the intensity of the signal from the EDX spectrum a quantitative evaluation of the chemical composition can be obtained. However, EDX cannot allow one to determine the localization of the different elements constituting the signal inside the sample. Throughout the evolution of EDX spectroscopy, the major struggle was to obtain an efficient collection of the X-ray signals. Through a continuous optimization of the X-ray detectors and their incorporation into aberration corrected S/TEM microscopes, the EDX-based elemental maps with atomic resolution are nowadays available[31]. The energy lost by the electrons from the electron beam when ionizing some of the specimen's atoms, can be also characteristic for each element constituting the specimen. The energy loss of the electron beam is used to perform EELS spectroscopy. In addition to elemental identification and quantification, EELS spectra analysis can identify a complex set of structural (i.e. atomic coordination and oxidation state), surface (i.e. vibrational modes of surface atoms) and optical properties[32,33]. However, in order to have access to these properties, a high energy resolution is required. The energy resolution in the EELS spectra is influenced by the electron spectrometer, but mostly by the energy spread of the electron beam. Today, with the development of field emission guns (FEGs) and energy monochromators an energy resolution of 10 meV is achievable[34].

The contribution of EM to the development of material science is inestimable. Traditionally, the role of EM was to measure the morphological, structural and chemical properties of a material and to correlate these properties with the functionalities of the material in real working conditions. Therefore, EM is by definition an *ex-situ* technique where only post-mortem samples were analyzed. However, a need to observe the transformations undergone by a material in its real environment and under real working conditions had always existed. There

have been numerous early attempts to implement *in-situ* EM techniques in the field of materials. The most successful one was the implementation of the *in-situ* heating technique. A furnace-based heating holder was used in 1960 to study the annealing effect on dislocations in aluminum[35]. The need to analyze some materials under environmental conditions (gas and temperature) was recognized by E. Ruska, one of the EM inventors, as he proposed in 1942 a design for a differentially vacuum pumped environmental microscope[36]. The influence of the reaction environment is critical for the evaluation of the geometric, composition and electronic structure of the catalyst, as well as in understanding its properties and behavior. However, the technological barriers led to a slow development of the environmental EM. Nevertheless, a small number of laboratories have independently developed environmental cells (E-cells) for the EM, based both on the Ruska's design and on the window-type E-cell design[37,38]. Their studies focused on catalysis processes, oxidation-reduction reactions, wet specimens in hydrated mediums and dynamic processes[39,40]. The need to observe in real-time the structural changes undergone by a material passed by an electrical current required the implementation of *in-situ* electrical probing. Its successful application came relatively late, in 1998, when Takayanagi reported the electrical probing of atomic-sized gold wires inside the EM[41]. The development of *in-situ* EM techniques was interrelated with the instrumentation advancement. In the last 20 years, the hardware and software revolution helped the rapid development of numerous *in-situ* techniques. This, together with the parallel development of ultra-high resolution S/TEM microscopes and their analytical capabilities had transformed the *in-situ* electron microscopy from a technique available only for large laboratories to one largely implemented worldwide. Nowadays, the real time dynamical observation of the structural and chemical changes of nanomaterials performing in various environments (reactive gas atmospheres, liquid mediums) or/and under thermal, electrical or mechanical stimuli is available at atomic resolution.

Sometimes, in order to fully understand the performance of a material under some working conditions (solid-gas/liquid phase reactions, optical response, etc.), it is necessary to obtain the real 3D structure of the material. Such an access leads to an unambiguous interpretation of the results and build up a relation between the structure and the reactivity or catalytic performance of the materials. Conventional and high resolution S/TEM images and the elemental maps are all 2D projections of 3D objects. The technique capable of reconstructing the 3D image of the object, based on the 2D S/TEM projections is the electron tomography (ET)[42].

The tomography, as a general technique applied in astronomy, medicine, etc., is based on complex mathematical principles, first proposed by Radon in 1917[43]. Electron tomography has been first applied for studying the morphology of living cells[44] in 1968. In material science the ET was applied more than 30 years later by the group of K. P. de Jong when investigating the nanoparticle distribution on hierarchical porous mordenite zeolites[45]. In the last 15 years, ET applied in material science has experienced a continuous development. The application of cryo- and low-dose electron tomography in the analysis on hydrated and beam sensitive materials allows their 3D analysis with nanometric resolution[46]. Today, ET can be applied not only to conventional bright-field TEM but to all related S/TEM techniques, i.e. high resolution and analytical S/TEM, electron diffraction and holography, HAADF[47,48,49,50].The advancement of the electron tomography was made possible by a combination of instrumentation innovations, the high computational power of modern computers and the development of new and more efficient reconstruction algorithms. Discrete reconstruction algorithms (DART)[51,52] have significantly improved the quality of the reconstruction and lowered the segmentation times, while equally slope tomography (EST) has allowed the first 3D reconstructions of metallic nanoparticles with atomic resolution[53,54].

In conclusion, the electron microscopy has come a long way from a simple imaging technique, to now as a complete work-station for nanoscience and nanotechnology. Now, on the same EM a large number of analyses can be performed consecutively without any change in the optics of the microscope. The same specimen can be analyzed under different atmospheric conditions at pressures up to 4 atm and temperatures close to 1000°C or under intense electrical and mechanical stress. An electron microscopiest should be able to perform an extensive set of S/TEM-based analysis, in order to obtain a complete characterization of its materials.

1.3 References

1. Williams, D. B. & Carter, C. B. in *Transmission Electron Microscopy* 3–22 (Springer US, 2009).
2. Einstein, A. On a Heuristic Point of View Concerning the Production and Transformation of Light. *Annalen der Physik* 132–148 (1905).
3. Reimer, L. & Kohl, H. in *Transmission Electron Microscopy* 45 (W. T. Rhodes, 2008).
4. Davisson, C. & Germer, L. H. Diffraction of Electrons by a Crystal of Nickel. *Phys. Rev.* **30,** 705–740 (1927).
5. Krumeich, F. Properties of Electrons, their Interactions with Matter and Applications in Electron Microscopy. at <http://www.microscopy.ethz.ch/downloads/Interactions.pdf>.
6. Ruska, E. The Development of the Electron Microscope and of Electron Microscopy. (1986). at<www.nobelprize.org>.
7. Knoll, M. & Ruska, E. *Z Phys.* **78,** 318 (1932).
8. Knoll, M. *Z. Tech. Phys.* **16,** 467–475 (1935).
9. Scherzer, O. Über einige Fehler von Elektronenlinsen. *Z Phys.* **101,** 593–603 (1936).
10. Hawkes, P. W. Aberration correction past and present. *Philos. Trans. R. Soc. Lond. Math. Phys. Eng. Sci.* **367,** 3637–3664 (2009).
11. Scherzer, O. Sphärische und chromatische Korrektur von Elektronen-Linsen. *Optik* **2,** 114–132 (1947).
12. Haider, M. *et al.* A spherical-aberration-corrected 200 kV transmission electron microscope. *Ultramicroscopy* **75,** 53–60 (1998).
13. Krivanek, O. L., Dellby, N., Spence, A. J., Camps, R. A. & Brown, L. M. Aberration correction in the STEM. *Inst Phys Conf Ser No 153 Sect. 2* (1997).
14. Dahmen, U. *et al.* Background, status and future of the Transmission Electron Aberration-corrected Microscope project. *Philos. Trans. R. Soc. Lond. Math. Phys. Eng. Sci.* **367,** 3795–3808 (2009).
15. Ramasse, Q. M. *et al.* Probing the Bonding and Electronic Structure of Single Atom Dopants in Graphene with Electron Energy Loss Spectroscopy. *Nano Lett.* **13,** 4989–4995 (2013).
16. Krivanek, O. L. *et al.* Atom-by-atom structural and chemical analysis by annular dark-field electron microscopy. *Nature* **464,** 571–574 (2010).
17. Fultz, B. & Howe, J. *Transmission Electron Microscopy and Diffractometry of Materials*. (Springer Berlin Heidelberg, 2013).
18. Williams, D. B. & Carter, C. B. in *Transmission Electron Microscopy* 197–209 (Springer US, 2009).
19. Williams, D. B. & Carter, C. B. in *Transmission Electron Microscopy* 23–38 (Springer US, 2009).
20. Williams, D. B. & Carter, C. B. in *Transmission Electron Microscopy* 39–51 (Springer US, 2009).
21. Mu, X. *et al.* Evolution of order in amorphous-to-crystalline phase transformation of MgF_2. *J. Appl. Crystallogr.* **46,** 1105–1116 (2013).
22. Reimer, L. & Kohl, H. in *Transmission Electron Microscopy* 211 (W. T. Rhodes, 2008).
23. Kilaas, R. in Proceedings of the 45th Annual Meeting of the Microscopy Society of America, 66–69 (1987).
24. MacLaren, I. & Ramasse, Q. M. Aberration-corrected scanning transmission electron microscopy for atomic-resolution studies of functional oxides. *Int. Mater. Rev.* **59,** 115–131 (2014).
25. Williams, D. B. & Carter, C. B. in *Transmission Electron Microscopy* 371–386 (Springer US, 2009).
26. Kiely, C. Electron microscopy: New views of catalysts. *Nat. Mater.* **9,** 296–297 (2010).
27. Hansen, L. P. *et al.* Atomic-Scale Edge Structures on Industrial-Style MoS2 Nanocatalysts. *Angew. Chem. Int. Ed.* **50,** 10153–10156 (2011).
28. Klie, R. F. *et al.* Enhanced current transport at grain boundaries in high-T c superconductors. *Nature* **435,** 475–478 (2005).
29. Egerton, R. F. *Electron Energy-Loss Spectroscopy in the Electron Microscope*. (Springer US, 2011).
30. Williams, D. B. & Carter, C. B. in *Transmission Electron Microscopy* 53–71 (Springer US, 2009).
31. Kothleitner, G. *et al.* Quantitative Elemental Mapping at Atomic Resolution Using X-Ray Spectroscopy. *Phys. Rev. Lett.* **112,** 085501 (2014).

32. Egerton, R. F. New techniques in electron energy-loss spectroscopy and energy-filtered imaging. *Micron* **34,** 127–139 (2003).
33. Keast, V. J. An introduction to the calculation of valence EELS: Quantum mechanical methods for bulk solids. *Micron* **44,** 93–100 (2013).
34. Krivanek, O. L. *et al.* Towards sub-10 meV energy resolution STEM-EELS. *J. Phys. Conf. Ser.* **522,** 012023 (2014).
35. Silcox, J. & Whelan, M. J. Direct observations of the annealing of prismatic dislocation loops and of climb of dislocations in quenched aluminium. *Philos. Mag.* **5,** 1–23 (1960).
36. Ruska, E. Beitrag zur uebermikroskopischen Abbildungen bei hoeheren Drucken. *Kolloid-Z* 212–219 (1942).
37. Parsons, D. F. Structure of wet specimens in electron microscopy. Improved environmental chambers make it possible to examine wet specimens easily. *Science* **186,** 407–414 (1974).
38. Baker, R. T. K., Barber, M. A., Harris, P. S., Feates, F. S. & Waite, R. J. Nucleation and growth of carbon deposits from the nickel catalyzed decomposition of acetylene. *J. Catal.* **26,** 51–62 (1972).
39. Baker, R. T. K. & Thomas, R. B. Continuous microscopic observation of the reaction of silicon with methane in the presence of iron. *J. Cryst. Growth* **12,** 185–190 (1972).
40. Oh, S. G. & Baker, R. T. K. In situ electron microscopy investigation of the behavior of supported cobalt particles. *J. Catal.* **128,** 137–147 (1991).
41. Ohnishi, H., Kondo, Y. & Takayanagi, K. Quantized conductance through individual rows of suspended gold atoms. *Nature* **395,** 780–783 (1998).
42. Ersen, O., Florea, I., Hirlimann, C. & Pham-Huu, C. Exploring nanomaterials with 3D electron microscopy. *Mater. Today* doi:10.1016/j.mattod.2015.04.004
43. Radon, J., Verh, B., Sachs, K. & Wiss, G. J. Radon, B. Verh. K. Sachs. G. Wiss. – Leipzig, Math. - Phys. Kl. 69, 1917, 262. *Math. Phys. kl.* 262 (1917).
44. De Rosier, D. J. & Klug, A. Reconstruction of Three Dimensional Structures from Electron Micrographs. *Nature* **217,** 130–134 (1968).
45. Koster, A. J., Ziese, U., Verkleij, A. J., Janssen, A. H. & de Jong, K. P. Three-Dimensional Transmission Electron Microscopy: A Novel Imaging and Characterization Technique with Nanometer Scale Resolution for Materials Science. *J. Phys. Chem. B* **104,** 9368–9370 (2000).
46. Nudelman, F., With, G. de & Sommerdijk, N. A. J. M. Cryo-electron tomography: 3-dimensional imaging of. *Soft Matter* **7,** 17–24 (2010).
47. Midgley, P. A. & Dunin-Borkowski, R. E. Electron tomography and holography in materials science. *Nat. Mater.* **8,** 271–280 (2009).
48. Kolb, U., Mugnaioli, E. & Gorelik, T. E. Automated electron diffraction tomography – a new tool for nano crystal structure analysis. *Cryst. Res. Technol.* **46,** 542–554 (2011).
49. Roiban, L. *et al.* Three-Dimensional Chemistry of Multiphase Nanomaterials by Energy-Filtered Transmission Electron Microscopy Tomography. *Microsc. Microanal.* **18,** 1118–1128 (2012).
50. Bals, S., Goris, B., Liz-Marzán, L. M. & Van Tendeloo, G. Three-Dimensional Characterization of Noble-Metal Nanoparticles and their Assemblies by Electron Tomography. *Angew. Chem. Int. Ed.* **53,** 10600–10610 (2014).
51. Batenburg, K. J. *et al.* 3D imaging of nanomaterials by discrete tomography. *Ultramicroscopy* **109,** 730–740 (2009).
52. Bals, S. *et al.* Quantitative Three-Dimensional Modeling of Zeotile Through Discrete Electron Tomography. *J. Am. Chem. Soc.* **131,** 4769–4773 (2009).
53. Mao, Y., Fahimian, B. P., Osher, S. J. & Miao, J. Development and Optimization of Regularized Tomographic Reconstruction Algorithms Utilizing Equally-Sloped Tomography. *IEEE Trans. Image Process.* **19,** 1259–1268 (2010).
54. Chen, C.-C. *et al.* Three-dimensional imaging of dislocations in a nanoparticle at atomic resolution. *Nature* **496,** 74–77 (2013).

Chapter II

A 3D insight on the catalytic nanopatterning of few-layer graphene

2.1. State-of-the-art

"Cutting" graphene: a route towards 1D graphene ribbons fabrication and increasing the surface accessibility of graphene flakes

Graphene, a two-dimensional crystal of sp^2 hybridized carbon atoms, is the basic building block for all graphitic materials[1]. The arrangement of the sp^2 bonded C atoms in a single-atom thick hexagonal lattice leads to unique physical[2,3] and chemical[4,5] properties. Among these properties, the high mobility of its charge carriers promotes graphene as an ideal material for new-generation electronics[1,4], while the chemical tunability of its high surface area makes it a promising material for the catalysis field[5,6]. Despite its exceptional properties, the widespread implementation of graphene in both the fields of electronics and catalysis remains a challenge. For semiconducting nanoelectronics, the fact that graphene is a zero-gap semiconductor is a major problem. One possible strategy for transforming graphene in a semiconductor with a finite band gap is to pattern it in quasi-one-dimensional (1D) structures, called graphene nanoribbons (GNRs)[7,8]. Their electronic properties will depend on parameters as width[7,9,10], shape[11,12], edge configuration[13,14] or functionalization[15,16] and bulk defects[17]. Several methods have been developed to fabricate GNRs. They can be separated into three categories: direct chemical routes[18,19], unzipping carbon nanotubes (CNTs)[20–22] and graphene flakes nanopatterning. The later method includes GNRs patterned by scanning tunneling lithography (STM)[23] and the catalytic nanopatterning of graphene and few-layer graphene (FLG) using metal nanoparticles (NPs) as "nanoscissors"[24,25].

The main drawback of using FLG flakes in the catalysis field comes out from their strong

tendency to restack through van der Waals forces upon drying. Therefore, their specific surface area and surface accessibility are strongly reduced[5] and this system is no longer adapted for catalytic applications, particularly as a support for gas-phase reactions. To overcome this problem, one proposed strategy is the catalytic nanopatterning of FLG using metal nanoparticles[26], which will create highly accessible nanochannels on the FLG surface. These nanochannels will most likely favor the development of new anchorage sites on the FLG surface, where the metallic and/or oxide active phases will adhere[27]. Consequently, the catalytic nanopatterning seems to be a reliable method for improving graphene's potential in achieving widespread applications in both the electronics and catalysis fields. In the next part the advancement achieved in the last decades in understanding and controlling the graphite patterning will be briefly discussed.

From coal gasification to graphene nanoribbons

There are two types of reactions which can lead to the graphite nanopatterning, depending on the gas used: hydrogenation[28,29] (H_2) and oxidation (O_2)[30,31]. Both of them were extensively studied in the last decades in the framework of production of the hydrocarbons from coal through hydrogenation[32] or removal of residual carbon deposited resulting during Ficher-Tropsh reactions[33]. Pioneering the research in the catalytic hydrogenation of graphite, A. Tomita and Y. Tamai[28] found that the reaction is catalyzed by a large number of transition metals as Rh, Ru, Ir, Pt, Ni, Pd, Co and Fe. The graphite oxidation was also found to be catalyzed by a large number of nanoparticles[30,31,33] such as Pt, Pd, Cu, V, Fe, Ni, Co and Ag. In a very simplified way, the catalyzed gas-graphite reaction can be described as follows: when a nanoparticle attached to a graphene-based structure is submitted to a H_2 or O_2 gas flow at rather high temperatures, it starts etching the carbon atoms along well-defined crystallographic directions, generating methane (eq. 1.1) and carbon monoxide (eq. 1.2) as reaction products. The schematic illustration of a nanoparticle channeling due to catalytic hydrogenation reactions is presented in Fig. 2.1.

$$C + 2H_2 \xrightarrow{t°C} CH_4$$ **eq. 1.1** (catalytic hydrogenation)

$$C + {}^{1}/_{2}\, O_2 \xrightarrow{t°C} CO$$ **eq.1.2** (catalytic oxidation)

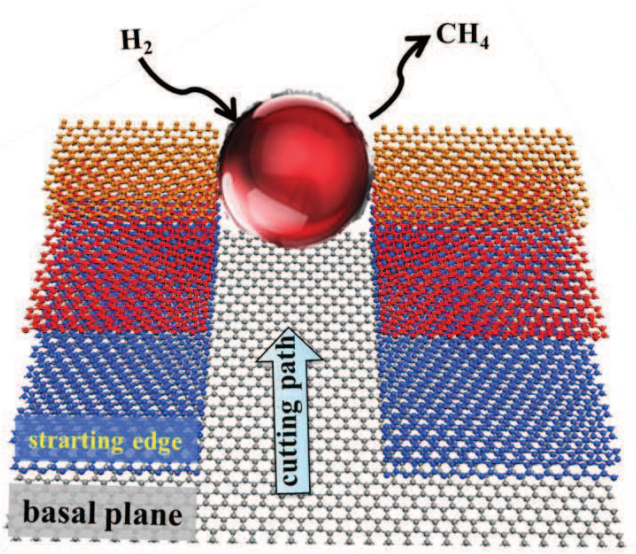

Figure 2.1. Schematic illustration of the FLG nanopatterning by a metallic nanoparticle via a catalytic hydrogenation reaction.

Although these reactions are simple looking, the catalyzed gas-graphite reactions constitute a complex system. Their complexity arises from the three implied "actors":

1. *The catalyst (the nanoparticles)* has the most significant influence on the reaction through its nature. Even though a large number of elements can support the catalysis, their relative efficiency varies from one to the other. For example, a Ni nanoparticle performs faster carbon removal rates than a Fe or a Co[34] nanoparticle. However, Co nanoparticles remain active even at temperatures approaching 1000°C, temperatures at which Ni and Fe tend to become inactive[33]. Moreover, the reaction parameters (carbon removal rates, the rate-limiting step and the C etching path) can be different even for the derivate of the same element. The different behavior in the catalytic oxygenation of CoO, Co_3O_4 and metallic Co is a clear example[33].

2. *The gas* nature of H_2 and O_2 is the second most important parameter. The differences between H_2 and O_2 come from the fact that some nanoparticles are more efficient in a given atmosphere (Ag in O_2, Fe and Co in H_2). This results from the direct interaction between the nanoparticles and the reaction gas through reduction or oxidation reactions. The most conclusive example is the phase transformation of Co during heating in an O_2 atmosphere. S.G. Oh and R.T.K. Baker[33] found that the oxide phases, CoO (475-640°C) and Co_3O_4 (640-880°C), etched the graphite substrate in a chaotic way (etching pitch), while the phase formed above 880°C etched along well-defined crystallographic directions. The phase transformation can be easily avoided when H_2 is used, by reducing the nanoparticle at a lower temperature (around 400°C for

CoO) before increasing it to reach the catalytic conditions of the reactions. In this way, a single type of etching will occur (channelling) and the temperature will only influence the carbon removal rates.

3. *The graphite substrate* influences the reaction through its topography (number of free edges and steps), the number of defect sites and its crystallography. The fact that a nanoparticle starts removing carbon atoms only if it is in direct contact with a graphite edge or a high-density defect site initially is a conclusive example[32].

The channels can be classified as either open-surface channels or sub-surface channels (tunnels)[35]. After investigating the catalytic actions of a large number of nanoparticles in both H_2 and O_2 gases, P.J. Goethel and R. T. Yang[30,35–39] propose that the catalytic reactions follow three sequential steps (Fig. 2.2a):

- the breaking of the C-C bonds at the nanoparticle-graphite interface;

- the C atoms diffusion through the nanoparticle's body to its surface;

- the C reaction with the chemisorbed gas molecules.

By considering the reaction mechanism they proposed, in the case of the catalytic oxidation the rate-limiting step is the breaking of the C-C bond on the forefront of the nanoparticle, while for the hydrogenation reactions the rate-limiting step is the reaction of the C with the chemisorbed H_2 molecules on the nanoparticle's surface.

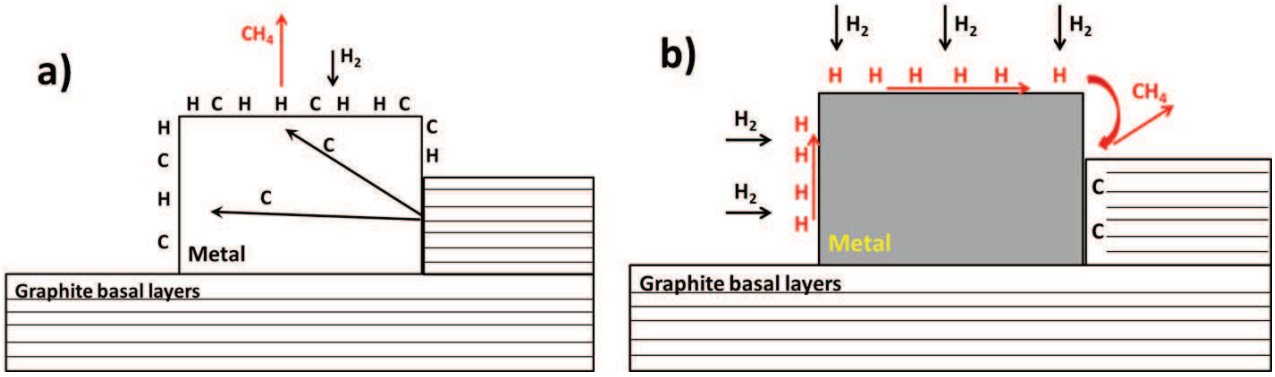

Figure 2.2. a) Schematic representation of the channelling mechanism in the metal-catalyzed C-H_2 reactions (adapted from P.J. Goethel et al. work[39]); b) Schematic representation of the channelling mechanism in the metal-catalyzed C-H reactions proposed by A. Tomita et al.[28] and G.A. L'Homme et al.[40].

Assuming that the reactivity of carbon towards atomic hydrogen and oxygen is higher than towards their molecules, A. Tomita et al.[28] and G.A. L'Homme et al.[40] proposed a more simple mechanism where H_2 and O_2 molecules are first dissociating on the nanoparticle surface and then their atoms migrate across the nanoparticle/carbon interface where they directly react with the C atoms at the graphene edge (Fig. 2.2b).

The mobility force, i.e. the force that allows the nanoparticles to move along well-defined crystallographic directions, was associated with the large surface energy along the edges containing dangling bonds[32,41]. It is assumed that the attractive force between the basal graphitic plane and the NP bottom facet ($\overrightarrow{F_r}$) which opposes to NP's motion is much smaller than the one appearing along the edge contact area ($\overrightarrow{F_m}$) (Fig. 2.3).

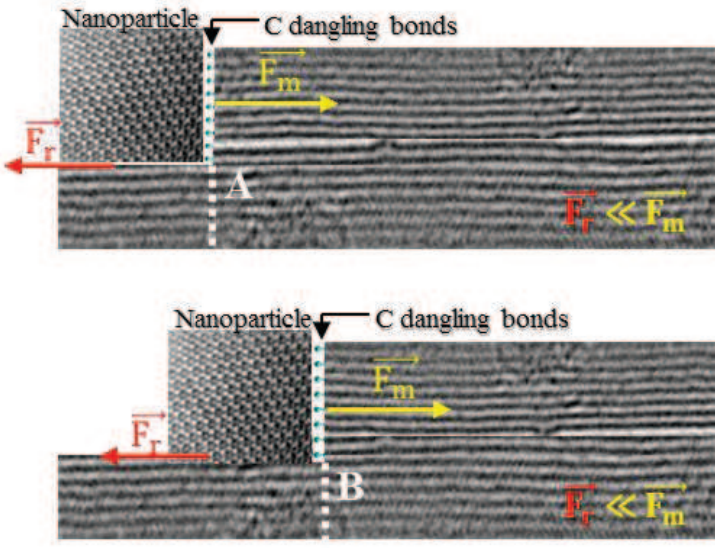

Figure 2.3. Schematic representation of the two main forces appearing during the channeling action: the basal interaction, $\overrightarrow{F_r}$, is opposing the motion of the nanoparticle created by the frontal attraction force $\overrightarrow{F_m}$.

Although the studies presented above revealed important aspects of the catalyzed gas-graphite reactions, the exact reaction mechanism remains under debate. However, the research in this area was revitalized by the discovery of the exceptional properties of the graphene nanoribbons (GNRs). As already mentioned, the catalytic nanopatterning of graphene and FLG was proposed as a viable method for the fabrication of the GNRs[42,43]. The first study to propose the catalytic nanopatterning of FLG as a method for "atomically precise graphene device fabrication" was conducted by S. S. Datta et al. [44] using Fe nanoparticles in a H_2 atmosphere. It was quickly followed by a number of studies addressing the influence of the catalysts nature (Ni, Co, Fe, Pt, Ru and Ag), their size, structure and initial localization as well as the importance of

the gas atmosphere conditions (gas type, pressure, temperature)[24,25,45–50] in controlling the nanopatterning process. As the aim of these studies was the creation of high quality GNRs, one important aspect pursued was the trajectory of the nanoparticles during the channelling activity. The fact that the active nanoparticles do not move in a chaotic way, but always parallel with the <11-20> and <10-10> crystallographic directions of graphite and that the channelling direction changes only with an angle that is multiple of 30° was an early observation[32,38]. However, due to a better understanding of the motion of the nanoparticles and of the technological advancement, the new generation of studies made a step forward by aiming at the control of the movement of the nanoparticles. L. Ci et al.[25,50] used a multistage cutting method to fabricate "specific well-defined shapes that could be used in the fabrication of graphene devices", while R. Wang et al.[49] used O_2 plasma pre-treatment to predefine the starting point for the channelling action. Although important advancement have been made in understanding the influence of the graphene topography (free edges, steps, existing channels)[24,25] and of the nanoparticle morphology[33,38,51] on the motion of the nanoparticles, a detailed investigation of the phenomenon is missing because most of the studies only use a 2D approach regardless of the number of the graphene sheets and of the interface between the nanoparticles and the surface of the graphene.

In this general framework, to characterize the catalytic nanopatterning of FLG flakes and deeply explore the characteristics of the obtained nanostructure, we used an approach combining electron tomography (ET) with high-resolution transmission electron microscopy (HR-TEM) and spatially resolved energy-electron loss spectroscopy (SR-EELS). This work provides original insights on the 3D shape of the etched trenches and their localization in relation to the FLG surface, as correlated with the FLG topographical elements: steps and edges.

2.2. Methods

2.2.1. Sample preparation

FLG decorated with $Fe_{3-x}O_4$ NPs

The FLG flakes have been synthesized via mechanical ablation of pencil leads assisted by an ultra-sonication process and followed by acid/base purification to remove the inorganic binder and separation from the weakly ablated species by decantation in toluene[52]. The decoration of the FLG surface by homogeneous $Fe_{3-x}O_4$ NPs was carried out using a solvothermal synthesis[53] consisting in the thermal decomposition of an iron stearate complex in a solvent with a high boiling point and in the presence of oleic acid (as surfactant) and of the FLG. In the solvothermal synthesis, 300 mg of FLG were dispersed in 20 mL of octyl ether (ALFA AESAR, 99%) under ultrasonication for 30 minutes. After the addition of 1.382 g (2.2 mmol) of iron stearate (Fe-stearate STREM CHEMICALS (9-10% Fe)) and 1.4 mL (4.4 mmol) of oleic acid (ALFA AESAR, 99%), the whole environment was heated up to 110°C without cooling. The goal of this latter operation was to dissolve the reactants and to eliminate the water and/or impurities. The cooling condenser was then added and the system was heated up to reflux (~290°C) under air, with a heating rate of 5°C/min^{-1}. The reaction mixture was then kept for 2 hours at this temperature. After cooling, the NPs and FLG were precipitated by adding an excess of acetone, followed by a centrifugation at 8000 rpm for 10 min. The resulting black precipitate was washed 3 times with hexanes: acetone mixture (50:50) and centrifugation (8000 rpm, 10 min).

Catalytic hydrogenation of FLG

The FLG nanopatterning using Fe-based nanoparticles in a H_2 atmosphere was performed *ex-situ* in a tubular reactor. The first step consisted in the reduction of initial Fe_3O_4 nanoparticles to metallic Fe at 400°C under a H_2:Ar (1:5) flow for 2h. After the reduction, the temperature was rapidly increased until it reached 800°C (the channelling temperature). The sample was maintained at that temperature for another 2h. The gas flow rate was 300 mL/min. After the treatment, the sample was stored in powder form.

All the procedures concerning the sample preparation were developed and implemented at ICEEPS Strasbourg by Dr. Walid Baaziz and Dr. Izabela Janowska.

2.2.2. Techniques

Conventional TEM, HR-TEM and STEM-EELS investigations

For the TEM analyses, a drop of the solution containing the nanopatterned FLG sample together with the catalyst ($Fe_{3-x}O_4$ nanoparticles) was deposited on a TEM cooper grid covered by a lacey carbon membrane. Conventional and high resolution TEM images were recorded on a JEOL 2100 F microscope working at 200 kV, equipped with a Cs probe corrector and a GATAN Tridiem imaging filter. The microscope had a high-resolution objective lens pole piece and the line resolution reached was ~0.2 nm. Atomic-resolved EELS measurements, as well as HR scanning TEM (HR-STEM) studies were performed on a probe-corrected STEM FEI Titan Low-Base 60-300 operating at 120 kV (fitted with an X-FEG® gun and Cs-probe corrector (CESCOR from CEOS GmbH)). EEL spectra were recorded using the spectrum-imaging mode[54] in a Gatan GIF Tridiem ESR spectrometer. The convergent and the collection semi-angles used for the data acquisition were 25 mrad and 80 mrad respectively, whereas the energy resolution was about 1.2 eV.

Electron Tomography

For the acquisition of tomography series, a drop of the solution containing the nanopatterned FLG sample was deposited on a TEM cooper grid covered by a holey carbon membrane. For the ET, the holey carbon film was preferred to the lacey one because it offers a better mechanical stability at the sample at high tilt angles, therefore minimizing position changes during the acquisition time, especially rotation, that induce alignment artifacts in the reconstruction. One drop of colloidal 5 nm Au nanoparticles solution was deposited on the membrane/FLG flakes followed by a mild plasma cleaning treatment in H_2/Ar for 5s. The tomography series were obtained for tilting angles spanning from -65° to +65° with a 2° Saxton scheme and subsequent series alignments were performed in the IMOD[55] software using the Au NPs as fiducial markers. Two types of reconstruction algorithms were used: a simultaneous iterative reconstruction technique (SIRT) and a discrete algebraic reconstruction technique (DART). For resolving the in-depth details at maximum resolution we used the SIRT algorithm implemented in a fast software running on multicore computers, Tomo3D[56]. The size of the TEM projections used for the reconstruction was 2k x 2k pixels and the tomogram thickness has been fixed at 2k. Because of the low contrast of the FLG, to obtain the large scale segmentation of the

tomograms is not a trivial matter. Therefore, we have used the segmentation abilities given by the discrete tomographic algorithms. In order to get suitable grey values of both the FLG and NPs for further segmentation, a masked SIRT step has been performed by following the steps described by Zuerner et al.[57] The unmasked SIRT reconstruction was analyzed to find the most likely boundaries within the layer. Using the masked SIRT reconstruction as a starting model and taking the grey values of its histogram as a basis, the DART step was performed. Dr. A. Wisnet and Dr. C. Scheu at Ludwig Maximilians University, Germany carried out the DART reconstruction. It is important to specify that the DART has been employed to improve data segmentation and subsequent modeling, whilst the volume analysis has been carried out on the volume reconstructed using the SIRT algorithm.

2.3. Advanced 2D characterization: HR-TEM and STEM-EELS

FLG/$Fe_{3-x}O_4$ nanoparticle composite (before nanopatterning)

Fig. 2.4a shows a TEM image of a typical FLG sheet, after the deposition of $Fe_{3-x}O_4$ nanoparticles only. The analysis of TEM images shows that the morphology of an individual aggregate is dominated by the presence of successive terraces on the FLG surface, due to the superposition of several individual sheets (see red arrows), whereas several steps can be observed on single FLG sheets (see yellow arrows). The nanoparticles have a narrow size distribution, with a mean diameter of about 7±2 nm and a good dispersion on the FLG surface. The presence of densely defects sites at the FLG steps will determine the preferential grow of the nanoparticles on these sites[53] (see Fig. 2.4b). Fig. 2.4c shows a HR-TEM image of a typical magnetite nanoparticle.

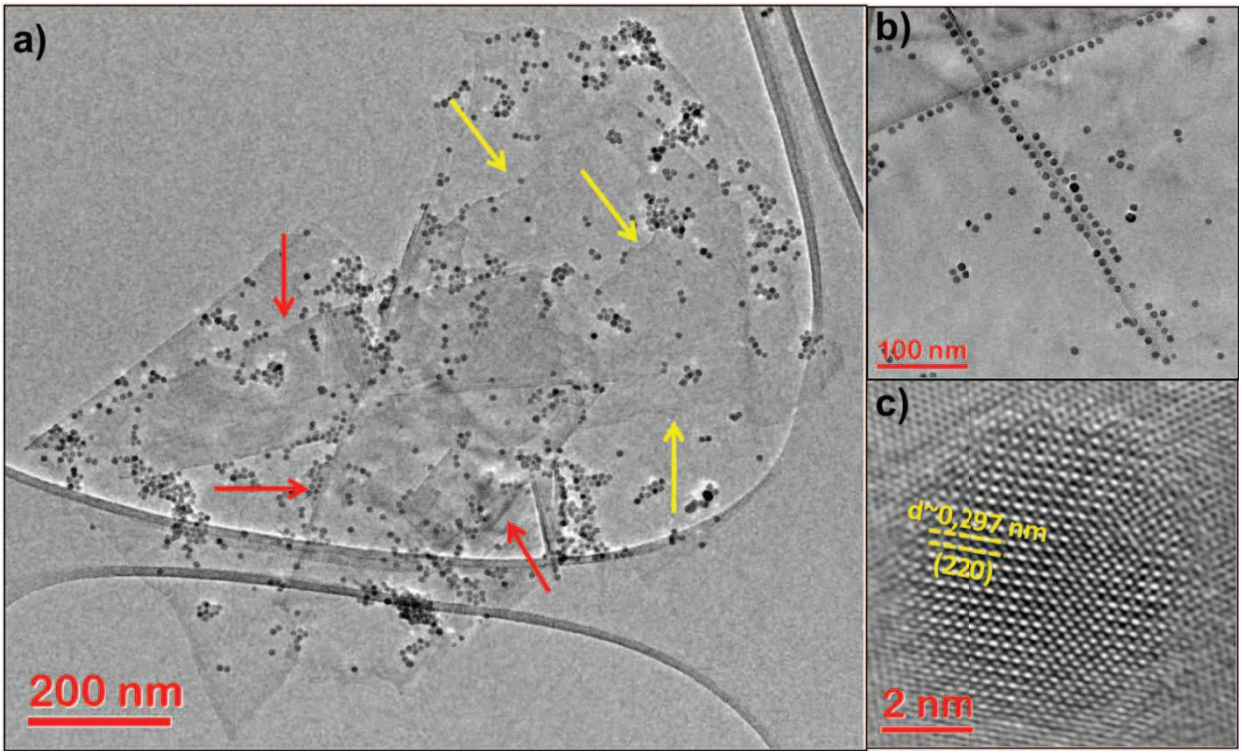

Figure 2.4. a) TEM image of a FLG flake decorated with $Fe_{3-x}O_4$ nanoparticles (red arrows show superposed FLG sheets; yellow arrows show steps the FLG); b) TEM image showing the preferential nanoparticle growing on the FLG flakes steps; c) HR-TEM image of a $Fe_{3-x}O_4$ nanoparticle sitting on FLG ($d_{(220)}$ ~ 0.297 nm).

Nanopatterned FLG/Fe based nanoparticle system

The morphology of the FLG flakes after the hydrogen assisted thermal treatment is presented in Fig. 2.5a. The FLG surface was completely transformed during the catalytic hydrogenation and exhibits channels with lengths ranging from 30 nm to 1 µm and widths lying between 10 and 100 nm. At high scale, the observation of the channelling seems a chaotic process but at a smaller scale (Fig. 2.5b) the channelling action appears as a totally ordered process. All of the channels appearing in Fig. 2.5b are moving parallel to the <11-20> direction, leaving the channel edges with a zig-zag morphology (Fig. 2.5c). In our experiment, channels oriented in the <10-10> direction (Fig. 2.5d) rarely appear. The anisotropy of the channelling action and especially the channelling preference for the <11-20> direction is a well-documented topic in the literature[24,25,32]. Most of the studies relate the anisotropy with the higher energy barrier for removing C atoms from a zig-zag edge (<10-10>) than from an armchair edge (<11-

20>). Moreover, A. Tomita and Y. Tamai proposed a second reason related to the number of active sites required to start the channel formation: three sites for channels in the <10-10> direction and only two sites in <11-20>[32].

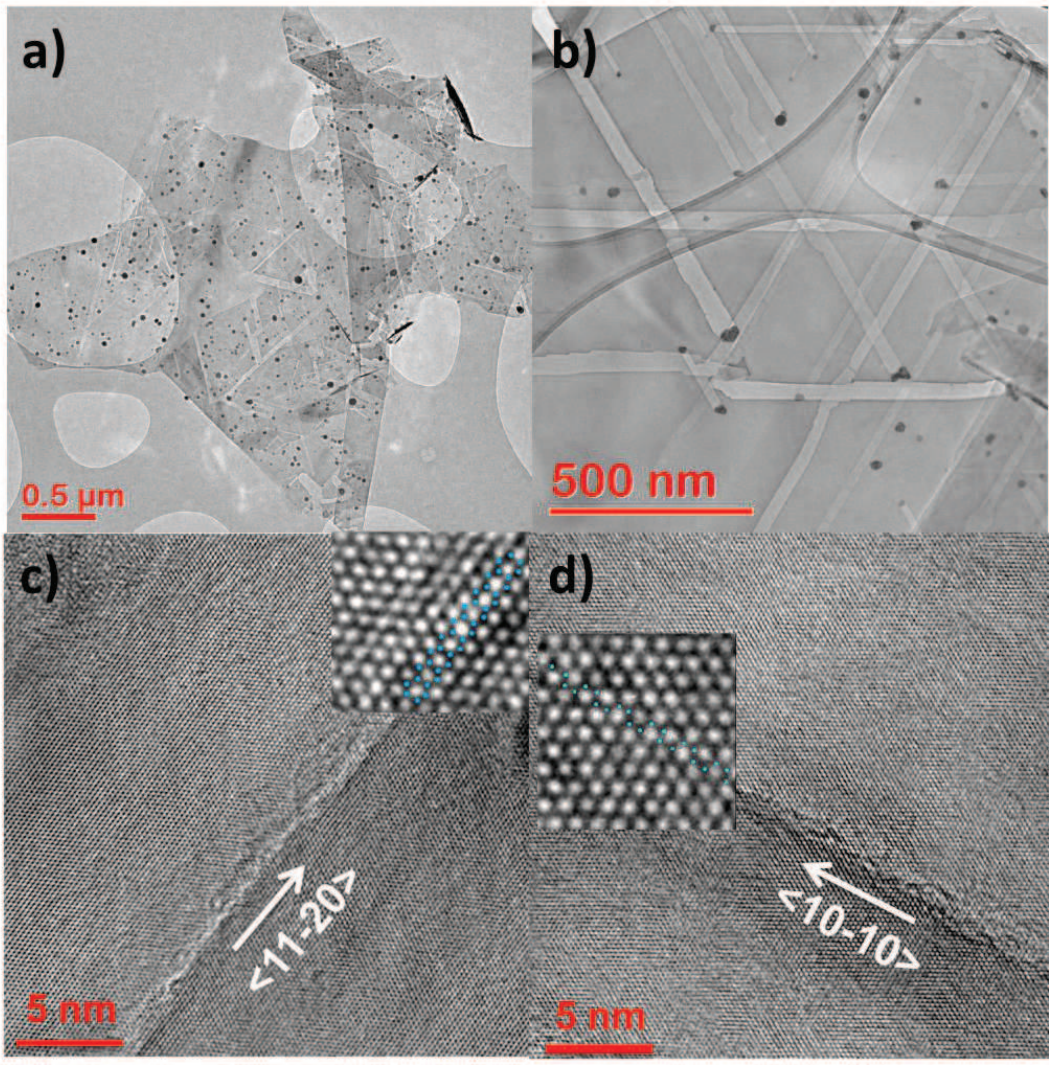

Figure 2.5. a) TEM image of a typical FLG flake after the catalytic hydrogenation; b) TEM image showing the preferential orientation of the channels parallel to the <11-20> direction; HR-TEM images illustrating the channels edge type: c) zig-zag and d) armchair morphology.

In the present experiment, the width of most of the channels seems to remain constant from the beginning to the end, allowing one to conclude that the size of the nanoparticles does not change significantly during the channelling action and no re-faceting or chemical

modification does occur. Moreover, the constant width of the channels shows that the channel walls and its bottom surface do not retain a significant amount of metallic atoms from the surface of an active nanoparticle. However, one should expect that some of the newly created sites, both from the channel walls and its clean bottom surface to retain a small number of Fe atoms, as found by R. Zan and co-workers[58], but not enough to decrease the initial size of the nanoparticle. As compared to the sample before the catalytic hydrogenation, various types of nanoparticles, with sizes ranging from 7 to 100 nm, along with different internal structures and geometrical configurations are identified (Fig. 2.6): core-shell with an empty space between core and shell (2.6a), hollow nanoparticles (2.6b) and core-shell with incomplete shell (2.6c). This variety of morphologies is induced by the native oxidation (in-air oxidation) of the metallic Fe NPs (obtained during the heat treatment in an H_2 atmosphere), during the sample manipulation outside the oven. No sample transfer in an inert gas atmosphere being available, the native oxidation is unavoidable. However, some important pieces of information can be extracted from this data. The thickness of the native oxide shell (a Fe_2O_3 phase[59]) formed around the metallic Fe is fixed at ~6 nm and a small gap (~1 nm) appears almost always between the core and the shell. When the diameter of the initial metallic Fe nanoparticle is smaller than 15 nm, the nanoparticle will be completely oxidized and will become a hollow nanoparticle (Fig. 2.6b).

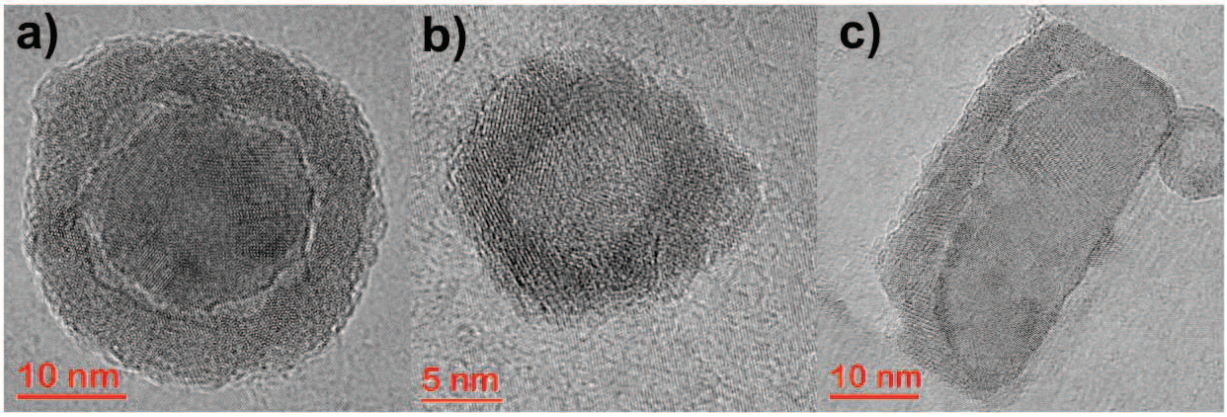

Figure 2.6. a) Core-shell nanoparticle with a void between the core (metallic Fe) and the shell (Fe_2O_3 phase); b) Hollow oxide nanoparticle; c) Core-shell nanoparticle with incomplete shell (confined inside a tunnel).

The complete oxidation is proved by spatial-resolved STEM-EELS (Fig. 2.7a), while the ET data (Annex A, Fig. A2.1) show that a small cavity in the shell is connecting the outer side with the hollow core. The void formation is associated with the Kirkendall mechanism of

oxidation, which favors the diffusion of Fe in the oxide layer with respect to the inward diffusion of oxygen[60]. The special case of nanoparticles with an incomplete shell (Fig. 2.6c) is due to the influence of the FLG support. The spatial-resolved STEM-EELS analysis (Fig. 2.7b) shows that the front part of the nanoparticle is a metallic phase, while the shell is an oxide rich phase. As will be seen later, this type of nanoparticle is found only in sub-surface channels (tunnels) and its incomplete oxidation is due to the protection offered by the tunnel's walls.

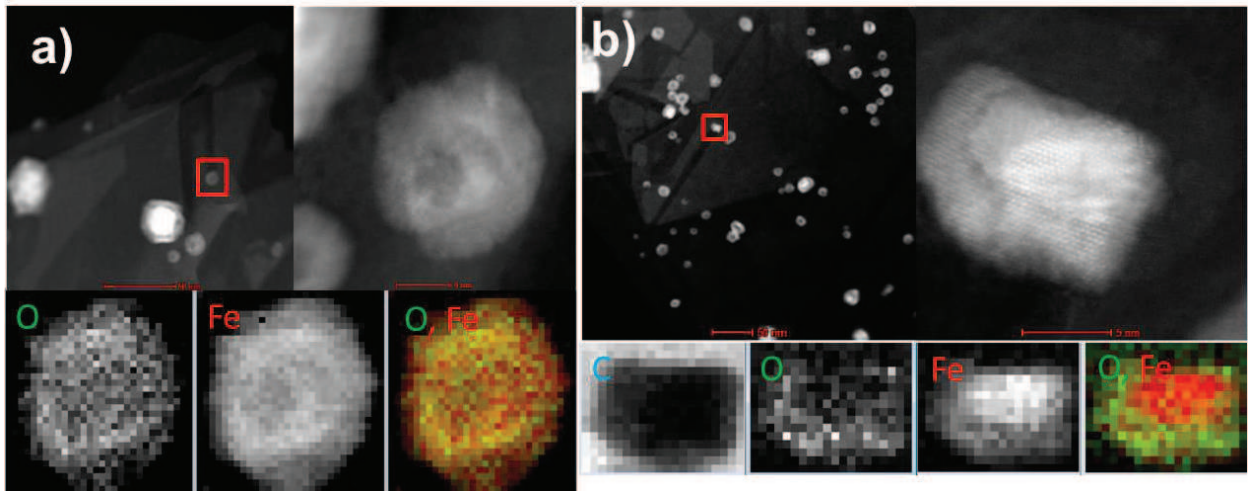

Figure 2.7. a) Completely oxidized hollow nanoparticle with a void as a core; b) Core-shell nanoparticle with incomplete shell (confined inside a tunnel). Scale bars are sized 5 nm. Chemical maps (extracted from the EELS spectrum-images acquired on the regions marked by red squares) corresponding to the distribution of carbon, oxygen and iron inside the particles. The RGB images are the relative oxygen-to-iron maps. They were obtained by superposing the corresponding elemental maps. Oxygen is represented in green, while iron is represented in red.

2.4. Electron Tomography

2.4.1. A 3D overview of the nanopatterned FLG by tomography

Based on the electron tomography analysis we were able to access crucial information on the exact topography of a FLG sheet. The analyses were thus carried out on several regions of the catalytically etched system in order to gain a deep understanding on the nanopatterning process. However, before presenting the results, in order to facilitate the understanding of the tomography data, the representation of the three directions (*xy*, *yz* and *xz*) will be briefly describe. The sketch in Fig. 2.8 presents the *xyz* orientations of slices from the reconstructed volumes in the geometrical configuration that will be further employed in the present work. The slice thickness is set by the voxel size of the tomogram (between 0.13 nm and 0.25 nm). The *xy* slice (gray), taken in a direction parallel to the FLG surface, presents the width and the length of the channels. The *yz* slice (yellow) presents the depth and length of the channels. Finally, the *xz* slice (green) offers a view of the depth and the width of the channels.

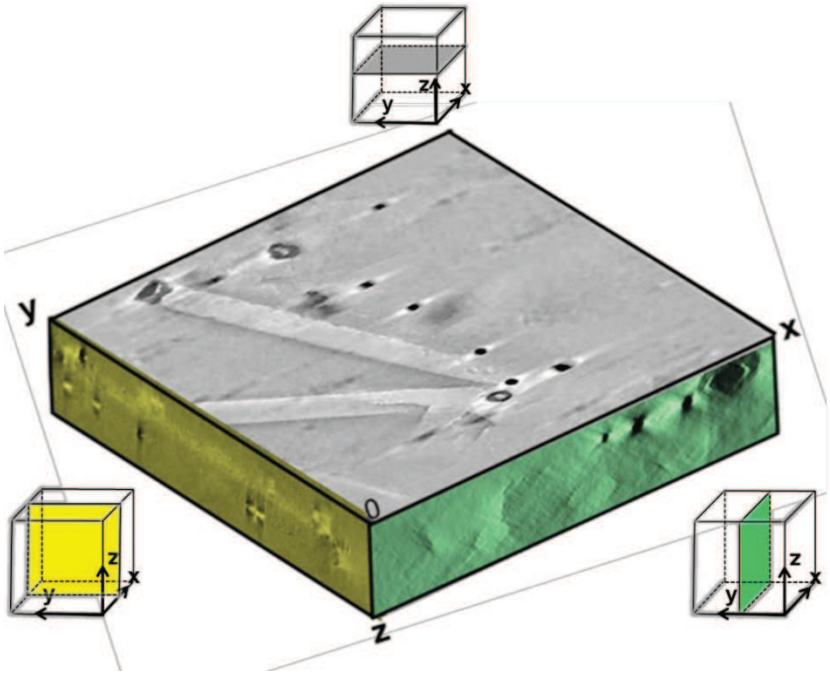

Figure 2.8. 3D representation of the specimen reconstructions: the *xy* plane in gray, the *yz* plane in yellow and the *xz* plane in green.

For instance Fig. 2.9a depicts a *xy* slice (longitudinal) through a reconstructed volume of a nanopatterned FLG. It shows that all the active nanoparticles, i.e. those participating in the nanopatterning process, are initially located at the edges of the pristine FLG or on its steps, whereas the nanoparticles situated on the FLG flat surface appear to be generally inactive. Accordingly, one may state that the driving force responsible for the FLG cutting closely relates to the interaction between nanoparticles and carbon atoms of the support localized on the edge of a terrace. A. Tomita et al.[32] show that the contact between the front side of the nanoparticle and the carbon atoms from an edge or a step creates a higher interaction than the one between the carbon basal plane and the bottom side of the nanoparticle. One should note that we focused exclusively on the deep-channelling action. However, the existence of monolayer channelling ~~it~~ is not excluded but the investigation of this process requires a special technique to enhance the monolayer edge contrast[30,38].

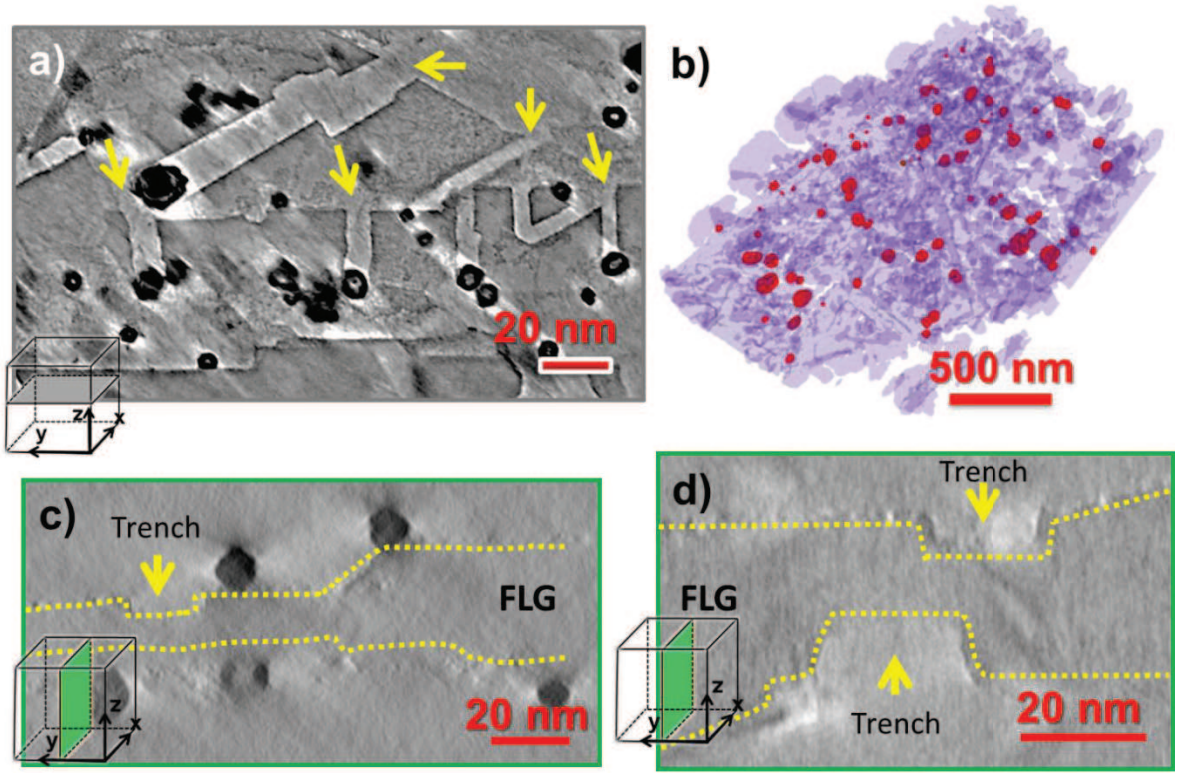

Figure 2.9. a) *xy* slice extracted from the reconstructed volume of a nanopatterned FLG area. Yellow arrows point to the initial position of the active nanoparticles; b) 3D model displaying a general view of the analyzed fragment. Nanoparticles are shown in red, whilst the purple color indicates the FLG flake; *xz* slices extracted from the reconstructed volumes showing nanoparticles (c) and channels (d) on both sides of the FLG support.

Fig. 2.9b displays a model of the distribution of the nanoparticles on the FLG support obtained using the DART algorithm. The DART algorithm successfully creates a visual representation of the nanopatterned FLG. However, one cannot use this reconstruction for extracting quantitative data due to the low contrast of FLG flakes. Therefore, we focused on the topographies reconstructed with the SIRT algorithm. Analyzing the SIRT reconstructed volume slice by slice in cross-section (*xz* slices), one identifies nanoparticles on both sides of the FLG support (Fig. 2.9c). It is important to mention that the localization of Fe-based nanoparticles on both sides of the FLG has no impact on the cutting process as trenches have been created on both sides of the support (see Fig. 2.9d).

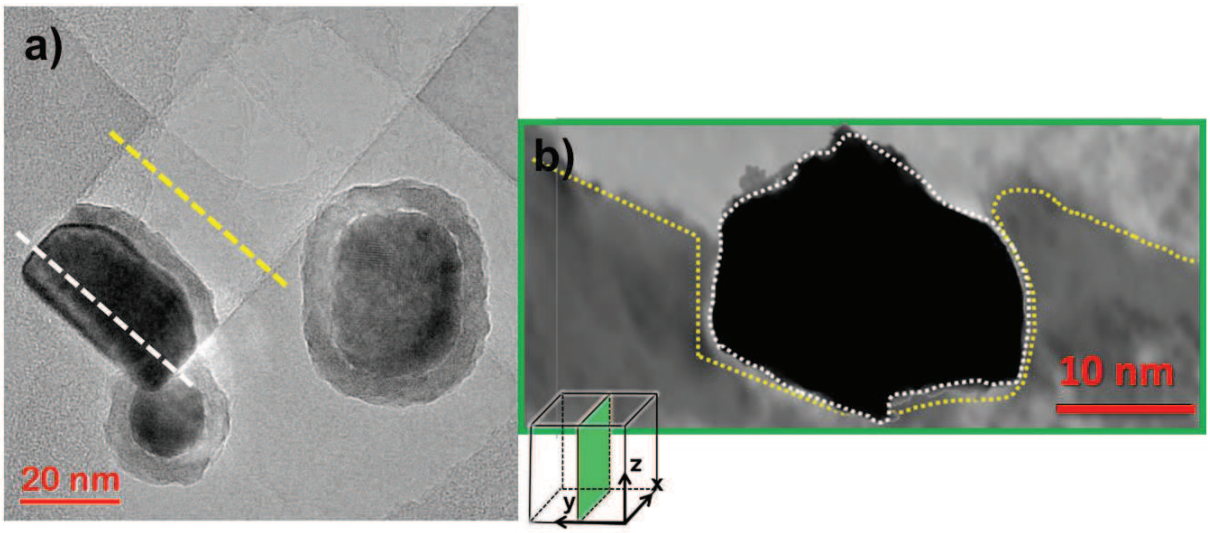

Figure 2.10. a) TEM projection of a channel and corresponding digging nanoparticle; b) Superposition of the *xz* slices of the nanoparticle (white line in Fig. 2.10a) and channel (yellow line) showing the close relationship between the 3D shape of the nanoparticle and the channel profile.

According to the cross-section views we present, the channel walls are not perfectly straight in terms of their atomic arrangement. However, note that the tomographic resolution achieved in our reconstruction is about 1 nm in the *z*-direction and therefore our hypothesis should be delimited accordingly. To highlight the one-to-one correspondence between the trenches and the associated nanoparticles, we have analyzed cross-sections within the volume by focusing on the nanoparticle's and the FLG's shapes within the very same channel (Fig. 2.10a). At this stage of the analysis one might assume that the main factor imposing the channel profile is

the 3D character (shape) of the active nanoparticle. By superimposing the cross-section slices through the channel's profile (yellow line) close to its end and through the nanoparticle's profile (white line), one identifies a close correspondence between the channel's shape and the section of the nanoparticle contacting the channel contour. However, the superposition is not perfect. This is due to both the limitation of the ET in reconstructing the nanoparticle/channel edges interface and to the fact that the shape of the nanoparticle can change because of the restructuration of the surface of the nanoparticle during the cutting process. The changes in the nanoparticle's surface during channelling come from the fact that the reaction takes place at high temperature (800°C). At this temperature, a superficial liquid-like layer can form and its thickness depends on the nanoparticle's size[61,62]. Another limitation of ET in conventional bright-field mode comes from the diffraction contrast created by any nanoparticle at certain angles and even by the channel's walls, which do induce artifacts in the reconstructed volume.

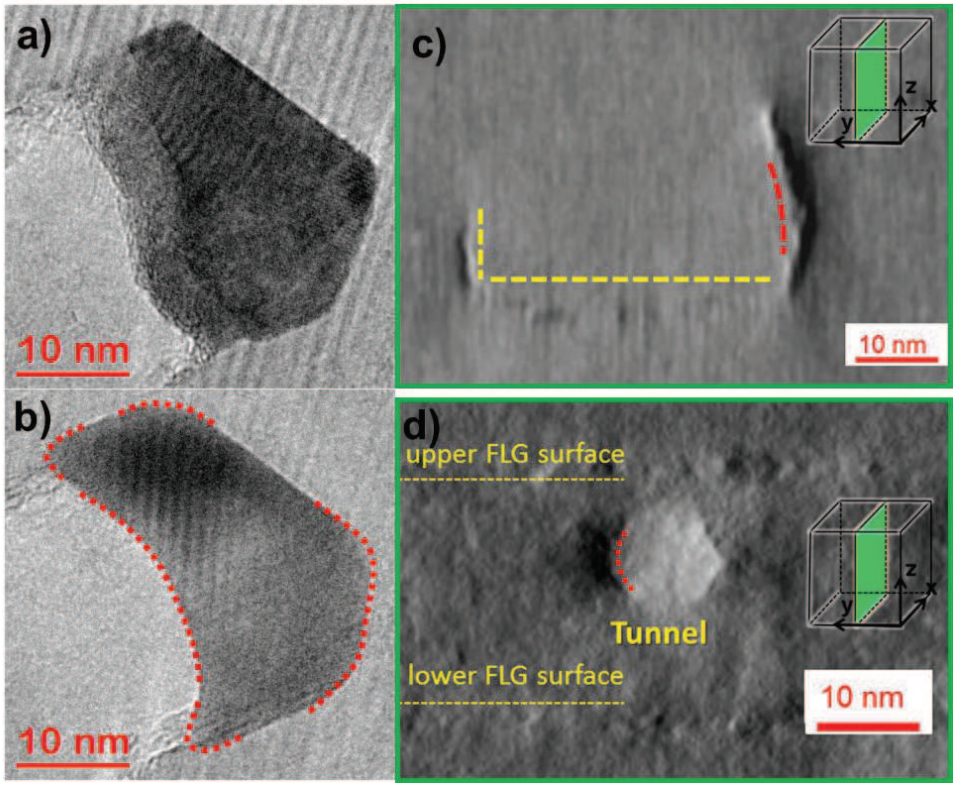

Figure 2.11. TEM image of a faceted nanoparticle after the catalytic hydrogenation recorded at room temperature (a) and reheated *in-situ* (vacuum) at 800°C (b); c) A *xz* slice through the volume reconstruction of a trench with an uneven wall side; c) A *xz* slice through the volume reconstruction of a tunnel.

Fig. 2.11a shows the image of an active NP at room temperature, while the image of the same NP acquired at 800°C (in-vacuum heating) is presented in Fig. 2.11b. While the main body of the nanoparticle remains a crystalline solid, its surface has a "melted-like" aspect made visible by the rounded edges between the NP's facets (red lines). Fig.2.11c shows an *xz* slice through an open-surface channel with uneven wall sizes. The small wall (~2 nm) is almost perfectly straight while the other one with a height of ~15 nm is clearly curved. This is due to the fact that, as the contact area between the nanoparticle and the FLG increases, the influence of the wall on the nanoparticle shape is also increasing. The curved walls are the dominant type of walls observed in the case of tunnels (see Fig. 2.11d) where the nanoparticle is confined between graphene on in five out of six directions. The real time observation of the channelling action presented in Chapter III will shed more light on the influence of the reaction conditions on the nanoparticle's shape.

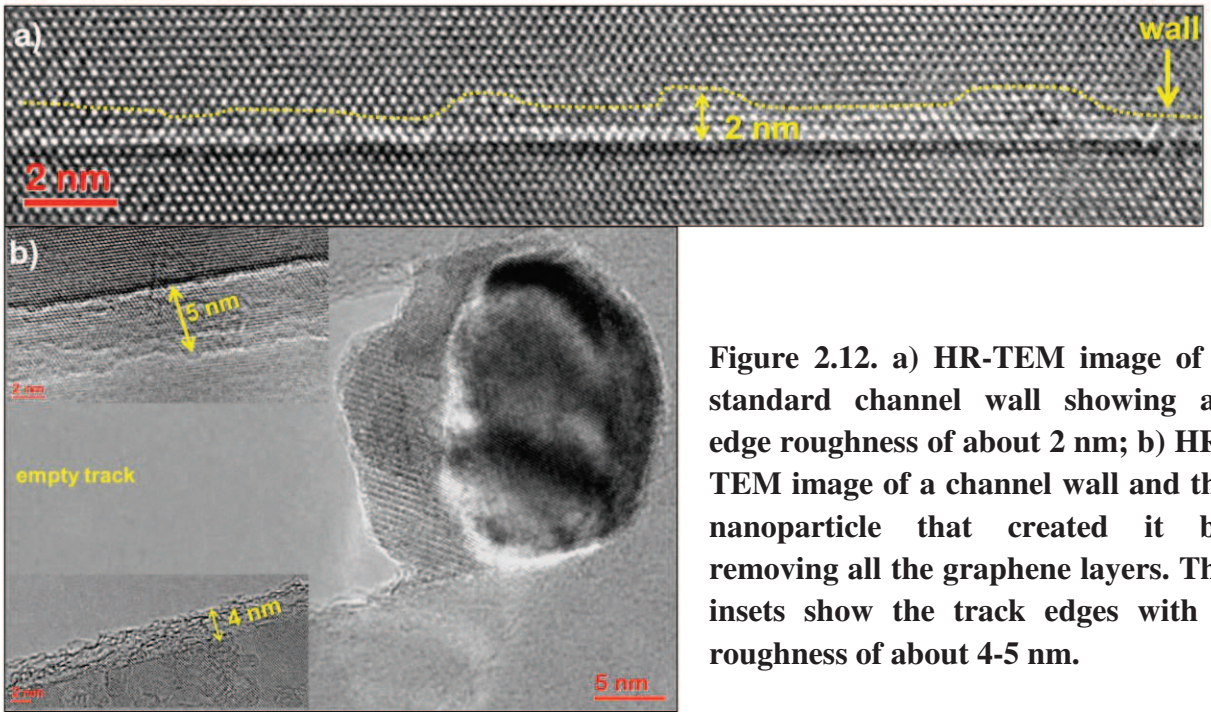

Figure 2.12. a) HR-TEM image of a standard channel wall showing an edge roughness of about 2 nm; b) HR-TEM image of a channel wall and the nanoparticle that created it by removing all the graphene layers. The insets show the track edges with a roughness of about 4-5 nm.

The roughness of the walls, which cannot be extracted from the ET pieces of data due to its resolution limitation, shows an interesting evolution. When the nanoparticles that create the channels are supported by basal graphene layers, the roughness is around 2 nm with small variations depending on the nanoparticle's size (see Fig. 2.12a). However, when a nanoparticle removes all the graphene layers, leaving behind an empty track (see Fig. 2.12b with insets), the

roughness of the edges is larger. This is probably due to a higher channeling rate appearing when the bottom interaction is missing (see Fig. 2.3), which can increase the disorder generated by the etching process.

2.4.2. The topographic influence on the nanoparticle motion

Nanoparticles cutting on flat FLG flake

By applying the same approach to other pairs of trench/NP, we were able to analyze the 3D shape changes of the trench along its length as a function of the initial topography of the FLG along the cutting length, i.e. constant vs variable thickness. In the case of a constant thickness of the FLG support, the analysis of individual channels along the cutting direction shows that their depths are constant during cutting, as shown in Fig. 2.13. This is easily showed by projecting the channel in the *yz* direction and cutting a slice through its center (Fig. 2.13b). In this way, the constant position of the basal plane throughout the whole length of the channel is highlighted. Therefore, the height of the step where the nanoparticle was initially located is the unique parameter defining the trench's depth.

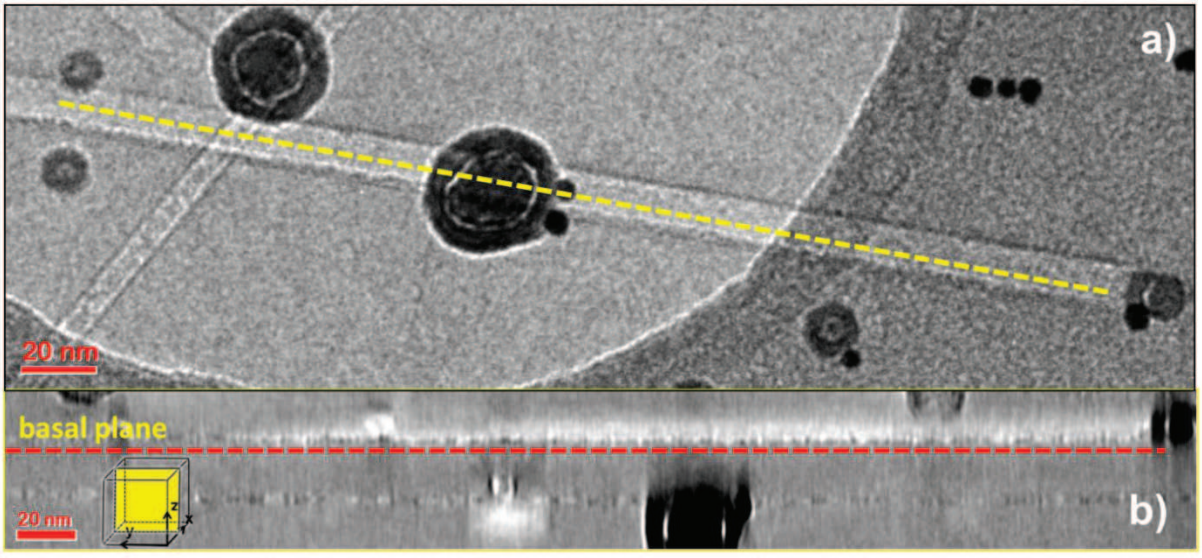

Figure 2.13. a) TEM image of a channel created in FLG area with a constant thickness; b) *yz* slice along the channel center (yellow line) showing the constant basal plane (red line).

One should note that a nanoparticle can lose the initial basal plane if it contacts an area rich in defects along its path, with defects propagating deeper than its initial basal plane. In this

scenario, the nanoparticle penetrates deeper in the trench, changing the initial basal plane. Identifying small changes (1-3 layers) in the depth of the channels using ET was not possible due to the resolution limitation. However, such changes in the morphology of the channels were occasionally identified by HR-TEM imaging.

However, the vast majority of few-layer graphene flakes are not uniform in thickness. The synthesis method and especially the powerful sonication of the initial expended graphite flakes are favoring the formation of graphene flakes with a disordered topography. Fig. 2.14 shows an *xz* projection of a 150 nm long FLG flake. The presence of two major changes in thickness (steps) can be observed only in such a small region. As the average distance covered by a nanoparticle is about 500 nm, we can assume that most of them will interact with one or more such topographic features during their catalytic action.

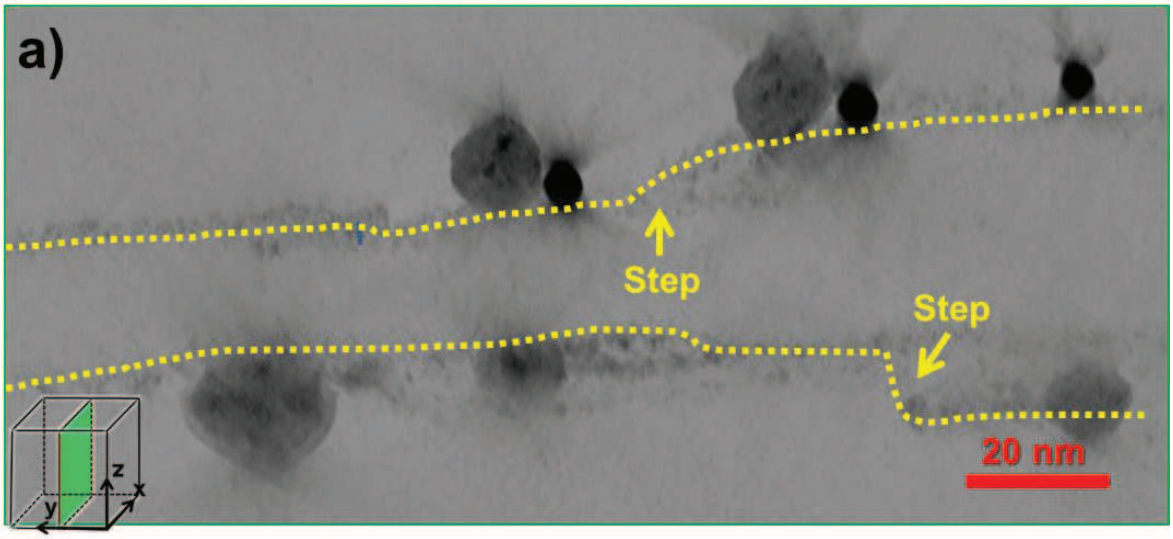

Fig. 2.14. *xz* projection of a FLG flake showing its rough topography.

Nanoparticle interaction with a step-up

The first situation is encountered when the active nanoparticle crosses a step or an edge of a second superimposed FLG sheet, the case of a step-up configuration (Fig. 2.15a). The TEM projection (acquired at 0°) of the channel selected for the tomographic analysis is presented in Fig. 2.15b, while a *xy* slice through the channel's reconstruction is shown in Fig. 2.15c. The importance of ET in reveling geometric characteristics of the channeling action is highlighted in Figures 2.12a and b. When this channel was selected for analysis, it was thought that the step-up feature was forming a 90° angle with the channel direction (red line in Fig. 2.15b). However, the reconstructed volume analysis revealed that the nanoparticle had crossed another step (white line) with a 30° tilt with respect to the channel direction. The initial step was found to be located on the other side of the FLG flake and the nanoparticle did not interact with it. This "confusion" highlights the interest of performing 3D-TEM studies of such systems once again. In the situation of the step-up interaction, the depth of the channel changes, as the nanoparticle remains in contact with the initial basal plane. The upper slice presented in Fig. 2.15d shows an yz slice taken close to the channel's right edge (yellow line in 2.15c). It directly shows the step's geometrical profile with a height of about 10 nm. The lower yz slice of Fig. 2.15d was taken through the center of the channel. It shows that the initial basal plane remains unchanged even after the nanoparticle crosses the step-up. Moreover, the encounter of the step induced no change in the cutting direction. After crossing the step, only the height of the channel's walls changes, as displayed in Fig. 2.15e. If one takes into account the relation between the profile of the trenches and the shape of the nanoparticles, one observes that the geometry of the trenches corresponds exactly to the geometrical characteristics of the nanoparticle at the origin of the trench. This correlation confirms that, even on the non-flat areas (i.e. step-like surfaces), the nanoparticles remain in contact with the initial basal plane during the entire channeling process and the active surface section of the nanoparticle is a function of the step-up height. The original points highlighted by Fig. 2.15 concern the ability of the electron tomography to provide primary visual 3D information on the shape of the trenches, with the emphasis on the characteristics of the walls. The depth and width of the as-created trench continuously change along its length, as they are imposed by the evolution of the cutting thickness within the FLG support. It is evident that these changes are closely imposed and controlled by the initial graphitic plane and the corresponding diameter of the active nanoparticle at a given position along the trench's length.

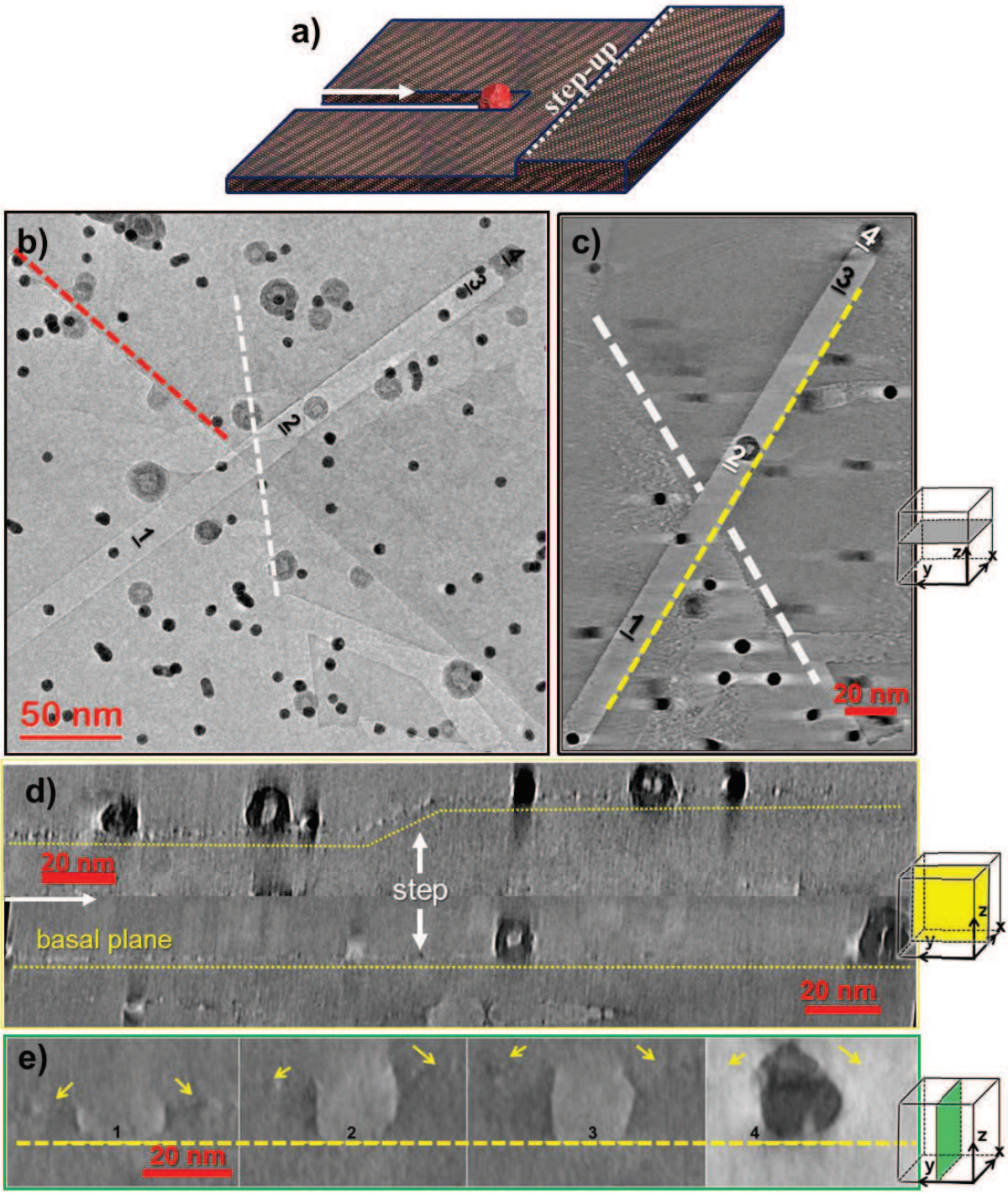

Figure 2.15. a) Schematic representation of the step-up type interaction; b) TEM image of the selected channel cut in a non-uniform FLG area; c) *xy* slice through the reconstructed volume of the channel presented in 2.15b. The white line highlights the position of the step-up. The 1 to 4 numbers show the position of the *xz* slices presented in 2.15e; d) *yz* slices through the right edge (top) (yellow line in 2.12c) and through the center of the channel (bottom); e) *xz* slices showing the evolution of the height of the channel's walls.

Tunnel formation

A completely different situation is observed when the active nanoparticles cross steps with heights higher than their diameters. In this case, one expects the nanoparticles to create subsurface channels, i.e. tunnels, according to P.J. Goethel and R. T. Yang[35]. Indeed, our 3D analysis allows a direct visualization of these tunnels developed inside the FLG, as evidenced by a series of TEM tomography slices presented in Fig. 2.16.

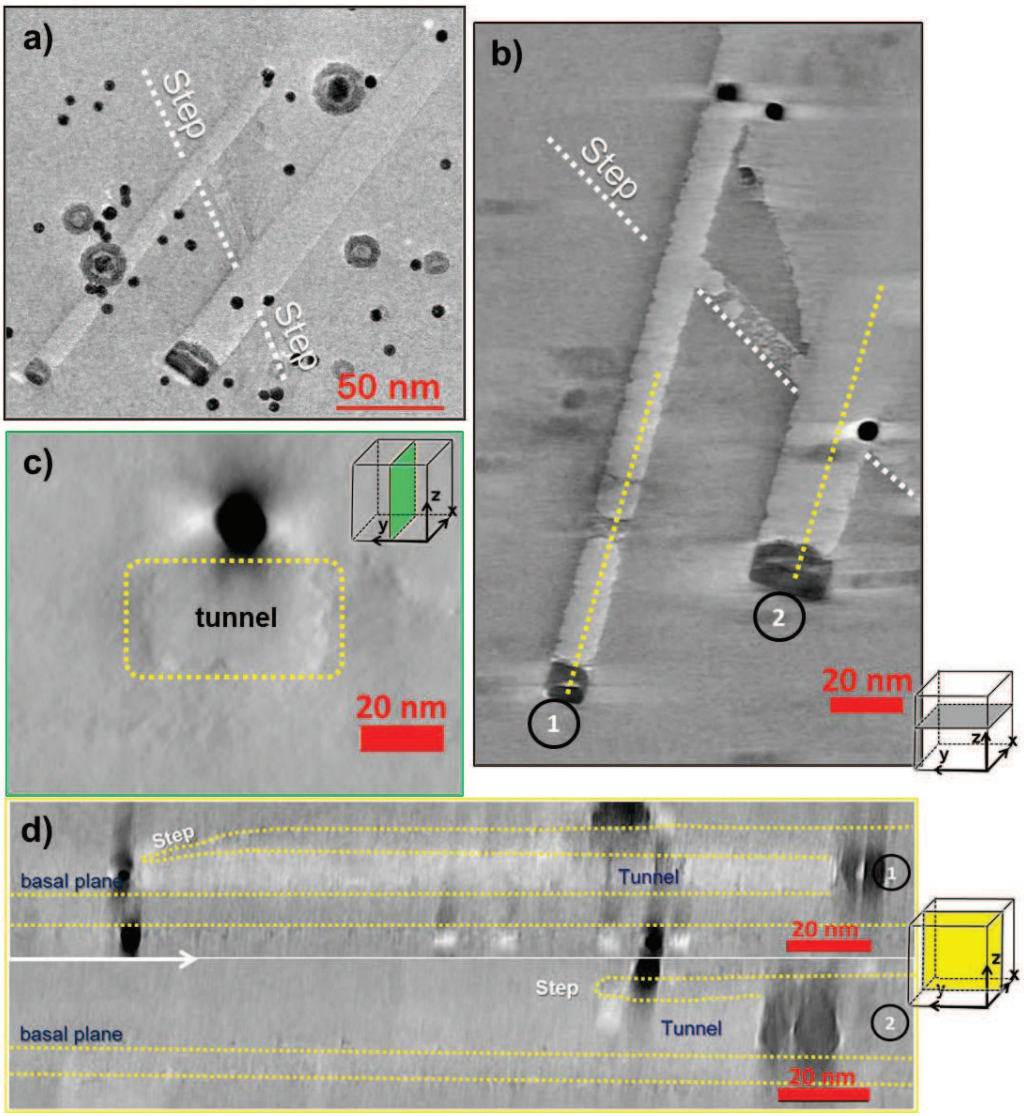

Figure 2.16. a) TEM image of two tunnels created in a non-uniform thickness FLG area; b) *xy* slice through the reconstructed volume of the tunnels presented in 2.16a. The white line highlights the position of the step-up; c) *xz* slice showing the "interior" of the tunnel number 2; d) yz slices through the center of the two tunnels at the position highlighted by yellow lines in 2.16b.

According to the tomographic slices redrawn from the volume (Figs 2.16b and 2.16d), one can state that we deal with tunnels dug by the iron-based nanoparticles that came in contact with a step thicker than the diameter of the nanoparticle. The contours of the tunnel are shown by the *xz* slice presented in Fig. 2.16c. Moreover, the *yz* slices show that even under these conditions the basal plane of the active nanoparticle remains unchanged.

Nanoparticle interaction with a step-down

Another finding is that the cutting process can stop or the cutting direction can change when the active nanoparticles cross a step-down (Fig. 2.17a) (a preexisting topographical feature on the surface of the FLG or another trench created previously) or a FLG free edge. This "free-edge sensitivity" behavior can be strictly attributed to the adhesion forces between carbon edges and the nanoparticles facets[25]. It is closely related to the contact area between the nanoparticle's facets and the trench walls, which depends on the nanoparticle's size, shape and position inside the trench.

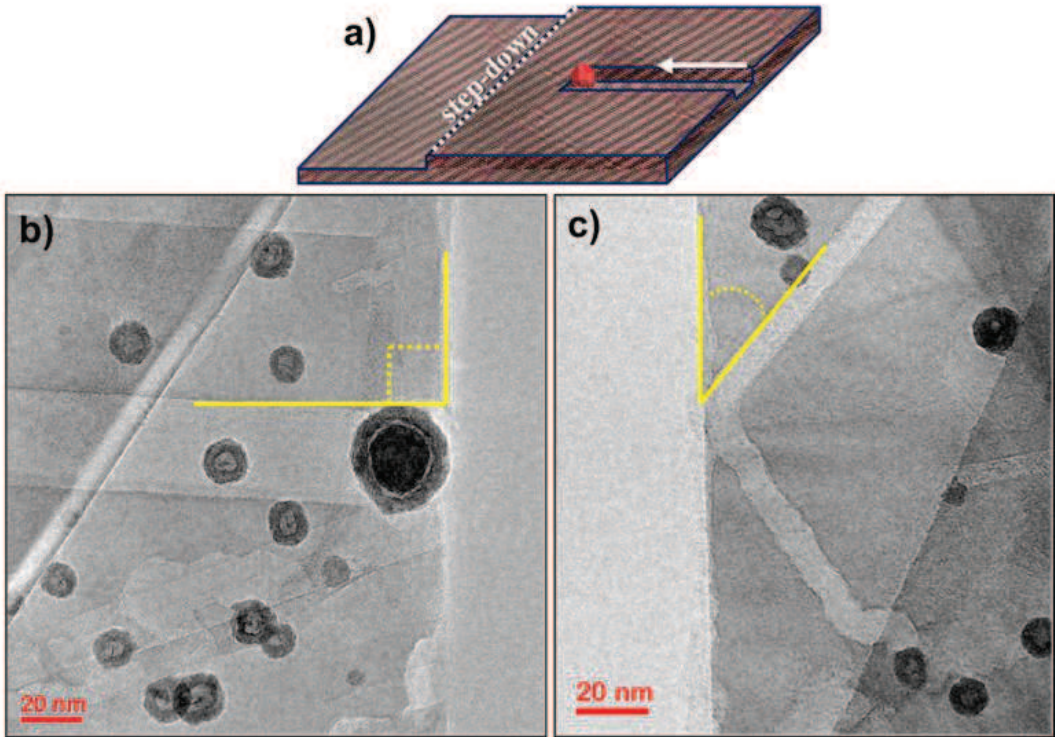

Figure 2.17. a) Schematic representation of the step-down type interaction; TEM images showing the case of a 90° (b) and 60° (c) free-edge approach.

The TEM image presented in Fig. 2.17a shows the case of a nanoparticle whose catalytic activity was immediately stopped when approaching a free FLG edge at a 90° angle. Fig. 2.17b shows the case of a nanoparticle that changed its channeling direction while approaching the edge of the FLG substrate. As compared to the previous situation, in this later configuration, the approach angle between the nanoparticle channeling direction and the FLG free edge is sharper. As a consequence, the contact of the nanoparticle lateral facets with carbon ensures sufficient "adhesion strength" to redirect the nanoparticle in another trajectory. Thereby, in the case of an/the active nanoparticle approaching free edges, the remaining contact area between the nanoparticle's lateral facets and the walls of the trench will determine if the particle stops or if it continues the cutting. As we have shown, the approach angle seems to be the main factor influencing the remaining nanoparticle/carbon contact area. However, the size and shape of the nanoparticle and the depth of the trench are also very important parameters. One should notice that for the above situations we assumed that the faceting of the nanoparticle doesn't change during the channeling action and especially when crossing the free edge. This assumption remains valid only when the nanoparticles are maintaining a solid crystalline body during their motion. Our environmental TEM experiments (discussed in the next chapter), as well as the one reported by F. Pizzocchero and co-workers[51], shows that when the surface of the nanoparticles is in a melted state, i.e. when there are droplets, the faceting of the nanoparticles is often changing due to strong surface tensions between it and the FLG edges. The change of the channeling direction of the nanoparticles when approaching a free edge in a sharp angle is seen as a good way of controlling the trajectory of the nanoparticles, and therefore of creating graphene flakes with well-defined shapes. Our investigation of such interaction was lacking in examples due to the large lateral size of the FLG flakes, therefore making it less probable for a nanoparticle with an average mobility distance of 500 nm to reach one FLG edge.

However, a particular situation was observed when the nanoparticles approach a folded free edge. The TEM image presented in Fig. 2.18a shows one of these situations. The FLG flake on which the nanoparticle is digging the channel is wrapped in two. The HR-TEM image of the folded edge (20 layers in thickness) is presented in Fig. 2.18b. The line contrast shows that the edge is a closed folded one. A schematic representation of the cutting process is represented in cross-section in Fig. 2.18c. The nanoparticle removes the entire upper folded layers and a few of the initial layers creating an open-surface channel. It is approaching the folded edge

perpendicularly (see Fig. 2.18a) and the cutting direction doesn't change until the nanoparticle approaches the edge. However, when reaching the folded edge, the initial basal plane that was kept constant during the whole cutting (see the yz slice in Fig. 2.18e) is lost. As the xz slice of the edge area shows (Fig. 2.18d), the nanoparticle starts digging inside the FLG flake creating a tunnel. As the channel's basal plane changes only at the folded edge point one can assume that the configuration of the bent graphene layers is responsible for such a dramatic effect. The channeling is a crystallographic dependent phenomenon, and therefore, changing the arrangement of the graphene layers has a dramatic effect on the process.

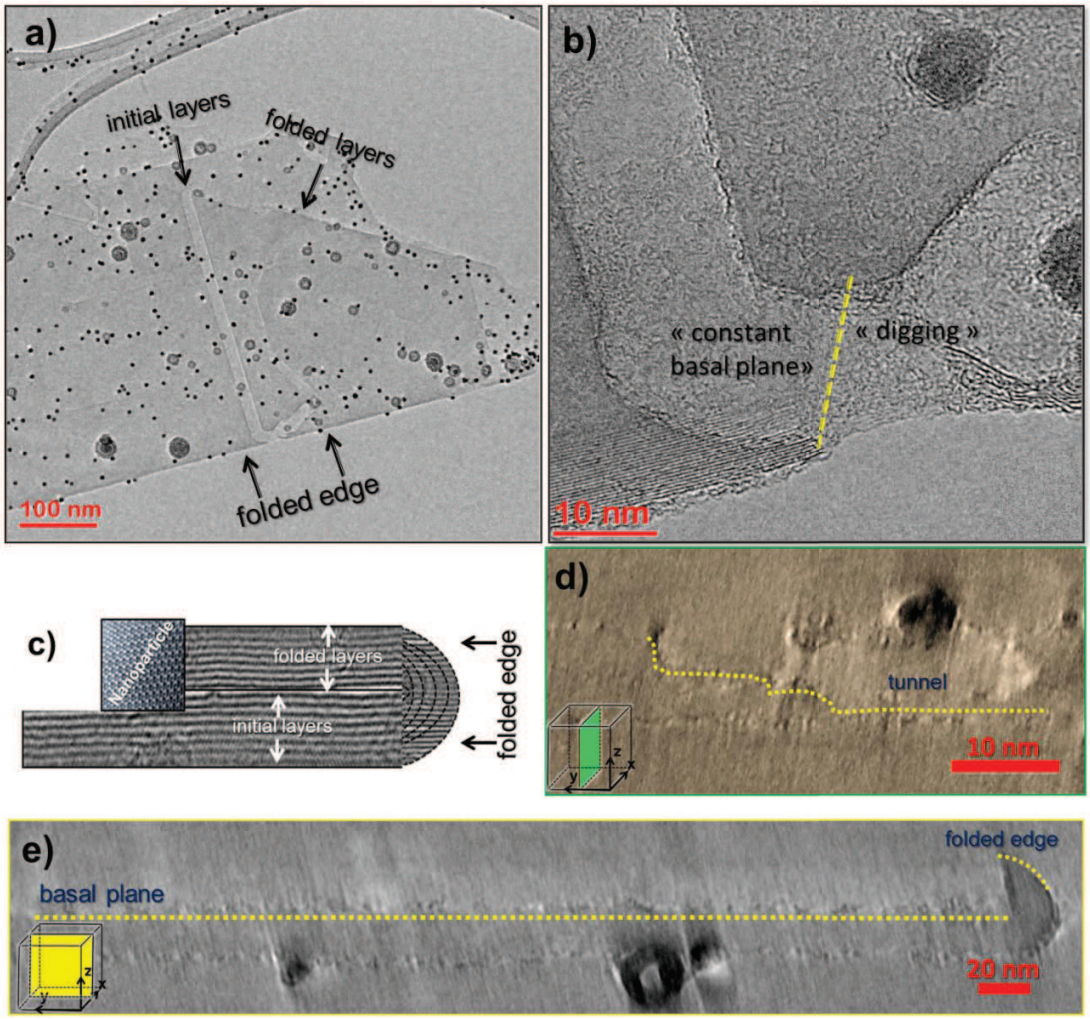

Figure 2.18. a) TEM image of a channel created in a folded FLG flake; b) HR-TEM image of the folded free edge. The yellow line marks the basal plane changing position; c) Cross-view schematic representation of this particular channeling situation; d) *xz* slice at the folded edge level showing the dramatic change of the basal plane level; e) *yz* slice along the length of the channels showing the constant basal plane maintained before reaching the edge.

Occasionally, we observe nanoparticles changing their channeling direction without any apparent reason, i.e. without crossing free edges or other channels. Fig. 2.19a shows a nanoparticle making two 90° turns while the one presented in Fig. 2.19b makes one 60° and two 90° turns.

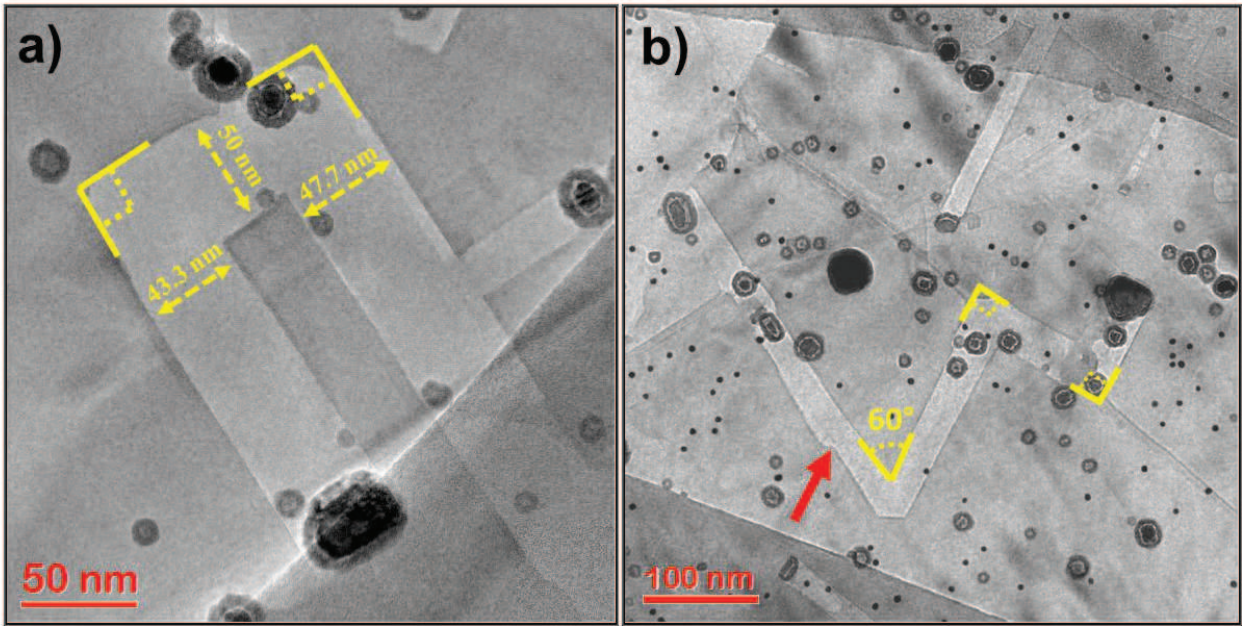

Figure 2.19. a) and b) TEM images of channels with multiple turning points created on FLG flakes with uniform thickness.

In order to identify if these sudden changes of direction are caused by topographical features of the FLG substrate, we performed ET on the area presented in Fig. 2.19b. We focused our attention on the 60° turning point. As highlighted earlier, the change in direction when the nanoparticle is approaching a free edge is caused by the adhesion forces between the lateral facets and the carbon walls. Considering this, one should expect, at the turning point emphasized in Fig. 2.20a, the topography of the FLG flakes to change. More precisely, one should find that the nanoparticle's right side facet should increase its contact area with the carbon wall to the detriment of the frontal facets. However, analyzing the area around the 60° turning in cross-section (*xz* and *yz* directions), no topographical feature was found, the flake being uniform in thickness. Instead, it was found that, at the time of turning, the nanoparticle is changing the initial basal plane. However, it does not do this by moving on a lower graphene layer (digging) but by rising itself on a higher plane. In order to show this, we extracted three *xz* slices on the positions highlighted by dotted lines in Fig. 2.20a. The first one (Fig. 2.20b) was extracted from the

channel's position right before the turning point (black line). The second one (Fig. 2.20c) presents the channel's profile just after the turning point (red line). The third one (Fig. 2.20d) goes through both positions, before and after the turning (yellow line). They show that after establishing a new direction of motion the height of the new channel is decreasing from ~12 nm to 7-10 nm. As the thickness of the FLG flake doesn't change, one can assume that the nanoparticle moved its basal plane a few nanometers higher. The yellow *xz* slice (Fig. 2.20d) shows that between the a) (before turning) and the b) (after turning) positions there is a height difference of about 5 nm. The basal plane change on a higher position would not be possible if the nanoparticle would be in a fully solid state. The fact that the nanoparticle can reshape itself during channeling, changing its initial basal plane, shows that it underwent a morphological transformation, at least at the surface level.

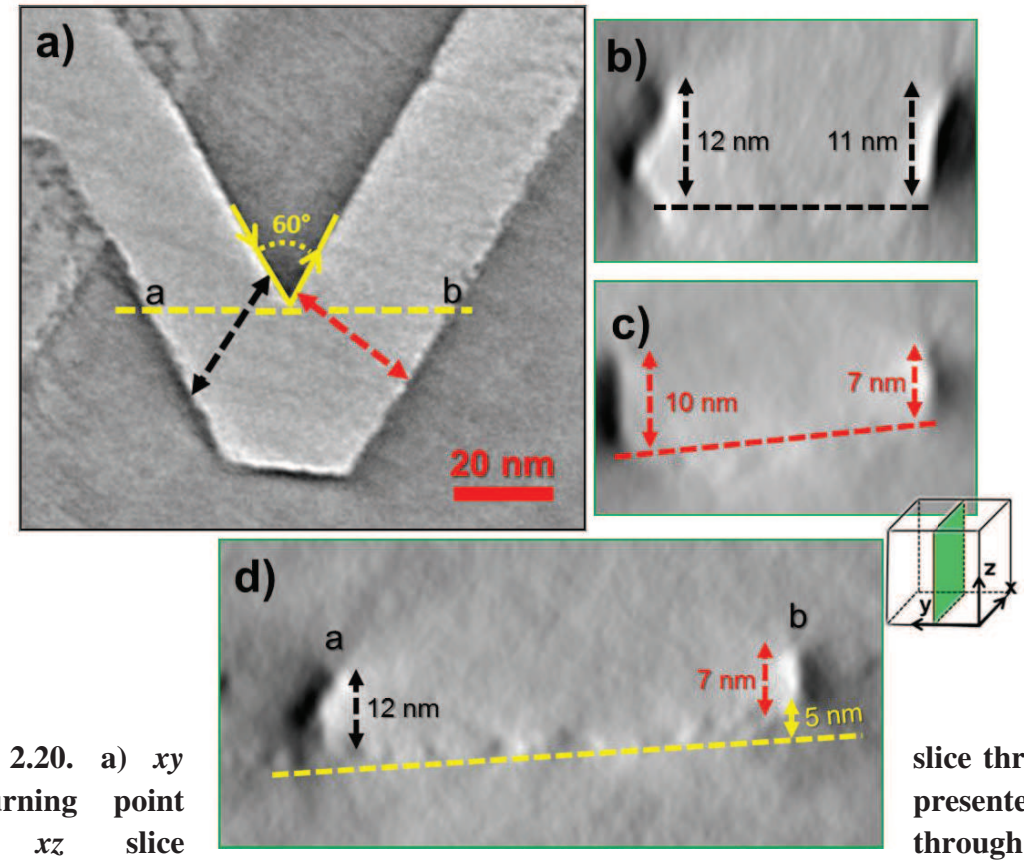

Figure 2.20. a) *xy* slice through the 60° turning point presented in Fig. 2.19b. *xz* slice through the position highlighted by black line (b) (before turning), red line (c) (after turning) and yellow line (d) in Fig. 2.20a.

Moreover, as shown in Fig. 2.19a, after each turning point the width of the channel is fluctuating, indicating a change in the size and therefore in the 3D shape of the nanoparticle. Changes in the width of the channels were observed in most of the turning cases, even for nanoparticles deflected due to the interaction with a step-down topographical feature.

The above examples show that when the nanoparticle turns without crossing free edges or step-down features, this is not caused by any major topographical feature. It demonstrates instead that some nanoparticles can be at higher temperature, partially losing the solid state, and the turning event can be related to the partial melted state and the continuous reshaping (refaceting) of these nanoparticles. The real-time observation of the channeling action inside an environmental TEM cell will shed more light on this dynamic process.

2.5. Discussion

Despite a large number of studies that were published recently on this topic, no valuable proof have been provided precisely locating the trenches within the FLG support. Based on 2D imaging only, the first advanced hypothesis was that we deal with the presence of intersecting trenches with different depths, located most probably on the same side of the FLG support. Due to its ability to furnish a 3D overview, the electron tomography identified the presence of independent non-intersecting trenches on both sides of the FLG support. From the TEM analysis point of view, one therefore associates the different contrasts in the 2D micrographs to superposition effects rather than to intersecting trenches.

The first conclusion drawn from the results shown above relies on the complexity of the process of catalytic cutting of FLG sheets. It strongly depends on both the topography of the carbon support and the morphology of the active catalyst. We have shown that the initial deposition of $Fe_{3-x}O_4$ NPs on both sides of the FLG sheets leads to a dual side cutting. This demonstrates the capacity of the catalytic hydrogenation to improve the “bulk” properties of FLG by generating a porous network with high accessibility.

The active nanoparticles are initially located at the edges of FLG sheets or attached to the surface steps, whereas the nanoparticles situated on the FLG flat surface are catalytically inactive. Since the 3D characteristics of the active NP is the main factor imposing the trench’s profile (the

shape of the walls), it is clear that, in order to create straight nanopatterns with smooth walls, a sharp control of the shape of the nanoparticles is imperative. Our HR-TEM investigation shows that, for most of the channels, the smoothness of the walls is lower than 2 nm. However, this smoothness is not enough for building high quality GNRs for which a perfect edge is required. Using Co nanoparticles, F. Schaffel and co-workers[48] reported an edge smoothness lower than 1 nm for the same experimental conditions (800°C, H_2 atmosphere). In this context, further investigations are necessary to adjust the shape of the active NPs and to refine the selectively of the deposited nanoparticles on the edges and steps.

The basal graphitic planes on which the nanoparticle fixes initially define the motion of the active nanoparticle during cutting. The basal plane and the cutting direction do not change when the nanoparticle crosses obstacles with "step-up" configurations defined by topographical steps or superimposed FLG sheets. If the thickness of these step-up obstacles exceeds the size of the nanoparticles, one assists at the creation of sub-surface channels (tunnels). By using the electron tomography as a main tool, the formation of tunnels as previously described by P.J. Goethel and R. T. Yang[35] is here directly confirmed. Nevertheless, the mechanisms responsible for this rather unexpected behavior remain unclear as the access of hydrogen to the NPs' surface is restrained. A. Tomita et al.[28] and G.A. L'Homme et al[40] (see *State of the art* section) proposed a reaction mechanism on which the C-H reaction takes place directly at the nanoparticle/FLG interface. In this case, two scenarios of H_2 supply at the interface can be envisioned. The first one assumes that the dissociation of the H_2 molecules takes place at the rear-facet of the nanoparticle, i.e. at the only part directly exposed to the H_2 atmosphere. Then, the atomic hydrogen migrates on the surface of the nanoparticle at the FLG interface. The obtained CH_4 molecules should follow the same path to the rear-facet of the nanoparticle, from where they desorb. The other scenario considers that the H_2 molecules can also diffuse through the graphene layers directly on the nanoparticle's surface and the reaction gas, CH_4, can be removed along the same path. Assuming that we have this scenario, a lower channeling rate should be observed for nanoparticles digging inside the FLG layers due to a slower H_2 supply/CH_4 desorption rate. In our experiment, no major difference between the mean length of the open-surface channels and that of the tunnels was observed. A better explanation of the tunnel formation is offered by P. J. Goethel et al.,[39] which proposed a reaction mechanism controlled by the dissolution of the carbon

atoms in the nanoparticle body (or only at its melted surface layer), followed by their transport at the open nanoparticle's rear-facet where the reactions with the molecular hydrogen takes place.

When the active nanoparticle encounters a step-down, more precisely a preexisting topographical feature on the FLG surface, another trench previously created or a free-standing graphene edge, one can assists at the stop of the cutting process or at a change in the cutting direction. When approaching a step-down topographical feature, the angle of approach together with the size of the nanoparticle, its shape and the depth of the channel will control the nanoparticle's behavior. If the conditions are reached and one of the nanoparticle's lateral facets maintains a sufficient contact area with the FLG, the adhesion force in the contact region will drag the nanoparticle on a new channeling track. The new channeling direction is most of the time at a 30° and 60° angle with respect to the previous direction. One special situation is represented by the folded free edges. As the FLG flakes were synthetized by the mechanical ablation of pencil leads assisted by an ultra-sonication process, folding is a common event and consequently also the interaction of the nanoparticles with such edges. However, when approaching folded edges, the nanoparticles are losing their initial basal plane by moving on a lower graphene layer, due to the curvature of the graphitic planes. Another important observation relates to the changes in the geometrical characteristics of the trenches when the nanoparticles change their channeling direction by interacting with step-down features or even when they turn on uniform FLG surfaces. In this case, after changing their cutting direction, the nanoparticles are generally moving on a different basal plane (an upper one). Moreover, the size of the nanoparticle and consequently the width of the channel are changing. As we will see in the next chapter, the nanoparticle does not simply turns at the turning point, changing one of its lateral facets in a new leading frontal facet. Instead, the process requires a certain reconfiguration of the nanoparticle before starting channeling in the new direction.

2.6. Subsequent applications of the catalytic nanopatterning

Since S.S. Datta and co-workers[44] proposed the catalytic hydrogenation as a method of patterning graphene and FLG with a nanoscale precision, significant advances have been reported (see *State of the art*). One important aspect is related to the viability of this method to produce both high quality graphene nanoribbons GNRs and high-surface area graphene-based catalytic substrates. We will now present some preliminary results concerning both of the above-mentioned applications.

2.6.1. From pencil leads to monolayer graphene nanoribbons

As we detailed in the *Sample preparation* (2.2.1), the source of FLG is a commercial available pencil lead, which is exfoliated by a solvent assisted mechanical ablation to a thickness of just a few layers. Then the FLG flakes are decorated with $Fe_{3-x}O_4$ NPs; this step is followed by the thermal treatment in an H_2 atmosphere during which the reduced (metallic) NPs do pattern the surface of the flakes with a well-defined network of channels. The catalyst (nanoparticles) is removed by an acid-based washing procedure (HNO_3, 80°C) and then the nanopatterned FLG is stored in powder form. So, is this network of "well-defined channels" convenient for creating GNRs? The answer is dependent on the shape of the GNRs that one wants to produce. For rectangular shapes it might be enough. Fig. 2.21 shows a schematic representation of rectangular GNRs fabrication through catalytic channeling. The approach is based on the "multistage" nanopatterning already reported by C. Lijie and co-workers[50]. The initial distance (d) between the nanoparticles decorating the graphene edge will define the width (t) of the nanoribbons, while the distance between the FLG edge and the initial channels (l) will set the length of the nanoribbons. However, to obtain such a control a number of problems need to be solved: i) controlling the size of the initial graphene flakes; ii) depositing NPs on a unique edge of the graphene flake for "one-way" cutting; iii) controlling the distance (d) between NPs; iv) controlling the size of the NPs (avoiding coalescence during heating); v) avoiding changes in direction during channeling. Apart from the aspects related to the controlled decoration with NPs, a perfect understanding of the channeling mechanism is required. Some of these aspects were discussed in the results section (edge smoothens, turning on uniform thickness areas, etc.). It is worth noticing that the system

presented is based on monolayer graphene, whereas we worked with FLG. The procedure of going from thick ribbons to monolayer GNRs will be presented later.

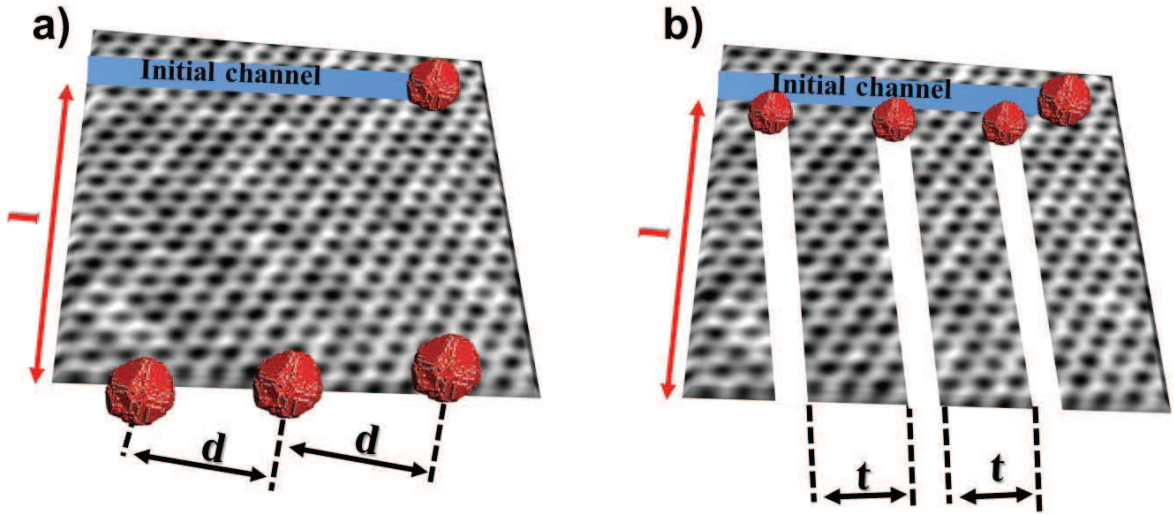

Figure 2.21. Schematic representation of rectangular GNRs fabrication using the catalytic nanopatterning of single layer graphene: a) before and b) after the last hydrogenation step.

The situation becomes more problematic when nanoribbons with a triangular shape are required. One way to create such GNRs is to take advantage of the interaction of active nanoparticles with the free edges of graphene flakes or with previously created channels (see "step-down" events in the *Results* section). Fig. 2.22 presents the ideal case of active nanoparticles deflected each time they reached the edges of the flake and the ones of the previous created channels. The approach requires a perfect control of the system's properties: i) the position of the NPs on the FLG edges; ii) their size and shape; iii) the initial depth of the channels; iv) the free-edge folding and so on.

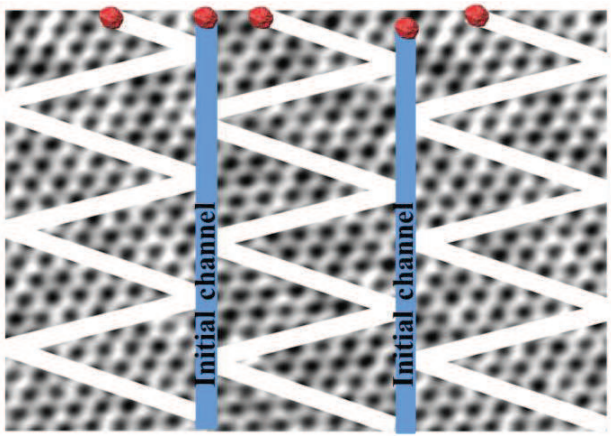

Figure 2.22. a) Schematic representation of triangle-shaped GNRs fabrication using the interaction of active NPs with a step-down type of feature: free edges and previous created channels.

Another way for obtaining triangle-shaped FLG sheets is to use the nanoparticle turning on a uniform FLG surface. In a related study[63] we reported a modified channeling procedure using ammonia (NH_3) as an atmosphere. The synthesis was conducted by Dr. I. Janowska at ICPEES Strasbourg. During the heating step, the NH_3 gas is decomposed in atomic N and H in a dissociation process catalyzed by the active surface sites of the nanoparticles. In a complex reaction mechanism, nitrogen diffuses in the bulk of the nanoparticles, resulting in highly faceted Fe_xN NPs. Fig. 2.23a shows the EFTEM elemental maps of an active nanoparticle (TEM image in Fig. 2.23b). The oxygen signal comes from the native oxidation due to the air exposure prior to the TEM analysis. The nitrogen presents a relatively uniform distribution in the core of the nanoparticle. The carbon map shows a channel with a V-shape end given by the similar shape of the active nanoparticle frontal facets. A TEM image of a non-oxidized nanoparticle with a V-shape arrangement of the frontal facets is shown in Fig. 2.23c. Although not exactly explained until now, this frontal faceting increases the turning probability of a nanoparticle on a uniform FLG surface, creating triangle shaped patterns. Fig. 2.24 shows two of these triangular patterns with sides of ~36 nm (a) and 150 nm (b). The size of the nanoparticle seems to define the size of the triangle sides: the smaller the nanoparticle, the smaller the side of the triangle pattern seems to be the general rule.

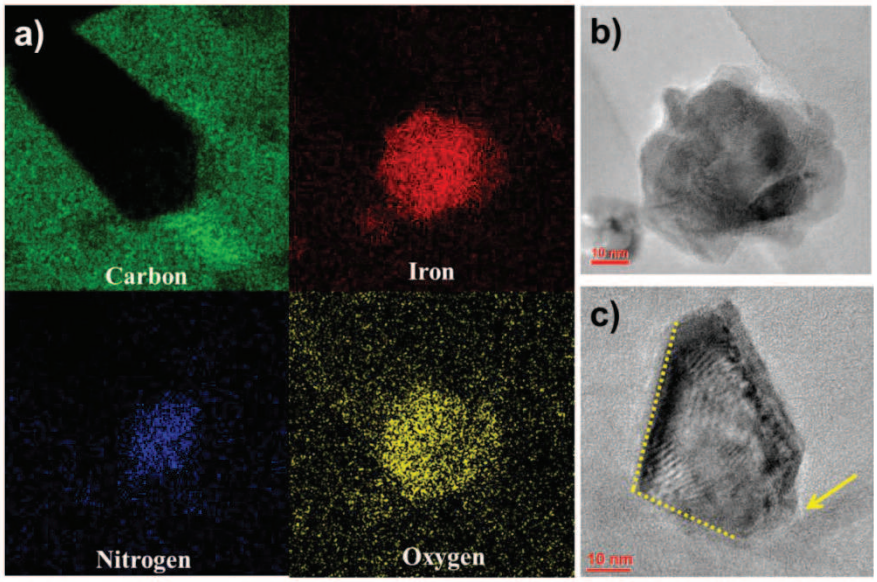

Figure 2.23. a) EFTEM analysis of an active nanoparticle obtained after a thermal treatment at 800°C (2h) in NH_3: Ar (50:50) atmosphere; b) TEM image of the nanoparticle shown in a). The irregular aspect is given by the native oxide shell; c) TEM image of a non-oxidized Fe_xN nanoparticle with V-shaped frontal facets.

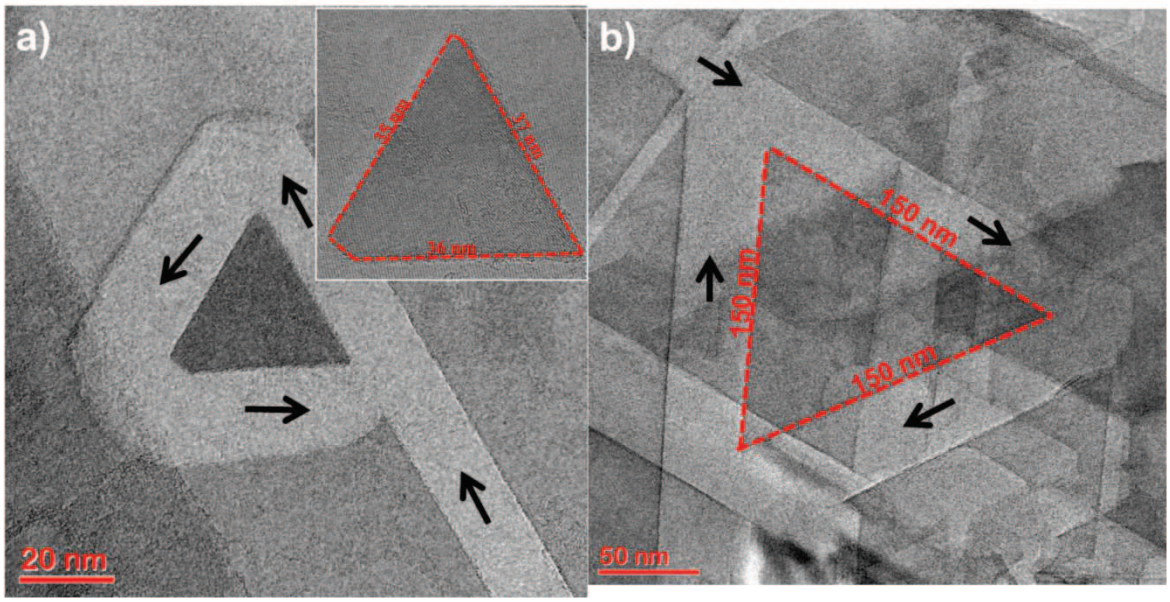

Figure 2.24. a) and b) Triangular patterns created by highly faceted Fe_xN nanoparticles due to their multiple turning points on uniform FLG surfaces.

However, the triangular nanopatterns presented in Fig. 2.24 are still embedded in the initial FLG flake and too thick to be used as nanoribbons. To extract the GNRs from such structures, one can apply a liquid-based exfoliation technique. The schematic representation of the exfoliation technique is shown in Fig. 2.25a. The first performed liquid exfoliation experiment of the powder FLG after the nanopatterning in an NH_3 atmosphere shows promising results. An exfoliated nanoribbon with a lateral size of around 270 nm is presented in Fig. 2.26b. The exfoliation was performed using a water-based exfoliation method previously reported[64]. These preliminary results show that the liquid exfoliation can be the solution for extracting the GNRs from the nanopatterned FLG. Otherwise, we should be able to directly nanopattern single layer graphene (SLG) flakes in order to produce single layer nanoribbons. Note that, the patterning of suspended SLG flakes was already reported. However, for large-scale applications, monolayer graphene sheets will have to be deposited on substrates which will significantly influence the motion of the nanoparticles.

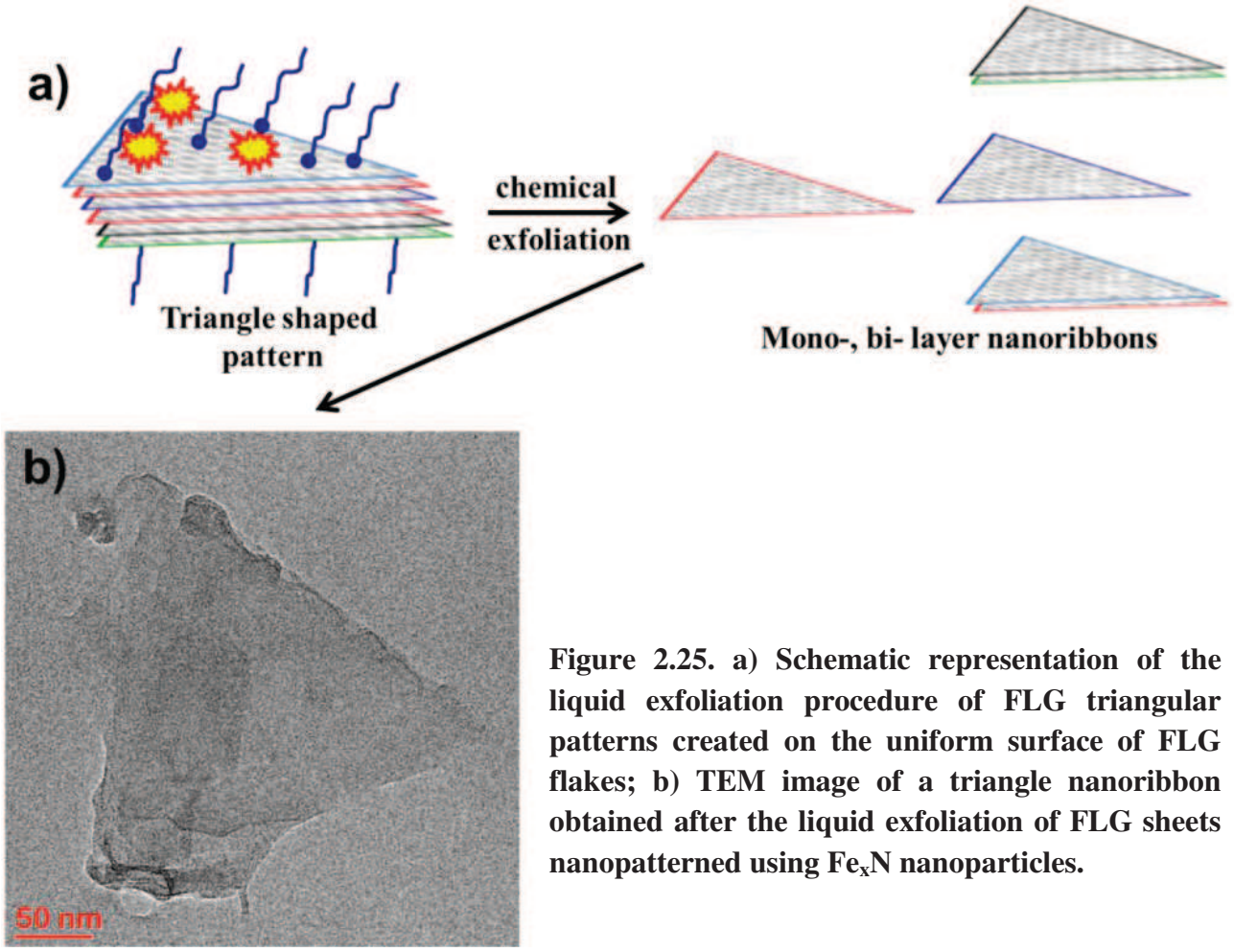

Figure 2.25. a) Schematic representation of the liquid exfoliation procedure of FLG triangular patterns created on the uniform surface of FLG flakes; b) TEM image of a triangle nanoribbon obtained after the liquid exfoliation of FLG sheets nanopatterned using Fe_xN nanoparticles.

2.6.2. Nanopatterned FLG flakes as support for nanoparticle catalyst

One of our expectations for applying the catalytic hydrogenation to FLG flakes was to increase their surface area and the number of adhesion sites for nanoparticles. As shown before, the dual side cutting leads to a considerable increase of the FLG surface accessibility. A schematic representation of the stacking arrangement of FLG sheets and of the nanostructured ones is shown in Fig. 2.26. By carefully adjusting the density of the channels at the surface of the FLG, the surface properties of the FLG powder can be easily controlled. In order to test the potential of the nanopatterned FLG flakes as supports for nanoparticle-based catalysts, magnetite ($Fe_{3-x}O_4$), nanoparticles were deposited by simply immersing the nanostructured FLG powder in a solution of $Fe_{3-x}O_4$NPs for 12h performed the deposition. The TEM analysis (Fig. 2.27) shows that the channels are preferentially filled with nanoparticles, compared to the flat surface of the

flakes, and this behavior can be attributed to the high density of adhesion sites available on the channel's walls. The channel's filling degree depends on its width and depth. Fig. 2.27a shows a filling geometry with two rows of nanoparticles deposited in contact with the walls of the channel, while Fig. 2.27b shows a 3D filling. *In-situ* thermal treatments at 700°C (Fig. 2.27c) show that the nanoparticles embedded in the channels (red rectangle) possess an increased sintering resistance compared to the ones decorating flat surfaces (yellow rectangles) due to a stronger adhesion of the nanoparticles to the channel's surface. In this way, the important role of the anchorage sites from the channel's walls is shown once again.

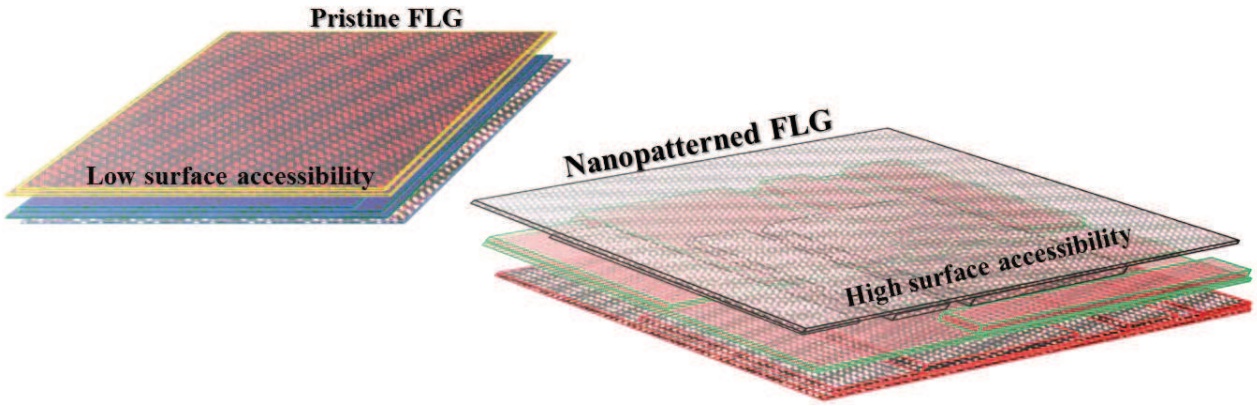

Figure 2.26. Schematic representation of the stacking arrangement of pristine and nanostructured few-layer graphene flakes.

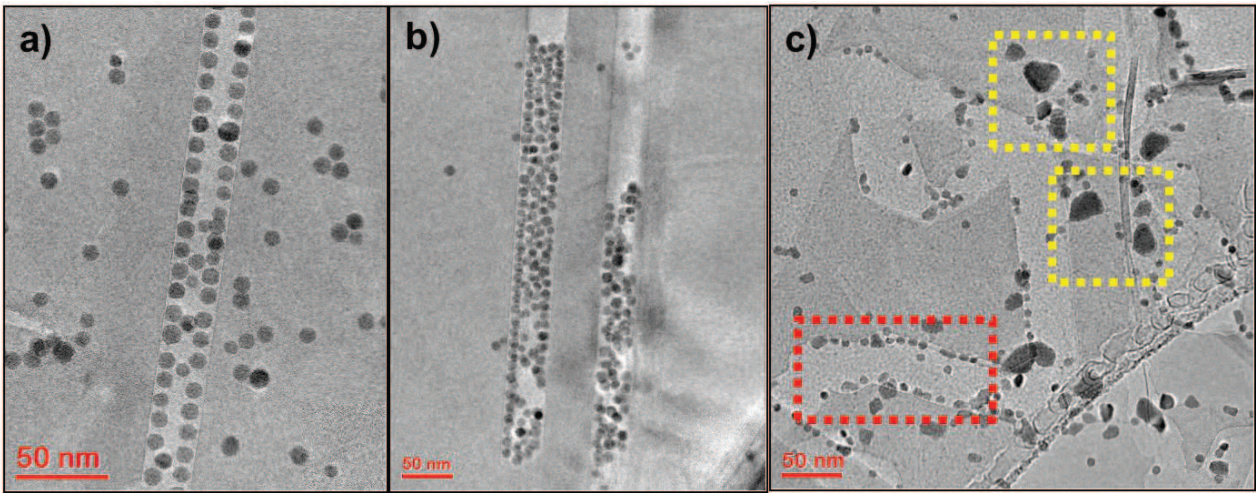

Figure 2.27. TEM images showing two different arrangement modes of the magnetite nanoparticle inside the channels: a) two-row arrangement and b) 3D irregular filling; c) TEM image showing the high sintering resistance (700°C) of the nanoparticle embedded in the channels (red) compared to the ones sitting on a flat surface (yellow).

2.7. Conclusions

This study demonstrates the ability of electron tomography in investigating processes at the nanoscale. The catalytic nanopatterning of FLG graphene, as revealed by ET, is a complex phenomenon depending both on the topography of the FLG substrate and the reaction conditions. Controlling the properties of the initial FLG substrate in terms of surface topography, edge type, flakes size, and thickness represents the first step for achieving a better control of the nanopatterning process. Moreover, a better understanding of the reaction mechanism and the influence of the structure of the nanoparticles in the catalytic hydrogenation is required. The present study reveals a number of important properties of the catalytic nanopatterning of FLG flakes by metallic Fe nanoparticles. These findings can help the optimization process, as it is required for the implementation of the FLG nanopatterning in large-scale applications.

2.8. Perspective

One major drawback of the catalytic nanopatterning is that during the heating step at 800°C the initial very narrow size distribution of the nanoparticles is changed in a broad one, due to uncontrolled coalescence. Therefore, controlling the lateral size of the channels is difficult. One way to overcome this problem is to take advantage of the Ag nanoparticles surface plasmons resonance. Silver nanoparticles are well known for their size selective absorption of UV and visible light. Moreover, the plasmonic heating effect[65] allows the selective heating of the noble metal nanoparticles without significantly increasing the temperature of the substrate. Applying this method to FLG flakes decorated with Ag nanoparticles one could obtain a size-selective channeling as a function of the wavelength of the incident light. As initially only the surface temperature of the Ag nanoparticle will increase, their coalescence will be drastically reduced. Therefore, their initial size should be preserved. Once the channeling process starts, the heating of FLG substrate has negligible effects, as the nanoparticles are entrenched in the channels. Our studies have shown that Ag nanoparticle can nanopattern the FLG substrate when exposed to UV light. In a future experiment the UV lamp will be replace with a wavelength-controlled UV laser in order to selectively excite the surface plasmons of the Ag nanoparticles.

2.9. References

1. Geim, A. K. & Novoselov, K. S. The rise of graphene. *Nat. Mater.* **6,** 183–191 (2007).
2. Novoselov, K. S. *et al.* Electric Field Effect in Atomically Thin Carbon Films. *Science* **306,** 666–669 (2004).
3. Castro Neto, A. H., Guinea, F., Peres, N. M. R., Novoselov, K. S. & Geim, A. K. The electronic properties of graphene. *Rev. Mod. Phys.* **81,** 109–162 (2009).
4. Geim, A. K. Graphene: Status and Prospects. *Science* **324,** 1530–1534 (2009).
5. Machado, B. F. & Serp, P. Graphene-based materials for catalysis. *Catal. Sci. Technol.* **2,** 54–75 (2011).
6. Zhu, Y. *et al.* Graphene and Graphene Oxide: Synthesis, Properties, and Applications. *Adv. Mater.* **22,** 3906–3924 (2010).
7. Chen, Z., Lin, Y.-M., Rooks, M. J. & Avouris, P. Graphene nano-ribbon electronics. *Phys. E Low-Dimens. Syst. Nanostructures* **40,** 228–232 (2007).
8. Han, M., Özyilmaz, B., Zhang, Y. & Kim, P. Energy Band-Gap Engineering of Graphene Nanoribbons. *Phys. Rev. Lett.* **98,** (2007).
9. Zhang, Q., Fang, T., Xing, H., Seabaugh, A. & Jena, D. Graphene Nanoribbon Tunnel Transistors. *IEEE Electron Device Lett.* **29,** 1344–1346 (2008).
10. Saroka, V. A., Batrakov, K. G. & Chernozatonskii, L. A. Edge-modified zigzag-shaped graphene nanoribbons: Structure and electronic properties. *Phys. Solid State* **56,** 2135–2145 (2014).
11. Brey, L. & Fertig, H. A. Electronic states of graphene nanoribbons studied with the Dirac equation. *Phys. Rev. B* **73,** 235411 (2006).
12. Xie, Y. E., Chen, Y. P., Sun, L. Z., Zhang, K. W. & Zhong, J. The effect of corner form on electron transport of L-shaped graphene nanoribbons. *Phys. B Condens. Matter* **404,** 1771–1775 (2009).
13. Son, Y.-W., Cohen, M. L. & Louie, S. G. Energy Gaps in Graphene Nanoribbons. *Phys. Rev. Lett.* **97,** 216803 (2006).
14. Wakabayashi, K., Fujita, M., Ajiki, H. & Sigrist, M. Electronic and magnetic properties of nanographite ribbons. *Phys. Rev. B* **59,** 8271–8282 (1999).
15. Kudin, K. N. Zigzag Graphene Nanoribbons with Saturated Edges. *ACS Nano* **2,** 516–522 (2008).
16. Chang, S.-L., Lin, S.-Y., Lin, S.-K., Lee, C.-H. & Lin, M.-F. Geometric and Electronic Properties of Edge-decorated Graphene Nanoribbons. *Sci. Rep.* **4,** (2014).
17. Chen, J.-J., Wu, H.-C., Yu, D.-P. & Liao, Z.-M. Magnetic moments in graphene with vacancies. *Nanoscale* **6,** 8814–8821 (2014).
18. Narita, A. *et al.* Synthesis of structurally well-defined and liquid-phase-processable graphene nanoribbons. *Nat. Chem.* **6,** 126–132 (2014).
19. Englert, J. M., Hirsch, A., Feng, X. & Müllen, K. Chemical methods for the generation of graphenes and graphene nanoribbons. *Angew. Chem. Int. Ed Engl.* **50,** A17–24 (2011).
20. Jiao, L., Zhang, L., Wang, X., Diankov, G. & Dai, H. Narrow graphene nanoribbons from carbon nanotubes. *Nature* **458,** 877–880 (2009).
21. Elías, A. L. *et al.* Longitudinal Cutting of Pure and Doped Carbon Nanotubes to Form Graphitic Nanoribbons Using Metal Clusters as Nanoscalpels. *Nano Lett.* **10,** 366–372 (2009).
22. Jiao, L., Wang, X., Diankov, G., Wang, H. & Dai, H. Facile synthesis of high-quality graphene nanoribbons. *Nat. Nanotechnol.* **5,** 321–325 (2010).
23. Tapasztó, L., Dobrik, G., Lambin, P. & Biró, L. P. Tailoring the atomic structure of graphene nanoribbons by scanning tunnelling microscope lithography. *Nat. Nanotechnol.* **3,** 397–401 (2008).
24. Campos, L. C., Manfrinato, V. R., Sanchez-Yamagishi, J. D., Kong, J. & Jarillo-Herrero, P. Anisotropic Etching and Nanoribbon Formation in Single-Layer Graphene. *Nano Lett.* **9,** 2600–2604 (2009).
25. Ci, L. *et al.* Controlled nanocutting of graphene. *Nano Res.* **1,** 116–122 (2008).

26. Wang, M. *et al.* Structural Modification of Graphene Sheets to Create a Dense Network of Defect Sites. *J. Phys. Chem. Lett.* **4,** 1484–1488 (2013).
27. Melinte, G. Nanoparticles deposition in the open-surface channels of nanostructured FLG, in preparation, (2016).
28. Tomita, A. & Tamai, Y. Hydrogenation of carbons catalyzed by transition metals. *J. Catal.* **27,** 293–300 (1972).
29. Tomita, A., Sato, N. & Tamai, Y. Hydrogenation of carbons catalyzed by nickel, platinum and rhodium. *Carbon* **12,** 143–149 (1974).
30. Goethel, P. J. & Yang, R. T. Mechanism of catalyzed graphite oxidation by monolayer channeling and monolayer edge recession. *J. Catal.* **119,** 201–214 (1989).
31. Baker, R. T. K., France, J. A., Rouse, L. & Waite, R. J. Catalytic oxidation of graphite by platinum and palladium. *J. Catal.* **41,** 22–29 (1976).
32. Tomita, A. & Tamai, Y. Optical microscopic study on the catalytic hydrogenation of graphite. *J. Phys. Chem.* **78,** 2254–2258 (1974).
33. Oh, S. G. & Baker, R. T. K. In situ electron microscopy investigation of the behavior of supported cobalt particles. *J. Catal.* **128,** 137–147 (1991).
34. Baker, R. T. K., Chludzinski Jr., J. J. & Sherwood, R. D. A comparison of the catalytic influence of nickel, iron and nickel-iron on the gasification of graphite in various gaseous environments. *Carbon* **23,** 245–254 (1985).
35. Goethel, P. J. & Yang, R. T. The tunneling action of group VIII metal particles in catalyzed graphite hydrogenation. *J. Catal.* **114,** 46–52 (1988).
36. Goethel, P. J., Tsamopoulos, J. A. & Yang, R. T. Modeling the channeling action of catalysts in gas-carbon reactions. *AIChE J.* **35,** 686–689 (1989).
37. Goethel, P. J. & Yang, R. T. Mechanism of graphite hydrogenation catalyzed by ruthenium particles. *J. Catal.* **111,** 220–226 (1988).
38. Goethel, P. J. & Yang, R. T. Platinum-catalyzed hydrogenation of graphite: Mechanism studied by the rates of monolayer channeling. *J. Catal.* **101,** 342–351 (1986).
39. Goethel, P. J. & Yang, R. T. Mechanism of graphite hydrogenation catalyzed by nickel. *J. Catal.* **108,** 356–363 (1987).
40. L'Homme, G. A. & Boudart, M. The ignition of carbon and its catalysis by platinum. *Symp. Int. Combust.* **11,** 197–202 (1967).
41. Datta, S. S. Wetting and energetics in nanoparticle etching of graphene. *J. Appl. Phys.* **108,** 024307 (2010).
42. Solís-Fernández, P., Yoshida, K., Ogawa, Y., Tsuji, M. & Ago, H. Dense Arrays of Highly Aligned Graphene Nanoribbons Produced by Substrate-Controlled Metal-Assisted Etching of Graphene. *Adv. Mater.* **25,** 6562–6568 (2013).
43. Ago, H., Kayo, Y., Solís-Fernández, P., Yoshida, K. & Tsuji, M. Synthesis of high-density arrays of graphene nanoribbons by anisotropic metal-assisted etching. *Carbon* **78,** 339–346 (2014).
44. Datta, S. S., Strachan, D. R., Khamis, S. M. & Johnson, A. T. C. Crystallographic Etching of Few-Layer Graphene. *Nano Lett.* **8,** 1912–1915 (2008).
45. Severin, N., Kirstein, S., Sokolov, I. M. & Rabe, J. P. Rapid Trench Channeling of Graphenes with Catalytic Silver Nanoparticles. *Nano Lett.* **9,** 457–461 (2008).
46. Schäffel, F. *et al.* Shedding light on the crystallographic etching of multi-layer graphene at the atomic scale. *Nano Res.* **2,** 695–705 (2009).
47. Schäffel, F. *et al.* Tracking down the catalytic hydrogenation of multilayer graphene. *Phys. Status Solidi C* **7,** 2731–2734 (2010).
48. Schäffel, F. *et al.* Atomic Resolution Imaging of the Edges of Catalytically Etched Suspended Few-Layer Graphene. *ACS Nano* **5,** 1975–1983 (2011).
49. Wang, R. *et al.* Cobalt-Mediated Crystallographic Etching of Graphite From Defects. *Small* **8,** 2515–2523 (2012).

50. Ci, L. *et al.* Graphene Shape Control by Multistage Cutting and Transfer. *Adv. Mater.* **21,** 4487–4491 (2009).
51. Booth, T. J. *et al.* Discrete Dynamics of Nanoparticle Channelling in Suspended Graphene. *Nano Lett.* **11,** 2689–2692 (2011).
52. Janowska, I. *et al.* Mechanical thinning to make few-layer graphene from pencil lead. *Carbon* **50,** 3106–3110 (2012).
53. Baaziz, W. *et al.* Few layer graphene decorated with homogeneous magnetic Fe_3O_4 nanoparticles with tunable covering densities. *J. Mater. Chem. A* **2,** 2690–2700 (2014).
54. Arenal, R. *et al.* Extending the analysis of EELS spectrum-imaging data, from elemental to bond mapping in complex nanostructures. *Ultramicroscopy* **109,** 32–38 (2008).
55. Kremer, J. R., Mastronarde, D. N. & McIntosh, J. R. Computer Visualization of Three-Dimensional Image Data Using IMOD. *J. Struct. Biol.* **116,** 71–76 (1996).
56. Agulleiro, J. I. & Fernandez, J. J. Fast tomographic reconstruction on multicore computers. *Bioinformatics* **27,** 582–583 (2011).
57. Zürner, A., Döblinger, M., Cauda, V., Wei, R. & Bein, T. Discrete tomography of demanding samples based on a modified SIRT algorithm. *Ultramicroscopy* **115,** 41–49 (2012).
58. Zan, R., Bangert, U., Ramasse, Q. & Novoselov, K. S. Metal−Graphene Interaction Studied via Atomic Resolution Scanning Transmission Electron Microscopy. *Nano Lett.* **11,** 1087–1092 (2011).
59. Papaefthimiou, V. *et al.* Effect of the Specific Surface Sites on the Reducibility of α-Fe2O3/Graphene Composites by Hydrogen. *J. Phys. Chem. C* **117,** 20313–20319 (2013).
60. Wang, C. M. *et al.* Void formation during early stages of passivation: Initial oxidation of iron nanoparticles at room temperature. *J. Appl. Phys.* **98,** 094308 (2005).
61. Homma, Y. *et al.* Role of Transition Metal Catalysts in Single-Walled Carbon Nanotube Growth in Chemical Vapor Deposition. *J. Phys. Chem. B* **107,** 12161–12164 (2003).
62. Shibuta, Y. & Suzuki, T. Melting and nucleation of iron nanoparticles: A molecular dynamics study. *Chem. Phys. Lett.* **445,** 265–270 (2007).
63. Baaziz, W., Melinte, G., Ersen, O., Pham-Huu, C. & Janowska, I. Effect of nitriding/nanostructuration of few layer graphene supported iron-based particles; catalyst in graphene etching and carbon nanofilament growth. *Phys. Chem. Chem. Phys.* **16,** 15988–15993 (2014).
64. Ihiawakrim, D. *et al.* A single-stage functionalization and exfoliation method for the production of graphene in water: stepwise construction of 2D-nanostructured composites with iron oxide nanoparticles. *Nanoscale* **5,** 9073–9080 (2013).
65. Adleman, J. R., Boyd, D. A., Goodwin, D. G. & Psaltis, D. Heterogenous Catalysis Mediated by Plasmon Heating. *Nano Lett.* **9,** 4417–4423 (2009).

Chapter III

In-situ observation of catalytic nanopatterning of few-layer graphene

As shown in the previous chapter, the catalytic nanopatterning of FLG is a complex phenomenon that depends on multiple factors related both to the FLG topography and to the morphology of the active nanoparticles. For some of the aspects investigated, *ex-situ* electron tomography (ET) had proved to be a reliable approach, especially when looking at the foot-print of the nanoparticle motion, i.e. the channels' profile. However, in some cases a restructuration of the active nanoparticles during the channeling process was clearly observed. The nanoparticle's behavior at the time when its channeling direction changed was of special interest. From the ET data we could not predict the real behavior of the active nanoparticle in such conditions. Therefore, the real-time observation of the nanoparticles patterning the FLG substrate is essential. Environmental electron microcopy (E-TEM) is the most appropriate technique for investigating dynamical processes, offering access to imaging and chemical analyses at near atomic resolution. First, we will briefly present the reduction of magnetite nanoparticle under H_2 atmosphere. The *in-situ* observation of the metallic Fe nanoparticles channeling on the surface of FLG is then studied in detailed.

3.1 Environmental electron microscopy

3.1.1 State-of-the-art

Traditionally, transmission electron microscopy (TEM) played an important role in understanding the structure of the catalysts involved in the heterogeneous catalysis reactions. Its importance arises from the near atomic resolution of the TEM technique, as well as from the existence of several associated conventional (electron diffraction) and analytical (EELS and EDX) tools. However, in most cases researchers were limited to investigating only the initial

(before reaction) and the final (after reaction) states of the catalyst materials. In the best case scenario, intermediate samples were extracted from the reaction environment and analyzed under TEM, offering a glimpse on the reaction dynamics. As the influence of the reaction environment is critical for the evaluation of the geometric composition and electronic structure of the catalyst, as well as in understanding its properties and behavior, the static catalyst transferred in the high-vacuum microscope column is often no longer representative for the dynamical catalyzed reaction[1,2] under study. The catalyst is expected to be in an unstable structure during the catalytic process and to rapidly change to a stable one when removed from the reaction medium. The development of environmental or vacuum transfer holders to protect the sample from oxidation in air, as well as of *in-situ* heating specimen holders for mimicking the temperature conditions of the reaction environment, has offered a significant improvement of the analysis conditions. Nevertheless, the growing need for real-time observation and analysis of nanomaterials in their reaction environment (gas or liquid) led to a strong collaboration between the material scientists and microscopists for transforming the electron microscope (EM) from an "imaging tool" to a "laboratory" for nanoscience and nanochemistry[3]. The solution has been the development of "environmental cells" (E-cells), which allows one to have access to the sample structure and chemistry under quasi-real working conditions. The research headed toward two directions leading to the development of two different but complementary techniques: differential pumped E-cells[4,5] and window-type E-cells[6,7].

Along with many other technological challenges that the early E-cell developers had to solve, like fitting the E-cell components between the objective lens pole pieces, finding a way to confine the gas at the sample level without contaminating the whole microscope's column was essential. This is because one of the main requirements for properly running an EM, which is to maintain a high vacuum environment especially at the electron gun level (10^{-6} Pa for a Schottky FEG and 10^{-9} Pa for a Cold FEG),[8] had to be preserved.

In a differential pumped system, the gas injected through a port on the objective lens pole piece is confined around the specimen stage by using restricting apertures placed along the microscope column and a modified differential pumping system. The aperture system reduces the gas leak and powerful turbo molecular pumps capture the escaped gas in the multiple stages delimited by the apertures with a pressure drop at each step[9,10,11]. This approach requires the modification of the entire microscope column transforming it in a dedicated environmental TEM

(E-TEM). Due to the vacuum requirements, the maximum achievable gas pressure at the sample level is about 20 Torr[12]. The gas path through which the electrons have to pass before reaching the specimen is about 7-10 mm, which is the equivalent of a 10 nm thick solid (at 7 Torr gas pressure). The temperature control is achieved by using heating stages, either conventional wire-heating or membrane-heating holders. The latter offers an increased mechanical stability, better temperature control and fast temperatures change rates (up to 10^6°C/s)[13].

The window-type E-cells (environmental closed cells) require little or no modification of the EM itself. The gas is confined between two electron transparent windows (amorphous SiN membranes) while the microscope's high vacuum is sealed[14,15]. All the cell's components (heating stage, SiN windows, gas inlets and outlets) are assembled on the sample holder[16]. Using 30 nm thick SiN windows, the gas pressure can go up to 1 atm, which allows one to get observation conditions as close as those operated in several catalytic processes and therefore avoiding the problem linked with the partial structural modification under low pressure gas medium. The distance between the lower and the upper windows varies between 5 μm and a few hundreds μm depending on the cell design, which is the equivalent of a few-nanometer thick solid (at 1 atm gas pressure). The heating stage based only on the membrane heating technique can easily reach 1000° C[17].

The advantages of the window-type E-cell over the dedicated E-TEM instruments are clear. The first one is a much lower acquisition price and also lower maintenance costs for the closed E-cells. The second one is the much higher gas pressure that can be applied inside a closed E-cell. Commercially available ones allow reactions to be performed up to 1 atm gas pressure. Moreover, a 4 atm H_2 pressure was already reported for a similar system[18].

The closed E-cells also offer the advantage of mobility between microscopes (if they share the same holder stage). Corrosive gases can be used in a closed E-cell while the dedicated E-TEM ones can only handle non-corrosive gases such as H_2, O_2, N_2, NH_3, CO, water vapors[12]. However, closed E-cells also present a number of disadvantages. The main drawback is represented by the very existence of the SiN windows. While in a dedicated E-TEM no additional object besides the gas layer does play a role in the image formation process, in a closed E-cell the gas restrictive windows can significantly reduce the image resolution. Nonetheless, atomic resolution was reported in a closed E-cell with ~30 nm thick windows at 1 atm gas pressure[16].

Another shortcoming, also related to the existence of the SiN windows, lies in tilting restrictions, because the effective thickness of the membrane is increasing as the tilt angle increases. A third disadvantage is related to the emission of highly-reactive secondary electrons by the SiN membranes when irradiated by the electron beam. These secondary electrons have a high reduction potential, influencing the normal reaction kinetics[19]. The main characteristics of the closed E-cells and the dedicated E-TEM are summarized in Table 3.1.

Table 3.1. The main characteristics of the differential pumped microscopes and windows-type E-cells.

E-cell type	Advantages	Disadvantages
Differential Pumped System (E-TEM)	Compatible with all types of specimen holders (STM/TEM, tomography, double-tilt).	Long gas path (7-10 mm): increased probability of electron/gas interactions.
	Pre-reaction removal of the surface contaminants in the high vacuum of the column.	Low gas pressure at the sample level: ~20 Torr. Limited to non-corrosive gases.
	Large solid angles of collection for X-ray signals	High acquisition and maintenance costs.
Window-type E-cell	High gas pressure: 1 atm	Low pre-reaction vacuum (1-3 Torr): large contamination at low temperatures.
	Low acquisition and maintenance costs. Mobility between microscopes.	Fragile SiN windows. Major difficulties in sample preparation. Limited to the investigation of nanostructures allowing dispersion in solvents.
	Short gas path (from 5 μm to a few hundred μm).	Difficulties to efficiently collect the analytical signals.
	Allows experiments performed under corrosive atmospheres.	SiN windows influence of the reaction path: decreasing of the spatial resolution, highly reactive secondary electrons, local heating.

Using the EM for environmental studies is a complex and challenging task. This is due to the small mean free path of the electrons in dense gases causing elastic and inelastic electron scattering[20,21]. These two types of electron-gas interactions affect both the imaging resolution and the reaction kinetics[19,22]. In order to properly correlate the results obtained in the confined space of a closed E-cell under the continuous exposure to the electron beam with the ones obtained in *ex-situ* reactors, a close understanding of the effect of the high energy electron beam in the

reaction kinetics is essential. The next part summarizes the progress made in the investigation of the electron beam's influence in environmental experiments.

3.1.2 "Imaging" chemical reactions under electron beams

The electron beam interaction with matter has always presented a dual quality. The first one arises from the fact that without an electron-sample interaction there could be no density contrast or phase-contrast imaging and no analytical signals, therefore, no electron microscopy. However, the inelastic interaction responsible for the creation of the analytic signals (electron energy loss, characteristics X-ray emission, secondary electrons/Auger electrons) can at the same time damage the analyzed sample[8]. Therefore, microscopists always had to find the proper imaging conditions (electron dose, exposure time, specimen temperature, and electron acceleration voltage) in order to preserve the initial state of the investigated material during its analysis. Through the same type of elastic and inelastic scatterings, the high-energy electron beam interacts with the gas atmosphere and the investigated sample inside an E-cell. Moreover, in a closed E-cell the electron beam also interacts with the SiN windows influencing the image formation and possibly the reaction kinetics. To help us visualizing the effect of each one of the E-cell's elements on the image formation and reaction path the schematic representation of the windowed environmental cell is shown in Fig. 3.1.

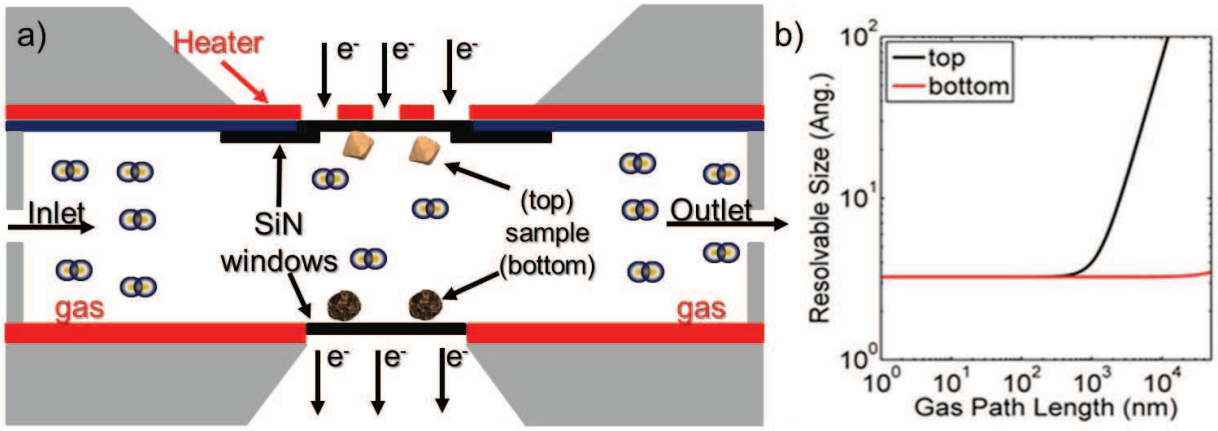

Figure 3.1. a) Schematic representation of a closed E-cell (adapted from L. F. Allard et al.[16]). Depending on the cell design the sample can be deposited under the upper window (top) or above the lower one (bottom). b) The effect of the sample position in the image resolution in conventional TEM (image taken from H. L. Xin et al.[17]).

Electron beam - SiN membranes interaction.

An elastic scattering event is by far the most likely interaction to happen between the incident electrons and the SiN membrane, as for all types of materials (gas, liquid, and solid)[23]. The multiple elastic scattering of electrons in the SiN membrane modifies the contrast of the image by increasing the background. A higher electron dose is necessary for maintaining a good S/N ratio of the recorded images (Rose's criterion for high resolution TEM S/N $\geq$ 5). The beam spreading depends on the membrane thickness (t) along a $t^{3/2}$ power low[20]. The chromatic blurring of the incident beam is due to inelastic energy losses. The low energy loss (plasmonic scattering) signal dominates the total inelastic scattering cross section[20,23]. The chromatic effects depend linearly on the thickness of the membranes (t) and, therefore, their influence in defining the image resolution is lower than the one of elastic blurring. Moreover, much of the effect of the plasmonic signal can be eliminated by filtering the transmitted electron beam in an image filter system, i.e. a post-column Gatan Image filter (GIF). Both elastic and chromatic blurring can be reduced by designing thinner SiN windows, with the usual thickness between 30 and 70 nm.

Even if the inelastic scattering of incident beams inside the SiN membrane does not have a considerable effect on the resolving power of the electron microscope, it can drastically influence the reaction kinetics through two distinctive mechanisms: phonon scattered electrons (local heating) and secondary electron (SE) emission (SE induced reduction). Although there is yet no detailed investigation of the local heating effect on SiN membranes, which are high temperature structural ceramics, one should expect the electron beam to influence the temperature of the irradiated area. The fundamentals of the phonon scattering show that the temperature gradient created depends on the thickness, the defects density, and the temperature of the membrane. If one of these three parameters increases, the electron beam induced temperature gradient will also increase[23]. Moreover, the formation of a silicon oxide layer (a low thermal conductor ceramic) on both sides of the SiN windows increases the influence of the electron beam in defining the local temperature. The SE emissions and their influence on the reaction paths have not been thoroughly studied yet. Both characteristic Auger electrons of energies between a few hundred eV to a few keV, and low energy SE (emitted from the conduction or valance bands) with energies in the range 1-5eV are easily absorbed and can be emitted only from the membrane surface[23,24]. However, with the catalyst sitting directly on the SiN membrane, the influence of these easily absorbed electrons in defining the reaction paths should not be

neglected[19]. One method proposed to reduce the influence of these effects on the environmental experiments, besides lowering the incident electron dose, is to deposit a thin conductive film on the inner part of the window prior to the sample deposition[25].

Electron beam – gas layer interactions.

To simplify the model of the electron interactions with the gas molecules and their influence in the environmental experiments, the gas layer is generally approximated as a solid membrane. The thickness of the gas layer is defined by the distance between the top and bottom SiN membrane and each μm of gas at atmospheric pressure can be approximated as a 1 nm thick solid. The fundamentals of the electron beam-gas interactions are the same as their interactions with the SiN membranes. Elastic scattering is the most probable event and increasing the electrons' path length through the gas and the gas pressure considerably reduces the resolving power of the microscope. Moreover, the inelastic scattering events cause a very undesirable process: the gas ionization. The ionization transforms the molecular gas in a plasma-like environment with highly reactive ions which have the potential of drastically changing the normal path of the reactions[19]. Furthermore, the elastic scattering of the electron beam increases in an ion gas layer compared with the molecular one, additionally deteriorating the image resolution. Lowering the acceleration voltage increases the cross section of both elastic and inelastic scattering events. The surprise was the much higher influence of the total beam current irradiating the gas environment compared with the local current (the part of the electron beam collected at the detector) in defining the imaging conditions. This shows that even the part of the electron beam which does not directly contribute to the image formation inelastically interacts with the gas environment and ions formed far from the imaging area will move through the image plane contributing to the elastic scattering[22]. The electron beam-gas interaction also depends on the gas nature and on the lifetime of the various ions created.

Electron beam – sample interaction

The direct effect of the beam on samples analyzed in environmental conditions is similar with the one appearing in vacuum experiments. There are three main types of beam-induced damage on the samples: radiolysis, knock-out damage and local heating. The radiolysis (inelastic scattering) affects mostly the polymer samples. The knock-out damage (displacement of atoms

from the crystal lattice) represents a fundamental problem for crystalline materials. As we discussed above, local heating is affecting mostly low-conducting ceramics and polymers.

At this point, one must discuss the importance of the sample position inside the cell. The schematic representation of the E-cell presented in Fig. 3.1a shows that the sample can be deposited either below the upper window or above the lower one. Positioning the sample below the first SiN windows is preferred for two reasons: it is favorable to EDX analysis and to the STEM working mode. Having the sample above the gas layer significantly increases the amount of characteristic X-ray captured by the EDX detectors. In order to maintain the minimum scanning probe broadening in the STEM mode, the sample must be sited above the gas layer. Moreover, since the image is formed point-by-point, the STEM resolution is not affected by the interactions of the existing beam with the gas phase. By contrast to the STEM mode, in high resolution TEM, the exit waves are easily affected by post-specimen interactions inducing elastic blurring. Therefore, it is highly recommended that for TEM experiments the sample be deposited on the lower SiN window. Fig. 3.1b shows the drastic influence of the gas layer on the image resolution in the TEM mode. When positioned below the gas phase, the resolving power seems to not be affected by the gas layer thickness. However, when the exit waves have to pass through the gas phase, the resolution drastically decreases for a gas thickness larger than 1 μm.

To summarize this part, one should remember that working with a close E-cell presents a higher degree of difficulty than the use of other *in-situ* TEM techniques. The electron beam interactions with the cell's components can drastically alter the reactions paths and the microscope performances. A good understanding of the beam-induced phenomena in the gas cells is necessary for an accurate interpretation of the obtained information. The understanding of all these possible artifacts will help for a better uncovering of the "real" operating catalytic process. The correct usage of adjustable parameters as the acceleration voltage, the total beam current, the current density, the gas pressure and the gas flow rates are important as well. Nevertheless, the inelastic interactions of the electron beam with the gas environment represent one way to analyze the reaction kinetics and the reaction products by measuring the electron energy loss (EELS). Another way is to connect the E-cell's gas outlet to a mass spectrometer allowing the real-time analysis of the reaction products.

3.2 Methods

3.2.1. Atmosphere Protochips™ windows-type E-cell

The experiments presented in this chapter were the first ones performed at IPCMS Strasbourg with the Atmosphere E-cell. Under a special commercial agreement, our institute purchased the first Atmosphere E-cell system sold in Europe. A part of the results obtained is currently used by the Protochips™ company for advertising the Atmosphere E-cell. For more details please visit http://www.protochips.com/.

A detailed description of the Atmosphere environmental cell is provided in the Allard L. F. et al. work[16]. A collection of photographs showing the E-cell's design is presented in Fig. 3.2. In this early design adapted for probe corrected STEM experiments, the small top-chip (Fig. 3.2b) incorporates the heating device, and therefore the sample is deposited on it. The function of the bottom chip (Fig. 3.2c) is the transmission of the current from the heater leads to the top chip and the sealing of the gas phase. A new design adapted for HR-TEM with the heating device incorporated directly on the bottom chip is already available.

One of the main advantages of the Atmosphere E-cell is represented by the strict temperature control offered by the membrane-based (MEMS) heating technology. The MEMS heating devices allow a temperature ramping from 20°C to 1000°C in just 1 ms. The small heating area (0.5 x 0.5 mm^2) creates only a small mechanical drift (thermal expansion induced drift).[13] Therefore, the stable conditions are rapidly restored after the temperature ramping, allowing high resolution imaging just a few seconds after the required temperature is reached. The high mechanical stability recommends Atmosphere E-cell as an ideal device for real-time studies of dynamical experiments, as the catalytic nanopatterning of FLG flakes. Moreover, each heating chip proposed by Protochips Inc. is independently calibrated in different gas atmospheres. This precise calibration eliminates the influence of small fabrication artifacts, allowing a temperature precision of ±1.5°C.

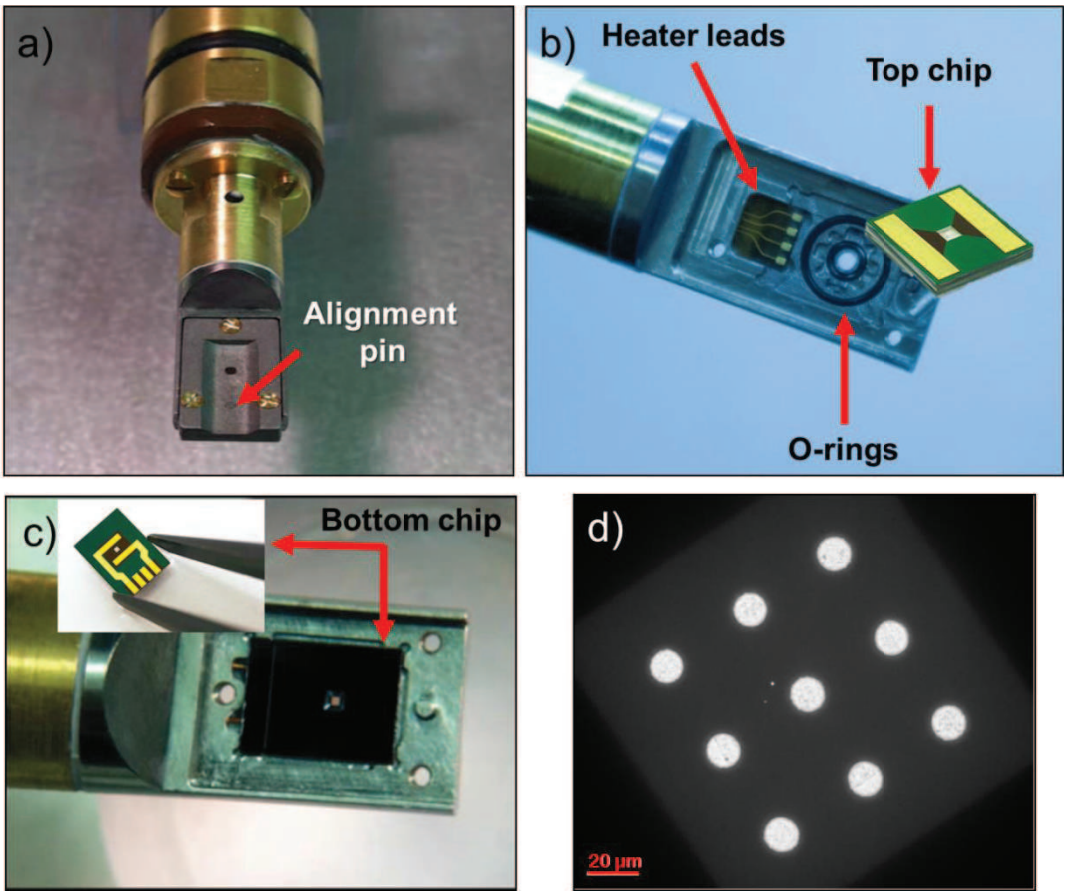

Figure 3.2. a) Bottom view of the Atmosphere E-cell holder compatible with JEOL UHP pole-piece configuration (2 mm gap). b) and c) Views of the inside of the E-cell. Images taken from Allard L. F. et al.[16]. d) Low-magnification image of the central part of the heating windows (SiC ceramic). The bright circles represent the analysis area covered only by SiN.

The small inner diameter of the gas supply capillary lines (0.175 µm) and also the small volume of gas added between the two windows (1.5 mm^3), supply only a small amount of gas (even at atmospheric pressure), therefore, in the unlikely event of a membrane failure inside the microscope the vacuum loss is not dangerous for the electron gun.

In order to reduce the bulging effect of the SiN windows appearing at high gas pressures, which significantly increases the path of the electrons through the gas layer, the heater membranes are regularly patterned with 6-10 µm holes. However, this limits the area of analysis and restricts thus the investigation of catalyst supports with high lateral sides (FLG flakes, CNTs).

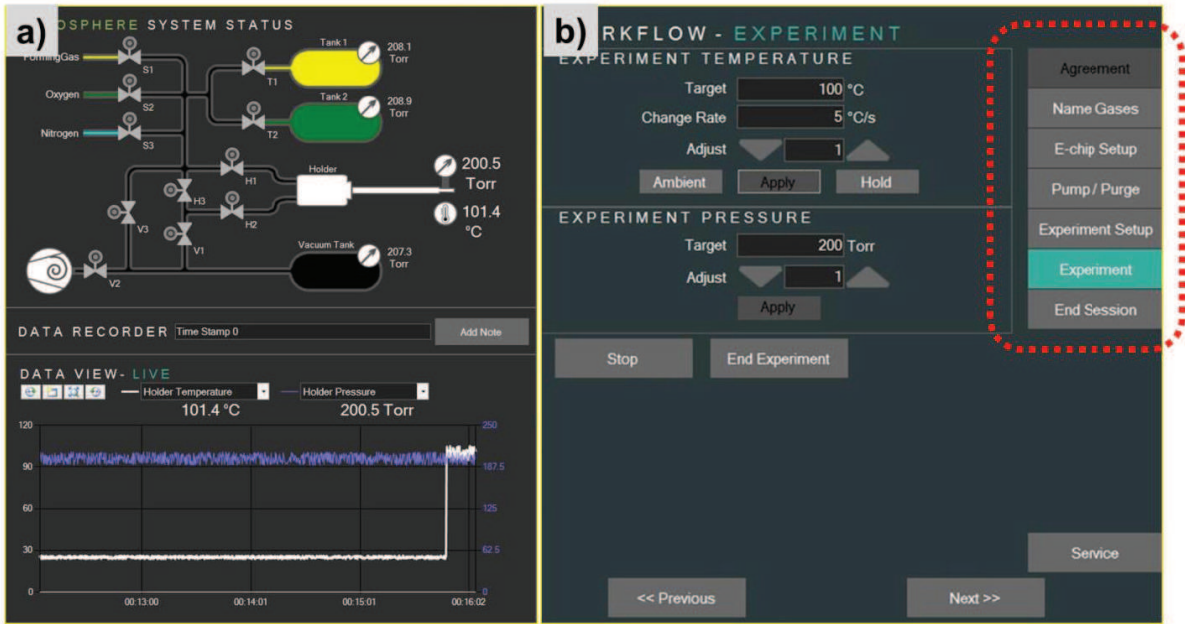

Figure 3.3. Atmosphere software. a) View of the manifold system containing the gas lines, valves, gas tanks and the dry mechanical vacuum pump. b) View of the software control panel (highlighted in red).

The computer controlled manifold is another major advantage of the Atmosphere E-cell system (Fig. 3.3a). It's allowing a fine control of the gas pressure at the specimen level (±2 Torr) both in static and flow mode. The entire gas cell is controlled by a user-friendly software (see Fig. 3.3b). Six successive steps (red rectangle in Fig. 3.3b) have to be followed for each experiment out of which purging the system and setting the reaction conditions are the most important. The cell's manifold does not allow (at the present time) the gas mixtures, thus in our early experiments we were obliged to use pure reactive gases. Presently the installation at IPCMS of an exterior system capable of controlling the mixture of reactive gases with inert ones (N_2, Ar, He) is ongoing.

As already mentioned (see Table 3.1) an important drawback of the closed E-cells is that the pre-analysis vacuum achieved inside the reaction chamber reaches at its best around 1 Torr. The holder is not connected to a turbomolecular pump, only to a dry pumping system capable of managing high corrosive gases. Therefore, the contamination inside the reaction chamber represents a major problem. For the air complete evacuation a purge program with inert gases is required before each experiment. However, the built-up carbon-base contamination under electron beam cannot be eliminated by the purge. As most of the samples are dispersed in organic

solvents (mostly ethanol), we can assume that the residual solvent represents the source of this contamination. The contamination especially affects the pre-reaction analyses of the sample of interest at room temperature. Fig. 3.4 shows a CoO-filled CNT observed prior to the reduction reaction at room temperature in 3 Torr of Ar. In the beam exposed area highlighted in yellow, a dense layer of carbon was built in a matter of seconds. This contamination layer is so thick and impermeable to gas that it prevents the CoO nanoparticle and the nanotube from the reduction action of H_2. The CNT regions outside this area (highlighted in red) were etched in an uncatalyzed hydrogenation reaction, while the central region seems unaffected by this phenomenon. To avoid the carbon-based contamination, a pre-heating treatment is necessary to remove surface bonded molecules, especially the solvent. The necessary temperature is around 200-250°C, and at this temperature, for some type of sample, structural changes can already appear. To lower the pre-reaction decontamination temperature, a few steps should be followed: the sample should be deposited on the chips at least 12h before the measurements and should be kept in vacuum (preferably inside the microscope). A pre-heating step can be performed inside the microscope using a contact chip (bottom chip in Fig. 3.2c) without a SiN membrane. This way, the temperature necessary for decontamination can be less than 150°C, significantly reducing the possibility of changing the structure of the analyzed sample.

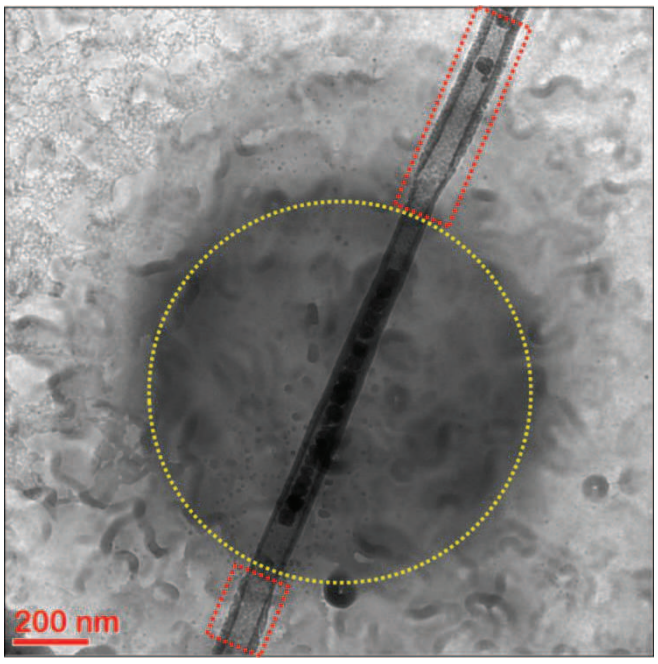

Figure 3.4. Carbon based contamination built-up around a CoO filled CNT in the pre-reaction analysis step in Ar at room temperature. The yellow circle highlights the beam exposed area before the H_2-based reduction, while the red rectangles show the regions outside the contamination area, which were etched during the hydrogenation reaction.

The plasma cleaning, which is the conventional way of reducing the surface contamination in electron microscopy analyses, shows limited improvements for the E-cell experiments. Moreover, the effects of the long plasma treatments on the endurance and thermal/electrical properties of the SiN membranes can be drastic, especially when using O_2 plasma.

3.2.2. Synthesis of FLG flakes decorated with $Fe_{3-x}O_4$ nanoparticles

The synthesis procedure of $Fe_{3-x}O_4$ nanoparticles is described in detail in Chapter II (Sample preparation, section 2.2.1). The graphene samples were synthetized from expanded graphite by surfactant-assisted high power ultra-sonication and are characterized by large surface areas (a few μm^2) and a few layers in thickness. In order to obtain the FLG decorated with magnetite nanoparticles, 100 mg of FLG powder were dispersed into 5 mL pure ethanol and slowly sonicated for 15 minutes. After the sonication, 10 mL of the as-prepared $Fe_{3-x}O_4$ nanoparticles suspension were added. After the phase separation, the solid FLG flakes now decorated with magnetite nanoparticles were filtered and washed out with pure ethanol. The sample was dispersed in pure ethanol.

3.2.3. Preparation of the experiment

A number of steps have to be followed in order to ensure the success of the experiments. The main steps are presented below.

1. Holder cleaning. The organic residuals from the holder tip can be cleaned (carefully) with isopropyl alcohol followed by a 2-5 min treatment in O_2/Ar plasma.

2. Chips cleaning. Prior to the sample deposition, the chips are successively cleaned in a bath of acetone and ethanol. Methanol is the ideal solvent due to its lower ability to induce carbon-based contamination during the pre-reaction analysis. However, it is also a toxic solvent and should be handled very carefully. Plasma cleaning the chips before the sample deposition is an optional step.

3. Sample deposition on the heating chips. The first observation is related to the brittleness of the SiN membranes. The user should never touch the membrane with a solid object or it would instantly crack. The second observation concerns the samples dispersed in solvents. One should carefully proceed with the deposition of the solvent drops on the heating membrane as the solvent can easily migrate on the other side, therefore depositing sample on the vacuum exposed membrane surface as well. This would make the analysis challenging as it would be very difficult to recognize which sample is exposed to the gas flow and which one is sitting in the vacuum of the column.

The deposition of FLG flakes with large lateral sizes in the 6-10 μm diameter observation areas (see Fig. 3.2d) is also challenging. In our case, the FLG flakes decorated with $Fe_{3-x}O_4$ nanoparticles were dispersed in pure ethanol. Simply dropping the solution on the inner part of the heating chip did not allow any graphene flake to be deposited on the SiN membrane. This is due to the rapid aggregation of FLG in free-standing solvent drops. Therefore, an improvised procedure has been used. A few drops of highly concentrated FLG solution were deposited on a glass microscope slide. Just before the complete evaporation of the solvent, the inner surface of the heating chip was stirred on the slide's surface. Using this approach, we were able to deposit FLG flakes on the SiN membrane without the risk of sample migration on the vacuum-exposed SiN surface.

4. E-chip pair loading. This is the most delicate step in the experiment preparation as most of the broken SiN membranes appear here.

5. Verifying the electrical contacts. This is done by connecting the holder to the main Atmosphere system and is automatically performed by the software. If an error appears, the holder has to be opened and the Au contacts have to be cleaned and aligned again.

6. Leak check. Broken membranes, insufficiently cleaned O-rings or misaligned E-chip pair can lead to gas leaks inside the microscope column. Therefore, the leaks test has to be performed before the holder insertion inside the microscope in an external holder pumping station.

After the holder has been safely inserted in the microscope's column the user has to follow the consecutives steps set by the Atmosphere software (see Fig. 3.3b).

3.3 The reduction of $Fe_{3-x}O_4$ nanoparticles

The reduction of the $Fe_{3-x}O_4$ nanoparticles is a complex process and unveiling the exact reduction mechanism requires a careful investigation of the reaction kinetics. The reaction kinetics of the $Fe_{3-x}O_4$ nanoparticles' reduction under H_2 flow depends both on the intrinsic properties of the nanoparticles (size, structure and surface chemistry) and on the external parameters (heating program, gas pressure and purity)[26,27]. However, as the catalytic nanopatterning of FLG in a controlled manner requires a Fe metal phase as active catalyst, some experiments related to the $Fe_{3-x}O_4$ reduction mechanism were made. Figure 3.5 shows the HR-TEM image taken under Ar atmosphere (~3 Torr) at 250°C of an initial magnetite nanoparticle with a face-centered cubic structure (d_{220} ~0.297nm).

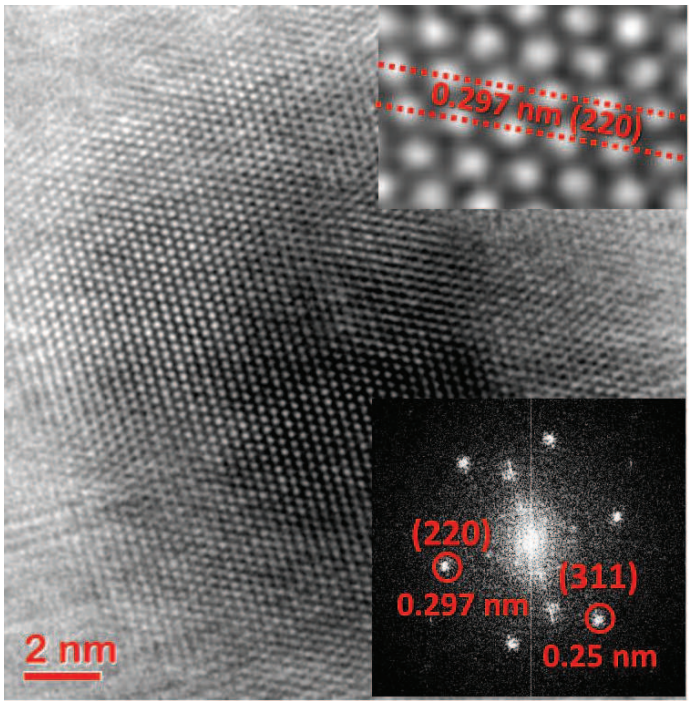

Figure 3.5. HR-TEM image of an initial Fe-based nanoparticle. The insets show the FFT of the initial image and a zoomed image of the same nanoparticle. The lattice spacing indicates a $Fe_{3-x}O_4$ nanoparticle (magnetite). Conditions: ~3 Torr Ar, 250°C.

The first observation related to the reduction of a nanoparticle under a H_2 atmosphere is the formation of void nanoparticles even at relatively low temperatures, i.e. 400°C. Figure 3.6a shows a group of $Fe_{3-x}O_4$ nanoparticles before the introduction of the H_2 gas; the image was recorded at a temperature of 250°C in Ar atmosphere without a FLG support. Once the Ar was pumped out, the system was purged with pure H_2 and the temperature was increased at 400°C at a rate of 1°C/s. The H_2 pressure at the sample level was about 100 Torr in the flow mode with a gas

flow rate around 1.2e^{-4} Torr·L/sec. Almost instantly, the majority of the nanoparticles have been transformed in hollow structures (Fig. 3.6b). The system was maintained at this temperature for 2h with no major morphological transformations appearing. When the temperature was increased to 500°C, some of the nanoparticles remained intact after the first step underwent the same transformation into hollow nanoparticles (Fig. 3.6c). At 600°C, the coalescence of the hollow nanoparticles started, as highlighted in Fig. 3.6d (red circles).

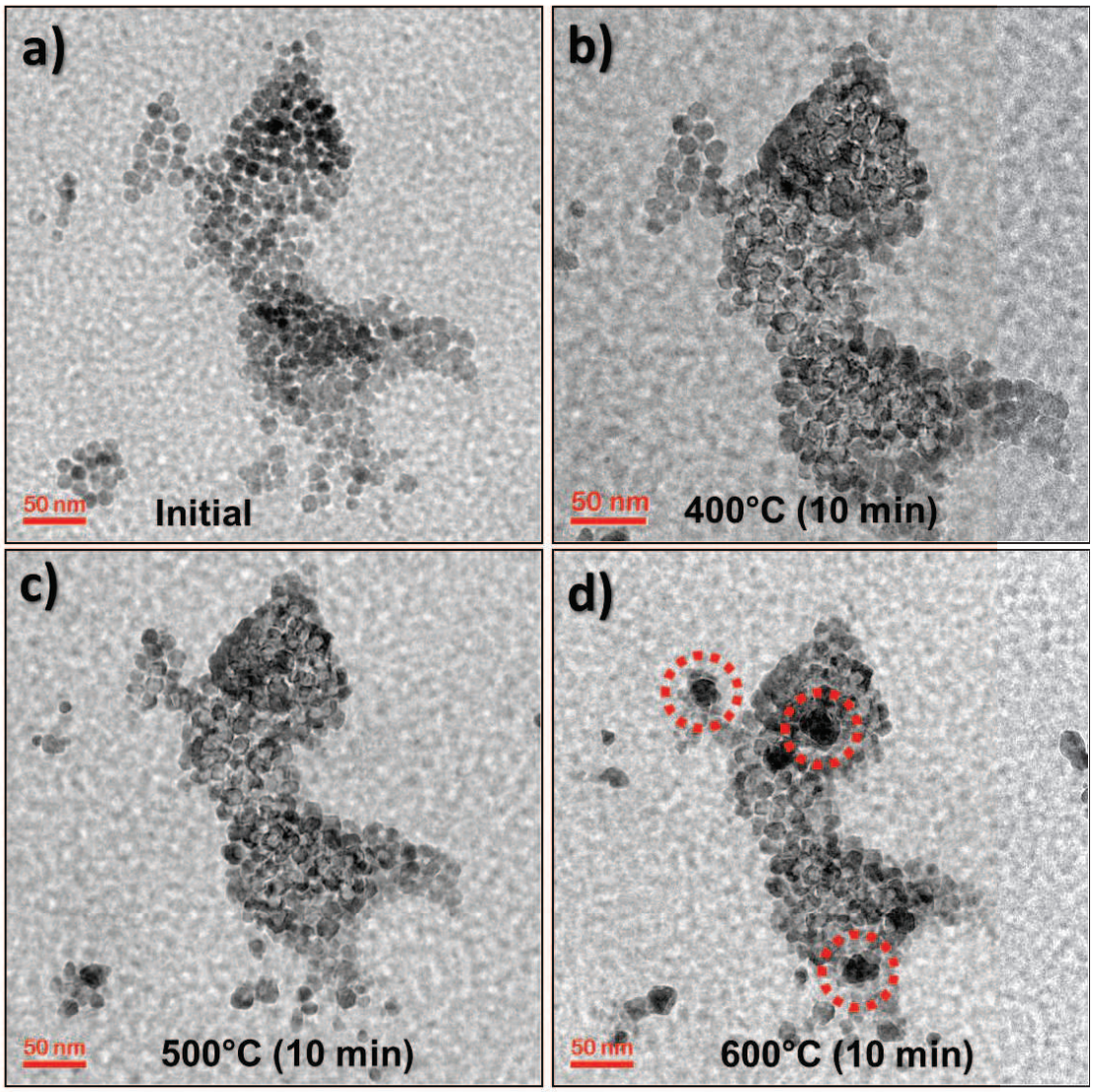

Figure 3.6. a) TEM image of a group of $Fe_{3-x}O_4$ nanoparticles recorded under an Ar atmosphere at 250°C. b), c), and d) The same nanoparticle group after thermal treatment at 400, 500 and 600°C, respectively, in 100 Torr H_2.

Figure 3.7a shows a higher magnification image (inverted contrast) of the hollow nanoparticles at 400°C. The initial $Fe_{3-x}O_4$ nanoparticles had a narrow size distribution of 12 ± 2 nm. The size of the void cores is about 7-9 nm and does not depend on the size of the initial nanoparticle. Instead, the thickness of the solid shell is increasing as the size of the nanoparticle is increasing. Imaging these intermediate hollow nanoparticles with a high resolution was nearly impossible due to their high instability under the electron beam. Fig. 3.7b presents a HR-TEM image taken with a very low dose. The inset FFT shows both the characteristics of metallic iron and oxide phases. The 0.29 nm lattice spacing assigned to the initial magnetite phase shows its incomplete reduction. The ~0.21 nm interplanar distance corresponds to $d_{(200)}$ of FeO (wustite), which is the intermediary phase between magnetite and Fe metallic phases ($d_{(110)}$ ~0.2 nm). However, due to the high sensitivity of the sample towards the electron beam, it was not possible to identify the spatial distribution of each phase.

The hollow nanoparticle coalescence process gains momentum after 600°C. Fig. 3.8a recorded at a temperature of 700°C shows a group of nanoparticles presenting a dual morphology with both coalesced and hollow nanoparticles. The HR-TEM analysis presented in Fig. 3.8b shows that the lattice parameters of the coalesced nanoparticles are characteristic to both ϕ and γ Fe phases ($d_{(110)}$ ~0.2 nm). For a complete transformation of the oxide nanoparticles in a metallic phase, the system has to be maintained at 700°C for ½ - 1h.

The observations presented above show an interesting reduction mechanism, i.e. the rapid transformation of the majority of the $Fe_{3-x}O_4$ nanoparticles into hollow nanoparticles once the system is heated at around 400°C in a H_2 atmosphere. However, the real-time observation of any structural/morphological transformation, in this case the void formation, represents an important objective in environmental experiments. In another experiment, the initial system containing $Fe_{3-x}O_4$ nanoparticles was heated at only 250°C in H_2 (100 Torr in the flow mode). The electron beam was used to add the additional thermal energy required for the transformation of $Fe_{3-x}O_4$ nanoparticles in hollow ones. The imaging conditions were 200kX magnification, 165 μA emission current and an electron dose between 500 and 1000 $e^-/Å^2$. The electron dose was obtained using the relation between the mean counts of the acquired images, the electron dose at the specimen level and the conversion rate of the CCD camera.

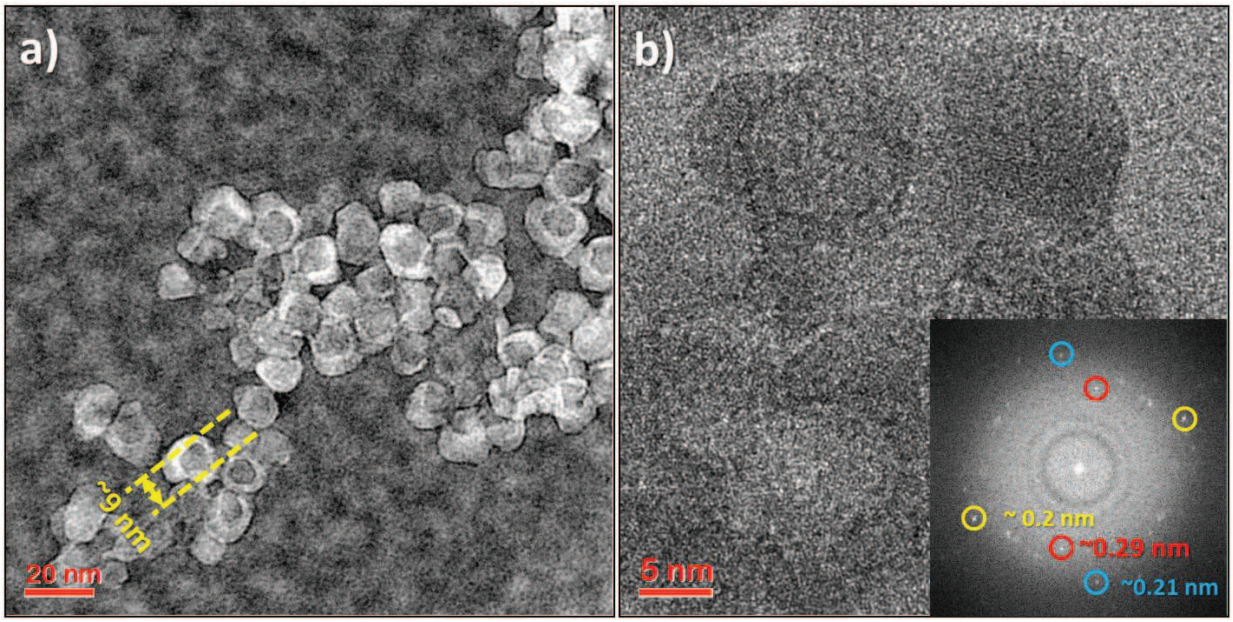

Figure 3.7. a) TEM image (contrast inversed) of hollow nanoparticles recorded at 400°C in a H_2 atmosphere showing the constant size of the void cores. b) HR-TEM image and its FFT of the hollow nanoparticles showing the iron phases mixture immediately after the void formation.

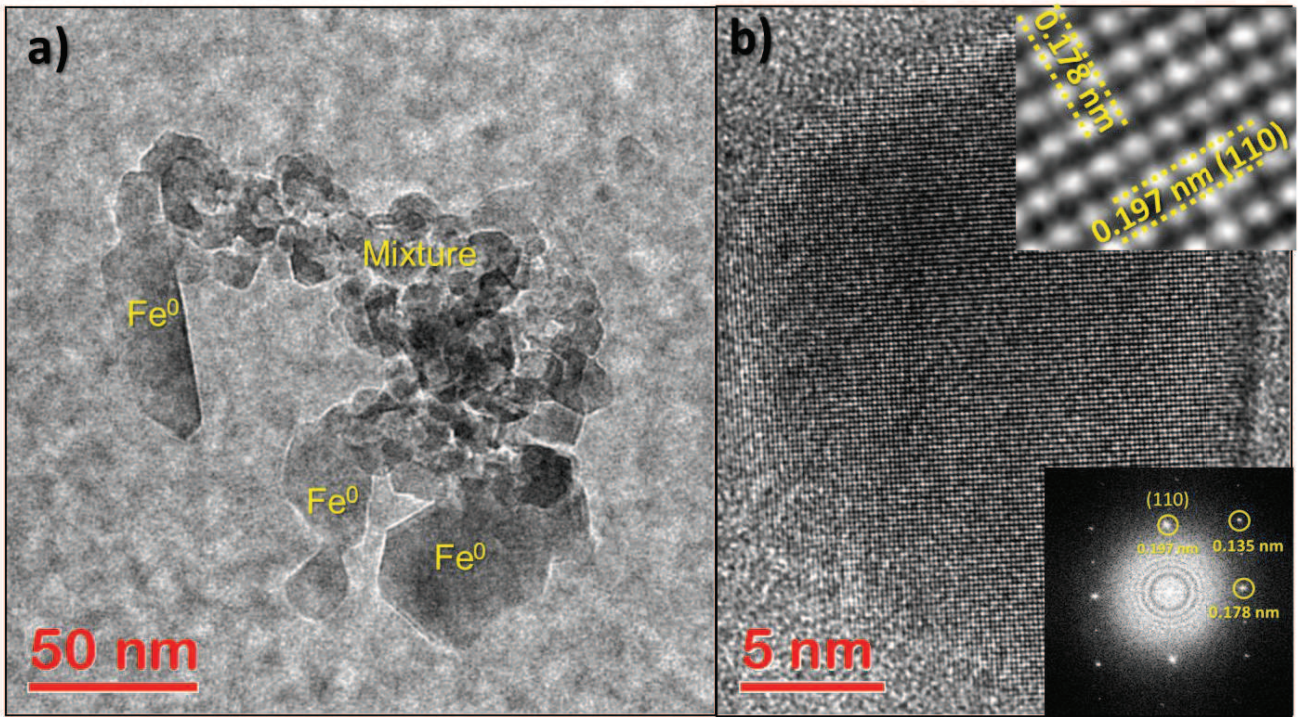

Figure 3.8. a) TEM image of a nanoparticle group acquired at 700°C presenting a dual morphology: coalesced and hollow nanoparticles. b) HR-TM image of a coalesced nanoparticle. The insets show its FFT and a zoomed image of the same nanoparticle. The lattice spacing indicates a Fe metallic phase.

A time series extracted from the recorded movie is presented in Fig. 3.9. Right after 4s, having been exposed to the electron beam, voids can be easily observed in both irradiated nanoparticles. However, the evolution of the hollow areas in these nanoparticles is different. The void forms first in nanoparticle A and after 4s it is occupying a volume at least twice the size of the one formed in nanoparticle B. After 10s, a new void appears in nanoparticle B which is clearly occupying its whole center after 26s. The spatial evolution of the void in nanoparticle A is difficult to follow, even if it seems to have a more superficial progression than the one in B. After ~45s of beam exposure, both nanoparticles are deeply transformed. Nanoparticle A simply melts and re-aggregates in a new nanoparticle, while B is exchanging its round shape with a cubic one. Nanoparticle B keeps its hollow state for another ~10s, after which it simply collapses. HR-TEM imaging shows that both resulted nanoparticles are Fe metallic phases.

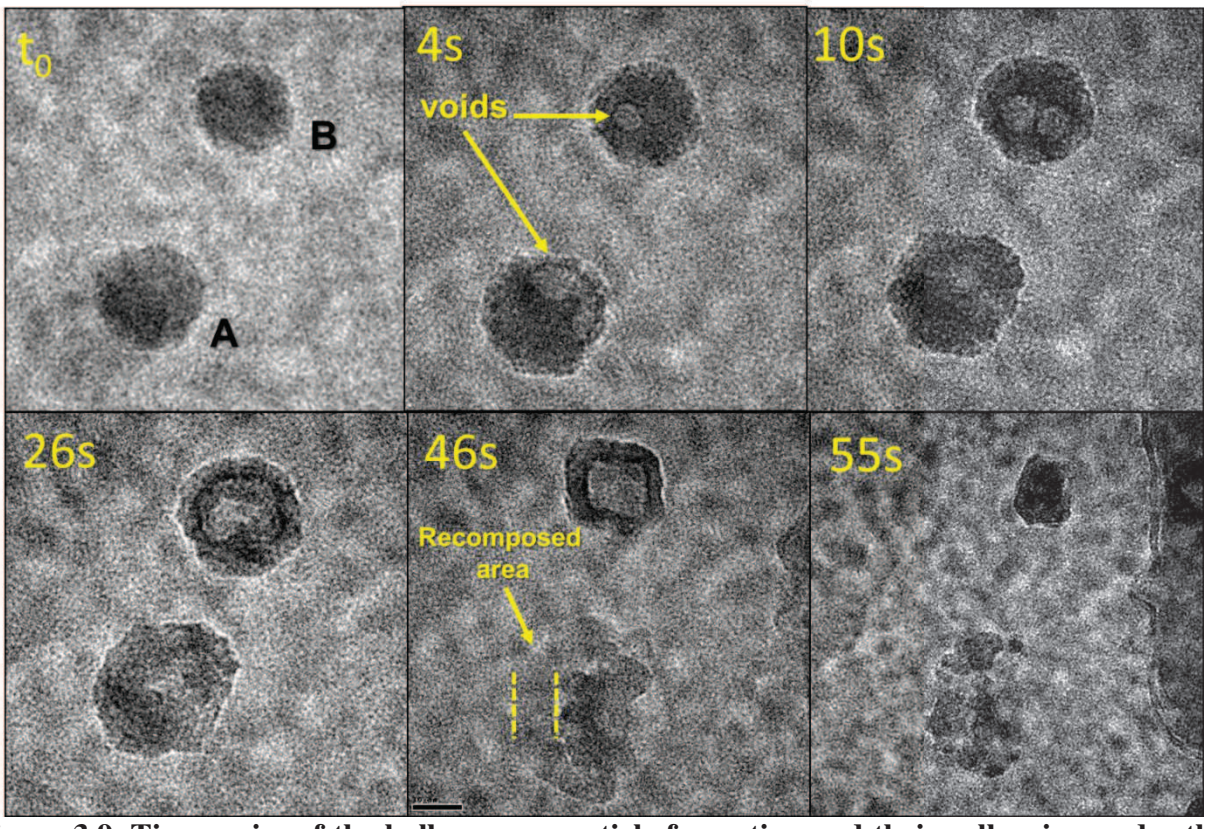

Figure 3.9. Time series of the hollow nanoparticle formation and their collapsing under the beam irradiation combined with the initial gas (100 Torr H_2 in flow mode) and temperature (250°C) conditions.

As presented in Chapter II (Fig. 2.6b), hollow oxide structures appear during the oxidation of metallic nanoparticles due to a difference between metal and oxygen diffusion rates ($D_{metal} > D_{oxygen}$) (Kirkendall mechanism). However, the formation of hollow structures during the reduction of oxide nanoparticles was not reported before, neither for *ex-situ* nor *in-situ* experiments. Our *ex-situ* experiments do not show any clear sign of such void structures during the reduction of magnetite nanoparticles. Therefore, one should consider other factors leading to these particular reaction kinetics. As discussed in the State of the Art section, the first suspect is the electron beam. However, in vacuum conditions, during many analyses of the magnetite nanoparticle, no hollow structures have been formed even for long exposure times to the electron beam. Moreover, these structures do not appear even in the pre-analysis of the sample inside the cell (Ar atmosphere, 250°C). As a consequence, one should consider that it is not the direct action of the electron beam on the nanoparticles that leads to the void formation, but the beam effect on the H_2 gas. Hydrogen molecules can dissociate due to the inelastic interactions with the electron beam, leading to the formation of a plasma-like atmosphere. The kinetics of the reduction reactions under an atmosphere of different hydrogen ion species is difficult to predict. The classical reduction mechanism proposes that H_2 molecules are first dissociated on the surface defects sites and the reductions is promoted by atomic hydrogen. Therefore, when atomic hydrogen species are directly supplied at the nanoparticle's surface, the reduction is more rapid and possibly follows a different course.

The hollow nanoparticle can be formed due to the influence of these highly reactive hydrogen species. The reduction rate is also significantly enhanced in the presence of pure hydrogen. During such a reduction process, the remaining oxide inside the iron oxide nanoparticle will diffuse towards the nanoparticle's surface in order to compensate the oxygen removed through the reduction process. The oxygen diffusion is accompanied by shrinkage of the core oxide, which could explain the formation of the hollow core inside the nanoparticle upon reduction. However, the electron beam can dissociate the H_2O molecules (formed during the reduction reactions) immediately after their formation, resupplying in this way the surface of the nanoparticle with oxygen species. This complex mechanism shows the difficulty of analyzing chemical reactions and their effects under the electron microscope.

The formation of hollow nanoparticles during the *in-situ* reduction of magnetite is an intriguing phenomenon. However, as it did not represent the main goal of the present study, the

investigations were limited. Nevertheless, we gained enough information in order to provide a pure metallic Fe phase at around 800°C for the catalytic hydrogenation of the FLG flakes.

3.4 Real-time observation and analysis of the catalytic channeling

3.4.1 Preparation of the channeling experiment

A dark-field STEM image of a representative FLG/$Fe_{3-x}O_4$ flake before the experiments is shown in Fig. 3.10a. The FLG flake is characterized by a large lateral size and significant edge folding. The $Fe_{3-x}O_4$ nanoparticles are preferentially deposited on the FLG flake's edges as can be seen in the Fig. 3.10b. They tend to form nanoparticle chains containing from 2 to 20 nanoparticles well bonded to each other by the residual surfactant.

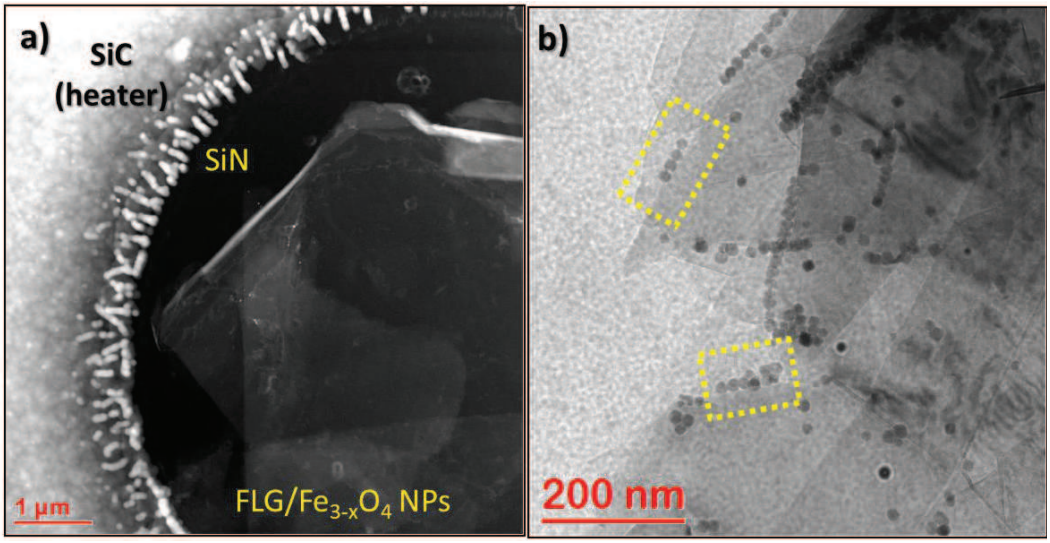

Figure 3.10. a) Low magnification annular dark-field STEM image of a FLG/$Fe_{3-x}O_4$ flake deposited inside the environmental cell before heating in a H_2 atmosphere. b) Bright field TEM image showing the nanoparticle preferential deposition on the FLG's edges (highlighted in yellow).

At this point one should briefly address the difficulties encountered in this part of the experiment.

1. The utilization of pure H_2 gas. As mentioned before, for the present experiments we did not have the possibility of diluting the reactive gas (H_2) by mixing it with inert ones (Ar, He, N_2). Using pure H_2 has a few consequences:

- H_2 has a high thermal conductivity (0.168 $Wm^{-1}K^{-1}$, measured at 25°C). It is 10 times higher than the one of pure Ar and 7 times the one of pure O_2 gas. This means a flow of pure H_2 gas can move more heat from the surface of the SiC/SiN films than any other gas, decreasing the local temperature.

- Pure H_2 is also an aggressive reaction gas. When mixed with Ar, the uncatalyzed hydrogenation of carbon-based materials can be neglected. However, when used in a pure form, the uncatalyzed hydrogenation of graphite can reach 10% of the total reaction yield (compared with metal-based catalyzed hydrogenation)[28]. This particular aspect creates important limitations for the experiments, as will be discussed later.

2. Temperature gradients on the FLG flakes. When deposited on the heating chip, due to their large lateral size and multiple folding, most of the flakes do not sit parallel with the membrane, but instead get a 3D like arrangement with only part of the flake in direct contact with the heater. This leads to the inhomogeneity of the temperature distribution on the surface of some FLG flakes.

3. Water contamination. The main sources of water traces are the ethanol solvent (original purity 99.9%, decreases if exposed to air) and the system of gas pipelines. Although the pre-reaction heating step determines the water evaporation, the vapors remain inside the micro-reactor. Water vapors can modify the normal path of the hydrogenation reactions. In order to eliminate the water traces together with other contaminants resulted during the pre-reaction heating, the system has to be completely re-purged with the reaction gas after the first heating step.

For the reduction of $Fe_{3-x}O_4$ nanoparticles on FLG flakes, the same procedure was followed as the one detailed in Section 3.3. After the reduction step at 700°C, the temperature is increased to 800°C with a ramping rate of 1°C/s. The thermal drift created by this temperature ramping is small enough to be corrected by using the microscope's piezo stage. However, the ramping is fast enough to ensure that the influence of the uncatalyzed edge hydrogenation, which rapidly increases in this temperature interval, is minimized.

3.4.2 Initiation of the channeling process

The first observation related to the catalytic action of metallic Fe nanoparticles is the instant start of the nanopatterning process, when the nanoparticles are in contact with a "fresh" FLG edge. The hydrogenation reaction is thermally activated and the channeling rates should increase with the temperature. However, we did not observe a step-by-step increase when the temperature was ramping, but the channeling started instantaneously. This has made the real-time tracking very difficult since it gives no time delay to choose which nanoparticle to follow in a high magnification observation (high magnification = small field of view). The only way to closely follow a nanoparticle during the cutting process was to instantly stop the heating after the nanopatterning had started and then directly increasing it back to 750°C followed by a manual step by step temperature increase until the cutting process is again observed. A number of factors can induce the instant catalytic hydrogenation of the FLG flakes: the high reactivity of the pure H_2, the existence of reactive H ions due to the beam-gas interaction and the uncontrolled heating transfer between the E-cell membrane and the suspended FLG flakes. As shown in the second chapter, the catalytic hydrogenation of graphene depends on the dissolution of carbon from the edges of the nanoparticle body/surface, on the dissociation of the H_2 molecules on the nanoparticle surface and also on the desorption of the formed CH_4. Therefore, in order to initiate the channeling, an equilibrium state between these three processes has to be reached. The dissociation of H_2 under the electron beam can affect this equilibrium, as it affected the kinetics of the nanoparticles' reduction. A direct supply of atomic hydrogen species on the surface of the nanoparticle means that one of the rate limiting steps of the channeling (the H_2 dissociation) is eliminated. Consequently, the velocity of an active nanoparticle can drastically increase.

Another phenomenon that can be responsible for the instant initiation of the channeling is the dissolution of carbon atoms from the FLG substrate by the nanoparticles, at temperatures lower than the one which can sustain the CH_4 formation. This dissolution appears during the temperature ramping, and becomes visible for some nanoparticles as a small carbon tail on one of the nanoparticle's sides (Fig. 3.11). The carbon tails appear when the concentration of the carbon dissolved in the nanoparticle's body reaches the saturation point and the carbon is rejected outside the nanoparticle. Therefore, when the required temperature for catalyzing the C/H reaction is reached, at first the carbon already dissolved in the nanoparticle body has to be removed in a C/H reaction. Until now it is not clear if the pre-channeling carbon dissolution is a

general behavior in the FLG channeling experiments. Moreover, carbon tails were never observed in *ex-situ* channeling experiments.

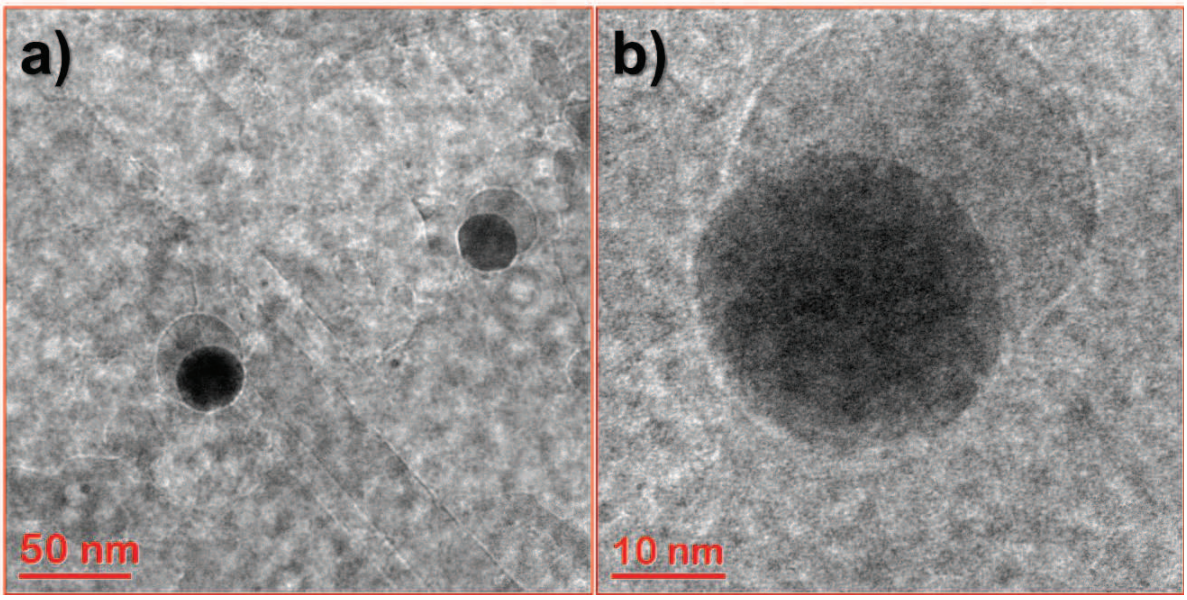

Figure 3.11. Nanoparticles growing amorphous carbon tails during the pre-channeling temperature ramping.

3.4.3 Catalytically active nanoparticles: unstable structures

The first real-time observation in high magnification of the nanopatterning activity of Fe nanoparticles was recorded at 775°C, using the above described procedure. The first observation relates with the fact that the nanoparticle undergoes rapid shape changes. To highlight this, two time series were extracted from one of the recorded movies (see Fig. 3.12). The nanoparticle is not only sliding back and forth on the FLG edge in order to remove the carbon, but it is also constantly changing shape during the whole process. Figure 3.12a shows how the nanoparticle goes through three distinctive shapes during a short 0.6s time interval. Indeed, the nanoparticle, well attached to the FLG edge, is sending lateral extensions on both right and left sides of the "equilibrium position". Fig. 3.12b shows an even more drastic transformation of the same nanoparticle. In the initial position, the contact surface of the nanoparticle with the FLG edge was about one quarter from its total available apparent surface. After going through dramatic morphology changes the contact area with the FLG edge increases up to one third. As shown in Fig. 3.12, the nanoparticles have a tendency to maximize their area of contact with the FLG edges

in order to achieve a more favorable energetic position. As discussed in the second chapter the adhesion force between the FLG edges and the nanoparticle facets is the force responsible for the nanoparticle motion. The same adhesion force allows and/or forces the nanoparticle to reshape itself using the edge as a 2D template. A number of studies showed that at this temperature iron nanoparticles should presents a superficial melted layer[29–31]. The ease with which the nanoparticle is remodeling itself cannot be attributed only to the strong superficial tension at the edge level, but also to the structure of the nanoparticle, in particular the liquid-like superficial shell. Moreover, the carbon tail resulted from the rejection of an excess of carbon inside the nanoparticle shows that the concentration of carbon inside the nanoparticle's body is close to the saturation point. This represents another evidence of the nanoparticle's quasi-liquid state, i.e. iron-carbon liquid solution, with an extremely high wetting character which allows it to maintain an intimate contact with the FLG border.

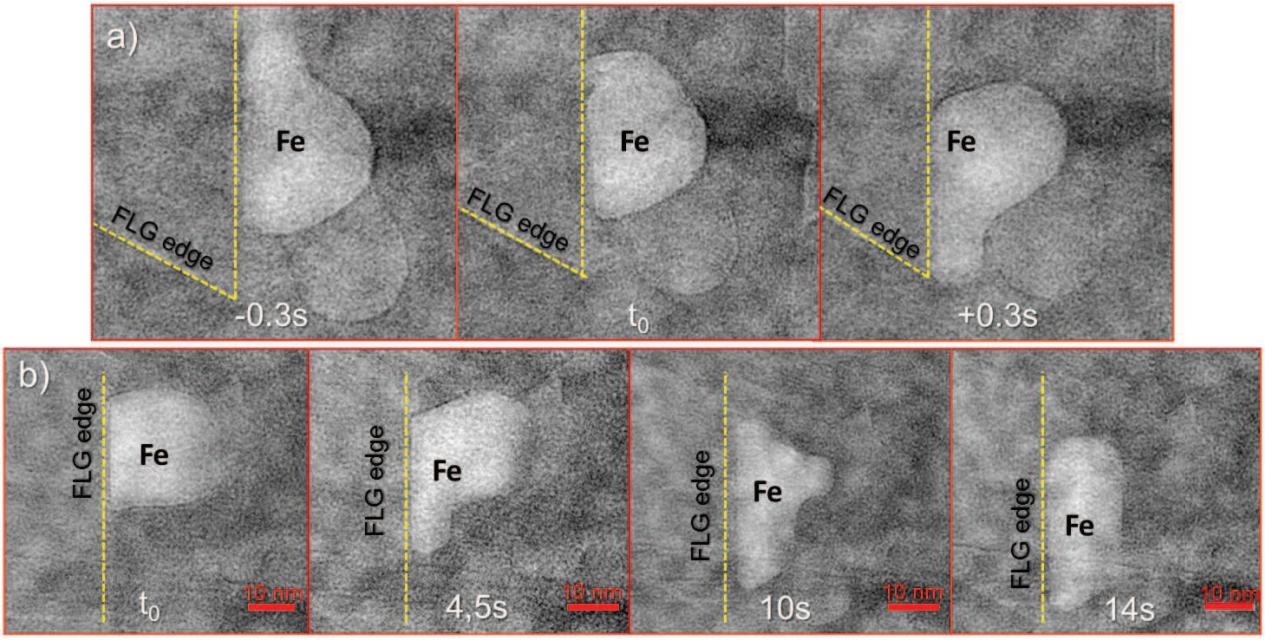

Figure 3.12. a) and b) Metallic Fe nanoparticle removing the carbon atoms from a FLG edge in an uncontrolled way. The drastic change in shape over small time intervals shows a melted state for this nanoparticle. The images were extracted from a movie recorded at 775°C with 0.33s time intervals. The LUT of all the images was inverted for improving the details' visibility.

3.4.4 Experimental insight in the channeling mechanism

The continuous restructuring of the nanoparticle body is clearly observed in the recorded movies. One interesting behavior is the slight change in contrast (thickness contrast: related to the thickness of the object along the electron beam) occasionally appearing in the front and lateral side of the nanoparticle. Fig. 3.13a shows one of these situations. The region denoted with A shows the thinner nanoparticle area, while B represents the main nanoparticle body. Fig. 3.13b shows two schematic representations (cross-section views) of the general accepted mechanism for the catalytic hydrogenation (1) and the one theoretically proposed by S. S. Datta[32] (2). The interface between the active nanoparticle and the FLG edge is generally accepted to be a straight one. However, the model proposed by the S. S. Datta who considered the active nanoparticles as liquid droplets shows a more dynamic type of interface. The nanoparticle changes in thickness close to its interface with the edge of the FLG, presented in Fig. 3.13a, can be directly related to this type of nanoparticle/FLG interface. Region A represents the part of the nanoparticle's body that migrates over the FLG edge, therefore appearing thinner. It is not contributing to the catalytic reactions, as it should remove the carbon atoms along the *c* axis (planar FLG surface). Therefore, the carbon is also supplied by the chemically reactive FLG edge as in case 1. Nevertheless, as in the case of tunnel formation, the mechanism of hydrogen supply using the available nanoparticle surface and the reaction with the carbon atoms directly at the interface is not feasible anymore. Therefore, the mechanism proposed by P.J. Goethel and co-workers[33], which predicts the hydrogen and CH_4 diffusion through the nanoparticle's body, can better explain the existence of this type of interfaces. The nanoparticle overlapping the FLG edge is a direct consequence of the high-surface energy created by the dangling C bonds available at the edge and the need of the nanoparticle to consolidate the large interface with the carbon phase. Moreover, this process is showing the low adhesion of the nanoparticle to the carbon basal plane. One should note that it is the first time that the existence of such nanoparticle/FLG edge stepwise interface is experimentally observed.

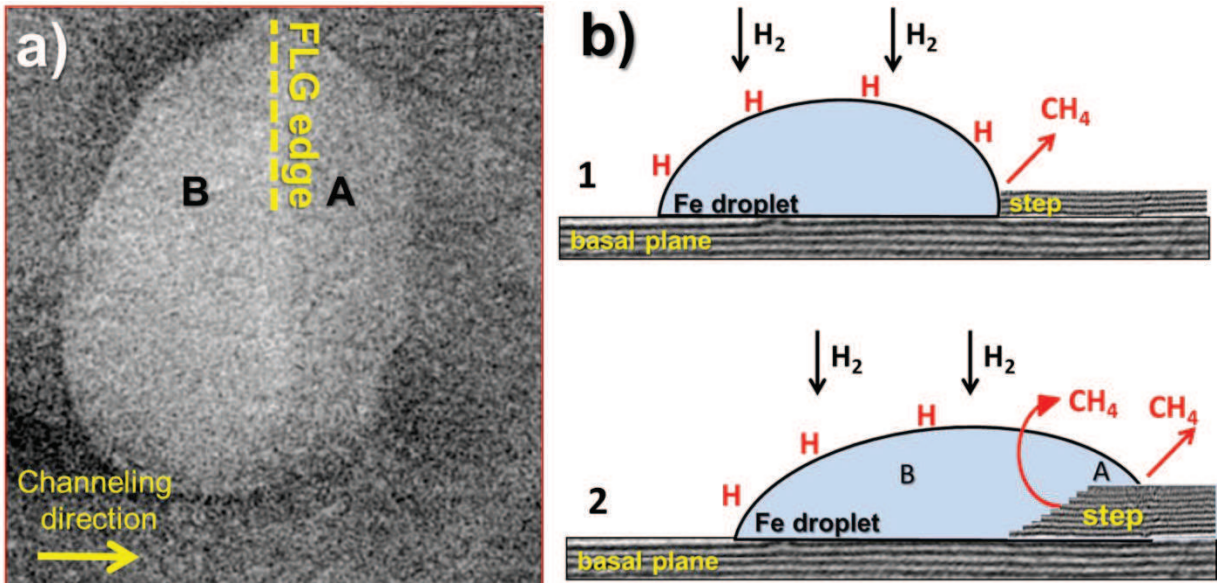

Figure 3.13. a) Active nanoparticle overlapping the FLG edge (image extracted from a recorded movie). The LUT of the initial image was inverted. b) Schematic representation in cross-section of droplet interaction with the FLG edge: (1) classical straight interface; (2) stepwise constructed interface.

3.4.5 From edge recession to channel formation

The above observations were made under a relatively high magnification condition (250kX) determining a relatively high electron dose. Therefore, in order to diminish the influence of the electron beam in the nanoparticles' patterning behavior, a lower magnification observation of the FLG patterning is required. Fig. 3.14a shows a time series of the catalytic activity of a metallic nanoparticle recorded at 60kX magnification (825°C). The nanoparticle shows the same dynamical morphology with high shape change rate in a short period of time. The superposition of the four images (after their alignment using the trench border as a reference) gives us a closer view of the rapid shape changes undergone by the nanoparticle (Fig. 3.14b). For positions 1-3, the nanoparticle is not creating a defined channel but is removing the carbon atoms from a rectangular open-ended area (zone A in Fig. 3.14c). The nanoparticle continues to move back and forth on the FLG edge until it starts creating a well-defined channel (position 4). This seems to be the common behavior for the active nanoparticles: removing the FLG edges by moving parallelly on them until a position which favors the channeling activity is reached. The surface area of zone A is ~4800 nm^2, drawn by the active nanoparticle in 10s. This gives a carbon area removal rate of

480 $nm^2 \cdot s^{-1}$. This value is much smaller than the area removal rate for the channeling activity (position 4), which is around 5500 $nm^2 \cdot s^{-1}$. The small removal rates in the "edge recession" activity compared with the ones of the channeling activity is common for all nanoparticles analyzed in this experiment.

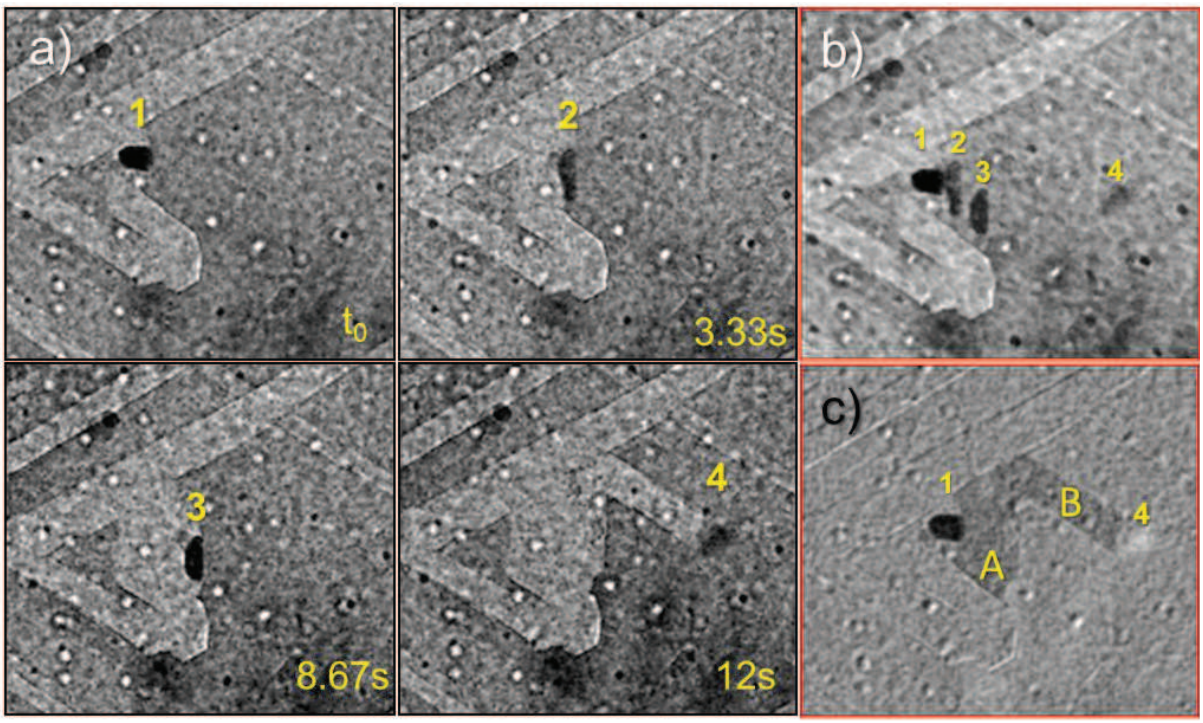

Figure 3.14. a) Low-magnification time series of a nanoparticle removing the carbon atoms from a FLG edge moving parallel on it. b) Z projection of the aligned time series from 3.13a. c) Calculated image from the first and the last image in the 3.14a highlighting the catalyzed carbon regions (zone A – edge recession, and zone B – channeling).

What triggers the transition from the edge recession to the channeling process? There are two possibilities. The first one is related to the influence of the FLG substrate on the catalytic cutting mechanism (the edge-related adhesion force and the anisotropy of the channeling). The second one, and probably the most important, is given by the crystallography of the nanoparticle, i.e. faceting shapes and sizes. Although until now no clear evidence between the channeling rates and the faceting of the nanoparticles was reported, considering the strong influence of the faceting on the carbon nanotube growing (the "inversed" mechanism of the channeling), one should not exclude a relation between the crystallography of the nanoparticle and the type of catalytic action. Another possibility is related to the concentration of the carbon dissolved inside the nanoparticle. Considering that the quasi-liquid aspect of the nanoparticle is increasing with

the carbon concentration, a higher concentration means a higher wetting of the FLG edge. Therefore, one can assume that the channeling activity starts only when a certain carbon concentration is reached. However, this assumption requires further investigations as the active nanoparticles can change multiple times between channeling activity and edge recession during the experiment.

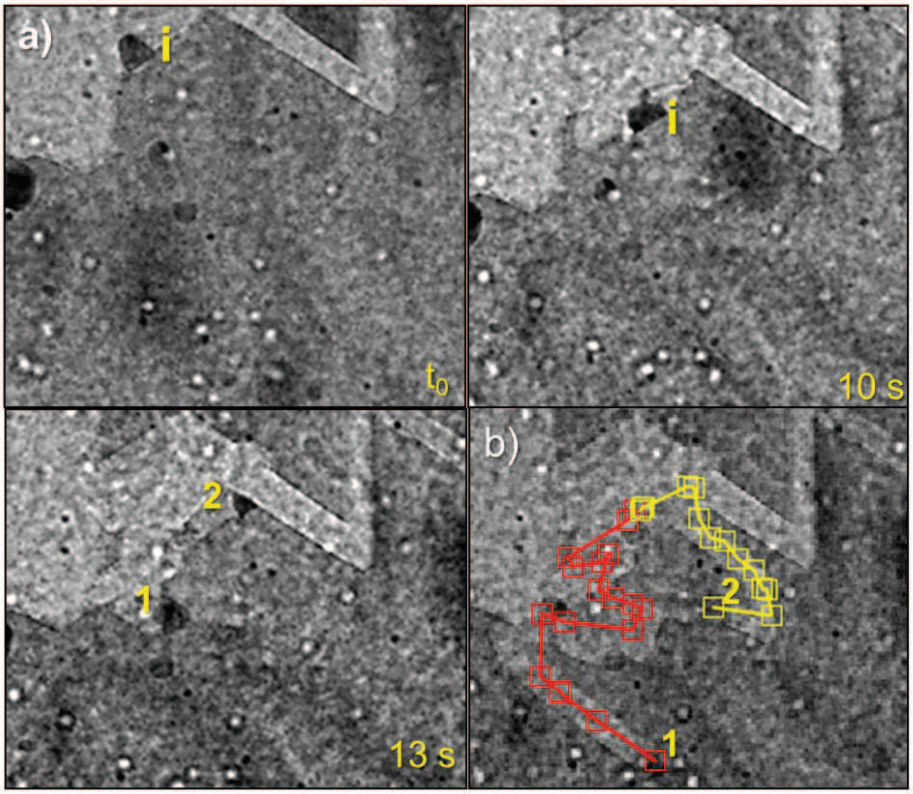

Figure 3.15. a) Low-magnification time series of a nanoparticle splitting into two independent ones due to the strong interaction with the FLG step. b) The channeling activity of the newly-formed nanoparticles.

3.4.6 Splitting of active nanoparticles

A more visual phenomenon showing the high surface energy appearing between the nanoparticle and the FLG edges is presented in Fig. 3.15. In this case, the nanoparticle reacting with the carbon step by moving parallelly on it breaks into two independent nanoparticles. Fig. 3.15a shows a time series of the experiments. After 13s of slowly catalyzing the FLG step as a single nanoparticle (60 $nm^2 \cdot s^{-1}$), the newly-formed twin nanoparticles start digging two

distinctive channels showed in Fig. 3.15b. The channeling rates of the twin nanoparticles (580 $nm^2 \cdot s^{-1}$) are much higher than the rates of the initial one. The splitting effect is created by the same tendency of the nanoparticles to maximize their area of contact with the FLG edge. In some cases the superficial tension at the edge favors the splitting, not the nanoparticle's shape reconfiguration. Moreover, by splitting the nanoparticles can dissolve carbon more efficiently in their matrix, compared with the initial nanoparticle. Through splitting, the equilibrium of hydrogenation conditions can be reached easier, favoring the channeling process.

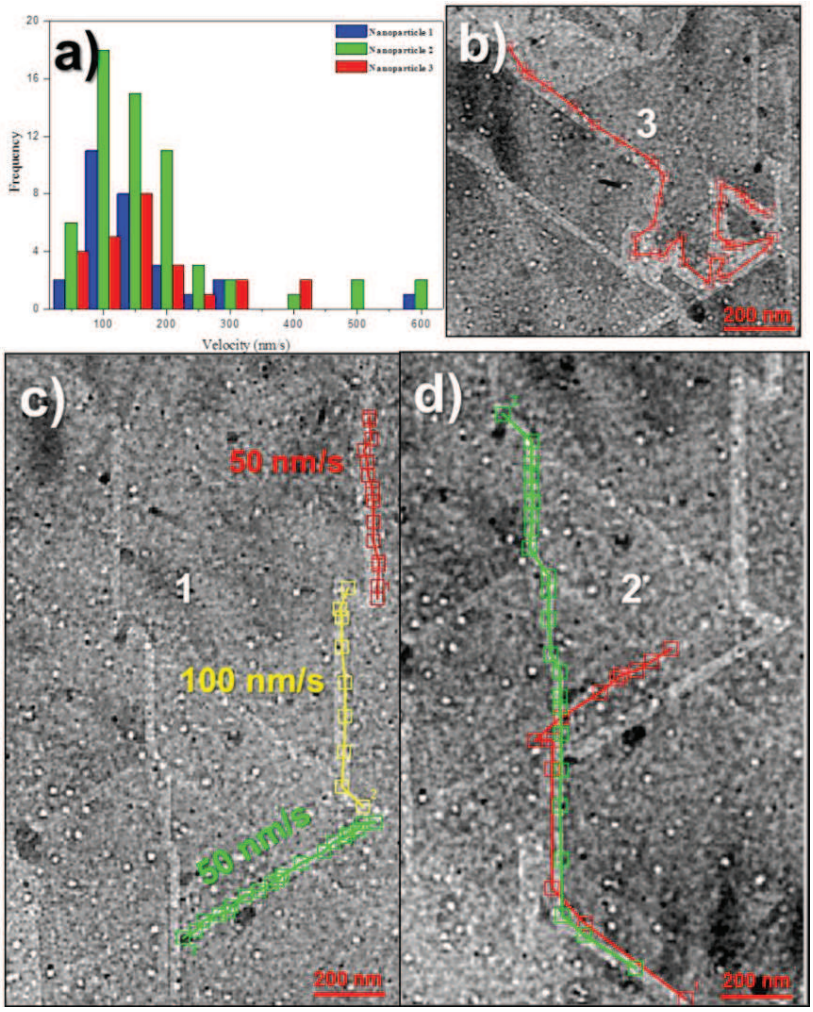

Figure 3.16. a) The frequency distribution of the absolute channeling velocities (nm^2•s-1) of the nanoparticles presented in 3.16b-d. The values were extracted from a recorded movie with a 0.33s time resolution and 2 nm x 2 nm pixel size. b-d) The trajectory of the three nanoparticles for which the velocities were calculated in 3.16a. The colored lines highlight the trajectories, while the squares highlight the position of the nanoparticle in each frame in the movie.

3.4.7 Channeling rates

When describing the nanoparticles' channeling action, it is much simpler to discuss in terms of channeling velocity. As we had no tool for determining the number of graphene layers removed catalytically by the nanoparticle during the environmental experiments, it was difficult to give a direct relation between the observed velocity values and the FLG support topography. The attempt to find a relation between the width of the channel (given by the size of the nanoparticle's front facet) and the channeling velocities gives mixed and inconclusive results. This shows that the continuous change in shape of the active nanoparticle even during channeling is more important in defining the channeling velocity than the value of the surface energy between the nanoparticle and the FLG. Fig. 3.16a shows a frequency distribution of the absolute channeling velocities of three different nanoparticles. The velocities were extracted from the recorded movies of the nanoparticles' motions (3 frames/s). Prior to the direct velocities measurements all images from the stack were manually aligned using the TomoJ program. The size of a pixel was 2 nm x 2 nm. It shows that contrary to the predicted behavior form *ex-situ* and theoretical observations, the channeling velocity of an individual nanoparticle is not uniform from the starting point to the final one. Highlighted in Fig. 3.16b-d by colored squares are the measured position points. The center of the nanoparticle was used as a position reference. The 0.33s time interval between each measured point was set by the framing of the recorded movies. The distributions of channeling velocities are centered around 100-150 $nm^2 \cdot s^{-1}$ for all three nanoparticles. However, channeling rates larger than 400 $nm \cdot s^{-1}$ were observed for the same nanoparticles. Adding to the irregularity of the channeling activity is the fact that the nanoparticle completely halts the carbon removal for periods between 0.3 and 2 s. This temporary inactivity is usually followed by a rapid channeling re-start. Moreover, the change in the channeling velocity is not constant. As Fig. 3.14c clearly shows, after a 50 $nm \cdot s^{-1}$ mean channeling velocity in the first part of its cutting activity and two consequent 60° turning points, the mean velocity is increasing at 100 $nm \cdot s^{-1}$ in the middle segment of the channel, to decrease again to 50 $nm \cdot s^{-1}$ for the last segment. Therefore, the irregularity of the channeling velocity cannot be related with a decrease of the nanoparticle's activity during the channeling, as some studies proposed.

3.4.8 The faceting influence on the channeling activity

To better understand the morphological changes of the nanoparticles during the catalytic activity and their influence on the channeling rates, a closer look on the active nanoparticle is required. Figure 3.17 shows a time series acquired at high magnification (250kX) of a nanoparticle during the change of the channeling direction on a uniform area of the FLG flake. The temperature of the system was around 775 °C. One should notice the rapid change of the initial nanoparticle facets (denoted R, F, and L) during the direction change process. At t_0, the L facet presents a longer contact area with the FLG wall than the R one.

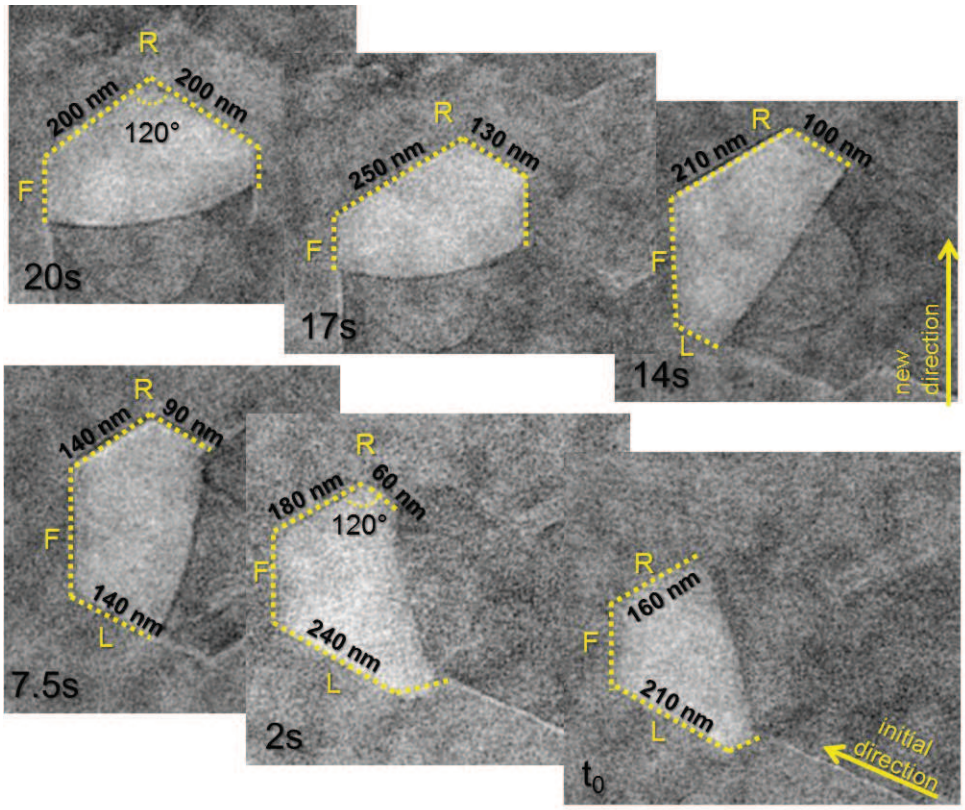

Fig. 3.17. Time series of nanoparticle faceting fluctuations during the change of the channeling direction on a uniform FLG area. The images were extracted from a recorded movie at a magnification of 250kX. The time resolution was 0.33 s. The LUT of the initial images was inverted for improving the details' visibility.

The interaction of the nanoparticle facets with the walls can be described using the contact area only if we consider the local FLG thickness constant. We should expect the

nanoparticle to turn in the direction given by the L facet, where a stronger interaction with the edge exists. However, after 2 s, a new small facet with a 120° orientation to the first one appears in the R direction. Still, at this point, the contact area of the L facet is larger than in the R one. However, a disequilibrium already appears and after 7.5 s the new direction had been already chosen. The contact with the FLG edge in the L direction is decreasing by a considerable amount. In the next 13 s the size of the two R facets will continuously change until they will reach a V-type front faceting with a segment size of around 200 nm. The change of the channeling direction seems to always be preceded by the formation of V-type frontal facets for the new leading facet. Moreover, during the turning of the nanoparticle, its channeling rate is the lowest measured in the cutting experiments (<1 $nm \cdot s^{-1}$).

The same rearrangement of the faceting appears when the nanoparticle approaches an edge, as presented in Figure 3.18. When the nanoparticle is reaching the FLG edge losing the frontal contact with the carbon, a slow refaceting is taking place that facilitates the turning of the nanoparticle and the continuation of the channeling process. One of the lateral facets, in this case the R1 facet, increases its contact area with the wall of the channel (5 s). At the same time, the contact of the L facet with the adjacent wall is lost. The size of the R1 facet continues to increase and a moment after the nanoparticle starts channeling in the new direction, a new frontal facet appears (R2), making a 120° angle with R1. The R2 facet continues to increase in size until a V-type frontal arrangement is reached.

The existence of facets with an increased affinity to carbon dissolution or carbon rejection is already known, but it is unclear why the nanoparticle aims at exposing these facets to the carbon edge through the continuous refaceting. Until now, an exact crystallographic indexation of these facets was not possible. However, it becomes clear from these observations that there is an affinity of some of the nanoparticle's facets to certain crystallographic directions in FLG. Electron diffraction coupled to the environmental experiments becomes the solution to solve the crystallography of both the FLG substrate and the metallic nanoparticle. Solving this aspect will open a unique way of controlling the channeling activity.

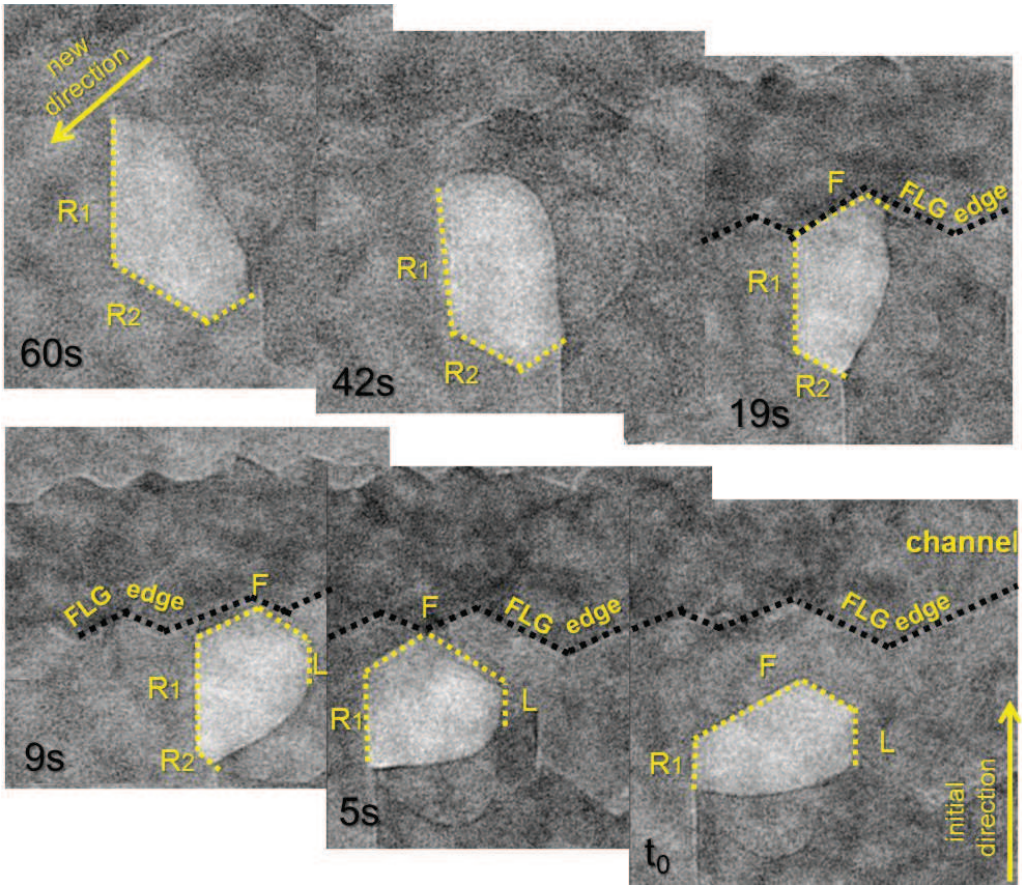

Fig. 3.18. Time series of a nanoparticle shape fluctuations due to the encounter of a step-down type FLG topography, i.e. a previous created channel. The images were extracted from a recorded movie at a magnification of 250kX. The time resolution was 0.33 s. The LUT of the initial images was inverted for improving the details' visibility.

As already shown in Fig. 3.14, the channeling rate of a nanoparticle with a stable structure is much higher than the rate of the ones with unstable faceting. This sudden shift from a structure under a continuous rearrangement to a stable one cannot be explained only by assuming the influence of one factor, the FLG crystallography or the faceting of the nanoparticle, but by a strong relation between them. Moreover, choosing a new direction of channeling when the nanoparticle turns in FLG areas with a uniform thickness can also be explained by the existence of such a relation. The stable structure of the nanoparticle disappears as fast as it appeared, and the refaceting process resumes. Fig. 3.19b-c shows three states of the same nanoparticle during the cutting process: unstable (a) and stable structures (b and c).

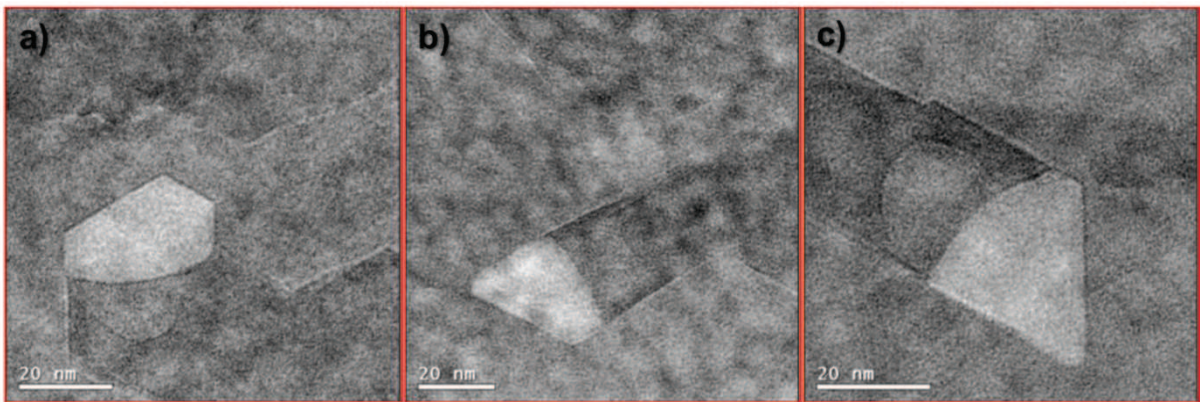

Fig. 3.19. a) Nanoparticle with a V-type frontal facets characterized by their continuous re-arrangement; b) and c) Nanoparticles with stable leading facets creating straight channels. The LUT of the initial images was inverted for improving the details' visibility.

3.5 Discussion

As these experiments are the first to be performed with an environmental E-cell in our group, a very important step is to understand and optimize this complex system. A major aspect is represented by the influence of the electron beam on the environmental TEM experiments. Understanding chemical-based experiments performed under direct exposure to the high energy electron beam is not straightforward. As the electron beam can alter the composition of the reaction gas, modify the local temperature around the sample or induce structural changes on the sample itself, all these aspects have to be considered when analyzing the results.

The first observation concerns the reduction of the initial $Fe_{3-x}O_4$ nanoparticles. It is the first reported observation of hollow structures formation in the H_2-based reduction of oxide nanoparticles. This phenomenon, which could be neither attributed to normal reduction kinetics nor the influence of the electron beam on the nanoparticle's structure, shows the strong alteration induced by the electron beam on the gas environment. The inelastic scattering underwent by the electrons passing through the hydrogen atmosphere changes its composition due to the ionization effects. The highly reactive hydrogen species formed alters the normal reaction path, significantly

accelerating the kinetics of the reduction. As the reduction starts at the surface of the nanoparticle, the oxygen species from the core will very rapidly diffuse towards the surface in order to compensate for the oxygen removed through the reduction. The rapid depletion of the nanoparticle's core of oxygen species will eventually lead to the formation of a hollow structure. However, in addition to the ionized hydrogen atmosphere, other factors (due to the influence of the electron beam) can interfere in the reduction kinetics. The most important one is the possibility for the H_2O molecules formed during the reduction of the nanoparticle to be immediately dissociated by the electron beam. In this way, the surface of the nanoparticle is resupplied with oxygen and hydrogen species and, therefore, it is difficult to predict the influence of such a phenomenon on the reduction path.

The real-time observation of the FLG nanopatterning by the metallic Fe nanoparticles showed a more complex and unpredictable channeling mechanism than the *ex-situ* investigations predicted. However, as demonstrated by the unusual reduction mechanism of the magnetite nanoparticles, the channeling conditions inside the micro-volume of the E-cell under the direct exposure to the electron beam can significantly change from the ones obtained in an *ex-situ* reactor. Therefore, this aspect was considered in the interpretation of the present results in the general context of the channeling mechanism.

The first observation relates with the unstable morphology of the active nanoparticles. In the pre-channeling period, when the nanoparticle is in contact only with the FLG edge and not enclosed between the restrictive walls of the channel, the nanoparticle is sliding back and forth on the edge, removing the carbon atoms in an edge recession sort of cutting. During the edge recession, the nanoparticles undergo continuous reshaping in order to maximize their interface with the carbon edge. Despite the dynamicity of the restructuration of the nanoparticles during this process, the edge recession is not very efficient from the point of view of the carbon removal yields. The carbon removal rate during the edge recession was found to be at least 10 times lower than during the channeling activity. In the general context of using the catalytic hydrogenation to nanopattern FLG sheets for different applications, the edge recession observed in the present experiments represents a major drawback (see Chapter II, section 2.6). However, this cutting behavior was not observed for the *ex-situ* nanostructured samples and, therefore, seems to be another effect of the special conditions created inside the E-cell. From the point of view of the cutting mechanism, the edge recession is caused by the melted state of the nanoparticles at these

temperatures (775-825°C), melted aspect which is enhanced by the high concentration of carbon dissolved in the matrix of the iron nanoparticle. Due to the high adhesion forces appearing at the nanoparticle/FLG edge interface, these quasi-melted structures undergo a constant refaceting process. The refaceting continues until an equilibrium position between the orientation of the facets and the crystallographic orientation of the FLG flakes is reached. After this point, the nanoparticle starts a rapid channeling activity in a well-defined crystallographic direction. The channeling does not become the permanent activity as the edge recession cutting resumes after the nanoparticle covers a certain distance. This shows that, even if the restructuration is less evident, it is still affecting the nanoparticles during the channeling activity. This behavior is sustained by the irregularity of the channeling velocity as the carbon removal rate of the same nanoparticle varies continuously during channeling.

The real-time observation of an active nanoparticle changing the channeling direction has shown an interesting mechanism. From the previous observation of the *ex-situ* nanopatterned samples (see *Step-down topography* in the second chapter) it was considered that when changing the channeling direction, the frontal facet of the nanoparticle is losing the active role "assumed" then by one of the lateral facets. No additional refaceting process was considered. However, the real-time observation shows that during the change of the cutting direction, both on uniform FLG surface or when reaching an FLG edge, the nanoparticle undergoes a slow and complex refaceting process. This process is very dynamic as the entire structure of the nanoparticle is changed. Although no precise indexation of the nanoparticle's crystallography during such a phenomenon was possible, it can be assumed that the refaceting process is necessary in order to achieve the equilibrium position (faceting vs. FLG crystallography) for the new channeling direction.

3.6. Conclusions

This study reports for the first time the *in-situ* analysis of the catalytic patterning of FLG flakes by metallic Fe nanoparticles. The aim of this real-time observation of the cutting process was to get an insight in some of the process properties that cannot be revealed by *ex-situ* investigations. Overall, the results presented in the present chapter show the complexity of performing environmental TEM-based experiments in the particular case of the catalytic nanopatterning. The *in-situ* perspective on the nanopatterning shows a more irregular process, i.e. variable channeling rates, constant refaceting and even the splitting of the active nanoparticles. Although incomplete at this moment, the present study represents an important step to understand the mechanism of the catalytic cutting process.

3.7 Perspective

The results presented above show that there is a strong correspondence between the orientations of certain facets of the nanoparticle with respect to the crystallography of the FLG substrate. Therefore, a new mechanism to combine the anisotropy of the channeling and the orientation/properties of the nanoparticle's facets is required. A real-time electron diffraction analysis is necessary in order to resolve the crystallography of both the FLG substrate and the active nanoparticle. Moreover, a better understanding of the carbon dissolution inside the nanoparticle matrix and the H_2 dissociation on its surface is essential in order to create a complete image of the cutting mechanism.

Related to the effect of the electron beam on the gas environment, *ex-situ* experiments capable of mimicking the environmental conditions obtained inside the E-cell are highly required. Using the plasma cleaning machines to create an ionized gas atmosphere might be a solution. Analyzing the gas compositional transformation under the influence of the electron beam using mass spectrometers installed on the gas output lines will increase the control for all environmental TEM experiments.

3.8 References

1. Helveg, S. *et al.* Observing gas-catalyst dynamics at atomic resolution and single-atom sensitivity. *Micron* **68,** 176–185 (2015).
2. Gai, P. L. Developments in in situ Environmental Cell High-Resolution Electron Microscopy and Applications to Catalysis. *Top. Catal.* **21,** 161–173 (2002).
3. In-situ Transmission Electron Microscopy - Springer. at <http://link.springer.com.scd-rproxy.u-strasbg.fr/chapter/10.1007/978-3-642-45152-2_3>
4. Ruska, E. Article on the super-microscopic image in high pressures. *Kolloid-Z* 212–219 (1942).
5. Boyes, E. D. & Gai, P. L. Environmental high resolution electron microscopy and applications to chemical science. *Ultramicroscopy* **67,** 219–232 (1997).
6. Double, D. D., Hellawell, A. & Perry, S. J. The Hydration of Portland Cement. *Proc. R. Soc. Lond. Math. Phys. Eng. Sci.* **359,** 435–451 (1978).
7. Parsons, D. F. Structure of wet specimens in electron microscopy. Improved environmental chambers make it possible to examine wet specimens easily. *Science* **186,** 407–414 (1974).
8. Williams, D. & Carter, B. in *Transmission Electron Microscopy* 3–22 (Springer US, 2009).
9. Wagner, J. B., Cavalca, F., Damsgaard, C. D., Duchstein, L. D. L. & Hansen, T. W. Exploring the environmental transmission electron microscope. *Micron* **43,** 1169–1175 (2012).
10. Petkov, N. *In Situ* Real-Time TEM Reveals Growth, Transformation and Function in One-Dimensional Nanoscale Materials: From a Nanotechnology Perspective. *Int. Sch. Res. Not.* **2013,** e893060 (2013).
11. Hansen, T. W. & Wagner, J. B. Environmental Transmission Electron Microscopy in an Aberration-Corrected Environment. *Microsc. Microanal.* **18,** 684–690 (2012).
12. Sharma, R. & Weiss, K. Development of a TEM to study in situ structural and chemical changes at an atomic level during gas-solid interactions at elevated temperatures. *Microsc. Res. Tech.* **42,** 270–280 (1998).
13. Allard, L. F. *et al.* A new MEMS-based system for ultra-high-resolution imaging at elevated temperatures. *Microsc. Res. Tech.* **72,** 208–215 (2009).
14. Creemer, J. F. *et al.* Atomic-scale electron microscopy at ambient pressure. *Ultramicroscopy* **108,** 993–998 (2008).
15. De Jonge, N., Bigelow, W. C. & Veith, G. M. Atmospheric Pressure Scanning Transmission Electron Microscopy. *Nano Lett.* **10,** 1028–1031 (2010).
16. Allard, L. F. *et al.* Novel MEMS-Based Gas-Cell/Heating Specimen Holder Provides Advanced Imaging Capabilities for In Situ Reaction Studies. *Microsc. Microanal.* **18,** 656–666 (2012).
17. Huolin L Xin, K. N. In Situ TEM Study of Catalytic Nanoparticle Reactions in Atmospheric Pressure Gas Environment. *Microsc. Microanal. Off. J. Microsc. Soc. Am. Microbeam Anal. Soc. Microsc. Soc. Can.* 1–11 (2013). doi:10.1017/S1431927613013433
18. Alan, T. *et al.* Micro-fabricated channel with ultra-thin yet ultra-strong windows enables electron microscopy under 4-bar pressure. *Appl. Phys. Lett.* **100,** 081903 (2012).
19. Sun, L., Noh, K. W., Wen, J.-G. & Dillon, S. J. In Situ Transmission Electron Microscopy Observation of Silver Oxidation in Ionized/Atomic Gas. *Langmuir* **27,** 14201–14206 (2011).
20. Jinschek, J. R. & Helveg, S. Image resolution and sensitivity in an environmental transmission electron microscope. *Micron* **43,** 1156–1168 (2012).
21. Butler, E. P. & Hale, K. F. *Dynamic experiments in the electron microscope*. (North-Holland Pub. Co., 1981).
22. Bright, A. N., Yoshida, K. & Tanaka, N. Influence of total beam current on HRTEM image resolution in differentially pumped ETEM with nitrogen gas. *Ultramicroscopy* **124,** 46–51 (2013).
23. Williams, D. & Carter, B. in *Transmission Electron Microscopy A Textbook for Materials Science*

24. Egerton, R. F. in *Electron Energy-Loss Spectroscopy in the Electron Microscope* (Springer US, 2011).
25. Woehl, T. J. *et al.* Experimental procedures to mitigate electron beam induced artifacts during in situ fluid imaging of nanomaterials. *Ultramicroscopy* **127,** 53–63 (2013).
26. Papaefthimiou, V. *et al.* Effect of the Specific Surface Sites on the Reducibility of α-Fe2O3/Graphene Composites by Hydrogen. *J. Phys. Chem. C* **117,** 20313–20319 (2013).
27. Rau, M.-F., Rieck, D. & Evans, J. W. Investigation of iron oxide reduction by TEM. *Metall. Trans. B* **18,** 257–278 (1987).
28. Tomita, A. & Tamai, Y. Hydrogenation of carbons catalyzed by transition metals. *J. Catal.* **27,** 293–300 (1972).
29. Homma, Y. *et al.* Role of Transition Metal Catalysts in Single-Walled Carbon Nanotube Growth in Chemical Vapor Deposition. *J. Phys. Chem. B* **107,** 12161–12164 (2003).
30. Shibuta, Y. & Suzuki, T. Melting and nucleation of iron nanoparticles: A molecular dynamics study. *Chem. Phys. Lett.* **445,** 265–270 (2007).
31. Shen, T., Meng, W., Wu, Y. & Lu, X. Size dependence and phase transition during melting of fcc-Fe nanoparticles: A molecular dynamics simulation. *Appl. Surf. Sci.* **277,** 7–14 (2013).
32. Datta, S. S. Wetting and energetics in nanoparticle etching of graphene. *J. Appl. Phys.* **108,** 024307 (2010).
33. Goethel, P. J. & Yang, R. T. Platinum-catalyzed hydrogenation of graphite: Mechanism studied by the rates of monolayer channeling. *J. Catal.* **101,** 342–351 (1986).

Chapter IV

Carbon nanotubes as nanodispensers for metal particles onto graphene

4.1. State-of-the-art

The continuous demand for reducing the size of electronic components has led technology to the nanometer frontier. As the device scaling and performance enhancement of silicon-based transistors cannot continue forever due to quantum limitations, a huge effort has been made for developing alternative technologies[1]. The astonishing physical properties of graphene[2] and carbon nanotubes (CNTs)[3] recommend them as promising candidates for the fabrication of nanodevices with applications in several fields. For instance, electrical interconnectors[4], pipelines for femtogramme mass transport[5–9] and nanoswitches[10,11] can be assembled from CNTs filled with metallic nanoparticles. In addition, graphene decorated with nanoparticles are gaining growing interest as alternative supports in the fields of optoelectronics[12], energy storage[13,14] and catalysis[15,16].

The prospects of delivering mass onto predefined locations in the femtogramme regime[17] or of generating nanowires[18] in a tube plead for developing adapted approaches for the investigation of mass transport in or out of CNTs. In the last few years, significant progress was made in the understanding of the phenomena at the basis of mass transport on the inner[19] and/or outer[20] surface of CNTs. Several phenomena were suggested as being the source of the metal migration. Electromigration force ($\overrightarrow{F_e}$) is proposed as the most important trigger of the metal diffusion inside CNTs[18,19,21]. However, phenomena as the thermomigration and thermal expansion, capillarity and nanotube's shell-shrinkage could also influence the metal transfer[17].

When the moving direction of the metal encapsulated inside a CNT is influenced only by the direction of the electrical current flowing through the system, the main component of the driving force can be attributed to the $\overrightarrow{F_e}$ force. Electromigration is the forced diffusion of charged atoms

and molecules on the surface of a substrate under the influence of an electric field and the associated electric current[22]. The particularity of this diffusion is that the atomic jumps are not randomly oriented[23]. The atoms of a structure passed by an electric current which are out-of-lattice-equilibrium will be dragged either in the direction of the electron flow or in the direction of the external electric field. A general expression of the $\overrightarrow{F_e}$ force is given in the eq. 4.1.

$$\overrightarrow{F_e} = \overrightarrow{F_w} + \overrightarrow{F_d} \quad \textbf{(eq.}\ 4.1)$$

where $\overrightarrow{F_w}$ is the electron mediated wind force and $\overrightarrow{F_d}$ is the direct electrostatic force[24,25].

The $\overrightarrow{F_w}$ force is created by the momentum transferred from the conduction electrons scattering on the atoms. Its expression is presented in eq. 4.2.

$$\overrightarrow{F_w} = Z_{wind} e \rho \vec{J} \quad \textbf{(eq}.\ 4.2)$$

where Z_{wind} represents the wind valence, e the elementary charge, ρ the electrical resistivity and $\vec{J}$ the current density.

The $\overrightarrow{F_d}$ force is caused by the action of a locally modified external electric field on the migration atoms. Its expression is presented in eq. 4.3

$$\overrightarrow{F_d} = Z_{direct} e \rho \vec{J} \quad \textbf{(eq}.\ 4.3)$$

where Z_{direct} represents the direct valence, e the elementary charge, ρ the electrical resistivity and $\vec{J}$ the current density.

Therefore, the total force acting on the metal atoms can be expressed as:

$$\overrightarrow{F_e} = (Z_{wind} + Z_{direct}) e \rho \vec{J} \quad \textbf{(eq}.\ 4.4)$$

Z_{wind} is a parameter set by the magnitude and the direction of the momentum exchange while the direct valence, Z_{direct}, accounts for the direct electrostatic force of the moving atom. The result of their sum is called the effective valence, Z^*[22–26].

The convenient expression of the electromigration force is:

$$\overrightarrow{F_e} = Z^* e \rho \vec{J} \quad \textbf{(eq}.\ 4.5)$$

The most important parameters controlling the $\overrightarrow{F_e}$ force are the effective valence, Z*, and the current density, $\vec{J}$. The effective valence is the parameter controlling the direction of atom's migration: a negative value leads to an atomic diffusion along the direction of the electron flow[23]. The current density sets the amount of mass moved and the velocity of the mass diffusion.

Another factor influencing the electromigration is the accessibility of the diffusing atoms to vacancies in the adjacent lattice sites[22]. Therefore, the nature of the substrate on which metallic atoms are diffused by the $\overrightarrow{F_e}$ force is an important parameter controlling the material transfer.

The pioneering work of Svensson et al.[26] emphasizes the role of the electromigration force on the nanoparticle transfer from CNTs employed as "nanopipettes" onto gold substrates. Today, however, only little is known on the mechanisms, conditions, and constraints governing the process of materials transfer from one support to another under the impact of an electrical potential difference. Here, we focus on the possibility of using CNTs filled with metal nanoparticles as a "pen" and a few-layer graphene (FLG) flake as a "paper board". By combining high-resolution transmission electron microscopy (HR-TEM) and scanning tunnelling microscopy (STM) via a specific sample holder (Nanofactory)[27], we are able to carry out the real-time observation of a nanoparticle (NP) transfer from the inner channel of a CNT onto FLG flakes. This approach can lay down the scientific ground work necessary for the development of nano-printing techniques. The study takes advantage of the electron energy loss spectroscopy (EELS) technique for monitoring the chemical changes that occur during nanoparticles transfer while the use of *in-situ* TEM-STM allows for the observation of the nanoparticles transfer process from a mechanistic perspective.

4.2 Methods

4.2.1 Synthesis of Fe_3O_4-filled CNTs and FLG sheets

The filling of commercial multi-wall CNTs with $Fe_{3-x}O_4$ nanoparticles was performed using the thermal decomposition of iron stearate[30], procedure that was used as well for the deposition of $Fe_{3-x}O_4$ nanoparticles on the FLG[31](see Methods, section 2.21). The graphene samples were synthetized from expanded graphite by surfactant-assisted high power ultra-sonication and are characterized by large surface areas (a few μm^2) and few layers in thickness. Meanwhile, an electrochemical etching method was used to prepare Au tips[32], which were used as contact bridges. For the manufacturing of both Au wire electrodes and tips, we have employed commercial 3 mm diameter wires and the tip diameter obtained was around 50 nm. After their synthesis has been performed, the $Fe_{3-x}O_4$ filled CNTs and graphene samples were dispersed in ethanol and subsequently deposited on the movable Au tip and the fixed Au wire, respectively.

4.2.2 Experimental TEM-STM setup

The two Au contacts (the tip and the Au wire) were fixed in the Nanofactory TEM-STM holder, which permits a sub-nanometre precision in sample positioning during the experiment. The schematic drawing of the experimental setup is shown in Fig. 4.1. Characteristic I(V) curves were recorded over the voltage interval 0-3V with a scanning time of 100 ms. The real-time observation (0.33s time resolution) and the HR-TEM imaging were performed using a JEOL 2100F microscope with a high voltage of 200 kV, equipped with a high resolution objective lens pole piece. Under this configuration, images with a spatial resolution of ~0.2 nm were recorded. EELS spectra were recorded using a GATAN Tridiem imaging filter in the parallel mode with a 2 mm aperture. For the experiments needing an *in-situ* heating, a few drops of $Fe_{3-x}O_4$ NPs filled CNTs ethanol solution were deposited on a holey carbon film, which was later mounted in a Gatan double tilt heating holder. The temperature ramp speed was about 0.5 °C/s.

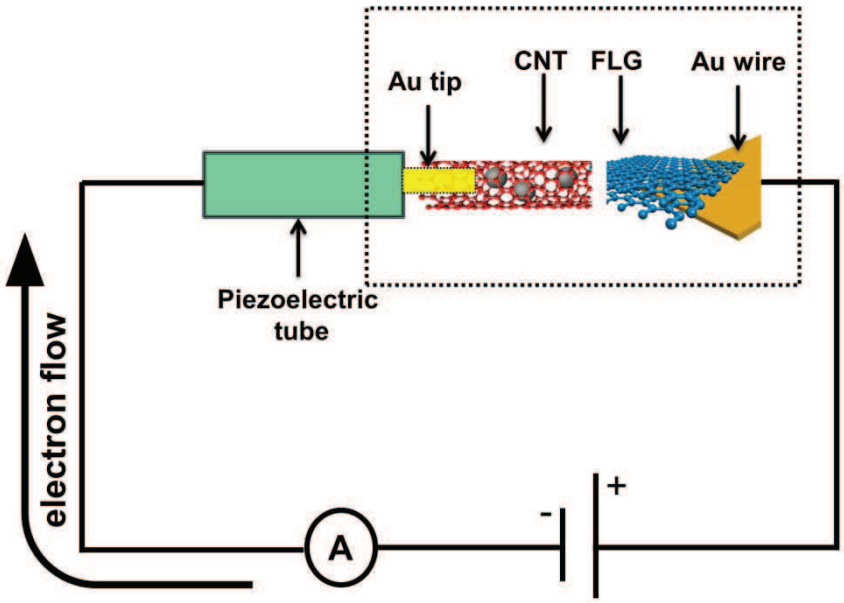

Figure 4.1. Sketch of the TEM-STM experimental setup. The setup used for the Joule activation of the conductivity of the CNTs, the nanoparticle transfer and manipulation on the FLG flakes.

4.3 Joule activation of carbon nanotubes conductivity

The experimental setup consists of a $Fe_{3-x}O_4$ filled CNT which is mounted on a sharp Au tip, on the one side, and on the other side an Au wire (0.3 mm in diameter) supporting a FLG sheet. The schematic drawing of the experimental setup is presented in Fig. 4.1. The use of CNTs as pipelines for material transport requires a high degree of filling with metal nanoparticles. The commercially available multi-walled CNTs with a large diameter appear as a natural choice, as they exhibit diameters between 35 and 50 nm ensuring large filling volumes.

A typical TEM micrograph of the $Fe_{3-x}O_4$ filled CNT is shown on Fig. 4.2a. The HR-TEM micrographs presented in Fig 4.3 show that the CNT external walls contain a large amount of residual amorphous carbon. However, the well-defined π^* and σ^* features in the EELS spectra (Fig. 4.2c – black line) do identify a sp^2-like network. The residual amorphous carbon within a CNT and the structural defects in the graphitic layers are expected to impact the tube behaviour when applying an electric potential. Indeed, when a bias voltage is applied to the CNT for the first time, the short (100 ms) current pulse abruptly changes the CNT's structure (Fig. 4.2b). At the same time, one can observe the graphitization of the amorphous carbon coating layer as

induced by the Joule annealing of the nanotube[28]. This effect is proved by the EELS spectra (Fig. 4.2c – red line), which shows the enhancing of the π* and σ* signatures of the graphitic structure with respect to the initial spectra. The characteristic I(V) curve as recorded on a raw $Fe_{3-x}O_4$ filled CNT (Fig. 4.2d, black line) is characterized by a significant jump in the current intensity in the voltage interval of 2-2.5 V. This backs up the occurrence of a carbon graphitization in the walls as identified by HR-TEM and EELS. Due to the fast recording of the I(V) curve (100 ms) in the present experimental conditions, the current outburst appears to be instant. However, when the bias is varied at a smaller rate, the current increase appears in a larger voltage interval. The nearly linear profile of the I(V) curve acquired in a second run (Fig. 4.2d – red line) demonstrates that the NPs/CNT system is converted to an Ohmic device.

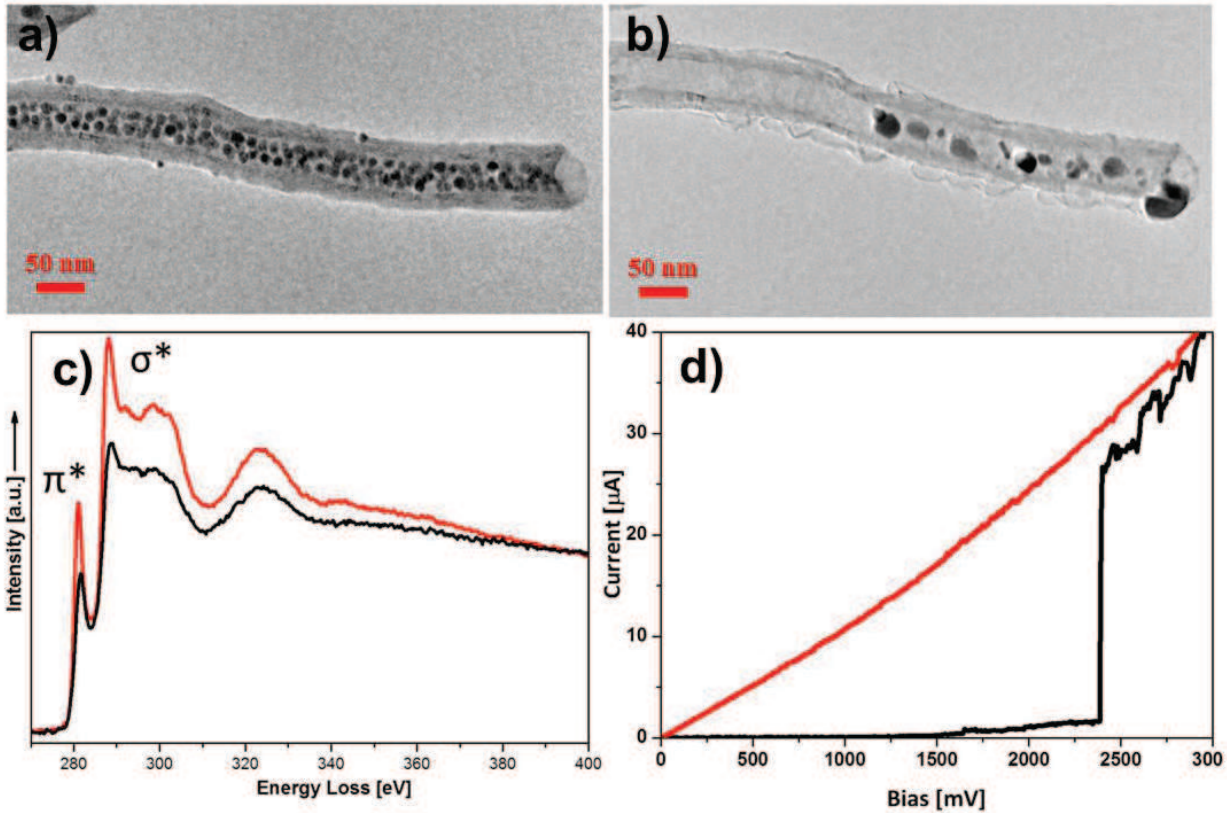

Figure 4.2. CNT filled with Fe based nanoparticles prior and after application of a bias voltage. a) $Fe_{3-x}O_4$ filled CNT (before) and b) Metallic Fe / Fe_xC_y filled CNT (after). c) EELS spectra of the CNT before (black line) and after (red line) a voltage pulse. d) Characteristics I(V) curves of the raw $Fe_{3-x}O_4$ filled CNTs (black line) and the Joule annealed CNTs (red line).

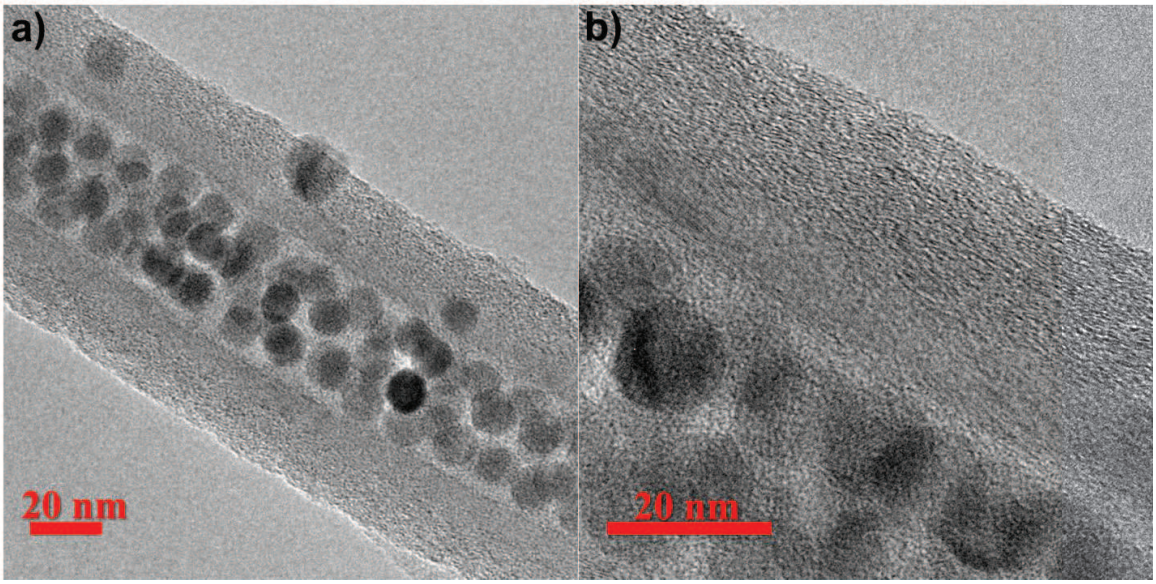

Figure 4.3. a) and b) HR-TEM images of the initial $Fe_{3-x}O_4$ filled CNTs showing the structure of their thick walls which contain a large amount of amorphous carbon.

Moreover, the encapsulated nanoparticles undergo a fast thermal or electrochemical reduction and a subsequent coalescence phenomenon, induced by the large thermal energy injected into the CNT via the Joule heating. The EELS spectrum displayed in Fig. 4.4a (red line) shows that after applying the voltage pulse, the O-K edge (~530eV) significantly weakens as compared to the initial spectrum of the $Fe_{3-x}O_4$ filled CNT (black line). Furthermore, the Fe L_3: Fe L_2 intensity ratio decreases from ~ 4.3 to ~ 2.8, prior and after the I(V) curve recording, a phenomenon related to the reduction of the $Fe_{3-x}O_4$ nanoparticles. The HR-TEM analysis of nanoparticles after the Joule heating process shown in Fig. 4.4b-c allowed the identification of pure metallic and iron carbide phases. To quantify the effect of the Joule heating in the reduction process of the Fe-based nanoparticles we performed an *in-situ* heating of the $Fe_{3-x}O_4$ filled CNTs. The EELS spectra shown in the Fig. 4.4d shows that the Fe L_3: Fe L_2 ratio decreases from ~5.5 at room temperature (black line), to ~3.7 (red line), 2.9 (blue line) after 30 minutes at 550°C, and 20 minutes at 750°C, respectively. Based on the good agreement between the EELS spectra of the Fe based nanoparticles acquired after the heating treatment under vacuum and the one acquired directly after the application of the current pulse, we have estimated that the temperature inside the CNT during the experiment is higher than 750°C. Moreover, during the application of the bias voltage, most of the nanoparticles localized inside the CNT migrate in the direction of the

electron flow through its inner channel. However, several nanoparticles do migrate through the nanotube's walls creating tunnel like structures as presented in Fig. 4.5.

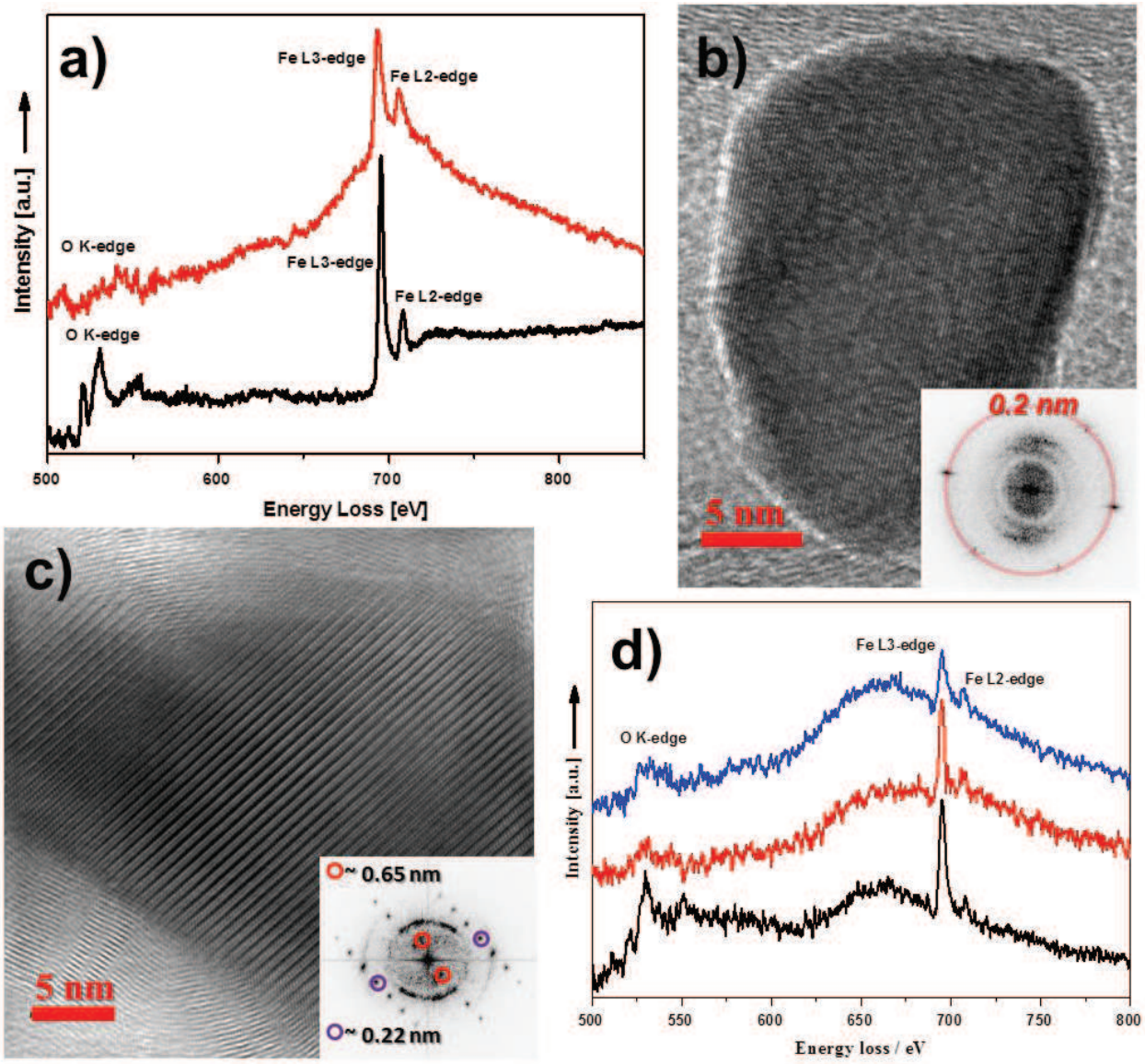

Figure 4.4. a) EELS spectra of the Fe based NPs filled CNT before (black line/ $Fe_{3-x}O_4$) and after (red line/metallic Fe and Fe_xC_y phases) the application of the voltage pulse.
b) HR-TEM image of a metallic Fe nanoparticle formed during the application of a voltage pulse on the $Fe_{3-x}O_4$ filled CNT. The FFT inset shows a lattice spacing of ~0.2 nm characteristic to both ϕ and γ Fe phases.
c) HR-TEM image of a Fe_xC_y phase resulting from the Joule annealing of the initial $Fe_{3-x}O_4$ filled CNT. The FFT inset shows a large lattice spacing characteristic to complex iron carbide phases.
d) EEL spectra of the Fe based NPs filled CNTs during *in-situ* heating black line - room temperature, red line – 550 °C for 30 min, blue line - 750 °C for 20 min.

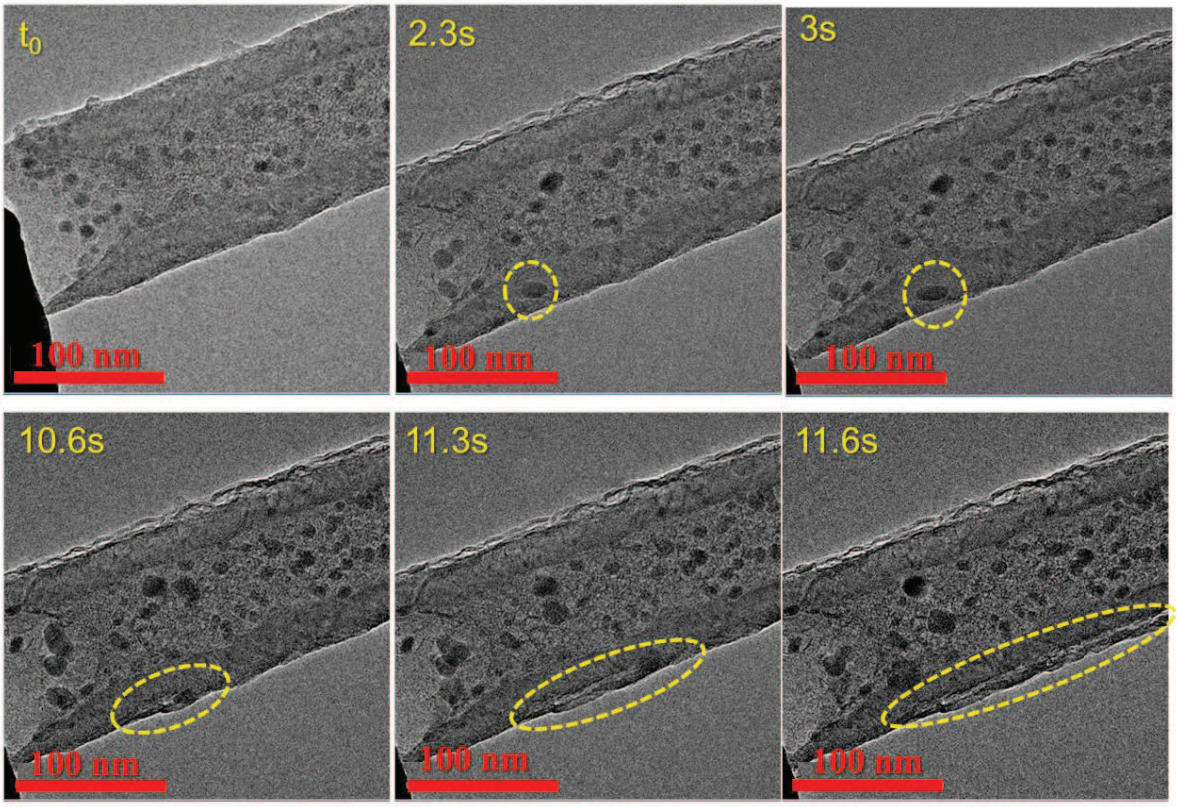

Figure 4.5. Time series of a Fe based NP digging a tunnel through the nanotube wall under the impulse from the electromigration force, $\overrightarrow{F_e}$. The total experiment time was under 12 s.

4.4 Nanoparticle deposition using raw nanotubes

The sketch of the experimental setup used for transferring nanoparticles from the CNT to the FLG sheet is shown in Fig. 4.1. The direct use of a raw nanotube leads to an uncontrolled migration of the nanoparticles under the application of a bias voltage. This results from the structural reorganization undergone by the CNT during the first application of the bias. The initial stage of the CNT/FLG system is presented in Fig. 4.6a. Some of the $Fe_{3-x}O_4$ nanoparticles are attached to the nanotube external surface. After the nanotube was connected to the FLG sheet the bias is stepped up by about 15mV/s. The first observation of the melting of the nanoparticles takes place after 72s at a current intensity of ~51μA. At first, the melting appears only for two small nanoparticles located in the close vicinity of the CNT/FLG contact. The fact that the melting starts with these particles shows that the contact resistance between the CNT and FLG is slightly higher than the overall resistance of the CNT and this generates a higher Joule heating in

the contact vicinity. Then the bias is kept at the same value for ~12s and no major modification occurs showing that the system's temperature rapidly reaches a uniform distribution.

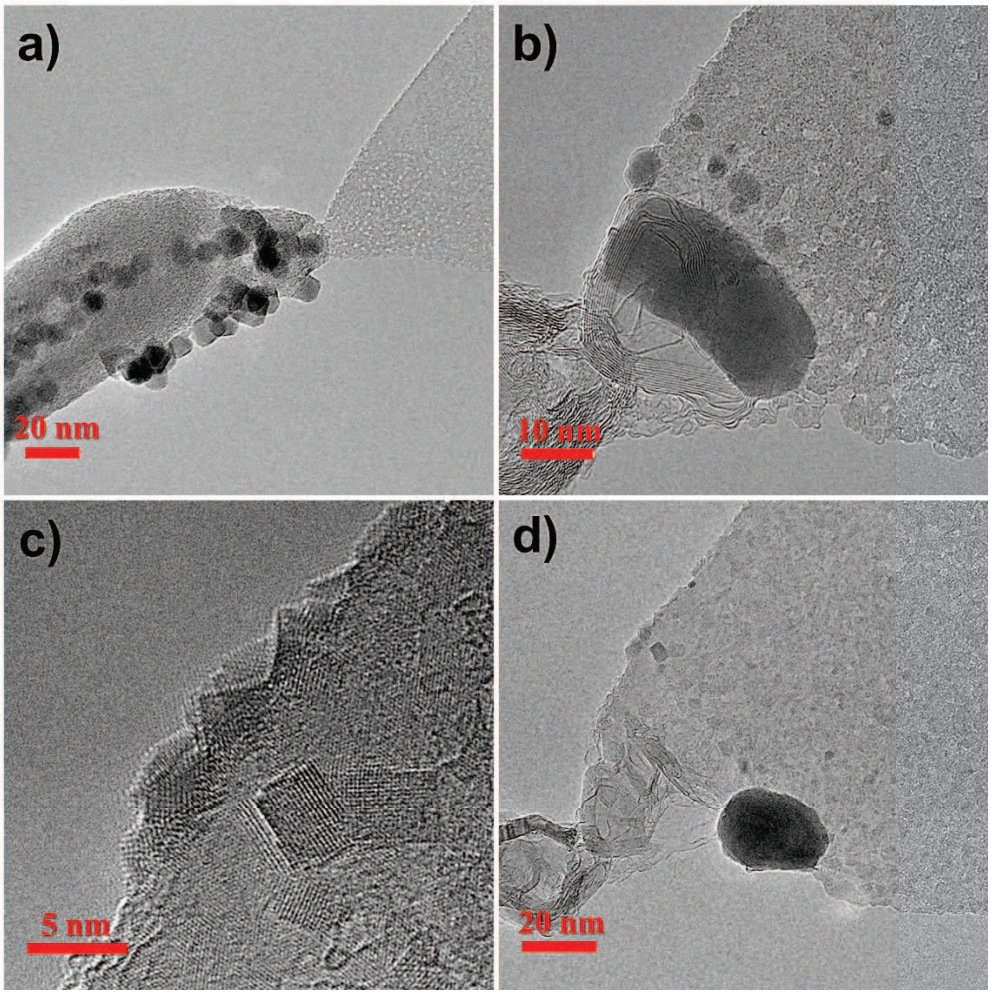

Figure 4.6. The uncontrolled transfer of Fe based NPs on the upper surface of a FLG sheet. a) The CNT/FLG system before the NP deposition; b) The graphitized CNT/FLG contact due to the Fe NP action at high temperature; c) Small Fe clusters decorating the surface of the FLG; d) The final state of the FLG flake decorated with iron NPs in a uncontrolled way.

When the bias is increased again, more nanoparticles melt close to the CNT/FLG contact point (56μA) followed by a rapid "backward" moving of the nanoparticles against the direction of the $\overrightarrow{F_e}$. The "backward" migration of the nanoparticles sitting at the end of a CNT close to the contact with the FLG sheet is a common phenomenon when the current is instantly jumping to higher values. This is due to a temperature gradient arising from the higher temperature reached at the contact point between the CNT and the FLG that forces the melted nanoparticles to move

to a colder region inside the CNT (thermomigration). The thermomigration force ($\overrightarrow{F_t}$) only appears when the current increases in an uncontrolled way and rapidly stops due to the stabilization of the system's temperature. The nanoparticle melting first appears inside the nanotube while the nanoparticles sitting on the tube walls remain stable for a longer time. Around a current intensity of 58μA nanoparticles appears on the FLG surface. The iron continues to accumulate on the FLG surface in an uncontrolled way and around a current intensity of 78μA, due to the high temperature reached, the nanoparticle graphitizes the CNT/FLG contact (Fig. 4.6b) making impossible the nanotube retraction. However the contact graphitization does not induce an increase of the current flowing through the system. When the bias is further increased the nanoparticles will start moving on the FLG surface continuing to graphitize it. At the end of the experiment, after reaching a maximum current intensity of 220μA, the FLG surface is decorated with a 30 nm in diameter metallic Fe nanoparticle and small iron clusters ripped off from the large nanoparticle (Fig. 4.6c-d).

4.5 CNT to FLG nanoparticle transfer by electromigration

It has been previously shown that the first application of a voltage pulse structurally reorganizes the CNT through graphitization (see Fig. 4.2b). A tube that has not been stabilized by such voltage pulses exhibits current intensity jumps as shown in Fig. 4.2d and is therefore not suitable for transferring nanoparticles to FLGs flakes in a controlled manner. In order to eliminate the current intensity uncontrolled jumps during the nanoparticle's deposition, a Fe NPs/CNT system with a stabilized structure was used. After establishing a contact between the CNT and the FLG sheet, a bias voltage is applied in such a way that the electrons flow through the nanotube in the direction of the FLG sheet. Under such conditions the nanoparticles in the CNT start to migrate along the tube channel towards the FLG substrate. The schematic representation of the experiment is presented in Fig. 4.7a. The first experiment identifies nanoparticles formation on the FLG edge for a bias of about 1.5 V (which corresponds to 40-60 μA) and a bias change rate of about 15 $mV \cdot s^{-1}$. The image of the initial CNT/FLG system shown in Fig. 4.7b allows one to identify the presence of a few number of nanoparticles located close to the CNT end at the FLG interface. The evolution of the system during the mass transfer from the CNT to the FLG edge versus time is presented in Fig. 4.7c.

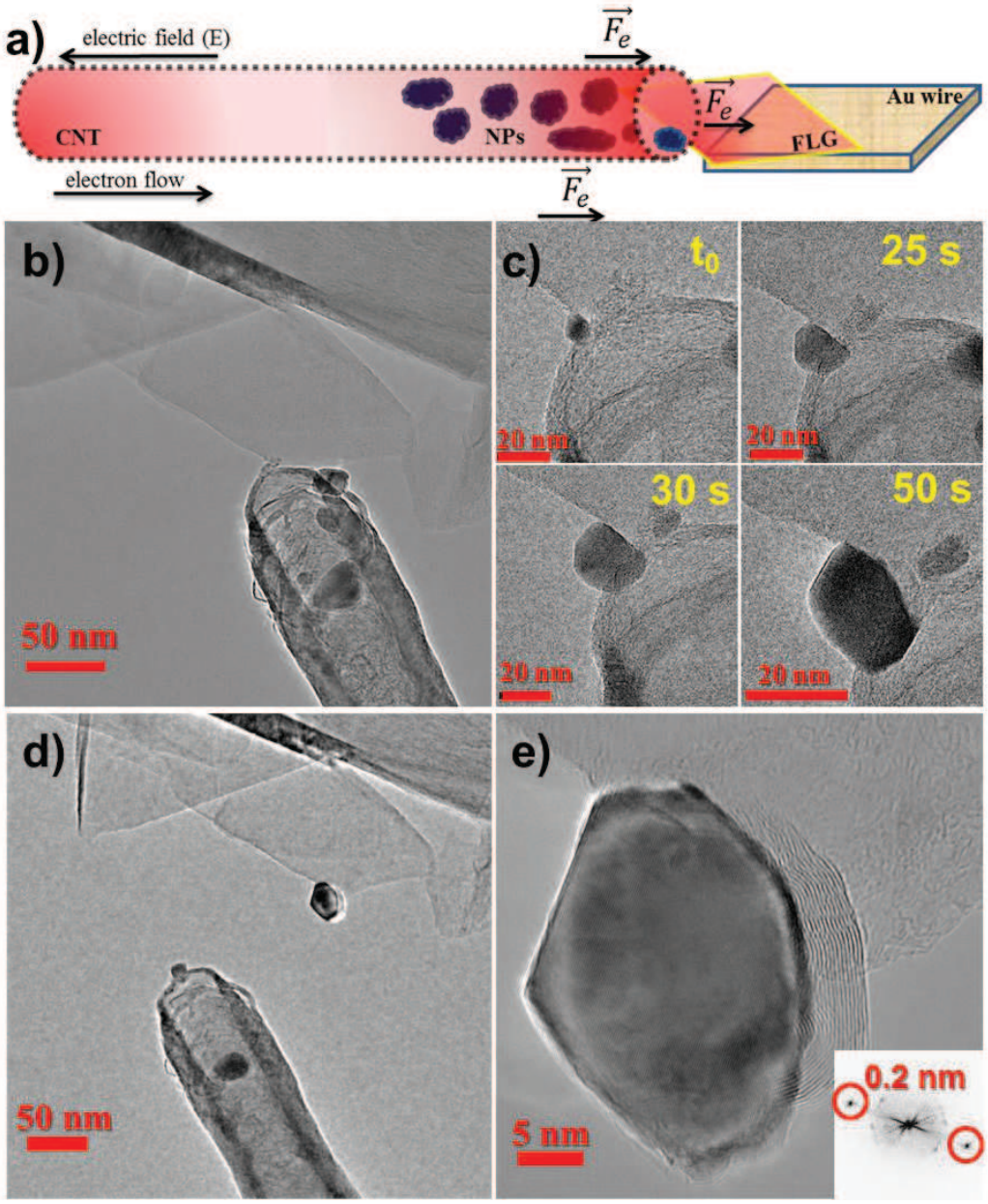

Figure 4.7. Controlled deposition of a metallic Fe nanoparticle on the edge of a FLG flake. a) Schematic representation of the experiment showing the forces acting in the system upon application of a bias voltage. b) The CNT/FLG system before the NP deposition. c) Time series of the NP growing (time resolution 0.33 s). d) The CNT/FLG system after the NP deposition on the FLG edge. e) HR-TEM image of the final NP grown at the FLG edge. The FFT inset identifies a lattice spacing of about ~0.2nm, characteristic to ϕ and γ metallic Fe.

A rapid shape change of nanoparticles during the application of bias voltage appears. This phenomenon occurs shortly before the nanoparticle seed attends the lateral edge of the FLG flake (at t = 0). This behavior indicates the surface melting as event preceding the particle transfer. Right after t = 0, the mass transfer through surface diffusion or drift of metal atoms starts and Fe

atoms continue to accumulate at the FLG edge increasing the size of the new nanoparticle. At t = 25s a diffraction contrast is observable, suggesting the presence of a crystalline aggregate acting as a seed for the subsequent growth of the nanoparticle. The nanoparticle growth progresses along both directions, parallel and perpendicular to the FLG border. It is remarkable that the nanoparticle's faceting does not vary significantly during the whole time lapse of the nanoparticle transport and growth. By resetting the bias to zero, the mass transfer instantaneously stops together with the nanoparticle evolution in terms of size and shape. Fig. 4.7d presents the final image of the FLG border decorated with the iron nanoparticle. According to Fig. 4.7a and 4.7d, the nanoparticles that were localized at the CNT's exit, at the beginning of the experiment, have "disappeared" almost completely, indicating their role as atoms reservoirs for the nanoparticle growth at the FLG edge. The recorded movies shows the matter of the initial nanoparticles slowly ripped out and further reassembled as new nanoparticle at the FLG edge. The images extracted from these movies (see Fig. 4.8) were used to follow the evolution of the apparent surface of the nanoparticles for the ones encapsulated in the CNT and growing on the FLG edge. A growth mechanism similar to Ostwald ripening was identified. Indeed, no direct migration of an entire nanoparticle from the CNT to the FLG sheet was observed. The HR-TEM image of the final nanoparticle sitting on the FLG border is shown in Fig. 4.7e. FFT analysis shows that the lattice spacing of the nanoparticle is about 0.2 nm, corresponding to metallic Fe phases[29].

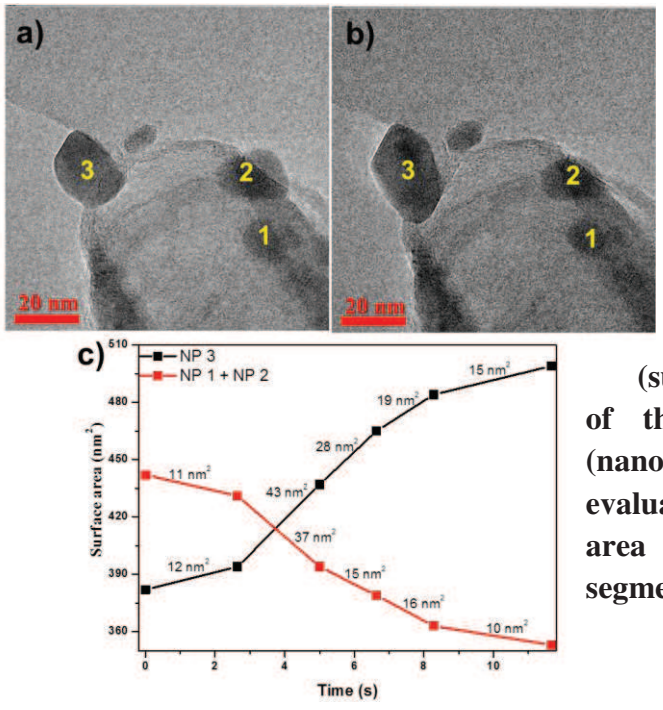

Figure 4.8. The evolution of the nanoparticles during a controlled deposition experiment. TEM images extracted from the recorded movie corresponding to the t_0 (a) and 11.66 s (b) positions. c) The evolution of the apparent surface area of the nanoparticles encapsulated in the CNT (summed area of nanoparticles 1 and 2) and of the one deposited on the FLG edge (nanoparticle 3). The numerical values evaluated for each time segment show the exact area loss (red segment) and gain (black segment) for the corresponding interval.

Another experiment of the controlled nanoparticle deposition is presented in Fig. 4.9. The real-time analysis of the nanoparticle transfer shows that even when the nanoparticle is incorporating mass very rapidly within 1s, the faceting aspect is maintained. However, by exposing the nanoparticle to high currents after the growing phase had been stopped, results in a slow but irreversible loss of the facets. The resulting nanoparticle is also a pure metallic Fe phase as for the majority of the nanoparticles transferred from the inner part of the CNT to the FLG sheets.

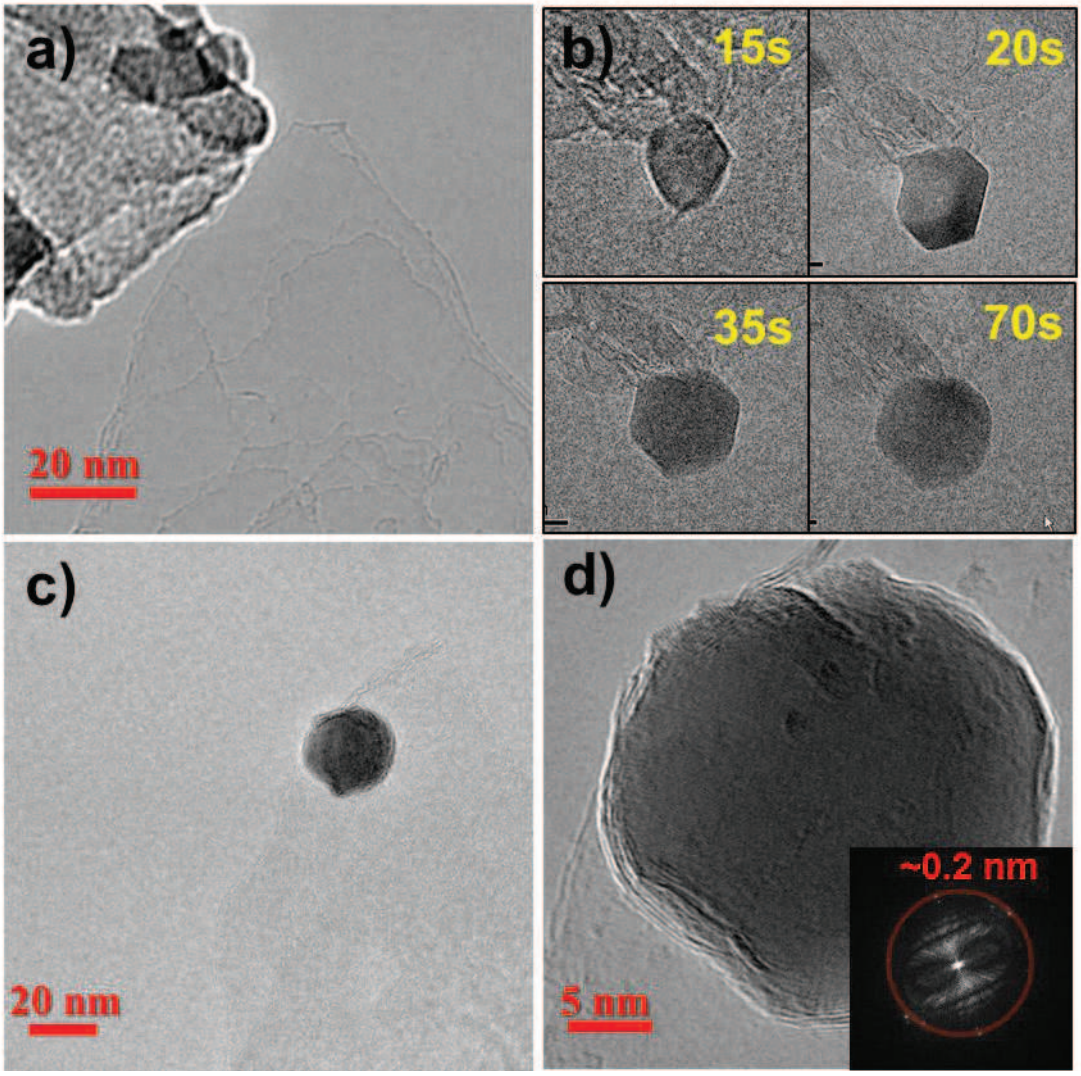

Figure 4.9. The controlled deposition of a metallic Fe nanoparticle on the upper surface of a FLG sheet. a) The CNT/FLG system before the application of the driving voltage; b) A time series of the nanoparticle growing (time resolution 0.33s); c) The FLG system after the nanoparticle deposition on its surface; d) HR-TEM image of the final metallic Fe nanoparticle deposited on the FLG surface. The FFT shows a lattice spacing of about ~0.2 nm, characteristic for ϕ and γ metallic Fe

4.6 Nanoparticles transfer under a high current

The next experiment shows how the directional transfer upon electromigration can be used to simultaneously deposit several nanoparticles, but with a significant loss of control in terms of final position and shape. Fig. 4.10a presents the image of the initial system, prior to the nanoparticle transfer. Fig. 4.10b displays a time series of a nanoparticle deposition when the contact between the CNT and the FLG flake is not made on the FLG border but directly on the upper surface of a FLG sheet.

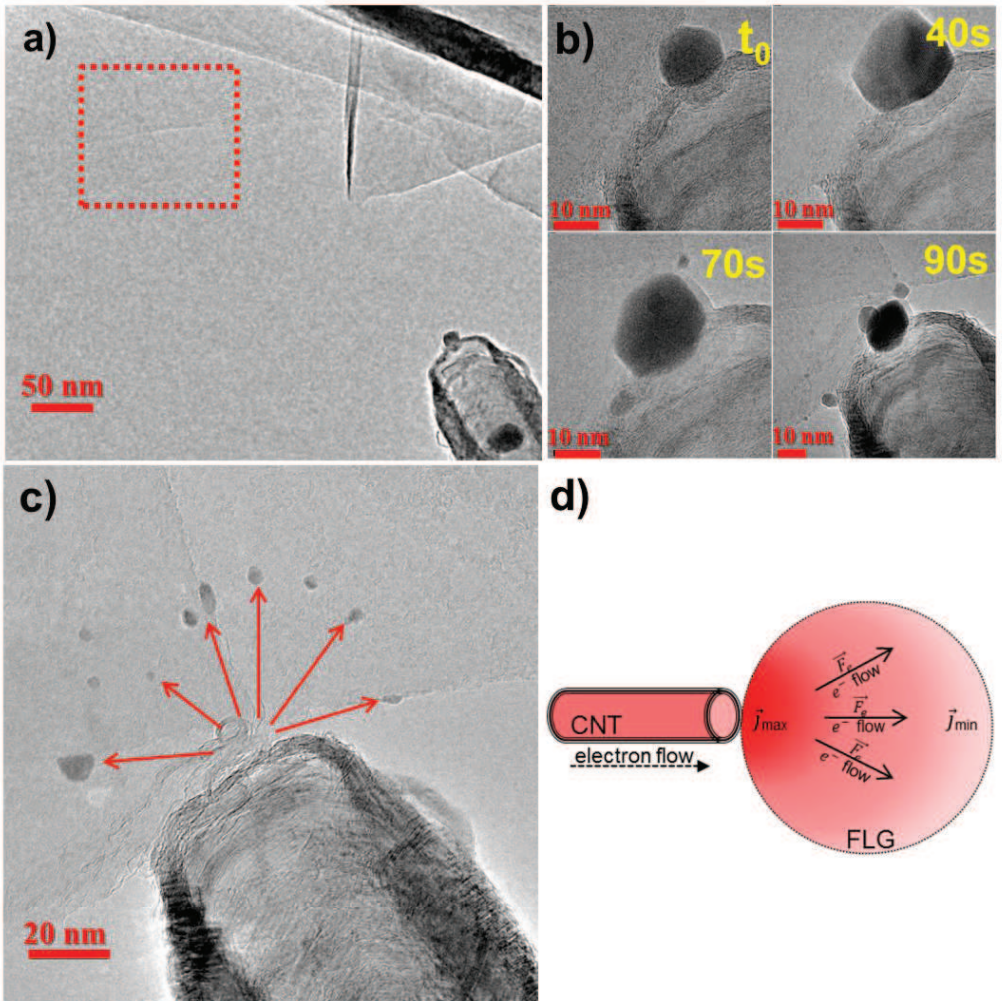

Figure 4.10. Fe based nanoparticles radially dispersed and scattered on the FLG surface. a) The CNT/FLG system before the nanoparticle transfer on the FLG surface. The exact location of the FLG area chosen for the nanoparticle transfer is highlighted by the red square. b) Time series of the uncontrolled nanoparticle growing on the upper surface of a FLG flake. c) HR-TEM image of the nanoparticles radially dispersed on the FLG surface due to the distribution of $\overrightarrow{F_e}$ forces. d) Schematic representation of the $\overrightarrow{F_e}$ forces distribution on a FLG surface crossed by an electrical current.

The nanoparticles growth process observed in the recorded movie shows that the crystalline structure of the nanoparticle remains unchanged during the growth process even when submitted to high currents, as it is verified by the occurrence of the same well-defined crystallographic planes all along the process. By increasing the applied bias voltage up to 2.5 V the current density on the FLG surface becomes high enough (current intensity ~110μA) to transfer sufficient direct impulse to the metal atoms. These atoms start then to migrate and eventually recompose small nanoparticles on the FLG surface, through a migration behaviour similar to Ostwald ripening. The first step consists in the formation of some nanoparticles on the FLG border near the CNT/FLG contact interface. A few seconds later, the nanoparticles start migrating and spreading on the FLG surface along directions having a radial distribution with respect to the contact position (Fig. 4.10c). The predicted distribution of the electromigration force on the surface of FLG sheet is schematically represented in Fig. 4.10d.

4.7 Nanoparticles transfer under inversed voltage polarity

Removing nanoparticles deposited close to the contact point between a CNT and a FLG sheet can be simply achieved by reversing the polarity of the applied voltage (see Fig. 4.11a). Fig. 4.12 shows a time series of a nanoparticle erasure experiment. The size of the initial nanoparticle decreases slowly as its composing atoms are dragged inside the CNT and reassembled as a new nanoparticle. The situation is more problematic when the nanoparticles are not located in the immediate vicinity of the contact point. Fig. 4.11b presents a time series of one of these experiments. The voltage is increased until the formation of small iron nanoparticles at the CNT/FLG contact is observed and then it is maintained constant. Some nanoparticles formed at the contact point start moving towards the nanotube but at the same time a bulk group is formed at the CNT/FLG interface (see Fig. 4.11c). The nanoparticle transfer continues for a few minutes until the nanoparticles or the atomic clusters close to the contact point are exhausted. Fig. 4.13 shows the evolution of the apparent surface area of the nanoparticles as deduced from the 2D projections acquired prior and after the transfer. Three groups of nanoparticles located at different distances from the CNT/FLG contact were considered. For these groups of nanoparticles, the estimated amount of mass lost during the experiment increases when the

distance between the nanoparticle and the CNT/FLG contact point diminishes. Such, the nanoparticles located in the close vicinity of the contact have lost around 13% of their mass, whereas the nanoparticles far from the contact have lost about 10% and 8% of their mass, for distances of about 80 nm and 100 nm from the contact, respectively.

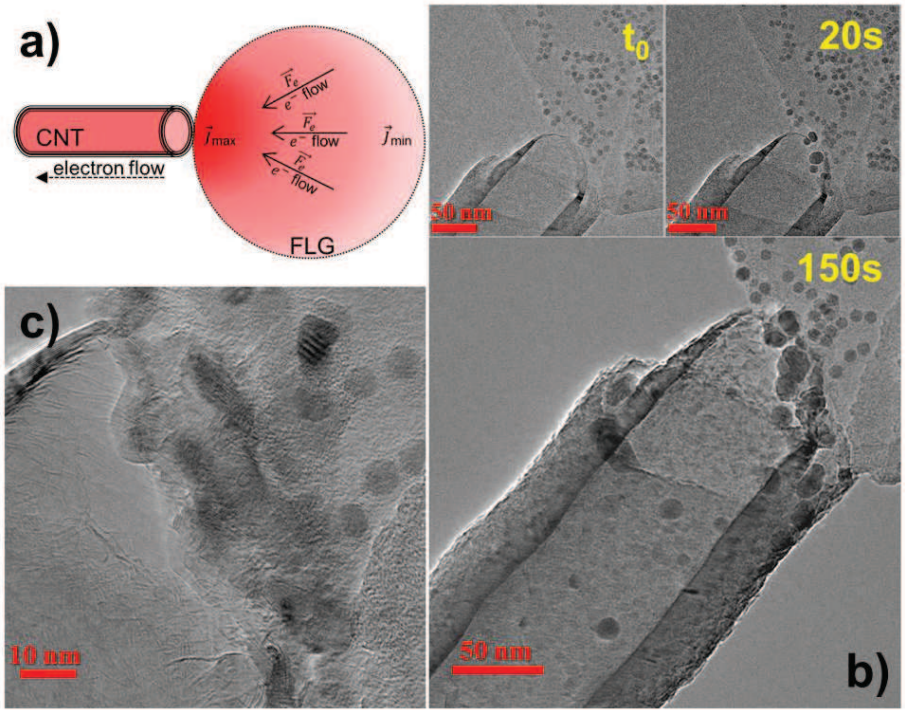

Figure 4.11. Fe based nanoparticles transfer from a decorated FLG flake to an empty CNT. a) Schematic representation of the forces distribution on a FLG surface under an electrical current (inversed polarity). b) Time series of the nanoparticles transfer inside the empty CNT. c) HR-TEM image of the bulk group of nanoparticles formed at the CNT/FLG contact after few-minutes of biasing.

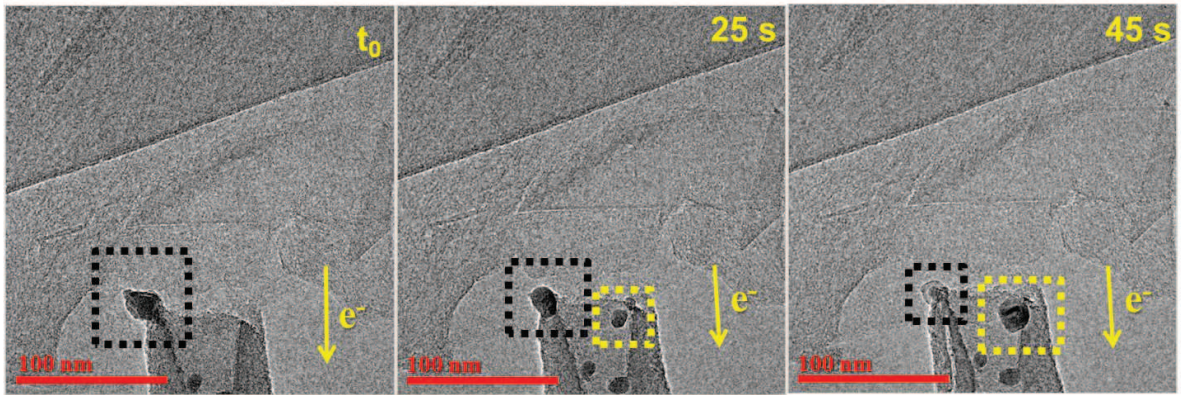

Figure 4.12. Time series of a nanoparticle removal experiment from a position close to the CNT/FLG interface. The positions of the initial and the one of the reassembled nanoparticle are highlighted by black and yellow squares, respectively.

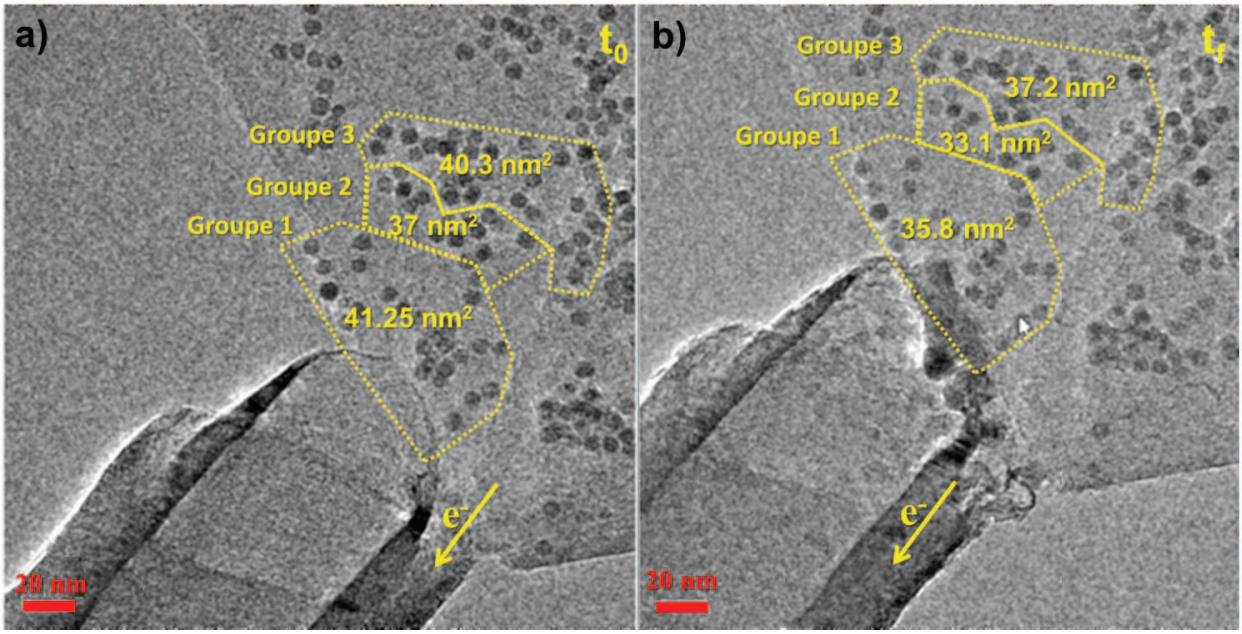

Figure 4.13. The evolution of the nanoparticle apparent surface during the erasing experiment shown in Fig. 4.11. a) TEM image of the initial system. The nanoparticles were divided into three groups as a function of their position with respect to the CNT/FLG contact (highlighted in yellow). The numerical values represent the mean surface area for the nanoparticles from each group. b) TEM image of the system after the erasing experiment. The differences between the mean apparent surfaces of the nanoparticles from each group before and after the erasing experiment are: ~5.5 nm^2 (13%) (group 1), ~3.9 nm^2 (10%) (group 2), and 3.1 nm^2 (8%) (group 3)

4.8 Discussion

The present study shows that CNTs can be efficient nano-pipelines for performing nanometric mass transfer in both directions between two conductive nanostructures, i.e. here from a CNT to a graphene substrate and vice-versa. By applying a bias voltage in such a way that an electron current flows through the nanotube in the direction of its contact point with the FLG, the transfer takes place from the inner part of the CNT to the FLG flakes. From a phenomenological point of view, a strong electro-migration force ($\overrightarrow{F_e}$) appears along the CNT under the application of the electrical field; this force is responsible for the dragging of the iron nanoparticles from the nanotube centre to the nanotube exit end. The $\overrightarrow{F_e}$ force is created by the interaction of the scattering electrons in the electric current that flows along the CNT and the

metal atoms localized on the CNT inner surface; it imposes a global movement to the metal atoms along the electron flow direction[19]. Such a transfer process "sustained" by the electro-migration force $\overrightarrow{F_e}$, is very sensitive to the slightest uncontrolled current variation (jumps) that leads to current correlated but uncontrolled nanoparticle transfer. The main factor responsible for the current jumps is the CNT raw structure and the presence of residual amorphous carbon covering its walls. As stated previously, the amorphous to graphitic transformation of the CNT wall through Joule heating and the Fe NPs/CNT system becomes an Ohmic device when a short exposure to voltage pulses (minimum two pulses) is carried out prior to deposition. Nevertheless, the transfer procedure e.g. voltage interval and number of applied pulses varies from one nanotube type to another. The current flow affects as well the structure of the nanoparticles encapsulated inside the CNTs, as the initial $Fe_{3-x}O_4$ nanoparticles are almost completely reduced to metallic and carbide phases through chemical reaction with the carbon phase of the nanotube walls. Note that the reduction of the $Fe_{3-x}O_4$ nanoparticles is expected to take place through Joule heating, but an electrochemical reduction reaction can also take place. By *in-situ* heating of the $Fe_{3-x}O_4$ filled CNTs, we obtained the same EELS spectral characteristics for the O-K and Fe-L edges as the ones achieved for the same system after applying the voltage pulses only at high temperature (≥ 750°C). The tunnel formation through the walls of the nanotubes caused by the reaction between Fe based nanoparticles and graphitic C shows the high chemical reactivity of the CNT walls regarding the encapsulated nanoparticles during the applied voltage pulses. Such high local reactivity can lead to the activation of a catalytic reaction between carbon and iron, with the eventual formation of Fe carbides. To overcome these reactivity-related drawbacks, the activation procedure needs to be closely controlled. The inner surface quality (defects presence, crystallinity) prior to the transfer experiment is the other key-parameter to account for. In this context, a careful selection of the CNTs as well the use of a well-defined activation protocols for the CNTs, in terms of voltage increasing rates, voltage intervals and number of the applied pulses will contribute to the improvement of the experiments reproducibility. The nanoparticles transfer from the CNT channel to the FLG flakes requires a step-by-step current increase. When the $\overrightarrow{F_e}$ force is gaining sufficient power it starts moving atoms from the inner channel of the nanotube to the FLG flake. During the transfer process, the metal atoms are weakly linked to the graphitic layer of the inner surface of the tube which is characterized by a small amount of steps and edges due to the previous annealing of the tube, facilitating thus their diffusion and directional drift.

The nanoparticle seed nucleates on the defect site localized at the closest distance to the CNT/FLG contact point. The growing behavior of the nanoparticle is set by the seed position on the FLG, i.e. on the planar surface or the edge. The nanoparticle's faceting is a continuous process occurring all along the particle growth, generally keeping a hexagonal external shape. The faceted aspect together with the phase and diffraction contrast observed in HR-TEM imaging during the growth process shows that the nanoparticle's temperature rapidly decreases in the direction perpendicular to the graphene substrate, which facilitates its continuous crystallization. The fact that the initial nanoparticle seeds act as cold-traps for the moving atoms also explains why only one single nanoparticle is formed. At the end of a transfer experiment most of the newly grown nanoparticles are in a pure metallic Fe phase. Nevertheless, Fe_xC_y phases identified by lattice spacing can be found occasionally. They could be due to a local excess of the temperature favouring the formation of carbide phases. The preferential formation of metallic Fe phases on the graphene surface even if, as a result the CNT activation, the metallic and carbide iron phases are found in comparable amounts in the CNT channel, is due to the difference between the diffusion properties of Fe and C atoms under the $\overrightarrow{F_e}$ force [29].

The real-time observation of the nanoparticle migration on the FLG surface shows how the CNTs can be used to simultaneously deposit more nanoparticles on the graphene substrate. The resulting radial distribution of the nanoparticles on the FLG surface can be associated with the radial distribution of the current lines away from the CNT/FLG contact point. The migration it is promoted by an Ostwald ripening-like mechanism. In the opposite configuration, when the current polarity is reversed, an empty CNT can be used to remove nanoparticles from a decorated FLG sheet. In this case the $\overrightarrow{F_e}$ force transports the metal atoms inside the nanotube where they will recompose forming new nanoparticles. However, a higher bias voltage (and thus a stronger $\overrightarrow{F_e}$) is needed for their transfer, as they should be generally collected from regions with low current density, far away from the CNT/FLG contact point. Therefore, keeping the system at a constant voltage, but below its breaking point will allow only the transfer of the nanoparticles located close the CNT/FLG contact.

4.9 Conclusions

Using a combined TEM and STM technique associated to electron spectroscopy, we were able to define conditions under which a reliable electrically controlled transfer of nanoparticles from the inner part of a CNT onto a FLG sheet can be performed. From a general point of view, the mass transfer requires four individual steps: the annealing of the tube, the chemical transformation or the reduction of the original particles, the particle transfer through the tube and the dispensing of the metal atoms on the graphene sheet. The erasing of already deposited nanoparticles can also be achieved by reversing the applied electrical voltage. The printing process described in this work mimics the process used in a "dye sublimation printer" and we therefore consider that this study is the proof-of-concept for the design of printing devices at the nanoscale.

4.10 Perspective

Future studies should provide a better control of the nanoprinting process. The tip could be automatically moved according to a geometric pattern allowing metal deposition in both continuous and discrete modes, as a function of the applied voltage.

During the experiments of the transfer of the nanoparticles, the CNTs and FLG flakes are continuously exposed to high energy electrons. The irreversible structural changes induced by this exposure are affecting the properties of the final FLG sheet decorated with the metallic nanoparticle. Moreover, the defects induced in the structure of CNTs and FLG sheets can also change the kinetics of the electromigration process. It is therefore necessary to decrease the exposure time to the electron beam during the *in-situ* probing experiments. New acquisition software designed exclusively for real-time *in-situ* TEM observations allow a better control of the electron dose. Working at an acceleration voltage lower than 80kV can significantly reduce the effect of the electron beam on the carbon nanostructures.

4.11 References

1. Avouris, P., Chen, Z. & Perebeinos, V. Carbon-based electronics. *Nat. Nanotechnol.* **2,** 605–615 (2007).
2. Geim, A. K. Graphene: Status and Prospects. *Science* **324,** 1530–1534 (2009).
3. Baughman, R. H., Zakhidov, A. A. & de Heer, W. A. Carbon nanotubes--the route toward applications. *Science* **297,** 787–792 (2002).
4. Close, G. F., Yasuda, S., Paul, B., Fujita, S. & Wong, H.-S. P. A 1 GHz Integrated Circuit with Carbon Nanotube Interconnects and Silicon Transistors. *Nano Lett.* **8,** 706–709 (2008).
5. Markus Löffler, U. W. Current-induced mass transport in filled multiwalled carbon nanotubes. *Adv. Mater. Deerfield Beach Fla* **23,** 541–4 (2011).
6. Coh, S., Gannett, W., Zettl, A., Cohen, M. L. & Louie, S. G. Surface Atom Motion to Move Iron Nanocrystals through Constrictions in Carbon Nanotubes under the Action of an Electric Current. *Phys. Rev. Lett.* **110,** (2013).
7. Golberg, D. *et al.* Copper-Filled Carbon Nanotubes: Rheostatlike Behavior and Femtogram Copper Mass Transport. *Adv. Mater.* **19,** 1937–1942 (2007).
8. Sun, L. *et al.* Carbon Nanotubes as High-Pressure Cylinders and Nanoextruders. *Science* **312,** 1199–1202 (2006).
9. Sutter, P. W. & Sutter, E. A. Dispensing and surface-induced crystallization of zeptolitre liquid metal-alloy drops. *Nat. Mater.* **6,** 363–366 (2007).
10. Dorozhkin, P. S. *et al.* A liquid-Ga-filled carbon nanotube: a miniaturized temperature sensor and electrical switch. *Small Weinh. Bergstr. Ger.* **1,** 1088–1093 (2005).
11. Sun, M. & Gao, Y. Electrically driven gallium movement in carbon nanotubes. *Nanotechnology* **23,** 065704 (2012).
12. Cao, A. *et al.* A Facile One-step Method to Produce Graphene–CdS Quantum Dot Nanocomposites as Promising Optoelectronic Materials. *Adv. Mater.* **22,** 103–106 (2010).
13. Wu, Z.-S. *et al.* Graphene Anchored with Co3O4 Nanoparticles as Anode of Lithium Ion Batteries with Enhanced Reversible Capacity and Cyclic Performance. *ACS Nano* **4,** 3187–3194 (2010).
14. Huang, X. *et al.* Graphene-Based Materials: Synthesis, Characterization, Properties, and Applications. *Small* **7,** 1876–1902 (2011).
15. Scheuermann, G. M., Rumi, L., Steurer, P., Bannwarth, W. & Mülhaupt, R. Palladium Nanoparticles on Graphite Oxide and Its Functionalized Graphene Derivatives as Highly Active Catalysts for the Suzuki−Miyaura Coupling Reaction. *J. Am. Chem. Soc.* **131,** 8262–8270 (2009).
16. Xu, C., Wang, X. & Zhu, J. Graphene−Metal Particle Nanocomposites. *J. Phys. Chem. C* **112,** 19841–19845 (2008).
17. Dong, Tao, Zhang, L., Zhang & Nelson, B. J. Nanorobotic Spot Welding: Controlled Metal Deposition with Attogram Precision from Copper-Filled Carbon Nanotubes. *Nano Lett.* **7,** 58–63 (2007).
18. Zou, R. *et al.* Melting of metallic electrodes and their flowing through a carbon nanotube channel within a device. *Adv. Mater. Deerfield Beach Fla* **25,** 2693–2699 (2013).
19. Král, P. & Wang, B. Material Drag Phenomena in Nanotubes. *Chem. Rev.* **113,** 3372–3390 (2013).
20. Regan, B. C., Aloni, S., Ritchie, R. O., Dahmen, U. & Zettl, A. Carbon nanotubes as nanoscale mass conveyors. *Nature* **428,** 924–927 (2004).
21. Suzuki, M. *et al.* Current-induced breakdown of carbon nanofibers. *J. Appl. Phys.* **101,** 114307 (2007).
22. Pierce, D. G. & Brusius, P. G. Electromigration: A review. *Microelectron. Reliab.* **37,** 1053–1072 (1997).
23. Lacerda de Orio, R. Electromigration Modeling and Simulation. at <http://www.iue.tuwien.ac.at/phd/orio/>

24. Sorbello, R. S. Theory of the direct force in electromigration. *Phys. Rev. B* **31,** 798–804 (1985).
25. Dekker, J. P., Lodder, A. & van Ek, J. Theory for the electromigration wind force in dilute alloys. *Phys. Rev. B* **56,** 12167–12177 (1997).
26. Svensson, K., Olin, H. & Olsson, E. Nanopipettes for Metal Transport. *Phys. Rev. Lett.* **93,** 145901 (2004).
27. Svensson, K., Jompol, Y., Olin, H. & Olsson, E. Compact design of a transmission electron microscope-scanning tunneling microscope holder with three-dimensional coarse motion. *Rev. Sci. Instrum.* **74,** 4945–4947 (2003).
28. Huang, J.-Y., Ding, F., Jiao, K. & Yakobson, B. I. Self-templated growth of carbon-nanotube walls at high temperatures. *Small Weinh. Bergstr. Ger.* **3,** 1735–1739 (2007).
29. La Torre, A. *et al.* Formation and characterization of carbon–metal nano-contacts. *Carbon* **77,** 906–911 (2014).
30. Baaziz, W. *et al.* Carbon nanotube channels selectively filled with monodispersed Fe3−xO4 nanoparticles. *J. Mater. Chem. A* **1,** 13853–13861 (2013).
31. Baaziz, W. *et al.* Few layer graphene decorated with homogeneous magnetic Fe3O4 nanoparticles with tunable covering densities. *J. Mater. Chem. A* **2,** 2690–2700 (2014).
32. Ren, B., Picardi, G. & Pettinger, B. Preparation of gold tips suitable for tip-enhanced Raman spectroscopy and light emission by electrochemical etching. *Rev. Sci. Instrum.* **75,** 837–841 (2004).

Chapter V

A 3D TEM insight in the hierarchical porosity of ZSM-5 and Y zeolites

5.1. State of the art

5.1.1. Post-synthesis induced mesoporosity in zeolitic materials

Zeolites are crystalline microporous materials possessing three-dimensional frameworks built out of corner sharing SiO_4 and AlO_4 tetrahedra (Fig. 5.1). The easy conversion of the surface properties of their uniform microporous network promotes zeolites as ideal materials for petrochemistry and fine-chemical processes[1,2]. Moreover, novel development in zeolite synthesis and post-synthesis treatments have broaden the zeolite application field to environmental protection, pollution control, green chemistry and biomass conversion[3]. Their application yield depends on both the size of the opening of the micropores (from 0.3 to 2 nm), the framework composition[4] (e.g. Si/Al ratio) and the surface chemistry. As their active sites are distributed in a confined space of molecular dimensions set by the size of the opening of the micropores, zeolites possess unique size and shape selectivity. However, the drawback in zeolite catalyzed reactions is that reactants and products may face severe diffusion limitations that often lead to pore blocking and catalyst deactivation by coke formation through secondary reaction of the intermediate products[5]. Consequently, various approaches have been designed to enhance molecular transport inside the microporous network of the zeolites. The two main methods involve i) the synthesis of nanosized zeolite crystals (instead of microcrystals), thus shortening the micropores (or diffusion) length[5–9] and ii) the introduction of a secondary network of larger pores connected to the native micropores (hierarchical zeolites) using acid or base leaching[10–12]. The second approach is preferred as in the first one the nanosized zeolites could suffer from increased coke deactivation.

The latter approach was introduced in the mid-1960s as researchers were trying to extend the application field of zeolitic materials[13,14]. As a function of the metal removed from the initial zeolite framework (Si or Al), the framework demetallation can be divided in three categories: dealumination, desilication and a combined etching of both alumina and silica network[15].

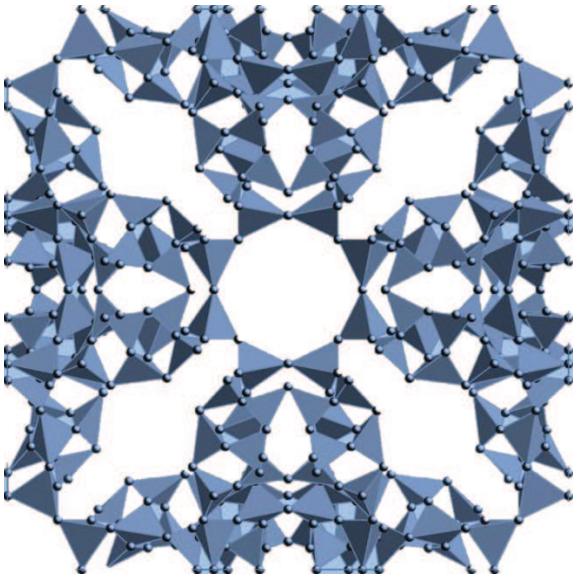

Figure 5.1. Schematic representation of a tetrahedral zeolite structure. Image adapted with approval from the website of Dr. Asel Sartbaeva's group: http://people.bath.ac.uk.

Dealumination can be induced by chemical treatments with tetraclorosilane or ammonium hexafluorosilicate or with high temperature steam[16]. Steaming, the most applied dealumination method, generates mesopores with a diameter between 10 and 20 nm, generally non-uniform in shape, although regular spherical and cylindrical shapes have been reported[11,17]. The density of the induced mesoporous network is a function of the steaming duration and the applied temperature[18]. As the mesopores are created by dissolving the alumina framework, the dealumination is limited to zeolites with high aluminum content[13]. Desilication is also extensively used for creating mesoporous networks in zeolites by leaching Si using OH^- radicals resulted from the dissolution of strong inorganic bases (mostly NaOH but also KOH and LiOH)[19]. Desilication can be applied to a wide range of zeolites with a Si/Al framework ranging from 4 to pure silica materials[12]. However, a high Al concentration prevents the Si dissolution, while a low one leads to an excessive removal of Si[20]. Therefore, introducing mesopores using desilication is optimal for zeolites with a Si/Al ratio between 25 and 50[21]. The mesoporous zeolites prepared by successive dealumination and desilication are affected by the substantial change in composition (Si/Al ratio) and by the deposition of extra-framework aluminum species in their pores and external surface. Therefore, a combination of dealumination and desilication treatments is required sometimes, in order to restore the properties (Si/Al ratio, acid sites, accessibility in the microporous network) of the modified zeolites[12].

5.1.2. New approach: simultaneous Si/Al demetallation by fluoride etching

The first study reporting the creation of a controlled secondary mesoporous network in zeolites by fluoride etching was conducted by V. Valtchev and co-workers[22]. In order to avoid the uncontrolled etching of the entire zeolite microcrystals, the samples were irradiated with a high-energy ^{238}U ion beam, creating thus amorphous areas within the zeolite crystals. Due to the higher etching rates of the amorphous regions in the HF solution compared with the crystalline areas, a selective and controlled etching was achieved without changing the initial Si/Al framework of the zeolite. However, the expensive intermediate step of ^{238}U ions bombardment makes this method not suitable for large scale production of hierarchical zeolites.

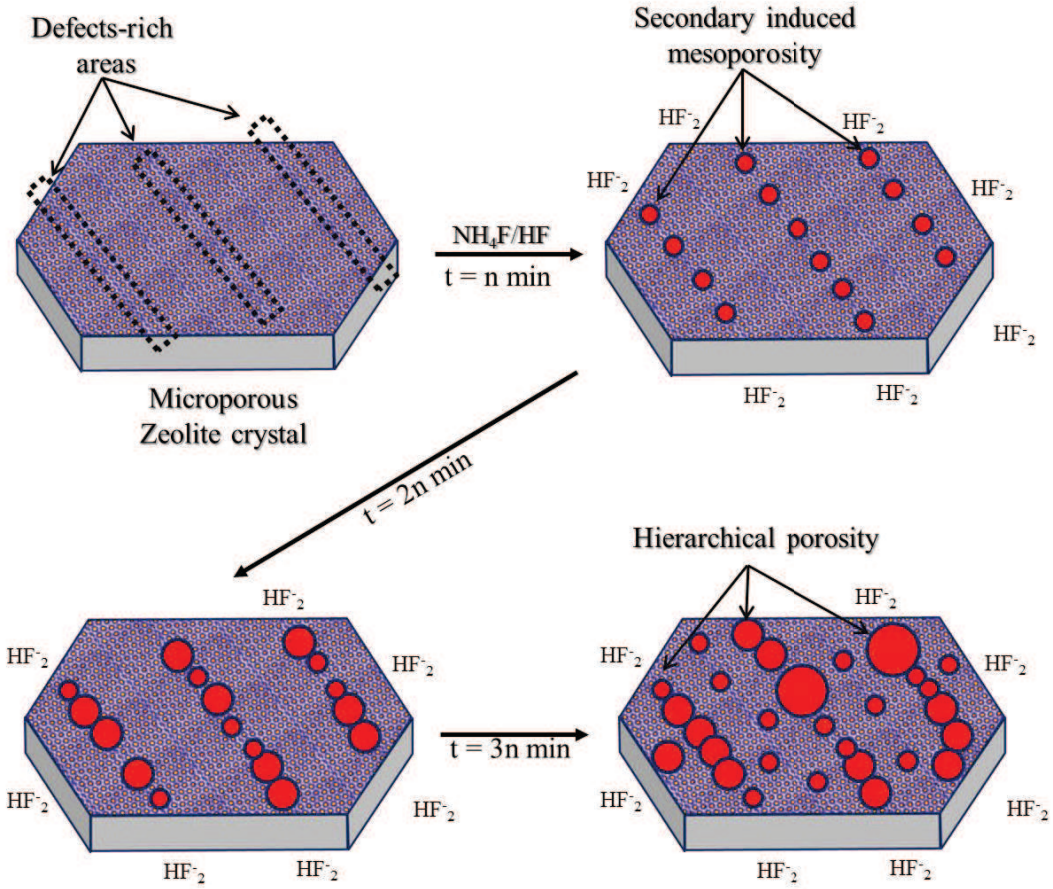

Figure 5.2. Schematic representation of the secondary porosity induced by fluoride etching on a zeolite crystal. The defect-rich areas are the first to be affected by the chemical treatment and for longer treatment times the etching spreads on other uniform areas.

Nevertheless, the advantages offered by the fluoride etching encouraged them to continue the research in this area and soon a new and less expensive method has been proposed[23]. Using a mixed NH_4F/HF solution, an indiscriminant Si/Al demetallation was obtained. The etching starts

from defect-rich sites, especially at the interface between individual crystals. The porosity of the new zeolites depends on both the severity of the fluoride etching (etching duration and solution composition) and on the properties of the parent zeolite. By fluoride etching, a controlled secondary porosity of large meso- and/or macropores can be induced in any zeolite type, irrespective of its framework composition[24,25]. A schematic representation of the evolution of the secondary porosity induced by fluoride etchings is shown in Fig. 5.2.

5.2. Hierarchical porosity induced by fluoride etching in ZSM-5 zeolites

Even from the beginning of the fluoride etching implementation, an important interest for inducing hierarchical porous networks in ZSM-5 zeolites was shown. ZSM-5 is one of the most important zeolite due to its various applications[26] like gas separation[27] or phenol production[28], but especially for its use in the petrochemical industry[1]. Its applications in petrochemistry include conversion of methanol into gasoline[29], interconversion of aromatic compounds[30] and separation of hydrocarbons from polar compounds (water and alcohols)[31]. Depending on the Si/Al ratio (from 12 to ∞), its properties can change from moderate hydrophilic to highly hydrophobic. ZSM-5 is a zeolite with high temperature (up to 1000 °C) and acid stability (pH 3)[32]. The microporous network is formed by a straight channel system with a free diameter of about 0.54–0.56 nm running parallel to [010] (b axis) and a sinusoidal channel system with the a diameter around 0.51x0.54 nm going parallel to the [100] axis (a axis)[31,33,34]. Both types of micropores are 10-member ring-opening and two schematic representations of their arrangement is shown in Fig. 5.3. This regular microporous network offers to ZSM-5 zeolites unequal shape selectivity,' but also induces strict diffusional limitations of large molecules to and from the active sites,[20] especially for bulky hydrocarbons[19]. Therefore, a secondary mesoporous network is required in order to facilitate the diffusion of molecules inside the zeolite's microcrystals and at the same time the elimination of the reaction products in the fluid mainstream, ensuring a low deactivation by coke formation.

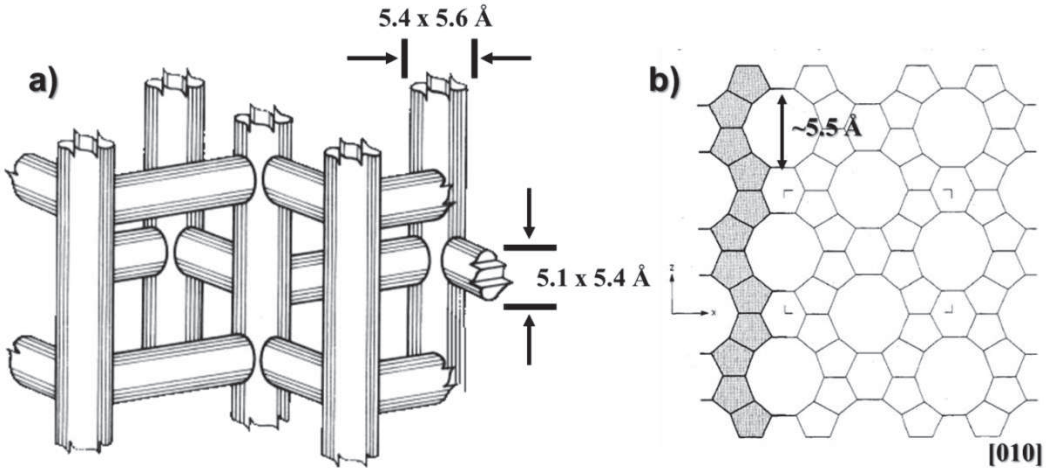

Figure 5.3. a) Schematic representation of the 3D arrangement of the micropores within a ZSM-5 zeolite. Adapted from www.chemgapedia.de b) Projection of the ZSM-5 framework along [010]. Highlighted in gray are the secondary building units (SBU). Adapted from reference [31].

In this general context, we describe in the first part of the chapter an electron tomography (ET) investigation of the secondary porosity induced in ZSM-5 zeolites (Si/Al = 19) using fluoride etching with a novel approach based only on an aqueous NH_4F solution (HF free). This study deals with the investigation of physical parameters such as the spatial distribution of the mesopores inside the zeolite grains, the size and the volume distribution of the pore, the overall porosity as well as the connectivity of the mesoporous network. The information regarding the properties of the secondary porous network extracted from 3D data are correlated with the ones offered by other characterization techniques such as N_2 sorption.

5.2.1. Methods

5.2.1.1. Fluoride etching procedure of the ZSM-5 microcrystals

A micrometer-sized commercial ZSM-5 sample (Süd-Chemie, NH_4-form) was used as a parent to prepare hierarchical materials. Fluoride media etching were carried out in NH_4F aqueous solutions in the following way: 10 g of the parent ZSM-5 zeolite was dispersed in 200 mL of 40 wt.% NH_4F aqueous solution under stirring and ultrasonication. Intermediate samples were collected at 15 min intervals. All the intermediate and final products were thoroughly washed using distilled water after the fluoride medium treatment. The samples treated by NH_4F

aqueous solution for 15, 30, and 60 min were denoted F-ZSM-5-15 min, F-ZSM-5-30 min, and F-ZSM-5-60 min, respectively. The synthesis was carried out by Dr. Qin Zhengxing and Dr. Valentin Valtchev in the Laboratory of Catalysis and Spectrochemistry, Caen, France.

Short description of the NH_4F etching mechanism

An ammonium fluoride solution presents both a weak acid and a weak basic character due to a double hydrolysis reaction in water. This results in the presence of a small amount of HF in equilibrium with other fluoride ions (F^-, HF^{2-}). During the dual hydrolysis reaction, NH_3 is released, changing the pH of the initial solution. The right shift of the dual hydrolysis reaction of NH_4F when the HF and HF^{2-} are consumed during the etching allows maintaining a constant concentration for these reactive fluoride species. In this way, the chemical etching of the zeolite framework is highly mild and controllable, since the HF and HF^{2-} are produced "in situ" in a highly controllable environment. The degree of zeolite dissolution can be finely tuned through the adjustment of parameters affecting the hydrolysis reactions.

5.2.1.2. Electron tomography

Sample preparation for tomography acquisition

Electron tomography analysis was performed on three of the hierarchical porous ZSM-5 samples: F-ZSM-5-15 min, F-ZSM-5-30 min, and F-ZSM-5-60 min. The samples were prepared by dispersing the zeolite powders in pure ethanol, and the dispersions were sonicated at low power for 2 minutes. Through sonication, small zeolite grains were detached from the microsized porous crystals and these grains, with a lateral size ranging from 100 nm to 400 nm, are the objects of interest for tomography. After sonication, one drop of solution was dispersed on holey carbon membrane, covering a 300 mesh Cu TEM grid. The concentration of the solution was adjusted in order to obtain the right amount of sample on the carbon membrane surface as large zeolite crystals would overlap the object of interest at high tilting angles. For assuring a good tilt series alignment, the carbon membranes were decorated with Au nanoparticles 5-7 nm in diameter prior to the sample deposition. The Au nanoparticles were used in the fiducial-based alignment procedure performed in IMOD software. The Au NPs are added on the membrane before the sample, in order to avoid the deposition of some NPs on the surface of the zeolite

grains. The tilt series were acquired in bright-field TEM using a JEOL 2100F microscope with a Gatan UltraScan CCD camera (2048x2048 pixels).

Choice of the acquisition mode

Under continuous electron beam irradiation, hierarchical porous zeolites can undergo severe framework shrinkage. The sample shrinkage depends on the exposure duration, acceleration voltage, current density on the sample and porosity of the zeolite grains. Our experiments were performed at 200 kV acceleration voltages and a constant current emission of the electron gun (160μA). Therefore, in order to keep the morphology of the samples unchanged, we had to carefully adjust two parameters: the exposure duration and the current density at the specimen level. For a conventional tilt series acquisition the total exposure time, including focus and tracking calculations, image acquisition plus the alignment of the specimen's eucentric height position, is about 2 hours. The electron dose in a standard TEM investigation of zeolitic materials is ~70 $e^-/Å^2$ (40 kx magnification). In such conditions, the F-ZSM-5-15 min sample underwent a ~5% shrinkage (measured in X and Y directions as the difference between the size of the initial and of the final object) while the F-ZSM-5-60 min shrank by more than 10%. Therefore, a method for acquiring tilt series which offers a significant reduction of the exposure time was used. This method is based on the Advanced Tomography plug-in implemented in the Gatan™ Digital Micrograph[35]. It offers the possibility of recalibrating the image focus and the sample tracking, performed after every tilting step, on a region far from the analyzed object (but along the tilt axis), and consequently considerably reducing the total exposure time to ~10 min. Using this method, tilt series with a good signal-to-noise ratio were acquired for the samples F-ZSM-5-15 min and -30 min with a sample shrinkage smaller than 0.5%. However, the sample F-ZSM-5-60 min was still suffering from significant beam damage. In order to preserve the sample's morphology, the conventional acquisition method (focus and tracking calculation on the sample) was adapted as follows: for each 2 images acquired (~30 s total exposition time, including focus and tracking calculation), the acquisition was paused for 1 minute. In this way, the local heating caused by the electron beam irradiation was evacuated and during the pausing period the temperature was brought back to the room temperature through heat sink in the mechanical support, therefore decreasing the dehydration of the zeolite samples. With this semi-manual acquisition method the total exposure time is the same as for conventional tilt series acquisitions

(2 h); however, due to the one-minute "resting time" after each two images, the total acquisition time was around 4 h.

Tilt series parameters

The size of the tilt series images was 2048x2048 pixels and the exposure time for an image was 1 s. The magnification depended on the lateral size of the grains, and normally lay between 40 kx and 60 kx. Therefore, the pixel size for an image varies from 0.25 to 0.16 nm. One should highlight that with a 50 kx magnification, a phase-like contrast created by the microporous network of the ZSM-5 zeolite becomes visible for certain tilt angles. Later in this chapter, we will detail the contribution of this type of contrast in our reconstructions. The minimum tilt angle for which we considered a series to be acceptable for tomography was ± 65°. Note that for a smaller angular range, the quality of the reconstructions is considerably affected by the missing wedge. The maximum tilting angle set by the design of the sample holder and the pole piece of the microscope was around ±74°. The tilt step that defines the number of images in a series was adjusted for each object as a function of the object thickness and the maximum tilt angle. The exact conditions for each tilt series is given in the Results section.

Tomogram reconstructions: SIRT

The tilt series were aligned using the Au NPs as fiducial markers in IMOD software[36]. The number of fiducial points for an alignment ranged from 10 to 15. For the reconstruction of the zeolite volumes, a Simultaneous Iterative Reconstruction Technique (SIRT) was used. The SIRT algorithm was implemented in a fast software running on multicore computers, Tomo3D[37]. The size of the TEM projections used for the reconstruction was 2kx2k pixels and the voxel size of the tomograms was set by the pixel size of the input images.

Tomogram reconstructions: Equally Sloped Tomography

Equally sloped tomography (EST) was developed in the group of Prof. Jianwei Miao at the University of California Los Angeles[38,39]. Unlike conventional tomography techniques, which require an interpolation step when changing from the polar coordinates of the TEM projections to the object's Cartesian coordinates; when an equal slope increment is used, a direct shift between the two set of coordinates is available through a fast Fourier transform, pseudopolar FFT (PPFFT). In this way, EST is reducing the reconstruction artifacts affecting the conventional

tomography techniques. From a practical point of view, EST requires the acquisition of a tilt series with an equal slope increment. Moreover, the number of initial projections required in EST is smaller than for other reconstruction algorithms, significantly reducing the irradiation duration. For EST, a tilt series of the F-ZSM-5-15 min sample was acquired at high magnification (80 kx) using the special tilting algorithms. The specimen tilting was performed manually using the digital control of the goniometer having a precision of ±0.1°. The series contained 62 TEM images.

3D model generation and quantitative analysis

Beside general observations regarding the morphological properties of the hierarchical zeolites, our investigation focuses on the quantitative interpretation of the tomography data. A quantitative analysis requires a 3D background-free model of the investigated object. The 3D models were created using the segmentation capabilities of the Slicer 3D free software. The exact information for each 3D model will be given in the Results section. To extract the information regarding the porosity of the zeolites, pore size, volume distribution and the connectivity of the pores, a separate model was created for the pores.

The 3D model of the mesopores network was created starting with the binary label of the zeolite body obtained in Slicer 3D. The first step is to use the FillHoles function. This automatically fills all the isolated pores from the zeolite label with material-based label (255 in 8-bit data type). The pores connected with the outer surface of the pores have to be closed manually by redrawing the zeolite external edges. As we will see later in this chapter, some samples required an additional step in order to close the porous network in an artificial solid shell. After the whole porous network is closed, the compact zeolite body is obtained. From this compact label volume, the initial porous label is subtracted, creating thus the label volume of the porous network alone. This label is then computed in the Slicer 3D for obtaining the 3D model. For the quantification of the pore size distribution, a 3D Object Counter plugin was used.

Other investigation techniques: *Nitrogen sorption*

Nitrogen adsorptions were performed with a Micromeritics ASAP 2020 automated gas adsorption analyzer. Prior to analysis, the samples were outgassed at 373 K for 1 h and 573 K for 10 h. Specific surface areas were determined from the BET equation. The total volume was given

by the nitrogen adsorbed volume at P/P0 = 0.99. The *t*-plot method was used to distinguish the micropores from the mesopores in the samples.

5.2.2. Classical TEM characterization

A series of TEM images of the parent zeolite microcrystal (P_ZSM-5) and of the hierarchical porous ones, obtained after the chemical treatment in ammonium fluoride, is presented in Fig. 5.4. One can easily observe the morphologic differences between the different zeolite crystals, starting with the non-porous aspect of the parent zeolite and followed by the gradually increasing porosity of the fluoride-etched samples.

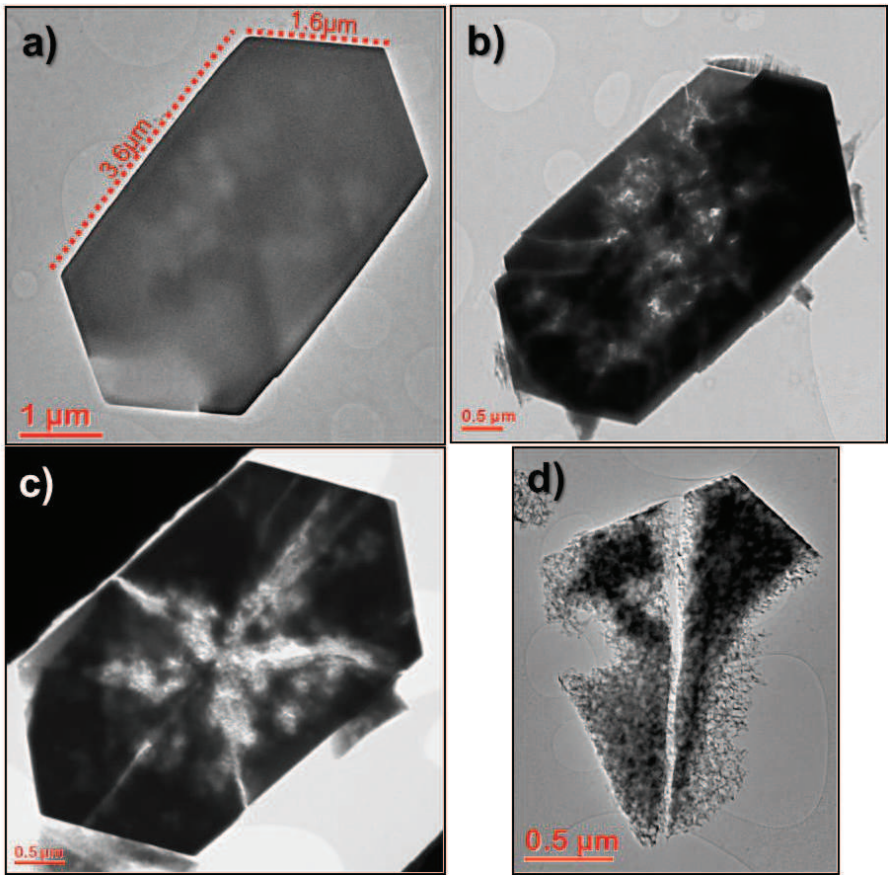

Figure 5.4. TEM images of the parent zeolite microcrystal (a) and of the hierarchical zeolite after 15 min (b), 30 min (c) and 60 min (d) of fluoride etching.

The hierarchical porosity becomes clearly visible for the F-ZSM-5-15 min microcrystals. It can be assigned to the bright areas visible in their centers and shows that the chemical etching removed the Si/Al network from one side of the crystals to the other. Fig. 5.5a shows a TEM image that characterizes the mesopores network on the microcrystal edge. Well-dispersed

mesopores predominate, round in shape and with a mean diameter of about 13 nm. The microcrystal becomes highly fragmented after 30 minutes of etching as shown in Fig. 5.4c and the density of the mesopores significantly increases compared to the 15 min sample (Fig. 5.5b). Due to the highly porous aspect, measuring the pore size from the TEM projections alone becomes a difficult task. Moreover, assigning a defined pore shape is also challenging as some of the walls between pores are completely etched, leading to the creation of a well-connected mesoporous network. After 60 minutes of etching, the morphology of the zeolite microcrystals is entirely modified to a connected porous network (Fig. 5.4d). The high porosity (foam-like aspect) of the F-ZSM-5-60 min sample is clearly shown in Figure 5.5c.

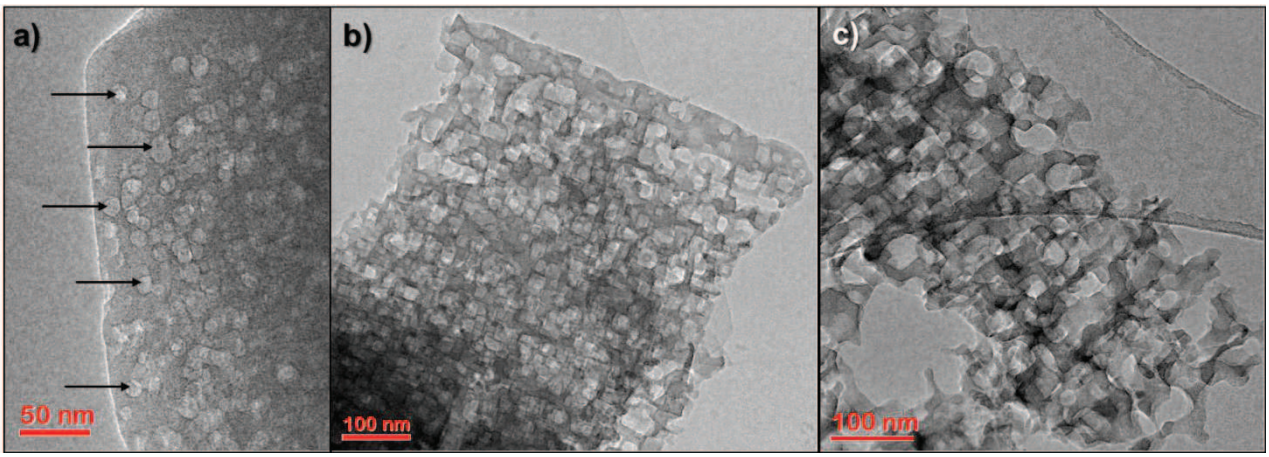

Figure 5.5. TEM images showing the arrangement of the fluoride-induced secondary porosity: a) F-ZSM-5-15 min (black arrows indicate the position of the mesopores), b) F-ZSM-5-30 min and c) F-ZSM-5-60 min.

Although the conventional TEM analyses reveal some general aspects related to the morphology of the samples, i.e. apparent shape and spatial distribution of the pores, pore size (for system in which pores do not overlap), important properties of the porous network remain hidden due to the fact that TEM images represent only 2D projections of 3D objects. Electron tomography is the best tool for extracting a complete characterization of the hierarchical zeolites at the nanometer scale. The information reveled by the ET includes: the 3D shape of the pores (inclusive for the dense porous network), pore size (including that the Z axis) and volume distributions, the exact location of the pores inside the zeolite grain and the quantification of the final morphology in terms of porosity and connectivity.

5.2.3. Electron Tomography

Hierarchical zeolite after 15 minutes of chemical etching (F-ZSM-5-15 min)

For the 15 min chemically treated sample, two tilt series were recorded. The first one was acquired with a 40kx magnification (pixel area of 0.25^2 nm^2) and contained a number of 87 images. A TEM projection of the selected zeolite grain is shown in Fig. 5.6a. A *xy* slice (longitudinal slice/normal plane with respect to the electron beam direction) through the center of the grain is presented in Figure 5.6b. Analyzing the zeolite's reconstruction in plane *xy* slice by slice, one can identify pores with apparent square and round shapes and diameters ranging from 3.5 to 20 nm. Studying the tomogram in the *yz* direction (transversal slices), one can observe the shape of some of the pores appearing slightly changed to a cylindrical-like one (Fig. 5.7).

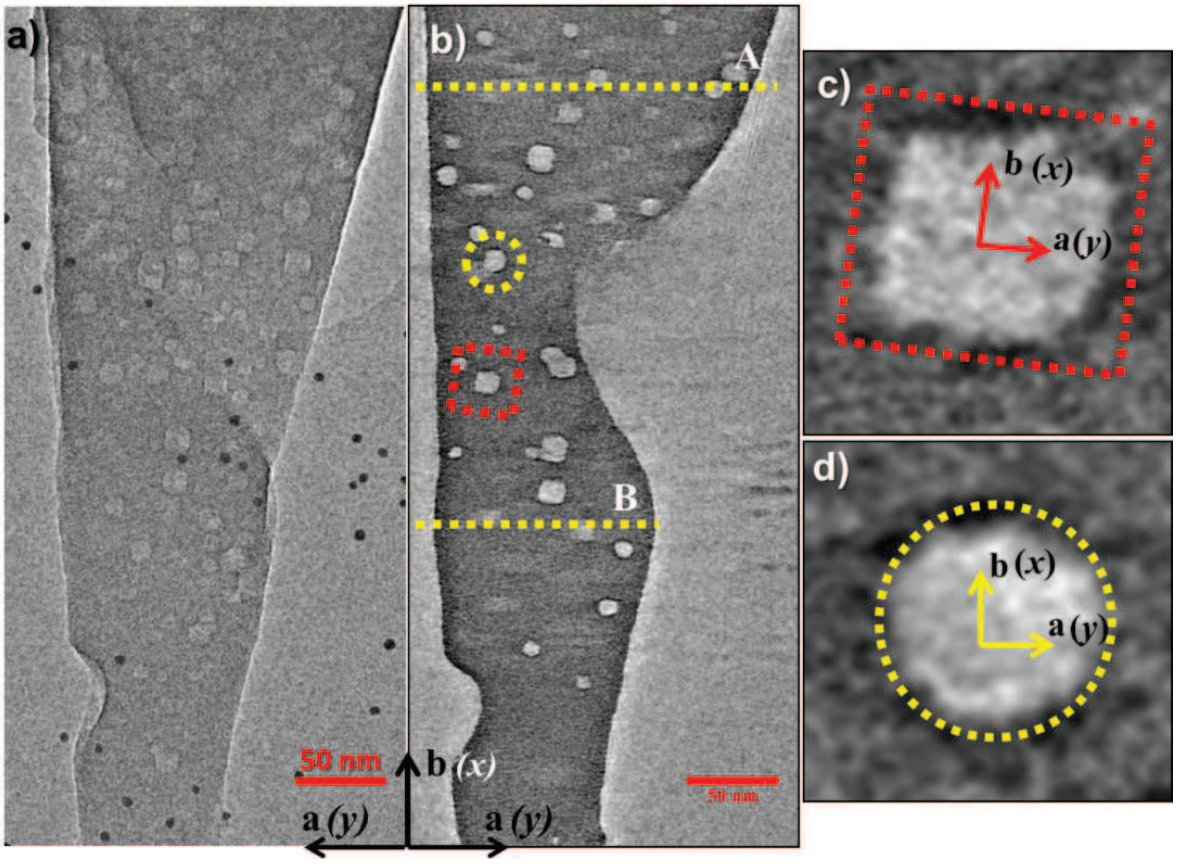

Figure 5.6 a) TEM projection (at 0°) of the zeolite grain (F-ZSM-5-15 min) chosen for electron tomography. b) *Xy* slice through the center of the tomogram. The yellow lines show the position of the *yz* slices presented in Figure 5.7. c) and d) Cropped regions of the *xy* slice showing the square- and round-shaped pores. The a and b axes correspond to the *y* and *x* direction in the present tomography.

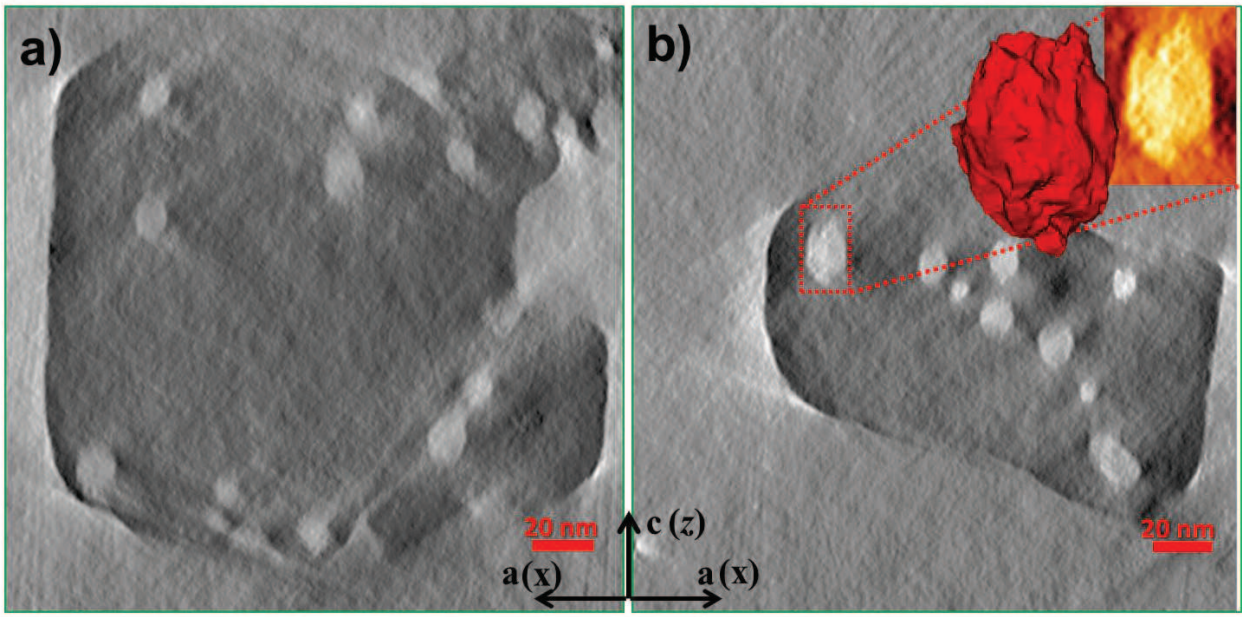

Figure 5.7. ***Xz*** **(transversal) slices through the reconstructed volume taken at the position highlighted in Figure 5.6b (F-ZSM-5-15 min). The insets show the 3D representation of the pore highlighted in red and the cropped image of the same area. The c axis is coincident with the** ***z*** **axis in the present tomography.**

The shape of the mesopores is an important parameter that can provide information on the mechanism at the origin of the zeolite etching. In the *xy* direction (Fig. 5.6b), pores appear either cubic (Fig. 5.6c) or round (Fig. 5.6d) in shape. Both shapes are "homogeneous" ones showing that both directions are etched with the same velocity. HR-TEM analysis shows that, for the present object, the **a** axis is oriented along the *y* direction, **b** along the *x* direction and **c** along the *z* direction. Therefore, the etching of the zeolite framework seems to propagate uniformly along the **a** and **b** axes. Analyzing the tomogram in the transversal directions (see slices in 5.7a-b), one can identify that the walls of the pores stretching in the *z* direction (along the **c** axis) can be either straight walls of cuboid mesopores or curved walls defining spherical mesopores. One important observation made from the cross-sectional analysis is that most of the cuboid pores present V-shape ends (Fig. 5.7b-insets). In these cases, one of the sides of the pore, which is perpendicular to the **c** axis, is always having a more prominent V-shape than the other. One can assume that the prominent V-shape side might be the propagation front of the etching inside the zeolite crystal. The size of the pores measured along the **c** axis is also increasing compared with the ones measured along the **a** and **b** axes. The ratio between the size of the *z*-oriented walls and the one

measured along *x* and *y* (considered as equal) varies between 1.3 and 1.5. This "elongation" of the pores along the **c** axis shows a higher yield of the etching reaction in this direction.

One important observation regarding the distribution of the pores inside the grain is that, as can be observed in Fig. 5.7a, in thick regions of the grain, the pores are concentrated close to the external surface. However, in thinner ones, the pores seem to be distributed inside the grain core as well. This observation is very important and is related to the mechanism of HF^{2-} ion diffusion inside the zeolite grains, and will be detailed later in this chapter.

The quantification of the induced porosity requires the reconstruction, the creation of the 3D model of the object. The zeolite body model as well as the pore model (see Experimental Section) were created using the initial reconstructed volume as an input file. Fig. 5.8 shows several views of the combined 3D models of the zeolite body (transparent blue) and pores (red) taken in different orientations. These 3D representations make it easier to observe the distribution of the pores inside the zeolite grain. For the present sample, one can observe that while most of the mesopores were created close to the external surface of the grain, few of them appear directly connected with the surface. The demetallation reaction responsible for the pore creation requires a good transport of both HF^{2-} ions (the etching agent) inside the zeolite crystals as well as the elimination of the metal fluoride reaction products. It is generally accepted that for the creation of the pores inside the zeolite crystal, the reaction agents and the residual products require a pore size larger than ~0.55nm, which is the diameter of the ZSM-5 micropores. However, carefully analyzing the initial volume of the closed pores inside the crystal, we did not found any "cracks" or small mesopores which connect the closed pore with the external surface or another pore connected to the outer surface. For this propose, we performed another acquisition at a higher magnification in order to increase the spatial resolution of the obtained tomogram and possibly observe these "cracks" or connectivities in the body of the zeolite. The results will be discussed later.

Analyzing the zeolite body and the mesopores 3D models separately, we obtained the exact numerical values of their volume: 2,948,756 nm^3 for the solid body of the zeolite and 90,300 nm^3 for the mesopores. Due to the presence of small artifacts in the pore, we have chosen for quantification only pores larger than the smallest pore visible in the initial tomogram. In this case the smallest pore identified was about 3.5 nm in diameter. The porosity was defined as the

ratio between the volume of the mesopores (V_m) and the bulk volume of the zeolite grain (V_b). From these values we have extracted an overall porosity of about 3%. Also, using the data set extracted from the 3D pores model, we were able to reconstruct the secondary pore size distribution. The data set used contains information regarding the volume and the surface of each individual pore from the secondary network. Therefore, assuming a specific pore shape, one can extract the size of each pore.

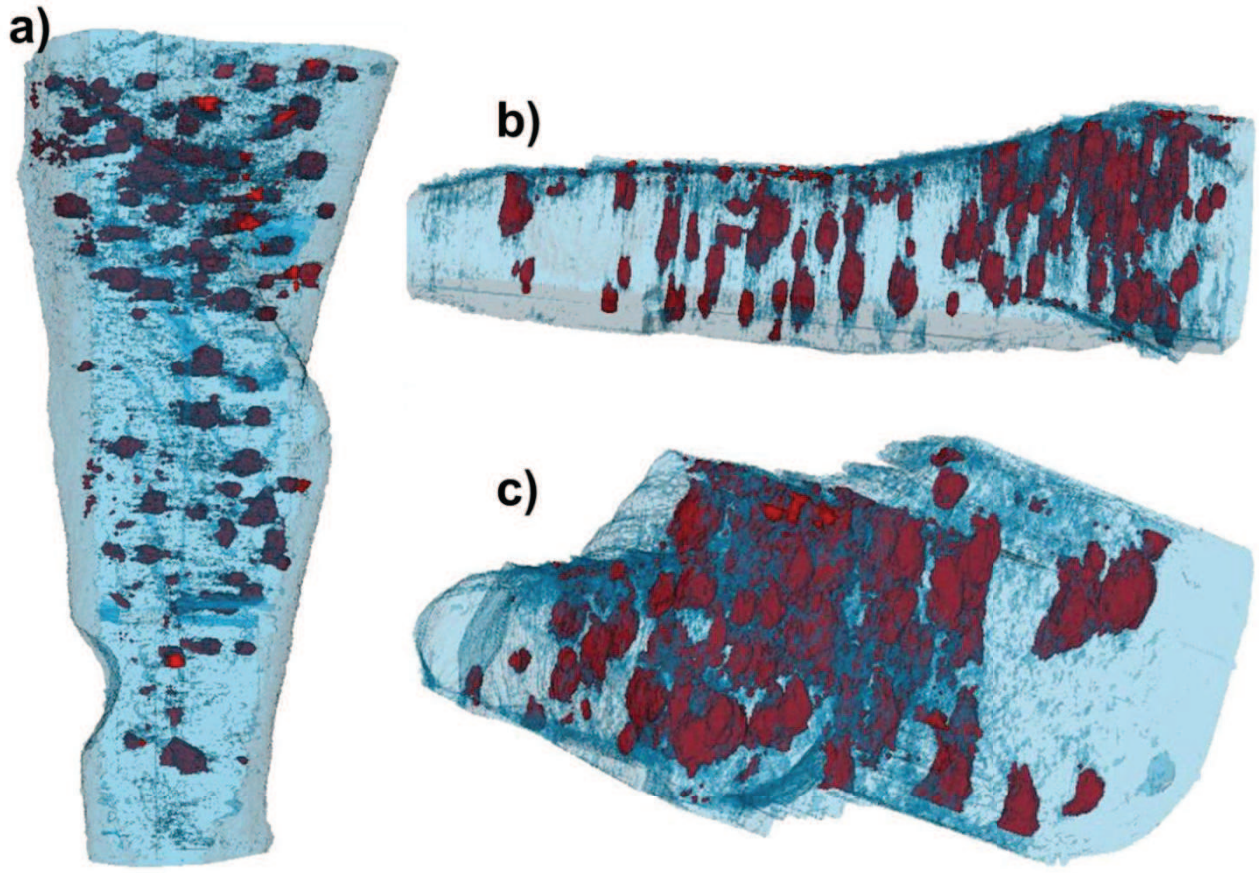

Figure 5.8. Snapshots of the zeolite 3D model (zeolite body in transparent blue, pores in red) acquired at different spatial orientations: *xy* - a), *xz* - b) *yz* - c).

The most appropriate pore shape that can be assumed is the spherical one. However, it can be easily observed that the shape of the pores is far from a perfect sphere (see the above discussion about the cuboid pores); however, it is the best option for a direct estimation of the diameter of the pores. Fig. 5.9 shows two types of pore size distributions: in a) the distribution is shown as a function of the pores appearance frequency, while b) takes into consideration the total

volume of the pores within a given size interval. One should highlight that the largest pore identified by scanning the initial reconstructed volume had a diameter of around 20 nm. However, the size distributions shown in Fig. 5.9 allow us to identify pores between 4 and 60 nm in diameter. This is due to the fact that some of the pores, especially in the thicker area of the zeolite grain, are interconnected. Therefore, the program used to extract the porosity data set is considering this cumulated volume as an individual pore. In this case, our spherical shape assumption becomes even more approximate. Nevertheless, important information can be extracted from these distributions. One relates to their frequency of appearance. Figure 5.9a shows that around 50% of the total numbers of pores are small mesopores between 4 nm and 8 nm in diameter. However, the distribution presented in Fig. 5.9b shows that these pores have a small contribution to the total porous volume. Moreover, all pores between 4 nm and 14 nm contribute with only ~3% to the total porosity and the pores between 14 nm to 20 nm have a ~7% contribution. The rest of the porosity is given by pores which apparently are larger than 20 nm. As discuss above, these pores are not individual closed pores, but a connected network formed by pores in the size interval between 4 to 20 nm.

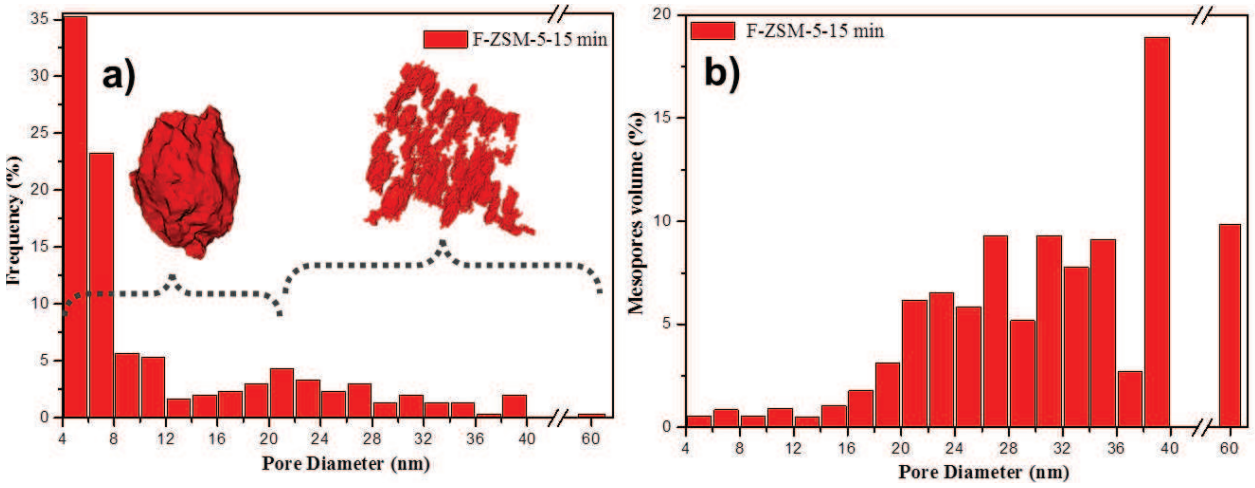

Figure 5.9. a) Pore size distribution of the F-ZSM-5-15 min zeolite as a function of their frequency of appearance in the mesopores network. b) Pore size distribution as a function of their cumulated volume.

Hierarchical zeolite after 30 minutes of chemical etching (F-ZSM-5-30 min)

As can be observed already from the TEM images (see Figs 5.4c and 5.5b), the hierarchical ZSM-5 zeolite becomes a highly porous structure after 30 min of fluoride etching. Electron Tomography is used once again for revealing the 3D properties of these structures. Fig. 5.10 shows the TEM projection of the selected zeolite grain.

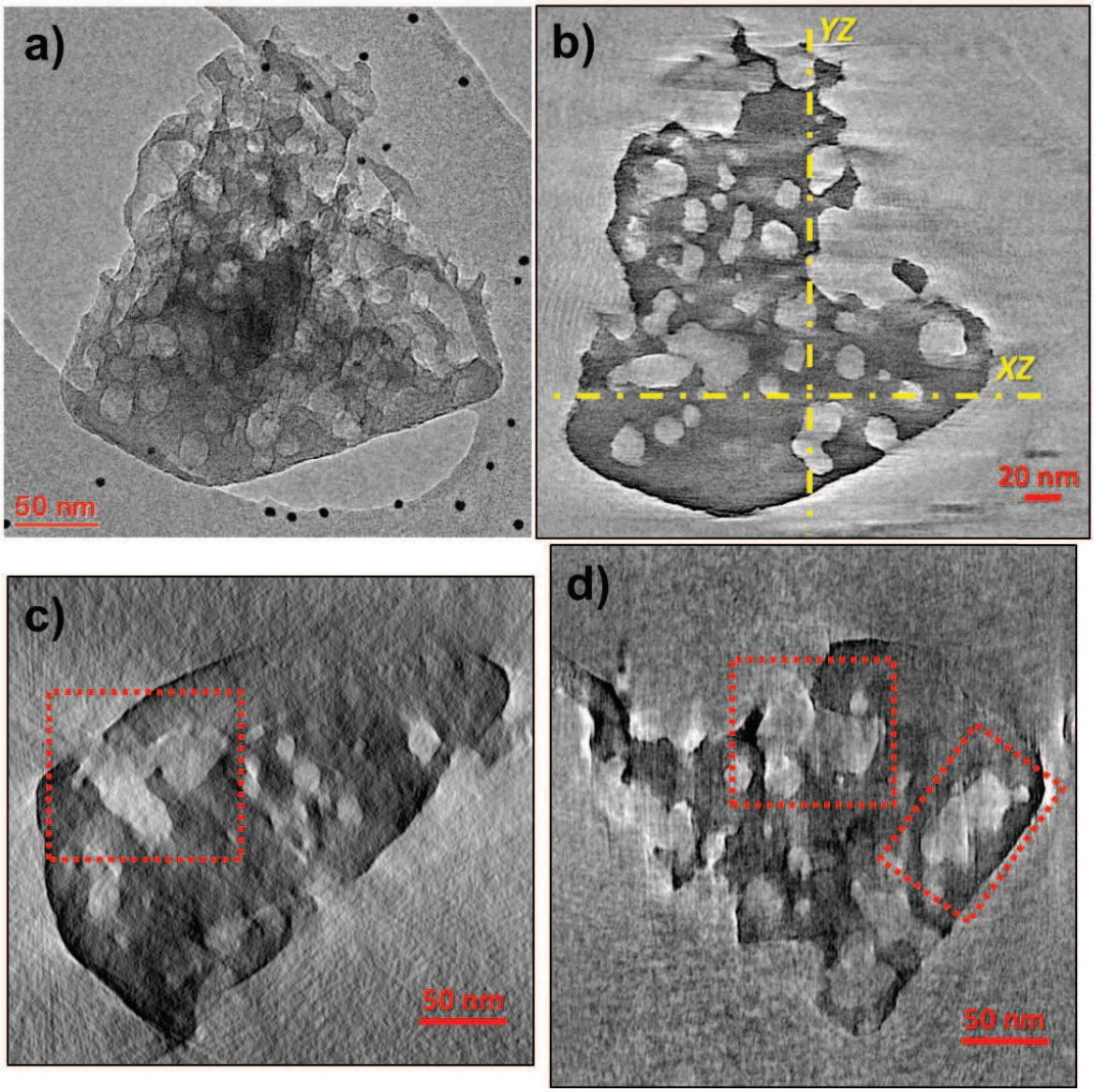

Figure 5.10. a) TEM projection (at 0°) of the zeolite grain selected for ET (F-ZSM-5-30 min). b) *xy* slice through the center of the reconstructed volume. The yellow lines highlight the cross-sectional directions presented in c) and d). c) and d) Slices in *xz* and *yz* directions, respectively, through the reconstructed volume at the positions highlighted in b).

The inhomogeneity of the secondary porosity distribution observable from the TEM image is directly visualized by ET. Fig. 5.10b shows a longitudinal slice through the reconstructed volume of the selected grain. It shows pores with both round (separate) and non-uniform connected shapes. Analyzing the tomogram slice by slice, we were able to see that for most of the connected pores the walls between the initial ones were completely removed, resulting in large-volume non-uniform mesoporous cages. This aspect is clearly evidenced by the cross-sectional slices (*xz* and *yz*) presented in Fig. 5.10c-d, where the area highlighted in red shows these large mesoporous cages. This represents a major difference between the present sample and the 15 min etched zeolite grains, as for the latter the connectivity between the mesoporous is realized only by partially breaking the wall between two or three individual pores. Furthermore, a large part of these mesoporous cages connects directly with the external surface of the zeolite grain.

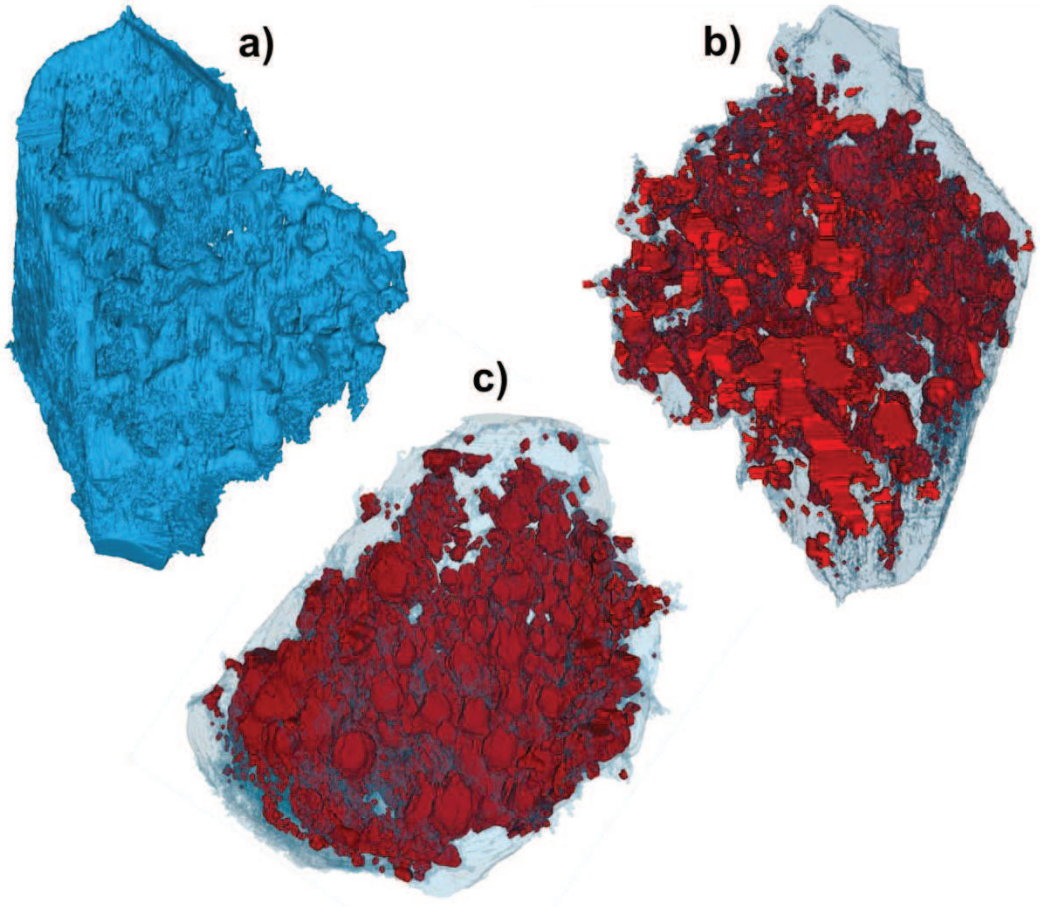

Figure 5.11. a) Snapshot of the zeolite 3D model (F-ZSM-5-30 min). b) and c) Snapshots of the zeolite body (transparent blue) and pores (red) 3D model.

A snapshot of the 3D representation of the zeolite body is presented in Fig. 5.11a. The apparent roughness of the surface is created by the high number of pores which are directly connected to the external surface. Fig. 5.11b and c present snapshots of the combined models of both the zeolite body (transparent blue) and the mesoporous network (red). They show a very dense and continuous porous network with some individual pores appearing spherical in shape. The common characteristic of the F-ZSM-5-30 min zeolite grains is the loss of the external smooth surface, replaced by a rough one. At this point, one should highlight the difficulties encountered during the creation of the 3D model of the mesopores. As most of the pores are interconnected and also connected to the external surface, the automatic procedure for creating the label of the pores is limited to the "closed" pores only. Therefore, for the connected pores a combined manual and computational pore "closing" procedure was required. In order to obtain the most accurate possible reconstruction of the pore network, the procedure had to be carefully adjusted.

The pore size distributions as extracted from the data sets of these two models are presented in Fig. 5.12. As the smallest pore identified in the tomogram was around 3 nm in diameter we started the quantification from this value, the rest of the small pores being labeled as impossible to model. Analyzing the volumes of each pore, we identified one "super" cage with a volume representing 90% of the total empty space of the grain ($V_m = 1185 \cdot 10^3$ nm^3). This "super" cage represents in fact the connected mesoporous network. It shows that the majority of the pores are well connected, forming a continuous system with direct access to the outer surface of the grain. Therefore, the pore size distributions presented in Fig. 5.12 represent only ~10% of the individual, unconnected pores and their interpretation becomes difficult. Nevertheless, as for the sample F-ZSM-5-15 min, the majority of individual pores are made of small mesopores ranging between 3 and 7 nm, while their contribution to the total volume space is around 10%. However, more than 55% of the total porosity is created by mesopores ranging between 15 and 24 nm in diameter. The overall porosity of the F-ZSM-5-30 min was found to be around 22%, which is significantly higher than that of the 15 min etched sample.

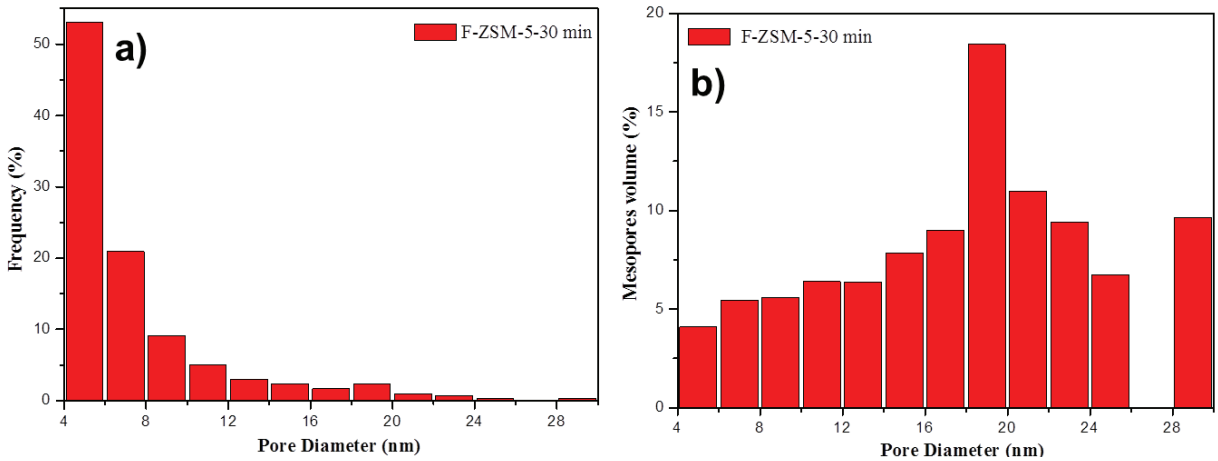

Figure 5.12. a) Pore size distribution of the F-ZSM-5-30 min zeolite as a function of their frequency of appearance in the mesopores network. b) Pore size distribution as a function of their cumulated volume.

Hierarchical zeolite after 60 minutes of chemical etching (F-ZSM-5-60 min)

As explained in the Experimental section, the zeolite samples chemical treated in fluoride solution for 60 min required, besides a manual-based acquisition mode, a low electron dose (~30% of the normal dose for TEM observations). This increases the noise in the TEM projection and consequently in the reconstructed tomograms. The pixel area of the initial projections was 0.25^2 nm^2 and the tilt series contained 87 images.

The TEM projection of the zeolite grain selected for tomography (Fig. 5.13a) shows a highly porous structure, which makes it very difficult to even produce the most basic description of the zeolite porous network. Fig. 5.13b shows a *xy* slice through the reconstructed volume of the selected grain. It shows a structure containing two types of mesopores: non-uniform large mesopores (> 50 nm) and small mesopores (5-25 nm). The non-uniform pores are formed by the removing of the walls between individual pores during the etching process, creating a completely connected meso- and macroporous network. The cross-sectional slices presented in Figs. 5.13a-b unambiguously show the "foam"-like morphology of these zeolite samples. The formation of the small mesopores appearing in some of the walls of the grain had most probably started in the last part of the etching treatment. However, the analysis of the 3D models has shown that the vast majority of these pores are also connected to the large mesoporous network.

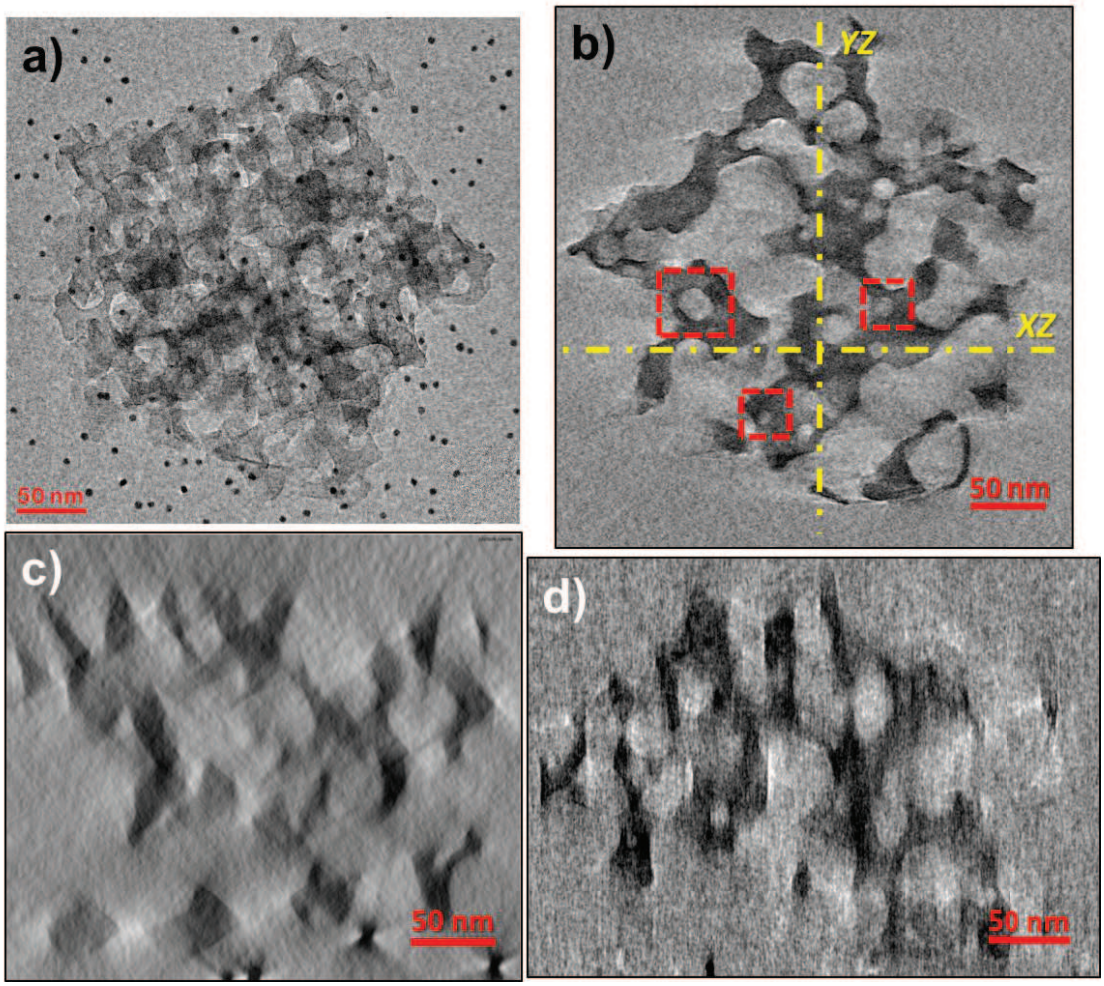

Figure 5.13. a) TEM projection (at 0°) of the zeolite grain selected for ET (F-ZSM-5-60 min). b) *xy* slice through the center of the reconstructed volume. The yellow lines highlight the cross-sectional directions presented in c) and d). The red squares highlight the position of the small intra-wall mesopores. c) and d) Slices in *xz* and *yz* directions, respectively, through the reconstructed volume at the positions highlighted in b).

The image of the resulting 3D model (Fig. 5.14a) shows once again the high degree of porosity for the 1h-etched zeolites. However, extracting the pore 3D model is a difficult task for this kind of samples. The major obstacle is represented by the direct access of all the pores to the outer surface of the grain. Using a similar procedure as for the previous sample leads to a poor representation of the pores, as the one presented in Fig. 5.14b (pores in red). The obtained 3D model directly shows the failure of this procedure for this porous grain in particular. The porosity values obtained from this 3D model data set of the pore are inconclusive. However, just by comparing the reconstructed volume of the present sample to the ones of the previous 15 min

and 30 min etched zeolites, one can unambiguously state that the porosity of the F-ZSM-5-60 min hierarchical zeolite is significantly larger.

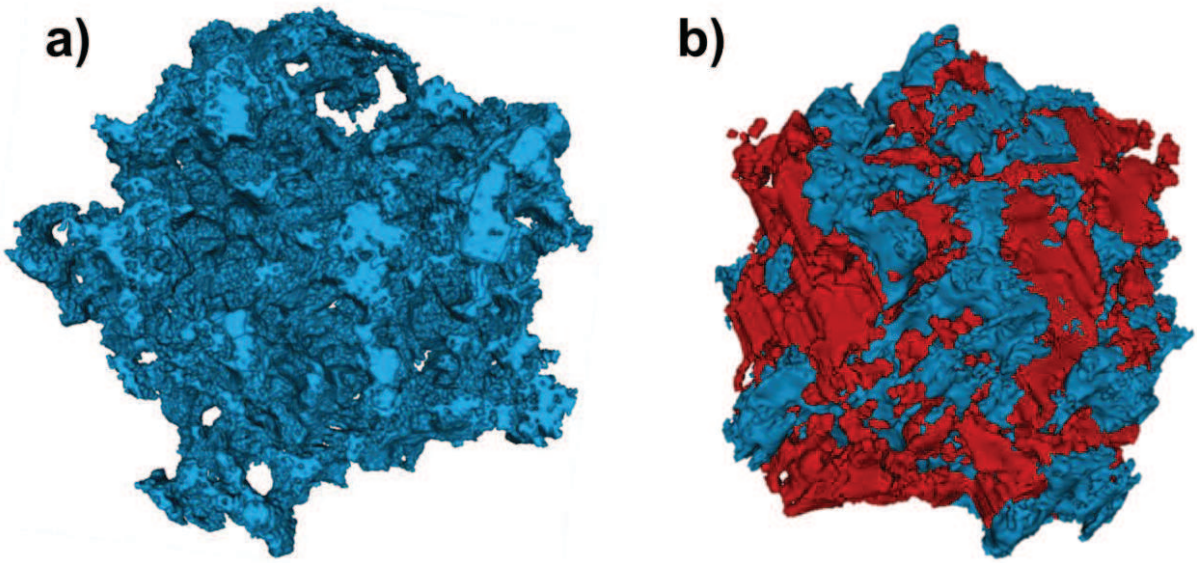

Figure 5.14. a) Snapshot of the zeolite body 3D model (F-ZSM-5-60 min). b) Combined 3D models of zeolite body (blue) and pores (red).

As a quantitative evaluation of the porosity was essential for our study, we acquired another tilt series at lower magnification (40kx), allowing us to increase the signal to noise ratio of the recorded projections. Fig. 5.15a shows a longitudinal slice through the tomogram of the selected grain. As for the previous zeolite grain, one can observe the "foaming" aspect indicating a highly porous morphology. Fig. 5.15b shows an image of the *xy* orientated 3D model of the zeolite body. Fig. 5.15c presents the combined 3D models of both zeolite body (blue) and pores (red). Highlighted by red squares are those external pores excluded from the model and therefore from quantification. The data set of the 3D model of the pore shows a pore connectivity approaching 100% and an overall porosity of around 47%. Nevertheless, the porosity could be even higher as some of the external pores were excluded from quantification.

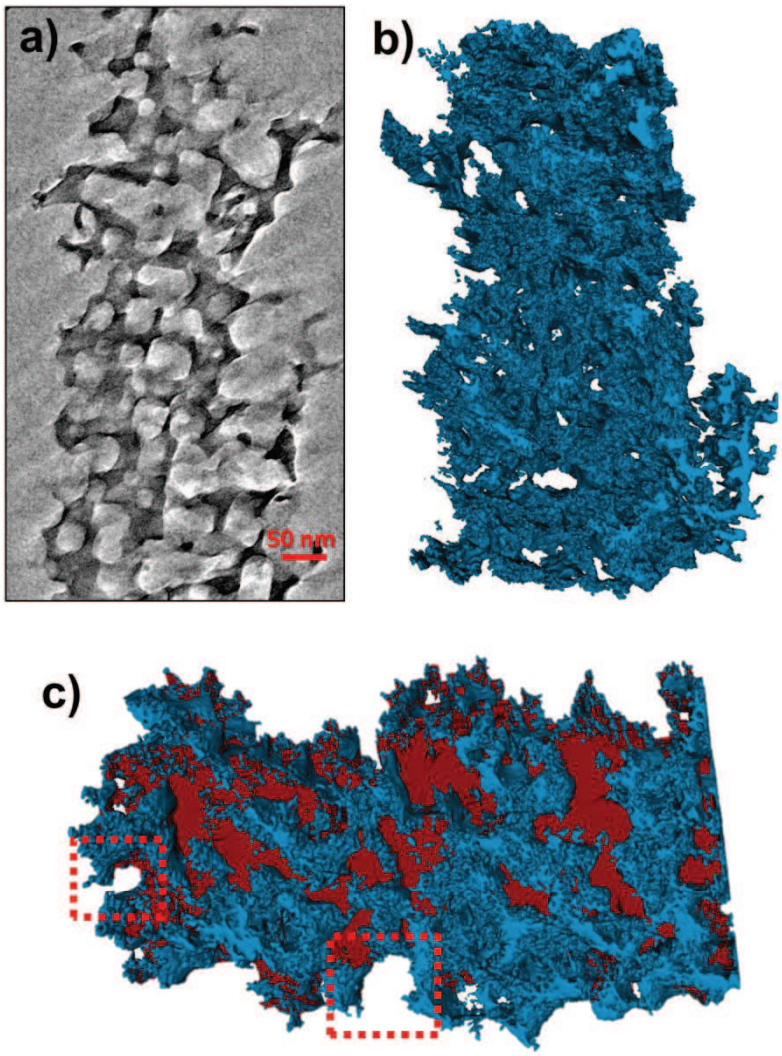

Figure 5.15. a) Longitudinal slice through the reconstructed volume of a second F-ZSM-5-60 min zeolite grain. b) 3D model of the zeolite body. c) Combined 3D models of zeolite body (blue) and pores (red). Red squares highlight some of the un-quantified external mesopores.

High magnification ET on the F-ZSM-5-15 zeolite sample

In the case of F-ZSM-5-15 min sample we have shown that some secondary mesopores created during the etching procedure seem to be completely isolated, i.e. they are not connected to the external surface of the grain neither directly nor through another mesopore. As discussed before, it is generally accepted that the etching starts on defects-rich areas with direct access to the fluoride solution flow, and from there the secondary porous network spreads inside the zeolite grains. This hypothesis comes from the fact that the fluoride species and especially the products of the reaction between them and the zeolite framework are large molecules requiring large channels for diffusion, larger than the ~0.55 nm that the intrinsic microporous network of the zeolite ZSM-5 can offer. Therefore, we have decided to acquire another tilt series for the 15 min etched zeolite using a high 80kx magnification in order to increase the resolution and thus try to observe the diffusion path for these isolated mesopores. The pixel size of the input images was 0.13 nm and the tilt series contained 109 images. The TEM image of the selected zeolite grain at 0° is shown in Fig. 5.16a. At this magnification factor the microporous network exhibits in the TEM images patterns that are similar to the ones created by the phase contrast ? imaging atomic lattices (HR-TEM). As in the case of HR-TEM images the patterns created depend on the orientation of the "channels" with respect to the incident electron beam. Therefore, this "angle-dependent" signal does not represent a monotonic type of signal required by electron tomography. Nevertheless, some interesting observations can be made from this type of reconstructions, as we will see later.

Returning to the diffusion path of the reactants/reaction products for the isolated mesopores, one can clearly state that even at this magnification we did not observe by ET any diffusion channel larger than ~1.1 nm. In the longitudinal (Fig. 5.16b) and cross-sectional (Fig. 5.16c) slices presenting some of the closed pores (red squares), one cannot identify any channels going from the pores to an area connected to the outer surface of the grain. The analysis was carried out slice by slice for all three orientations of the tomogram.

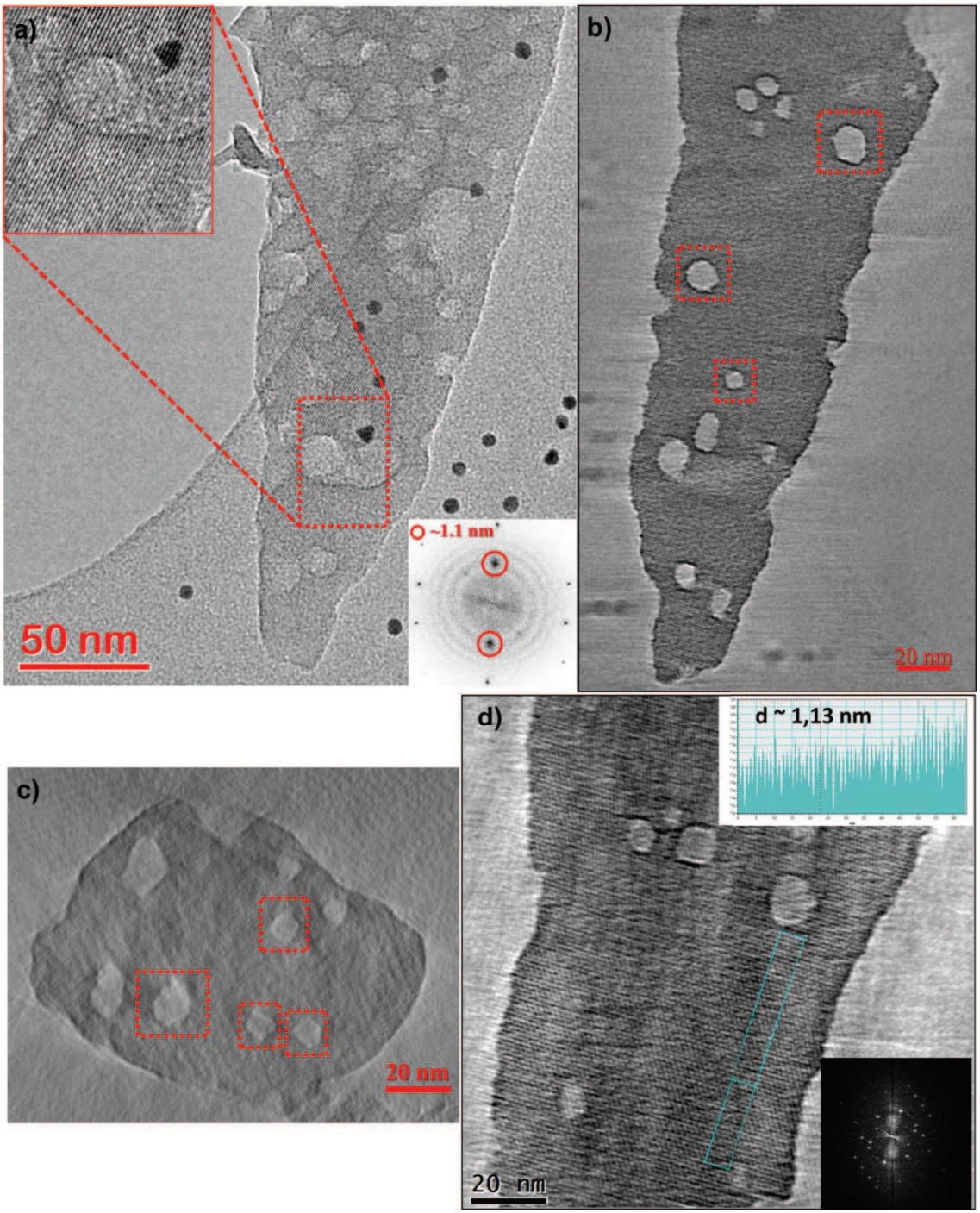

Figure 5.16. a) TEM image of the selected zeolite grain acquired at 0° (ZSM-5-15 min). The insets show the FFT of the image and a cut on its central part displaying the well-oriented patterns of the microporous channels. b) *xy* slice through the reconstructed volume. c) *xz* slice through the reconstructed volume. Red squares highlight the position of some isolated pores. d) ABSF-filtered *xy* slice showing the well-oriented pattern obtained in the tomogram of the selected zeolite grain. The insets show the FFT of the same regions and a line profile perpendicular to the features of the main line with a distance of ~1.13 nm.

Therefore, taking into consideration the ET results, one can state that some closed mesopores can be formed inside the zeolite grain with no other diffusion path for the reactants/reaction products than the intrinsic ~0.55 nm in diameter microporous network. At this point we do not have an evaluation of the diffusion properties through the microporous network (how long inside the zeolite microcrystal the reaction solution can penetrate, difference in size for the isolated pores and open pores etc.). However, it is clear that in parallel with the rapid etching of defect-rich areas directly exposed to the reaction environment, the fluoride solution diffuses through the microporous network inside the zeolite crystal until it finds the proper conditions, i.e. free Si/Al-OH groups, and, as a result, the etching reaction can spread around that point creating a secondary closed pore. The fact that macropores can appear easily after a short treatment time around the main defect lines in the microcrystal shows that the reaction is much faster in areas directly exposed to the reaction flow compared with areas where the diffusion takes place only through the network of micropores.

The phase-like contrast created by the two systems of microporous channels (see Fig.5.3) was also reconstructed in the tomogram. Fig. 5.16d presents a *xy* slice filtered by an ABSF deconvolution filter showing patterns similar to the ones appearing in high magnification imaging of the ZSM-5 zeolite. The FFT and the line profile inserted show the high degree of periodicity of this contrast with main d spacing around ~0.11 nm, the same as the one obtained in the tilt series images. Even if we cannot claim that the well-oriented line contrast appearing in this reconstruction represents the "image" of the microporous network, some interesting observations can be made. Fig. 5.17a with inset shows a magnified zone of the *xy* slice after the smoothing of the noise, showing well-defined microporous-like cages. For comparison, a HR-TEM image of the cages of the micropores oriented in the [010] direction is shown in Fig. 5.17b. One should notice that the magnification at which the HR-TEM image was acquired was not high enough for allowing the complete resolution of the secondary building units (see Fig. 5.3b) from the entrance of the channels, and consequently the entrance of the micropores appears to be ~0.11 nm. Although not perfectly identical, the longitudinal slices present a network of microporous cages with lattice parameters very close to the ones obtained for the ZSM-5 zeolite from the HR-TEM imaging. The well-defined microporous-like cages appear mostly at the edges of the reconstructed object due to the fact that these regions are thinner.

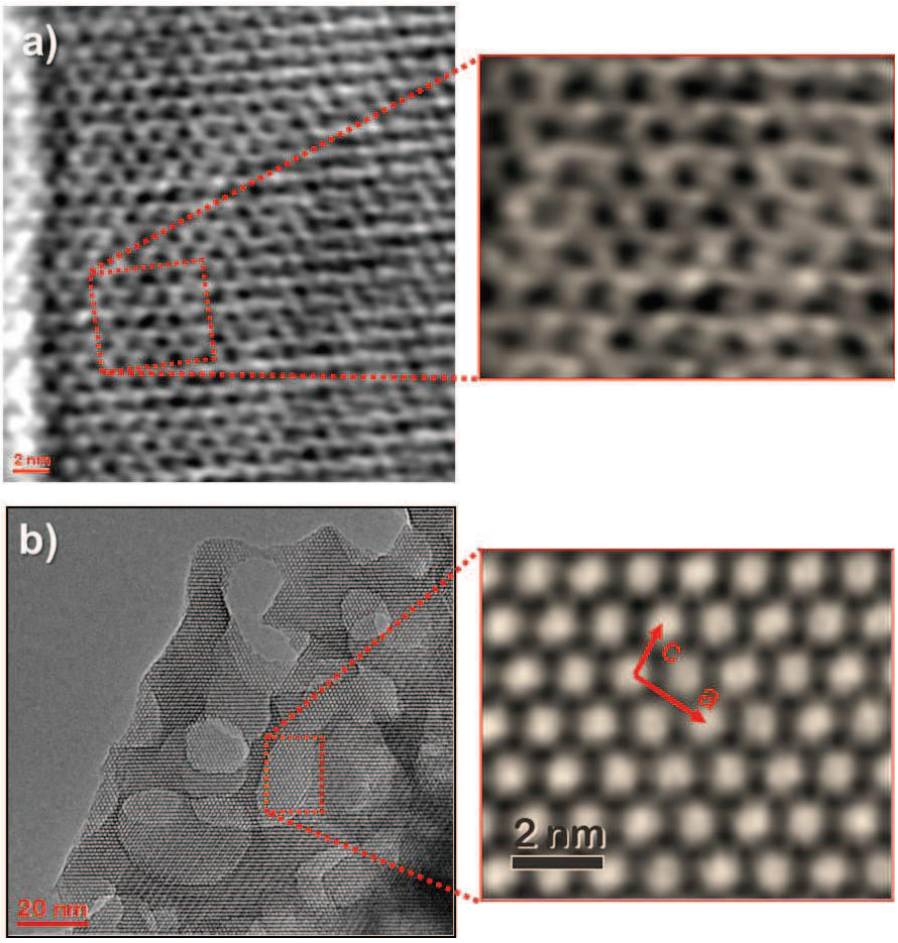

Figure 5.17. a) Longitudinal slice after the ABSF filtering showing a network of microporous-like cages. b) HR-TEM image of the microporous network acquired at a magnification lower than the one required to resolve the secondary building units of the ZSM-5 framework.

In HR-TEM images (inset in Fig. 5.17b) the phase contrast is predominant. The tomography slices (Fig. 5.16d and 5.17a) contain a mixture of density contrast and phase contrast which were also contained in the tilt series images. The advantage of a 3D representation of the microporous network is that, by numerically slicing the object, a direct visualization of the packing defects can be obtained. The visualization of local disruptions of the micropores network is not possible in HR-TEM images due to superposition effects.

Using a careful segmentation procedure, we were able to tentatively represent the reconstructed "microporous network" in a 3D model. First the 3D model of the zeolite body was created from the re-binned tomogram. Two snapshots of the 3D model are presented in Fig. 5.18. The *xy*-clipped image shows that the line-contrast is maintained even in the 3D model.

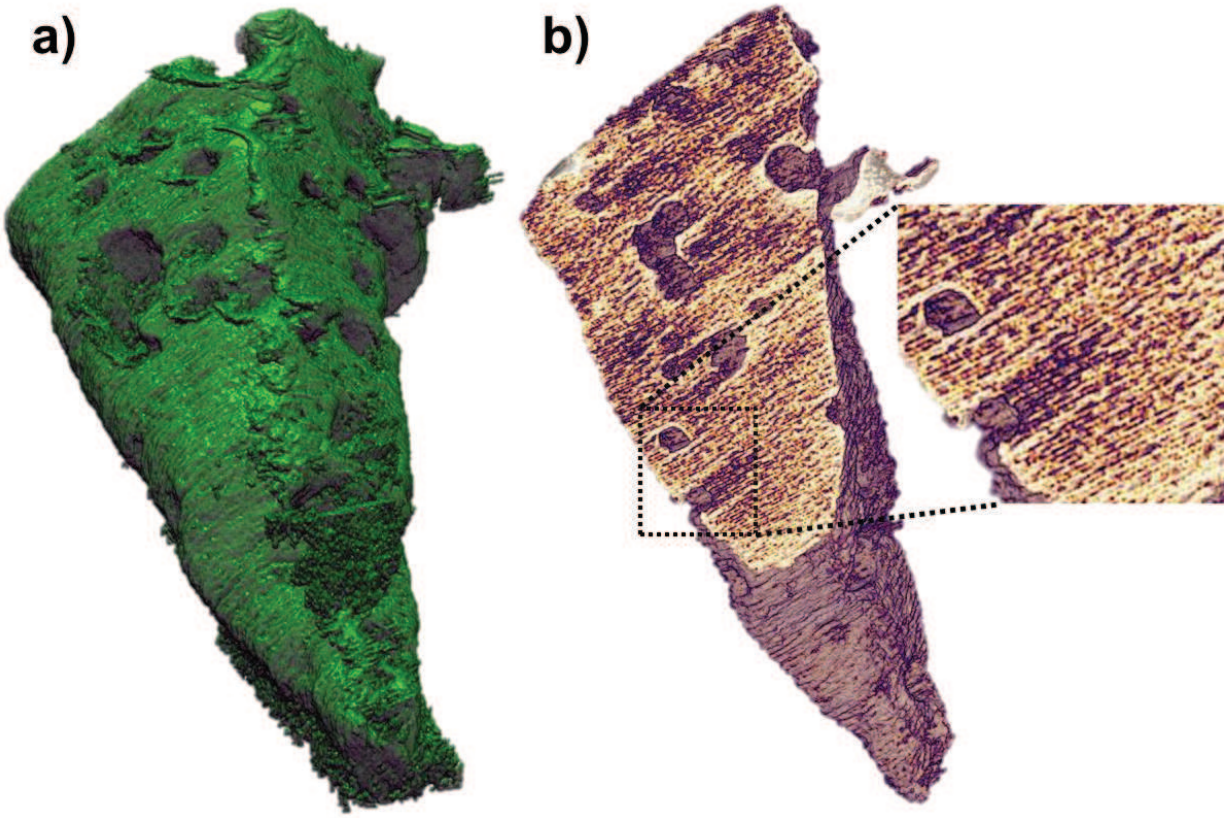

Figure 5.18. a) Snapshot of the external surface of the zeolite body 3D model. b) Snapshot of the clipped zeolite body 3D model in the xy direction.

The pore model was reconstructed using the zeolite body model as an input with no further processing of the body label. The 3D model of the "microporous network" only is presented in Fig. 5.19a. While some reconstruction and segmentation artifacts are presented, a high degree of arrangement is maintained. A combined model for both the mesopores created during the fluoride etching and the "microporous network" is presented in Fig.5.19b. At this point of the present investigation, the 3D model of the line-contrast has no quantitative meaning. However, it shows the advancement of the recording, reconstruction and segmentation techniques that allow such a resolution to be maintained even after the segmentation step. The conventional way for recording the tilt series (equal or adjusted tilting algorithms) does not represent the proper method for obtaining 3D signals from microporous zeolites with high resolution. However, new ET reconstruction techniques like the Equally Sloped Tomography (EST) combined with acquisition setup built by taking into account the crystallography of the investigated sample can overcome the limitations of the classical tomography and offer a real image of the "phase-like" features.

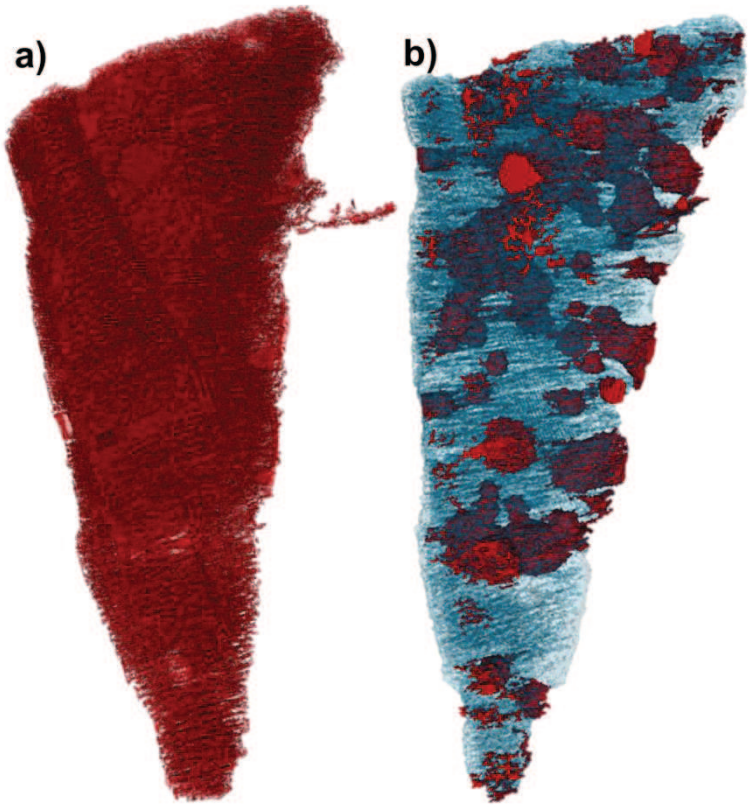

Figure 5.19. a) External view of the "microporous" network 3D model. b) External view of the combined 3D models of the "microporous" network and the mesopores created during the fluoride etching.

Encouraged by the results presented above, we started the project of using EST for the reconstruction of the "microporous network" in ZSM-5 zeolite samples. The interest for EST is given by a number of factors. First, EST is offering a very precise alignment of the tilt series, based on the object's center of mass. For the previous tomography (Fig. 5.17) with a resolution of about 1 nm (in the *xy* direction), we used a fiducial-based alignment. However, using this alignment method we cannot achieve a resolution higher than ~1 nm. Using the center of mass alignment, J. Miao and co-workers[40] already reported atomic resolution in the reconstruction of a Pt nanoparticle. Secondly, compared with the iterative methods (ART, SIRT), the resolution of EST reconstructions is higher due to the direct pseudopolar FFT transformation of the polar coordinates of the projections and the Cartesian ones of the object. A project was started between the EM group at IPCMS and the team of Prof. Miao at UCLA to adapt the EST method to our materials. Our aim was to obtain 3D atomic resolution for the zeolite materials allowing the visualization of all the internal features of their internal microporous network. A 3D

experimental-based atomic resolved view of the internal structure of the zeolites can lead to a better understanding of their behavior in various reaction environments. Fig. 5.20 shows some of the preliminary results obtained for the ZSM-5 zeolite. In Fig. 5.20a a 0.13 nm thick *xy* slice presents a relatively disordered microporous network (empty space in dark blue, wall in light blue). However, the patterns (red circles) identified in the FFT corresponding to the 1.1 nm lattice distance show an existing order. Moreover, by projecting the entire reconstruction along the *z* direction, we obtained a clear image of the microporous network (Fig. 5.20b). Nevertheless, at this point a number of difficulties have to be overcome. The first one relates to the acquisition of tilt series with an equal slope, which at this moment can be made only manually, resulting in long exposure times and the subsequent shrinkage of the object. The second is created by the fact that the EST software cannot work with the large data set obtained in TEM tomography. Therefore, updating the software capabilities is necessary.

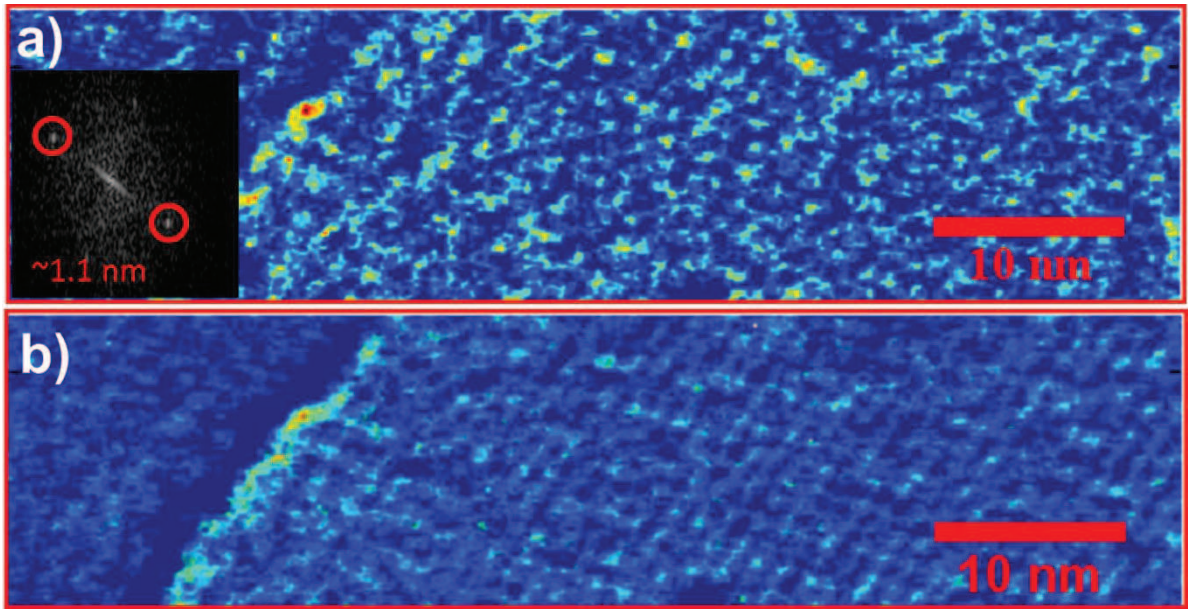

Figure 5.20. a) *xy* slice (0.13 nm thick) through the EST reconstructed volume of the ZSM-5-15 min zeolite. The insets show the FFT of the image. b) Projection along the *z* axis of the reconstructed volume.

5.2.4. Conclusion and perspective

The first conclusion drawn from this part of the fifth chapter is related to the morphological evolution of the investigated ZSM-5 samples. After 15 min of fluoride etching a uniform network of mesopores is formed. Their size ranges from 3.5 to 20 nm and their shape can be either spherical or cuboidal. Around 10% of the total pore volume (~0.17 $cm^3 \cdot g^{-1}$) is given by the contribution of separated pores, whereas the rest comes from the contribution of interconnected cages (2-3 pores). The grains of the zeolites present a low porosity of about 3%. The morphology of the zeolite grains significantly changes after 30 min of etching. As the etching spreads around, some of the walls of the pores are removed, creating a well-connected network of mesopores. As for the F-ZSM-5-15 min sample, only around 10% of the total pore volume (~0.16 $cm^3 \cdot g^{-1}$) comes from individual pores. The rest is given by a "super" cage formed by a completely interconnected network of mesopores, with direct access to the external surface of the grain. The sample porosity is around 22%. After one hour in the fluoride bath the zeolite microcrystals are losing their external shape, becoming foam-like materials. Their porosity exceeds 47% and the pores are all connected to the outer surface of the grains.

Another important observation is related to the etching mechanism and the formation of the mesopores. Contrary with what we expected, mesopores can be created inside the zeolite crystal with the etching agent and the reaction products moving in and out of the crystal through the network of micropores. Moreover, all the reaction products seem to be completely eliminated from the zeolite crystal in the main reaction stream, as no contrast assigned to the amorphous layer of these products was identified. The fluoride etching presents a small anisotropy as the mesopores appear elongated along the zeolite's **c** axis.

The present study has also assigned a quantitative dimension to the electron tomography data. At this point, the most reliable quantitative analysis is the porosity of the samples which has been presented earlier. However, one should highlight that in this study a considerable effort was made in order to increase the accuracy of these pieces of data. By taking advantage of high computational capacity and through careful manual adjustments, we maximized the resolution of the obtained 3D models. Another important quantitative analysis is the pore size distribution. Through our approach, the pore size distribution as a function of their frequency and, more

importantly, of their cumulated contribution to the total pore volume were successfully represented. Moreover, a direct quantification of the pore interconnectivity was possible.

A correlation between the ET and the N_2 sorption data is currently under way. When constructing a pore size distribution, extracted either from ET or sorption data, a certain shape of the pores has to be assumed. In N_2 sorption measurements, the mathematical models used to create the pore size distributions (BJH, Dollimore-Heal and DFT pore size reports) make different assumptions for the shape of the pores, leading thus to different results. Moreover, the connectivity of the porous networks creates even bigger challenges for these models[41]. Therefore, using ET to extract information about the shape of the pores and their interconnectivity and then reconstructing the N_2 sorption-base pore size distributions by taking in consideration these data, can lead to a considerable improvement of the accuracy of the sorption measurements.

Table 5.1. Porosity information determined by ET and N_2 sorption.

Sample	General observations	Porosity $^{(ET)}$ (%)	$V_{meso}{}^{(ET)*}$ (cm^3/g)	Interconnectivity of the pores	$V_{meso}{}^{**}$ (cm^3/g)	$S_{BET}{}^{***}$ (m^2/g)	$V_{mic}{}^{***}{}^{*}$ (cm^3/g)
P-ZSM-5	Non-mesoporous	-	-	-	0.02	377	0.18
F-ZSM-5-15 min	Uniform porous network	3	~0.17	Small connected cages of 2-3 pores	0.09	391	0.17
F-ZSM-5-30 min	Well-connected porous network (loss of the external surface)	22	~0.16	90% of pores connected in a "supercage"	0. 13	406	0.17
F-ZSM-5-60 min	Highly porous (foam aspect-loss of the crystal shape)	47	~1.15	All the pores are connected in a "supercage"	0.28	395	0.17

ET: *volume mesopores; N_2 sorption: **volume mesopores ;***BET surface area; ****volume micropores.

The present study also shows that the ET of zeolitic materials with resolution higher than 1.1 nm is possible. Creating an experimental-based 3D representation of the microporous network is of crucial importance as it could shine more light on the catalytic performances of these materials. The joint project between IPCMS and the Coherent imaging Group from UCLA also aims at obtaining ET of zeolitic materials with atomic resolution by using the Equal Slope Tomography approach. Table 5.1 summarizes the quantitative data obtained from ET together with some important pieces of information offered by the N_2 sorption analysis.

5.3. Hierarchical porosity induced by fluoride etching in zeolite Y

Zeolite Y is one of the first synthetic zeolites that has been made commercially available[42] and nowadays is one of the most important materials in the field of catalysis. The main applications include the catalytic cracking of petroleum into gasoline range components, hydrocracking and petrochemical synthesis[5,11]. Zeolite Y is part of the Faujasite family of zeolites together with Zeolite X and EMT. It presents a 3D microporous network (sodalite cages) with a pore entrance diameter of ~0.74 nm and an interior cavity size of about 1.2 nm (Fig. 5.22). Even with a pore entrance with about 0.2 nm larger than the one of the ZSM-5 zeolite, the applications of zeolite Y are restricted by the same limitations in diffusion, imposed by the blocking of the micropores. Therefore, as in the case of the ZSM-5 zeolite, a hierarchical network of pores is required in order to fully exploit the catalytic properties of the acidic surface of zeolite Y.

This second part of Chapter V presents the 3D TEM analysis of the hierarchical porosity induced by a fluoride-based etching on the Y zeolite family. This study deals with the investigation of morphological parameters such as the spatial distribution of the mesopores inside the zeolite grains, the size and the volume distribution of the pores, the overall porosity as well as the connectivity of the mesoporous network as a function of the fluoride etching.

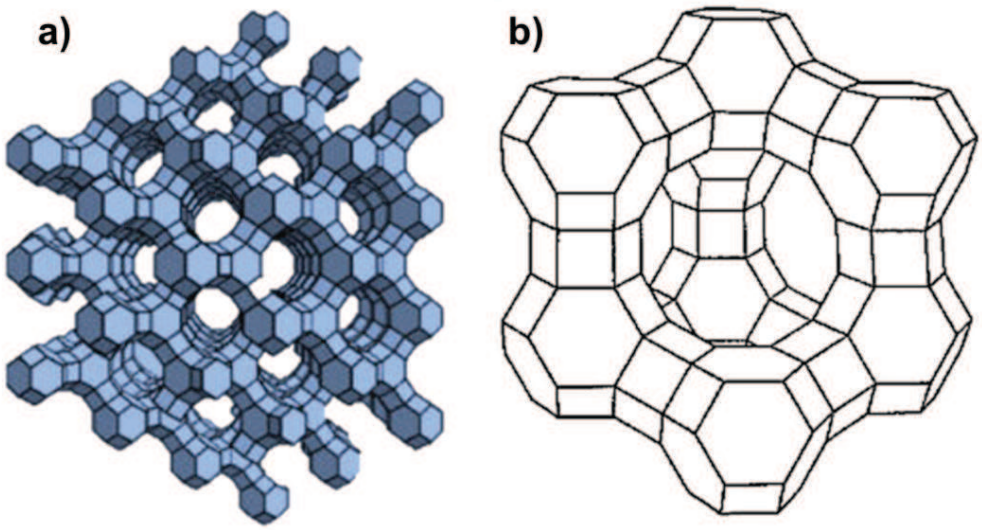

Figure 5.21 a) 3D representation (simulate) of sodalite cages network in zeolite Y. Adapted from reference[43]. b) 3D representation (simulation) of a sodalite cage unit. Adapted from reference[44].

5.3.1 Experimental details

Fluoride etching procedure of the Y zeolite crystals

For the fluoride-based etching of zeolite Y, 7.5 g of starting crystalline zeolite were dispersed in 30 mL of 25 wt% of NH_4F aqueous solution under stirring and ultrasonication. All the intermediate samples were thoroughly washed using distilled water after the fluoride medium treatment and dried at 100°C. The samples treated by NH_4F aqueous solution for 5, 15, 30, 60 and 120 min were denoted F-ZeY-5 min, F-ZeY-15 min, F-ZeY-30 min, F-ZeY-1h and F-ZeY-2h. The synthesis was carried out by Dr. Qin Zhengxing and Dr. Valentin Valtchev in the Laboratory of Catalysis and Spectrochemistry in Caen, France.

Sample preparation for tomography acquisition

The procedure is similar to the one described for the measurements of the ZSM-5 zeolites (see 5.2.1.2).

The microtome cutting and the subsequent analysis of some of the zeolite Y samples was necessary in some cases. The cutting of the samples was performed by Dris Ihiawakrim.

Electron tomography

As porous zeolite Y samples showed a higher stability under the electron beam as compared to the ZSM-5 samples, all the tilt series acquisitions were performed using the conventional acquisition mode, i.e. focus and tracking on the zeolite grain of interest. However, as for the ZSM-5 samples, the porosity increment leads also to an increase of the sample's shrinkage during acquisition. Therefore, the electron dose at the sample level had to be adjusted accordingly.

The fluoride etching creates a particular type of hierarchical porosity in the zeolite Y samples. Compared to the ZSM-5 etched samples, the obtained pores in zeolite Y are much smaller especially for the samples treated with short etching time (F-ZeY-5 min, -15 min and -30 min). Therefore, one major problem was represented by the focus changes in the tilt series during their automatic recording. This led to a rejection of some tilt series acquisition and a restart on a different, non-irradiated region of the grid. For the F-ZeY-15 min and -30 min, up to four tilt series were acquired and reconstructed in order to obtain the best "3D image" of the fluoride-induced secondary porosity.

5.3.2. Classical TEM characterization

The TEM images of the parent zeolite grain and the same after different treatment durations are presented in Fig. 5.22. As can be easily observed, following the morphological evolution from the conventional TEM imaging is not straightforward. No major differences between the parent zeolite (Fig. 5.22a) and the 5 min etched sample (Fig. 5.22b) can be identified. The appearance of secondary pores is visible after 15 min of etching (Fig. 5.22c) and increases with the etching exposure. The particularity of the secondary pores created in zeolite Y is their apparent uniform distribution. Moreover, even the porous aspect can be observed after 15 min of chemical treatment, a quantification of the pore size is difficult due to the continuous-like aspect of the porous network. The crystals of the zeolite Y are characterized by an inhomogeneity of the sizes and shapes. Their lateral size lies between 200 and 500 nm. No direct visualization of the secondary porosity homogeneity as a function of the crystal size was possible. However, some observations regarding the spatial distribution of the pore network are presented in the ET section.

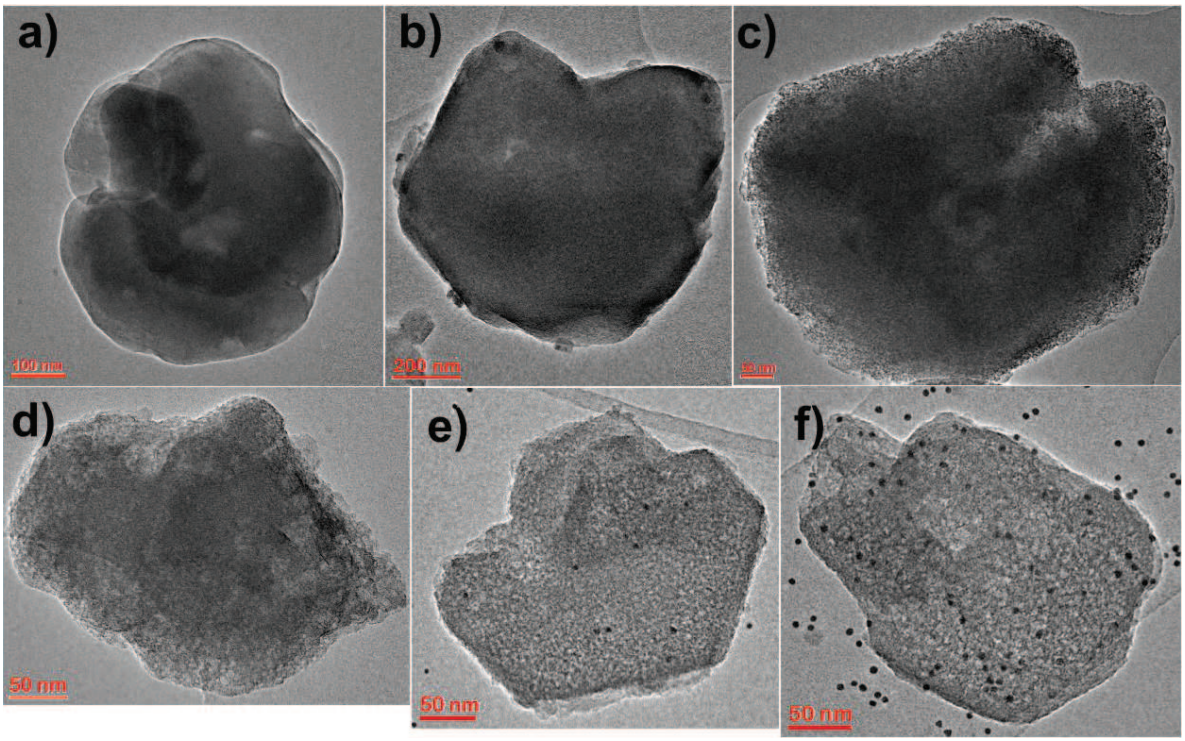

Figure 5.22. TEM images of the parent zeolite Y crystal (a) and of the hierarchical zeolites after 5 min (b), 15 min (c), 30 min (d), 1 h (e) and 2h (f) of fluoride etching.

5.3.3. Electron Tomography

To completely solve the internal morphology of the zeolite crystals in terms of porosity type of pores, geometrical characteristics, and pore size distribution as a function of the treatment duration in a fluorite solution an electron tomographic study was necessary.

Zeolite Y after 5 minutes of chemical etching (F-ZeY-5 min)

As shown in Fig. 5.22, after 5 min of fluoride etching the zeolite grain shows little sign of a secondary induced porosity. This is due to a relatively slow removal of the Si/Al framework. N_2 sorption measurements (not presented here) show a small increase in the total volume of the micropores, which is attributed to a discrete removal of the walls between the micropores cages. The small size and the low concentration of the secondary porosity in this sample have led until now to inconclusive tomography results. The only TEM technique which can unambiguously support the existence of these pores is HR-TEM. However, as already presented, the thickness of the zeolite grains does not allow such an analysis. Consequently, thin sample slices of about 60 nm were cut with the microtome and further analyzed.

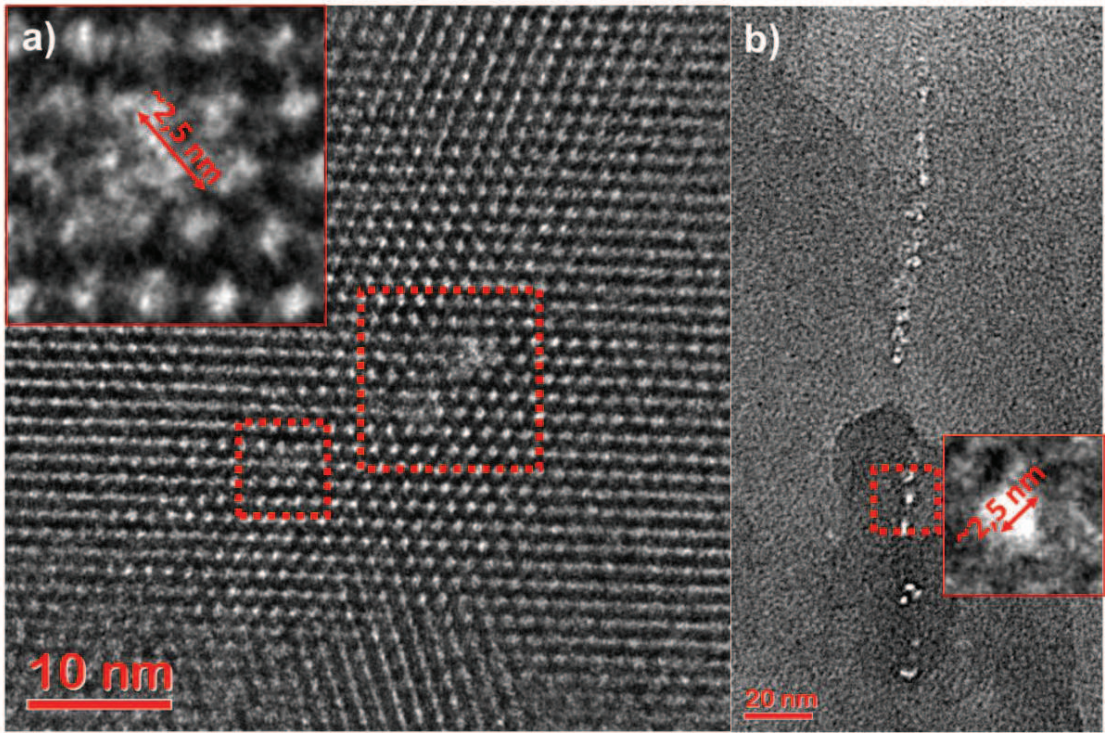

Figure 5.23. a) HR-TEM image of the F-ZeY-5 min zeolite sample showing the dissolution of some of the walls of the micropores. B) TEM image of the same sample showing a row of these secondary pores stretching along a defect rich line.

The corresponding HR-TEM analysis (Fig. 5.23) identified the existence of small pores of about 2.5 nm in diameter which are formed by the removal of the entire wall system of one micropore cage, and therefore merging the surrounding pores in larger cage (see inset in Fig. 5.23a). Fig. 5.23b shows that these pores aligned themselves along specific directions, which most probably coincide with the line of interface between two zeolite nanocrystals.

Hierarchical zeolite Y after 15 minutes of chemical etching (F-ZeY-15 min)

A TEM projection of a zeolite grain after 15 min of fluoride etching is shown in Fig. 5.24a. The image shows an apparently porous grain with small pores (~2 nm) visible only in the grain's thin regions due to a more pronounced superposition effect in thick areas. The reconstructed volume of this grain presented as a *xy* slice in Fig. 5.24b shows few small mesopores between 2 and 5 nm (yellow circles) and some large (10-20 nm) irregular mesopores (yellow rectangles). One should notice that the irregular mesopores appear only in some of the analyzed grains due to several initial high-density crystal defect sites more easily etched by the bifluoride ions. These mesopores are not representative of the induced mesoporous network. The results presented in Fig. 5.24b indicate that pores with a diameter ranged between ~2-5 nm only contribute with a small extent to the total porosity of the zeolite. However, this assumption seems not to be in agreement with the grain aspect presented by the TEM image showing a more porous morphology. A better image of the mesoporous network is offered by the *xz* slice (Fig. 5.24c). Moreover, applying a threshold function on the reconstructed volume, one can better visualize the position of these apparently hidden mesopores (Fig. 5.24d). The problem of the low visibility of small mesopores is created by a combined effect of their small size and the relatively large thickness of the zeolite grain, which makes the reconstruction of the porosity network very sensitive to focus modifications during the recording time and delocalization contrast of the grain appearing for some angles. Nevertheless, by carefully adjusting the threshold values, we were able to create the 3D model of both the zeolite body and the porous network. Fig. 5.25a shows a *xy/xz* clipped 3D model of the zeolite body alone, while the combined 3D models of zeolite body and the mesoporous network are shown in Figures 5.25b-c. These 3D representations provide a clear view of the network of mesopores inside the zeolite grain, which is presenting a general uniform distribution and only some small regions close to the external surface of the grain are

depleted of pores. The quantitative data set extracted from 3D models shows an overall porosity of around 5%. However, all the pores smaller than 2 nm in diameter were excluded from the quantification. The data set extracted from the 3D pore model and computed assuming a spherical shape of the pores shows a pore size distribution between 2 and 48 nm. Note that we have considered for the pore size distribution only the pores between 2 and 15 nm, as larger pores are considered as supercages of connected mesopores or/and as large mesopores visible in Figs. 5.24b and 5.25a. From the total pore volume, only about 40% is due to the contribution of mesopores in the interval 2-15 nm and the rest comes from larger cages. Nevertheless, the size distributions of the pores in the 2-15 nm size interval can be considered as representative for the whole induced mesoporous network and used for understanding the fluoride etching effect.

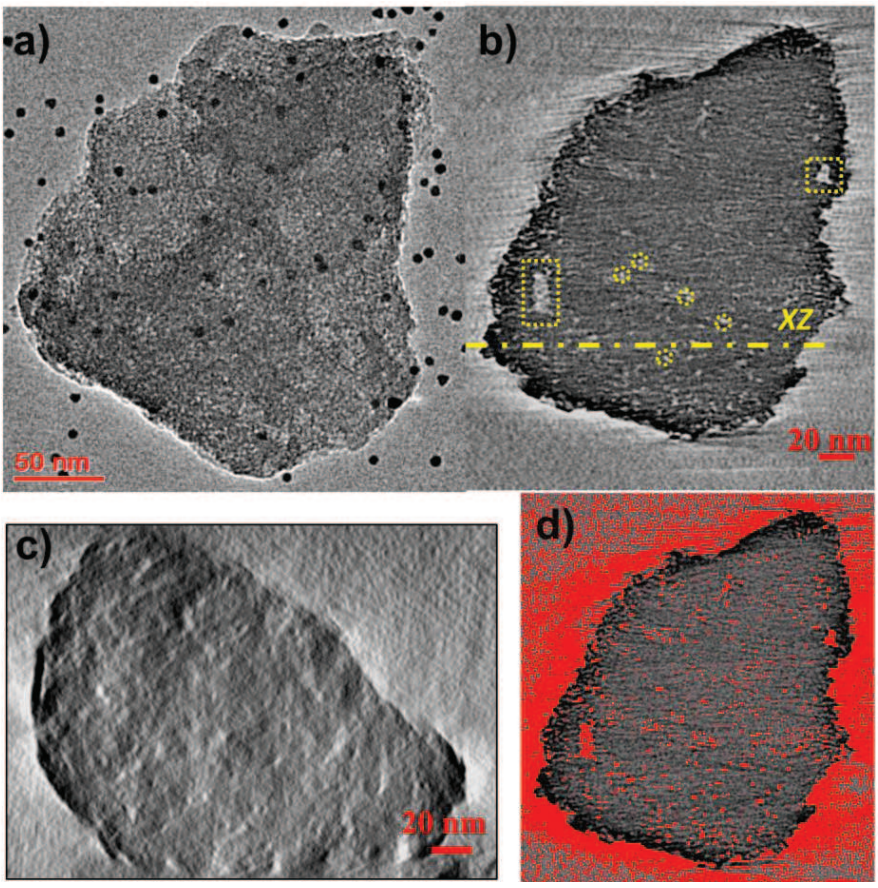

Figure 5.24. a) TEM projection of the F-ZeY-15 min hierarchical zeolite Y. b) *xy* slice through the reconstructed volume of the selected grain. Yellow rectangles and circles highlight the position of the irregular large mesopores and regular small ones, respectively. c) *xz* slice through the reconstructed volume at the position highlighted in 5.24b. d) Color thresholding of the *xy* slice from 5.24b.

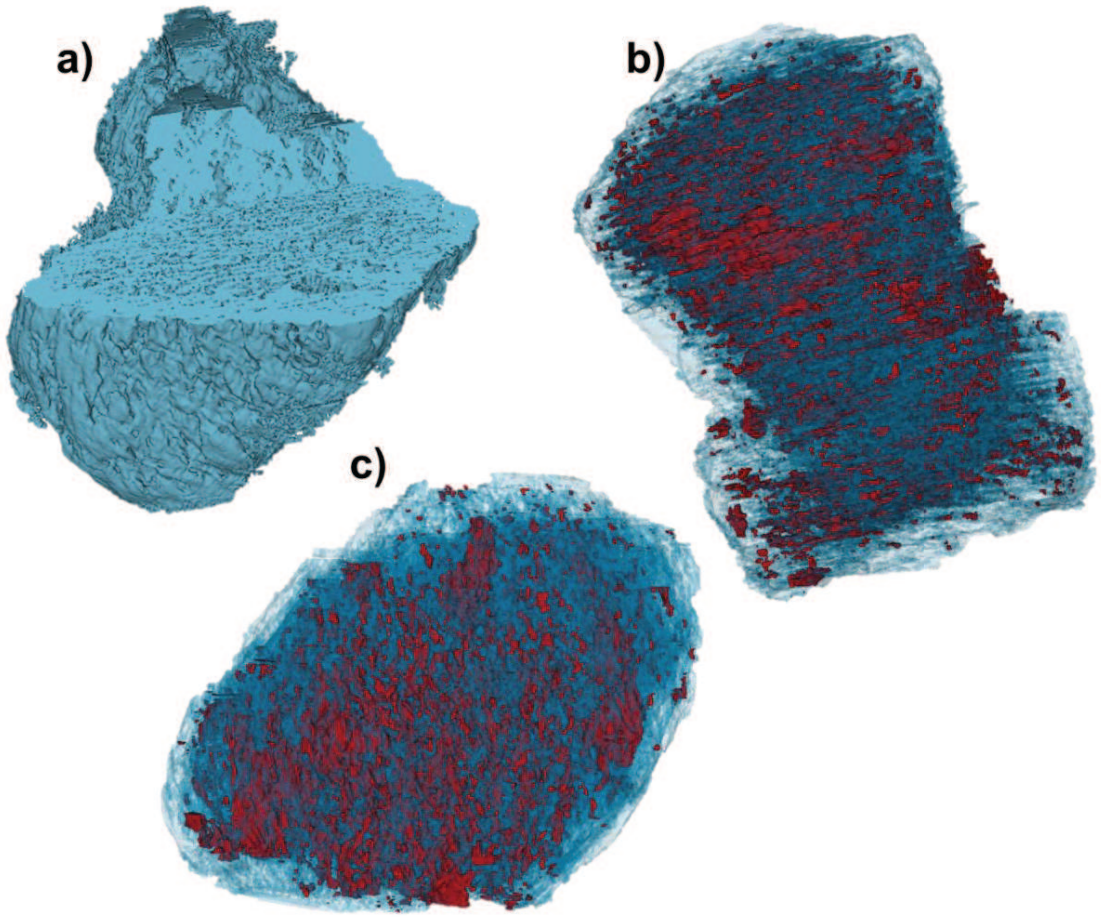

Figure 5.25. a) 3D model of the zeolite body cut in the *xy* and the *yz* directions. b) *xy* and c) *xz* oriented snapshots of the combined 3D models of zeolite body (transparent blue) and mesoporous network (red).

The results of the quantification are presented in Fig.5.26a and reveal that about 60% of the mesopores have a diameter ranging between 2 and 3 nm (bar centered at 3 nm). Another considerable part of the fluoride induced mesopores (~30%) have a diameter lying between 3 and 5 nm, while mesopores larger than 5 nm do rarely appear. The pore size distribution as a function of their contribution to the total pore volume is presented in Fig. 5.26b. It shows that pores between 2 and 3 nm (though they represent the majority of the secondary mesopores) have a moderate contribution of ~14% (the same as pores between 7-9 nm and 9-11 nm) to the total porosity, while the pores between 3-5 nm give the most consistent contribution of about 26% to the total pore volume.

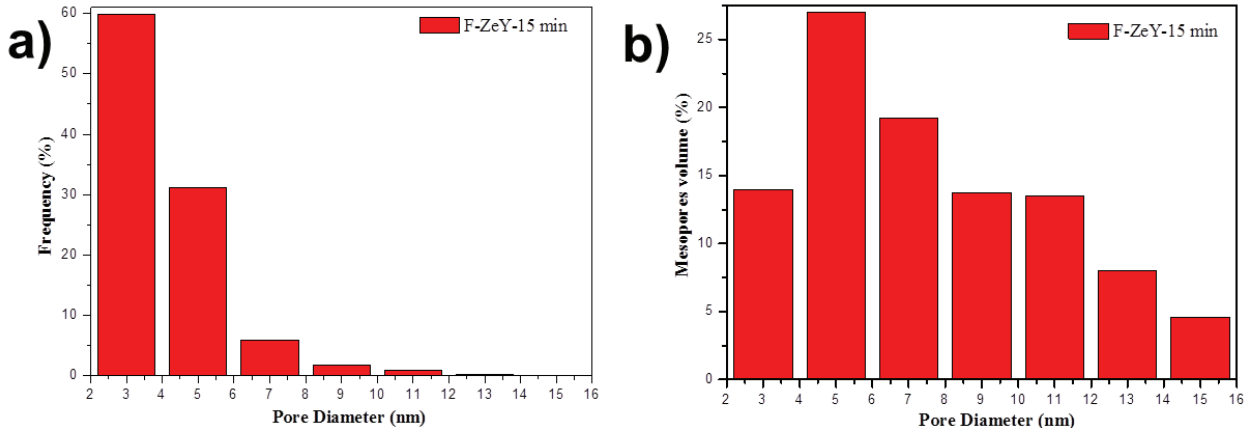

Figure 5.26. a) Pore size distribution as a function of their frequency of appearance in the network of mesopores for the zeolite sample submitted to 15 min of fluoride etching. b) Pore size distribution as a function of their cumulated volume.

In order to create a clearer image of the porosity in the size interval of 2-5 nm (a better resolution) the F-ZeY-15 min sample was cut by the microtome to a thickness of about 40 nm and a tilt series was acquired on one of the sliced grain (see *Sample preparation for tomography* section 5.3.1). The TEM image of the selected grain is presented in Fig. 5.27a. One should notice that for cut samples the fiducial Au nanoparticles used for series alignment have to be deposited after the cutting procedure and therefore some of the fiducials will also be covering the specimen surface. This has major consequences in the tomogram as the high contrast created by the Au nanoparticles will overlap with the low contrast of the zeolite. The presence of Au fiducials induces artifacts and one way of decreasing their influence is to deposit them on the opposite side of the membrane/resin. In this way the delocalization contrast will affect only the lower side of the specimen, which is anyway affected by the membrane's signal (see Fig. 5.28).

The tilt series acquisition was performed at 60kx magnification with a pixel size of 0.16 nm. The reconstructed volume of the ~40 nm thin zeolite grain gives a much better view of the secondary porosity. As can be seen in Fig. 5.27b (*xy* slice) a relatively dense network of small mesopores between 2 and 3 nm in diameter (yellow circles) is well dispersed inside the zeolite grain, verifying the results of the pore size distribution presented previously (Fig. 5.26). Moreover, the present reconstruction helps us identify even smaller micropores of about 1-1.5 nm in size. However, the contrast built-up by the intrinsic microporous network of the zeolite Y, will determine the existence in the reconstructed volume of a network of well-oriented lines. As we

already discussed for the ZSM-5 zeolite, this type of contrast can create in the obtained tomograms features of shapes similar to the shape of the microporous cages.

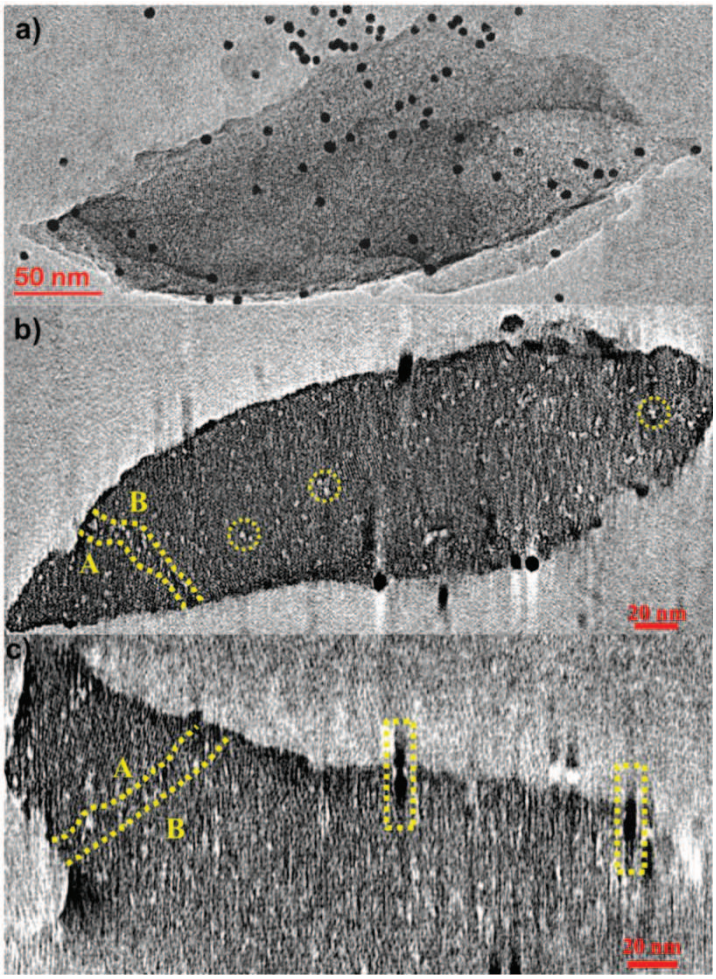

Figure 5.27. a) TEM projection of the selected 40 nm thick F-ZeY-15 min zeolite grain. b) *Xy* slice through the reconstructed volume of the selected grain. Yellow circles highlight the position of small 2 to 5 nm in diameter mesopores induced by the fluoride etching treatment. Yellow lines show the position of the interface between two crystalline domains. c) *Xz* slice through the reconstructed volume showing the interface between two different crystalline domains, noted A and B. Yellow rectangles highlight the regions affected by the Fresnel contrast of the Au fiducials.

The calculated 3D models (Fig.5.28) cannot exclude the microcages-like features, and therefore they appear as part of the porous network. Although these features show the high quality of our reconstructions and 3D models, their presence affects the precise quantification of the secondary porosity created during the etching process. Nevertheless, this periodical contrast

allows us to distinguish between parts of the zeolite grain with different orientations of the microcages network. This effect can be seen in Fig. 5.27b-c which identifies two regions (A and B) in the zeolite grain with different orientation of the networks. Moreover, at the interface a higher concentration of 2-3 nm in size mesopores appears, stretching from one side to another of the interface (yellow rectangle). This finding is in agreement with the one obtained for the 5 min etched sample, where a preferential alignment of the secondary pores along specific directions was observed (see Fig. 23). This interface between different crystalline domains formed during the nucleation of the zeolite Y experiences a more rapid etching in this early stage of the fluoride treatment.

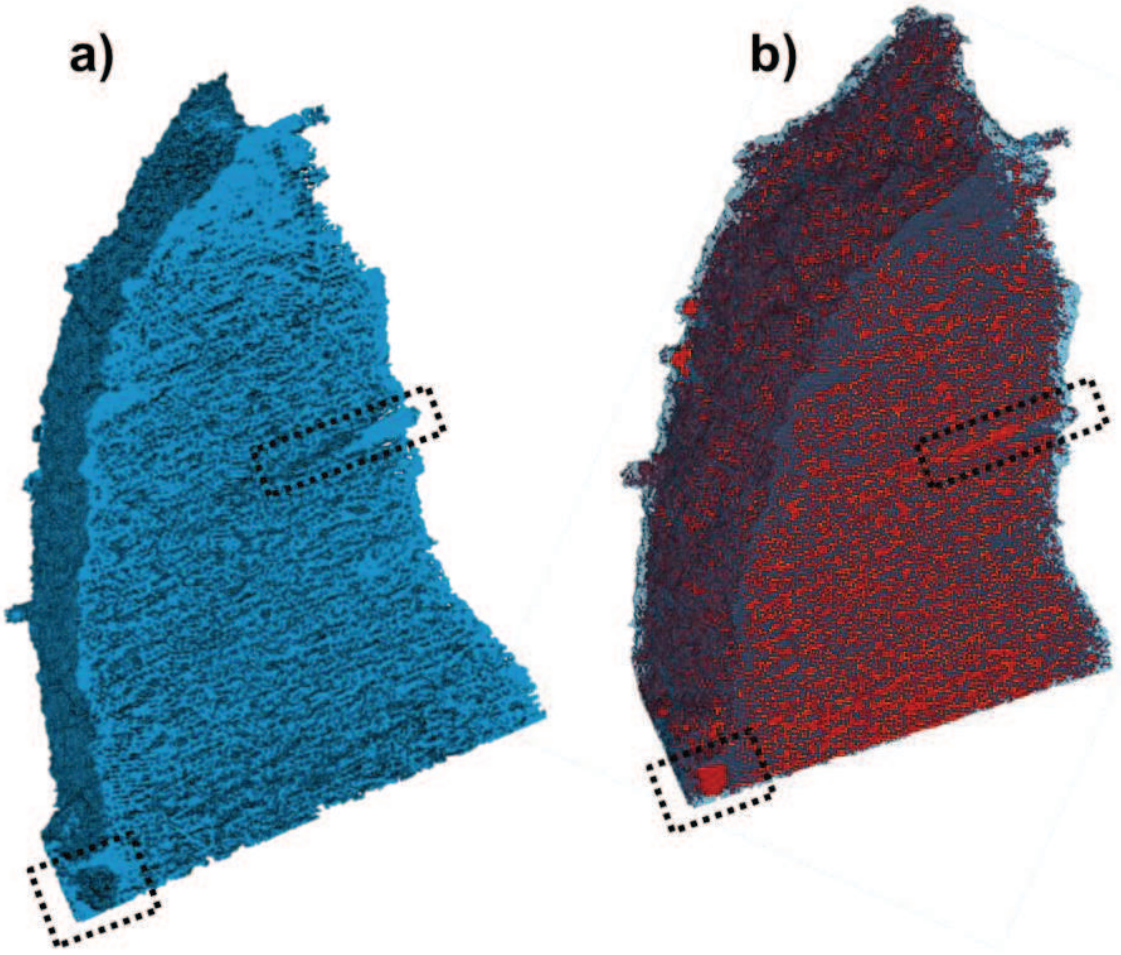

Figure 5.28. a) 3D model of the zeolite body clipped in the *xy* direction. b) *S*napshot of the combined 3D models of the zeolite body (transparent blue) and micro- and mesoporous network (red). Black rectangles highlight the regions affected by the Fresnel contrast of the Au fiducials markers.

Hierarchical zeolite Y after 30 minutes of chemical etching (F-ZeY-30 min)

A TEM image of the selected etched zeolite grain is presented in Fig. 5.29a. Compared to the 15 min etched sample, one can directly observe the enhancement of the grain's porosity aspect and the slight increase of the size of the pores. The longitudinal slice through the reconstructed volume presented in Fig. 5.29b highlights the porosity increase. The analysis of the size of the pores shows individual pores ranging from 2 to 8 nm in diameter. An evident increase in density of pores larger than 5 nm with an irregular shape can be observed. In some cases the merging of two subsequent mesopores creating a larger irregular one can be observed.

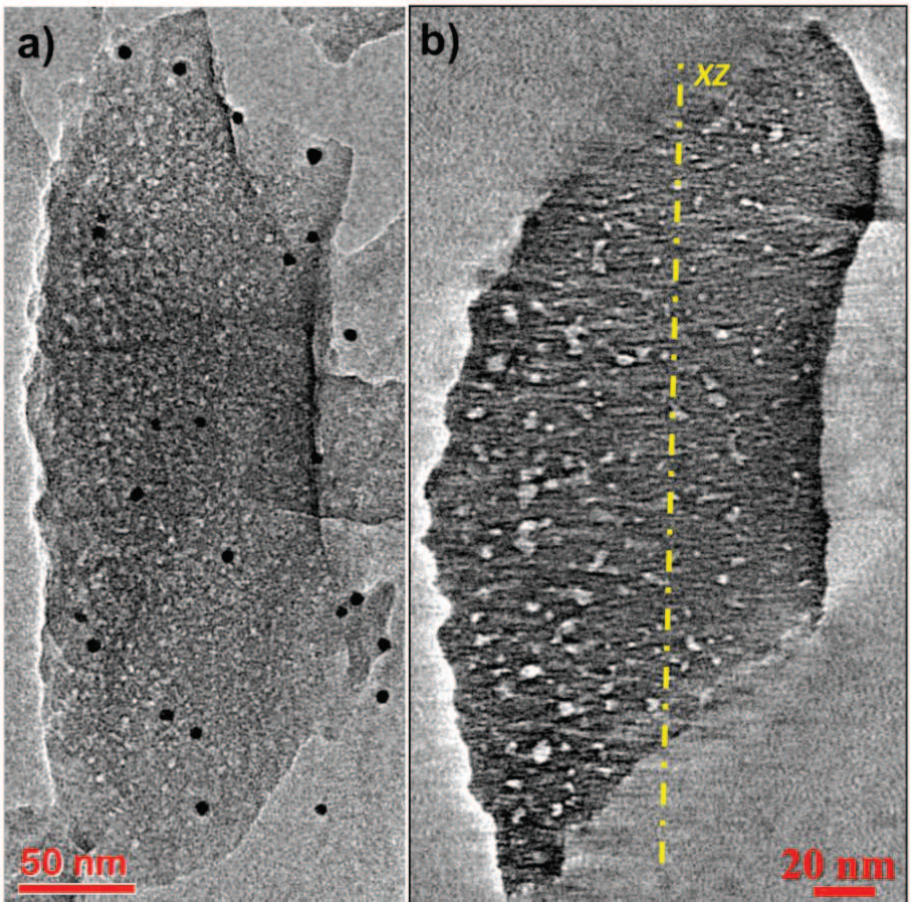

Figure 5.29. a) TEM projection of the selected 60 nm thick F-ZeY-30 min zeolite grain. b) *Xy* slice through the reconstructed volume of the selected grain.

Another perspective of the zeolite's secondary porosity is given by the cross-sectional analysis slice by slice (*xz*) presented in Fig. 5.30a. The shape of the pores appears to be more regular when observed in the *z* direction, with a preference for spherical and some cylindrical shapes. Two snapshots of the *xz* superposed 3D models of the zeolite body and mesopores are presented in Fig. 5.30b. Besides the fact that the *xy* and *xz* slices do not show a uniform dispersed

porous network the 3D pore model shows an overall uniform distribution of the pores inside the zeolite grain. The quantification of the data using the 3D models estimates the overall porosity to be 11%. As for the previous sample, in the representation of the pore size distribution we only took into consideration the pores ranging between 2 and 15 nm in diameter. However, the pores in the 2-15 nm size interval represent only ~42% from the total pore volume of the grain. As for this particular grain no large mesopores created due to an amplified etching in defects-rich areas was observed, one can conclude that the rest ~58% of the pores volume is distributed as a well-connected mesoporous network. A similar ratio between individual and connected pores was found for the previous 15 min treated sample.

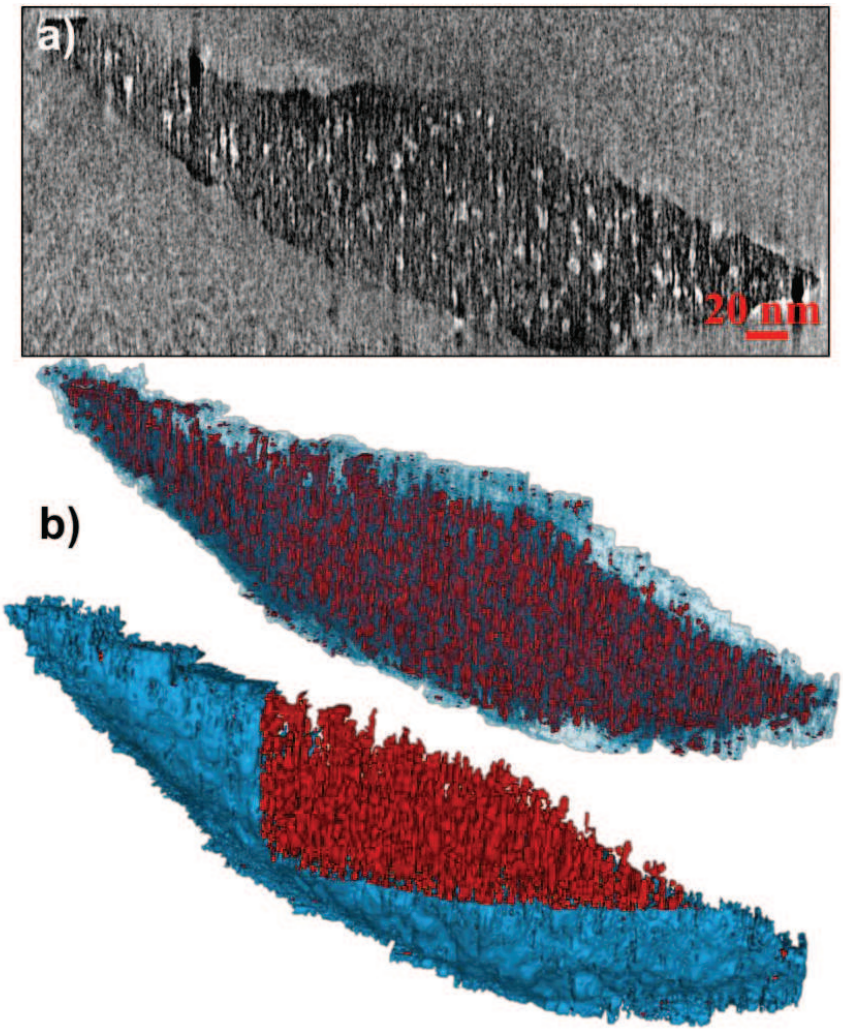

Figure 5.30. a) Cross-sectional (*xz*) slice of the F-ZeY-30 min zeolite sample. *S*napshots of the combined *xz* orientated 3D models of zeolite body (blue) and mesoporous network (red).

The pore size distributions (Fig. 5.31) were created taking into consideration only the individual pores. Comparing the pore size distributions of the 30 and 15 min etched samples, one can observe a decrease of the number of pores in the size interval 2-3 nm from ~60 to ~51%, while the pores in the size interval 3-5 nm seem to appear with the same frequency (30%). As observed also from the direct analysis of the tomogram, the pores between 5 and 7 nm in diameter have an appearance frequency growing from 5 to 10%. The contribution of the pore size intervals to the total porosity change in accordance with the frequency distribution, as pores in the size interval 2-3 nm and 3-5 nm decreases both by ~7%, while the contribution of the pores in the 5-13 nm interval remained the same.

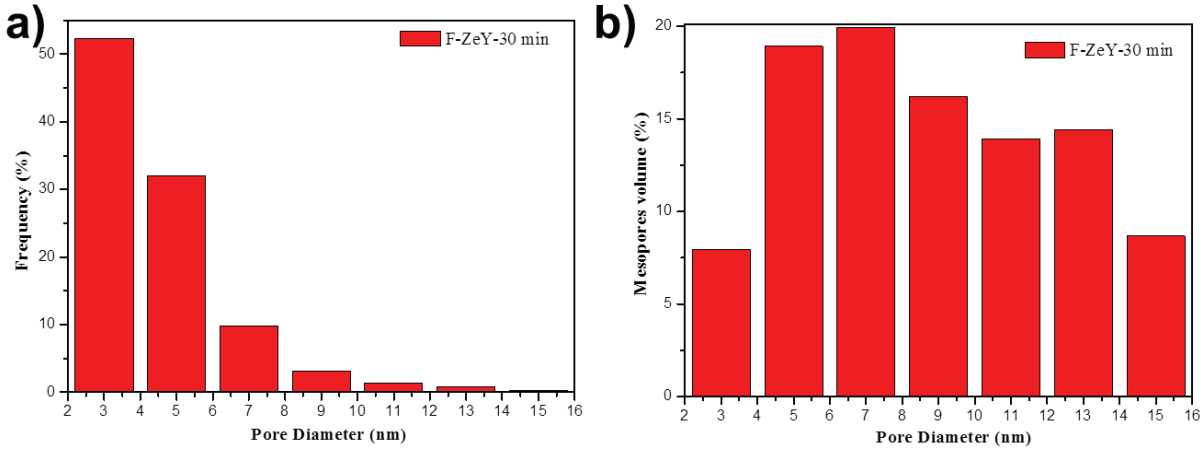

Figure 5.31. a) Pore size distribution as a function of their frequency of appearance in the network of mesopores of the F-ZeY-30 sample. b) Pore size distribution as a function of their cumulated volume.

Hierarchical zeolite Y after 60 minutes of chemical etching (F-ZeY-1h)

The TEM image presented in Fig. 5.32a shows a mesoporous zeolite Y nanocrystal after 1h of fluoride etching. The TEM projection does not show significant difference of the apparent morphology between this sample and the previous 30 min etched one. However, ET shows a clearer picture of the secondary mesoporosity. The *xy* slice from Fig. 5.32b shows a dense mesoporous network with individual pores and a large number of connected ones. The size of the individual pores ranges between 2 and 12 nm, while the size of the connected ones depends on the number of the pores forming the "local" connected network. Observed in the *yz* direction, the porous network has an even more connected aspect and forms a continuous network stretching from the upper surface to the lower one.

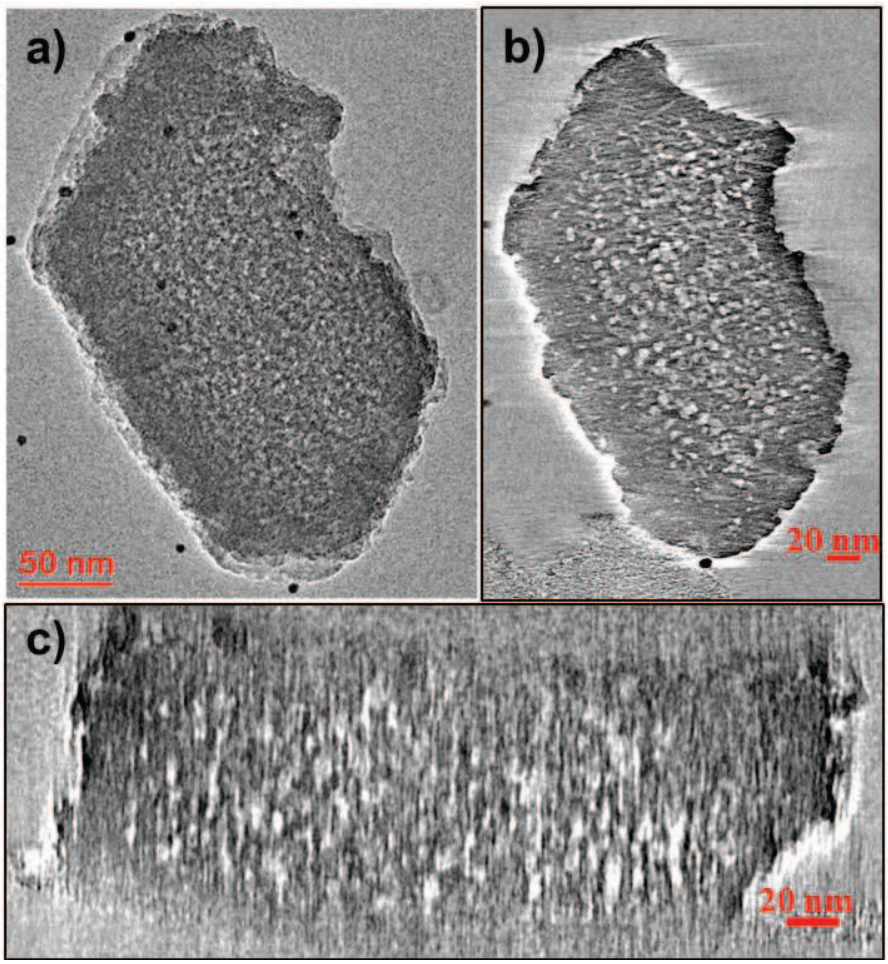

Figure 5.32. a) TEM projection of the F-ZeY-1h hierarchical zeolite Y. b) and c) *xy* and *yz* slices through the reconstructed volume of the selected grain.

The 3D models presented in Fig. 5.33 directly show the well-connected network of mesopores. Their volume quantification gives an overall porosity of about 15%, compared to the 7% and 11% observed for the previous 15 and 30 min etched samples. In the representation of the pore size distribution (Fig. 5.34), only the pores in the interval 2-15 nm were included. However, these pores, represent only 13% from the total volume of the grain. Due to their interconnectivity the rest of the pores are creating a "super" cage. As can be easily seen in Figs 5.32 and 5.33, a large number of pores have direct access to the grain's outer surface, consequently one can state that around 90% of the secondary porous network is directly accessible. Compared with the previous samples where only around 50% of the total pore volume was coming from the contribution of the connected "super" cage, the dramatic increase to 90% shows a major transformation of the sample morphology after 1h of etching. The difference can also be seen in the pore size distributions. The proportion of the pores in the interval 2-4 nm is increasing to

more than 80% (from ~50% for the F-ZeY-30 min) at the expense of the pores in the near 4-6 nm interval. Moreover, the pores on the interval 2-4 nm have the most important contribution to the total pore volume (around 30%), compared with the previous samples, where their contributions was on average 7-15%. Also, very noticeable is the drastic decrease of the contribution of the pores on the interval 6-16 nm, compared with the previous samples. Apparently, this finding challenges the direct observation of the large pore incensement after 1h of treatment compared with the previous etching time. The following explanation could be put in advance to explain such an observation. The 1h long fluoride etching has the effect of increasing the size of the pores created in the initial stage of the treatment, but also other sites are etched by the fluoride species and new pores continuously appear. Therefore, what the pore size distributions show is that new pores are created at a higher rate than the expansion of the initial pores.

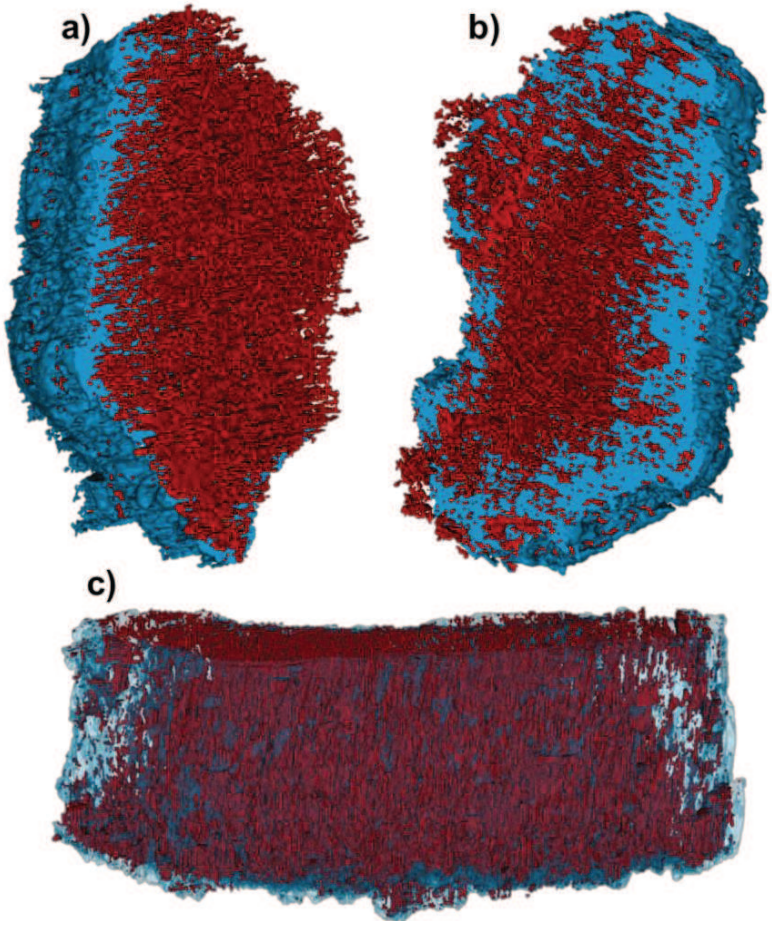

Figure 5.33. a) and b) Superposed 3D models of the zeolite body (blue) and pores (red). The zeolite body's model was clipped in the *xy* direction. c) Superposed 3D models of the zeolite body (blue) and pores (red) oriented in the *yz* direction.

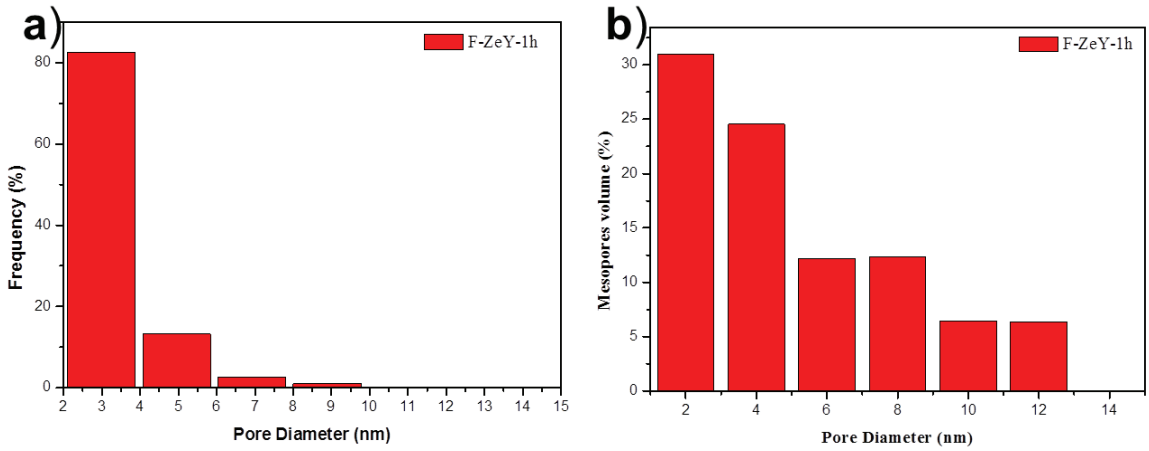

Figure 5.34. a) Pore size distribution as a function of their frequency of appearance in the mesopore network of the F-ZeY-1h sample. b) Pore size distribution as a function of their cumulated volume.

At this point the analysis of the zeolite sample after 2h of etching is underway. The preliminary results shows an increase of the porosity to about 26% compared with the 1h etched sample that shows only 15%.

5.3.4. Conclusion and perspective

The first conclusion is related to the particularities of the etching mechanism in zeolite Y samples. As shown by the HR-TEM analysis of the F-ZeY-5 min sample, the appearance of secondary pores in the early stages of the treatment is conditioned by the existence of some packing defects in the microporous network. Very few pores are created after 5 min of etching and their diameter is set at around 2.5 nm. After 15 min of chemical etching, the secondary porosity becomes visible through TEM imaging. Electron tomography shows that the porous network is made out mostly by pores ranging between 2 and 5 nm in size, with a relatively uniform distribution inside the crystal. The size of the pores is increasing after 30 min of etching, with the pores in the interval 3-7 nm gaining the most important contribution to the total pore volume. The 1 h treated sample shows a dramatic increase of the pores in the interval 2-3 nm, which are generating more than 30% of the grain porosity. This unexpected behavior is due to the disequilibrium in the kinetics of the formation of new pores and their size expansion. This shows that the size evolution of the pores is not linear and after a certain treatment duration there is a slowdown of their size expansion. However, for representing the pore size distribution of this

sample, only around 13% of the total porosity was quantifiable (see the above discussion). Consequently, this assumption should also be verified using other techniques (N_2 sorption). The evolution of the overall porosity shows an increases from 7% for the 15 min etched sample to 11% (30 min), 15% (1h) and reaches around 26% for the 2h sample. Although the porosity is increasing with the etching time (as expected), the evolution is not linear. Considering the porosity of the initial sample to be zero (the porosity created by the secondary mesopores, not the intrinsic microporous – based porosity) we can observe that in the first 15 min of etching the porosity increase by 7%, whereas the increase in the time interval 15 - 30 min is only around 4%, from 7% to 11%. In the time interval 30 - 60 min, the porosity increase rate is around 4%, meaning a decrease from 4% / 15 min to only 2%. In the time interval 60-120 min, it seems that the porosity is increasing with about 2.7% at every 15 min. This slowdown of the porosity is increasing, meaning that a slowdown of the zeolite framework's etching is an important observation concerning the fluoride etching mechanism in zeolite Y. Establishing a complete image of the etching mechanism based on other investigation techniques as well is currently under progress.

Besides the precise quantification of the morphological properties, electron tomography at high magnification offered a direct evidence of the formation of pores along the interface between two zeolite grains with different orientations. In the first stages of the etching (5 and 15 min), the shape of the pores can be approximated as spherical. However, as the etching progresses and their size increases, the shape of the pores becomes more and more irregular. The increase of the interconnectivity of the pores amplifies this perception. Presently the investigation of the etching anisotropy is still in progress.

The electron tomography investigation of the secondary porous network created in zeolite Y grains by a fluoride etching treatment revealed important pieces of information that can be used for understanding the dissolution mechanism of the Si/Al framework by fluoride specified. Moreover, the porosity quantification helps our colleagues in their attempt to optimize the morphological properties of these materials for further applications.

As discussed in the Section 5.2.3, the potential of the Equal Slope Tomography to give a 3D representation at atomic resolution of zeolitic materials can help us understand chemical mechanisms such as fluoride etching. Of special interest is the application of this method for the

5 min etched sample in order to create a 3D crystallographic map of the induced pores in the early stages of their evolution.

5.4. General conclusions and perspectives of Chapter V

This chapter presents a 3D-TEM based study of the secondary porosity induced by a fluoride-based etching in two families of zeolites, ZSM-5 and zeolite Y. A complete description of the electron tomography protocol (acquisition conditions, segmentation procedure and quantification) is proposed. By carefully adjusting this protocol as a function of the samples properties, a reliable 3D representation of the morphological properties of the zeolite samples was obtained. Moreover, this adjustable protocol has allowed for the analysis of a large number of samples, moving tomography a step forward in becoming a fast technique with large-scale applications.

The 3D-TEM approach offered precise pieces of information about the size of the pores and their spatial distribution, the overall porosity and the connectivity of the porous network. Moreover, direct information about the dissolution mechanism of the Si/Al framework was extracted from the obtained topographies. By carefully controlling the acquisition parameters, a 3D image of the microporous network of the ZSM-5 zeolites was obtained. These results open a way for obtaining a real (experimental) 3D image of the micropores cages, of uttermost importance after post-synthesis treatments of the zeolites, which might help in understanding and predicting the catalytic behavior of these materials.

Of real interest is the analysis of these hierarchical zeolites using Energy Filtered TEM electron tomography (3D-EFTEM). However, the beam sensitivity of these materials is a major drawback in obtaining their 3D elemental distribution. Combining the 3D-EFTEM with the EST technique in order to obtain high quality reconstruction with the smallest possible electron dose is therefore of high importance.

5.5. References

1. Choi, M. *et al.* Stable single-unit-cell nanosheets of zeolite MFI as active and long-lived catalysts. *Nature* **461,** 246–249 (2009).
2. Vermeiren, W. & Gilson, J.-P. Impact of Zeolites on the Petroleum and Petrochemical Industry. *Top. Catal.* **52,** 1131–1161 (2009).
3. Cejka, J., Corma, A. & Zones, S. I. *Zeolites and Catalysis: Synthesis, Reactions and Applications*.**1,** (Wiley-VCH, 2010).
4. Chen, C.-Y. & Zones, S. I. in *Zeolites and Catalysis: Synthesis, Reactions and Applications* (Cejka, J., Corma, A. & Zones)*,* 155, (Wiley-VCH, 2010).
5. de Jong, K. P. *et al.* Zeolite Y Crystals with Trimodal Porosity as Ideal Hydrocracking Catalysts. *Angew. Chem.* **122,** 10272–10276 (2010).
6. Awala, H. *et al.* Template-free nanosized faujasite-type zeolites. *Nat. Mater.* **14,** 447–451 (2015).
7. Qin, Z., Lakiss, L., Tosheva, L., Gilson, J-P., Vicente, A., Fernandez, C., Valtchev, V., *et al.* Comparative Study of Nano-ZSM-5 Catalysts Synthesized in OH− and F− Media. *Adv. Funct. Mater.* **24,** 257–264 (2014).
8. Mintova, S., Gilson, J.-P. & Valtchev, V., Advances in nanosized zeolites. *Nanoscale* **5,** 6693–6703 (2013).
9. Ng, E.-P., Chateigner, D., Bein, T., Valtchev, V. & Mintova, S. Capturing Ultrasmall EMT Zeolite from Template-Free Systems. *Science* **335,** 70–73 (2012).
10. Tapasztó, L., Dobrik, G., Lambin, P. & Biró, L. P. Tailoring the atomic structure of graphene nanoribbons by scanning tunnelling microscope lithography. *Nat. Nanotechnol.* **3,** 397–401 (2008).
11. van Donk, S., Janssen, A. H., Bitter, J. H. & Jong, K. P. de. Generation, Characterization, and Impact of Mesopores in Zeolite Catalysts. *Catal. Rev.* **45,** 297–319 (2003).
12. Zhengxing Qin, Jean-Pierre Gilson, Valentin Valtchev, Mesoporous zeolites by fluoride etching. *Curr. Opin. Chem. Eng.* **2015,** 1–6 (2015).
13. McDaniel, C. & Maher, P. in *Molecular Sieves* **186,** 186–195 (1968).
14. Young, D. A. Hydrocarbon conversion process and catalyst comprising a crystalline alumino-silicate leached with sodium, US3326797 A, 1967.
15. Valtchev, V., Majano, G., Mintova, S. & Pérez-Ramírez, J. Tailored crystalline microporous materials by post-synthesis modification. *Chem. Soc. Rev.* **42,** 263–290 (2012).
16. Triantafillidis, C. S., Vlessidis, A. G. & Evmiridis, N. P. Dealuminated H-Y zeolites : Influence of the degree and the type of dealumination method on the structural and acidic characteristics of H-Y zeolites. *Ind. Eng. Chem. Res.* **39,** 307–319 (2000).
17. Qin, Z., Shen, B., Yu, Z., Deng, F., Zhao, L., Zhou, S., Yuan, D., Gao, X., Wang, B., Zhao, H., Liu, H, A defect-based strategy for the preparation of mesoporous zeolite Y for high-performance catalytic cracking. *J. Catal.* **298,** 102–111 (2013).
18. Salman, N. *et al.* Effect of temperature and time in the hydrothermal treatment of HY zeolite. *Microporous Mesoporous Mater.* **90,** 339–346 (2006).
19. Abelló, S., Bonilla, A. & Pérez-Ramírez, J. Mesoporous ZSM-5 zeolite catalysts prepared by desilication with organic hydroxides and comparison with NaOH leaching. *Appl. Catal. Gen.* **364,** 191–198 (2009).
20. Groen, J. C. *et al.* Creation of hollow zeolite architectures by controlled desilication of al-zoned ZSM-5 crystals. *J. Am. Chem. Soc.* **127,** 10792–10973 (2005).
21. Verboekend, D. & Pérez-Ramírez, J. Desilication Mechanism Revisited: Highly Mesoporous All-Silica Zeolites Enabled Through Pore-Directing Agents. *Chem. – Eur. J.* **17,** 1137–1147 (2011).
22. Valtchev, V. *et al.* High Energy Ion Irradiation-Induced Ordered Macropores in Zeolite Crystals. *J. Am. Chem. Soc.* **133,** 18950–18956 (2011).
23. Qin, Z. *et al.* Chemical Equilibrium Controlled Etching of MFI-Type Zeolite and Its Influence on

Zeolite Structure, Acidity, and Catalytic Activity. *Chem. Mater.* **25,** 2759–2766 (2013).
24. Valtchev, V., Qin, Z. & Gilson, J.-P. Method for the preparation of synthetic crystalline zeolite materials with enhanced total pore volume, PCT / IB2014 / 001490.
25. Chen, X. *et al.* In situ and post-synthesis control of physicochemical properties of FER-type crystals. *Microporous Mesoporous Mater.* **200,** 334–342 (2014).
26. Louis, B. & Kiwi-Minsker, L. Synthesis of ZSM-5 zeolite in fluoride media: an innovative approach to tailor both crystal size and acidity. *Microporous Mesoporous Mater.* **74,** 171–178 (2004).
27. van Bekkum, H., Geus, E. R. & Kouwenhoven, H. W. in *Studies in Surface Science and Catalysis* (ed. J.C. Jansen, M. S., H. G. Karge and J. Weitkamp) **85,** 509–542 (Elsevier, 1994).
28. Häfele, M., Reitzmann, A., Roppelt, D. & Emig, G. Hydroxylation of benzene with nitrous oxide on H-Ga-ZSM5 zeolite. *Appl. Catal. Gen.* **150,** 153–164 (1997).
29. Jayamurthy, M. & Vasudevan, S. Methanol-to-gasoline(MTG)conversion over ZSM-5. A temperature programmed surface reaction study. *Catal. Lett.* **36,** 111–114 (1996).
30. Ono, Y., Adachi, H. & Senoda, Y. Selective conversion of methanol into aromatic hydrocarbons over zinc-exchanged ZSM-5 zeolites. *J. Chem. Soc. Faraday Trans. 1 Phys. Chem. Condens. Phases* **84,** 1091–1099 (1988).
31. Olson, D. H., Kokotailo, G. T., Lawton, S. L. & Meier, W. M. Crystal structure and structure-related properties of ZSM-5. *J. Phys. Chem.* **85,** 2238–2243 (1981).
32. van der Gaag, F. J. *ZSM-5 type zeolite: Synthesis and use in gas-phase reactions with ammonia*. Technische Universiteit Delf, TR (1987).
33. Dedecek, J., Balgová, V., Pashkova, V., Klein, P. & Wichterlová, B. Synthesis of ZSM-5 Zeolites with Defined Distribution of Al Atoms in the Framework and Multinuclear MAS NMR Analysis of the Control of Al Distribution. *Chem. Mater.* **24,** 3231–3239 (2012).
34. Slamet, S., Nasikin, M., Tsutsui, T. & Kojima, T. Review on H-ZSM-5 Catalyst for Production of Hydrocarbons From Renewable Organic Compounds. *Jurnal Teknologi* 328–336 (2008).
35. Advanced DigitalMicrograph Software Training, at <http://www.gatan.com/advanced-digitalmicrograph-software-training>
36. Kremer, J. R., Mastronarde, D. N. & McIntosh, J. R. Computer Visualization of Three-Dimensional Image Data Using IMOD. *J. Struct. Biol.* **116,** 71–76 (1996).
37. Agulleiro, J. I. & Fernandez, J. J. Fast tomographic reconstruction on multicore computers. *Bioinformatics* **27,** 582–583 (2011).
38. Mao, Y., Fahimian, B. P., Osher, S. J. & Miao, J. Development and Optimization of Regularized Tomographic Reconstruction Algorithms Utilizing Equally-Sloped Tomography. *IEEE Trans. Image Process.* **19,** 1259–1268 (2010).
39. Scott, M. C. *et al.* Electron tomography at 2.4-angstrom resolution. *Nature* **483,** 444–447 (2012).
40. Chen, C.-C. *et al.* Three-dimensional imaging of dislocations in a nanoparticle at atomic resolution. *Nature* **496,** 74–77 (2013).
41. Seaton, N. A. Determination of the connectivity of porous solids from nitrogen sorption measurements. *Chem. Eng. Sci.* **46,** 1895–1909 (1991).
42. Breck, D. W. Crystalline zeolite Y. U.S. Patent 3, 130,007 April 21, (1964).
43. Zheng, Y., Li, X. & Dutta, P. K. Exploitation of Unique Properties of Zeolites in the Development of Gas. *Sensors* **12,** 5170–5194 (2012).
44. Boddenberg, B., Rakhmatkariev, G. U., Hufnagel, S. & Salimov, Z. A calorimetric and statistical mechanics study of water adsorption in zeolite NaY. *Phys. Chem. Chem. Phys.* **4,** 4172–4180(2002).

Conclusions and perspectives

In this thesis, advanced Transmission Electron Microscopy (TEM) techniques were used to investigate the properties of three types of functionalized materials: nanopatterned few-layer graphene (FLG), carbon nanotubes (CNTs) and mesoporous zeolites.

Catalytic hydrogen-carbon reactions were used in the nanopatterning of FLG flakes by iron nanoparticles with a network of highly orientated channels. At first, the properties of the nanoparticles' motion during the channeling action were studied *ex-situ* by electron tomography. The results revealed the strong influence of both the topography of the FLG substrate and the morphology of the active nanoparticles in defining the characteristics of the channeling process. The nanoparticles initially located at the edges or attached to the steps on the FLG flakes create open-surface channels and tunnels with orientations, lengths and morphologies defined by the crystallography and the topography of the carbon substrate. The cross-sectional analysis of the 3D volumes highlights the role of the active nanoparticles' geometric profile on the channel size and shape, with emphasis on the evolution of the basal plane within the resulting channels. The real-time observation of the channeling process in an environmental gas cell (Protochips™ Atmosphere) focused on understanding the influence on the nanoparticles' morphology in the nanopatterning dynamics. It revealed a more complex channeling mechanism than the *ex-situ* investigations predicted. The channeling rates were not constant as the nanoparticles' velocity varied from a few $nm \cdot s^{-1}$ to a few hundred $nm \cdot s^{-1}$. The continuous restructuring of the quasi-melted iron nanoparticles was proposed to be at the origin of the channeling rates variation. The existence of two cutting mechanisms, edge recession and straight channeling, and the permanent shifting of an active nanoparticle between them, were associated with the existence of an affinity between some nanoparticles' facets to certain crystallographic orientations of the FLG substrate. As showed by the direct observation of the nanoparticles during the change of the cutting direction, this affinity can also be responsible for the nanoparticles' turning on FLG's uniform areas.

Later, the controlled transfer of iron nanoparticle on suspended graphene flakes was achieved and observed in real-time using a TEM-STM holder (Nanofactory™). In studying the electromigration of iron-based nanoparticles from carbon nanotubes, we have shown the

availability of all the ingredients necessary for printing discrete digits at the nanoscale level. A Joule-induced annealing procedure has been designed to ensure a reproducible behavior of the tube acting as the "pen" in the writing process. The tube filled with metal can then deposit, through an Ostwald-like ripening mechanism, metal nanoparticles on the surface of the graphene sheet in a position-controlled way. Reversing the voltage ensures the electromigration of the nanoparticles from the graphene surface into the nanotubes, demonstrating the erasing capability of the carbon nanotube "pen", thus opening the way for error corrections. The protocol of reaching the control of the transfer, the chemical and structural transformations undergone by the $Fe_{3-x}O_4$ nanoparticles and the CNT, the growing mechanism of the newly formed nanoparticles and other related phenomena are investigated.

In the last part of the thesis, the evolution of the secondary mesoporosity in fluoride treated zeolites was studied using low-dose bright field electron tomography. Besides understanding the dissolution mechanism of the Si/Al framework in ZSM-5 and Y zeolites, the approach manages to increase the viability of the electron tomography in extracting quantitative data as the pore size and their spatial distribution, the overall porosity and the connectivity of the porous network. The above presented parameters were used to create an evolution model of the secondary porous network as a function of the fluoride etching times. A resolution higher than 1.1 nm was reported, allowing the direct visualization of the microporous cages in ZSM-5 zeolites and the interface of different crystalline domains in zeolite Y.

The studies presented in this thesis open new perspectives for the optimization of the properties of the carbon nanostructures and zeolitic materials and for the development of new investigation approaches based on electron tomography techniques. Combining the *in-situ* TEM techniques with electron tomography, both in real-time or in post-reaction mode, will allow a precise quantification of the reaction dynamics and the effects on the investigated materials.

Annex A

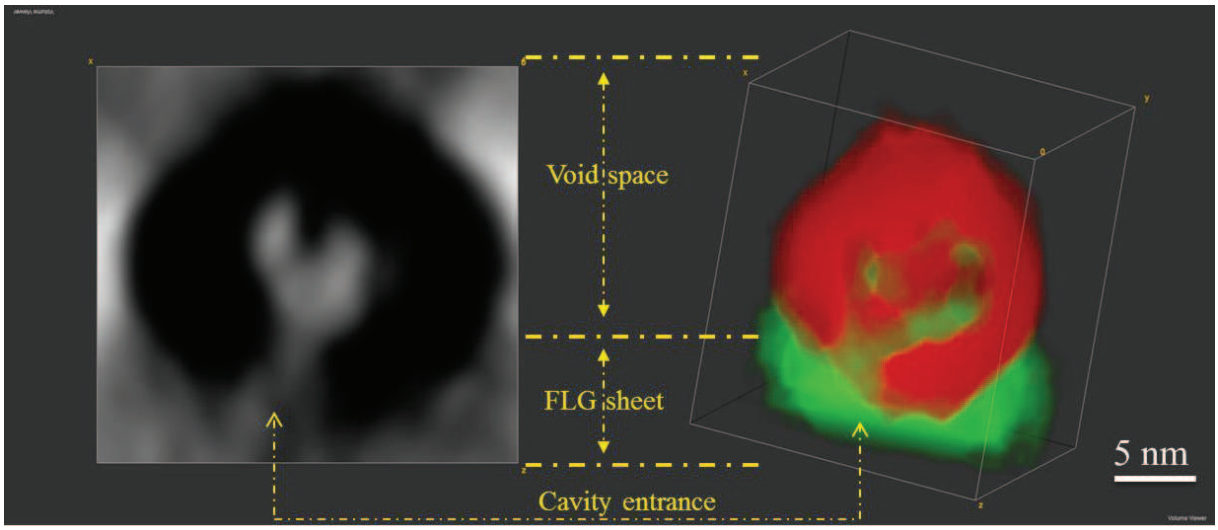

Figure A2.1 Electron tomography investigation of the hollow iron oxide nanoparticles. Left: cross-sectional slice through a hollow NP; the shell cavity in contact with the FLG sheet. Right: the corresponding 3D model with iron-based NP in red FLG sheet in green.

Annex B

Article accepted for publication in Chemistry – A European Journal, 2015

3D study of morphology and dynamics of zeolite nucleation

G. Melinte, V. Georgieva, M-A. Springuel-Huet, A. Nossov, O. Ersen, F. Guenneau, A. Gedeon, A. Palčić, K. N. Bozhilov, C. Pham-Huu, S. Qiu, S. Mintova and V. Valtchev

Abstract

The principle aspects and constrains of the dynamics and kinetics of zeolite nucleation in hydrogel systems are analyzed on the basis of a model Na-rich aluminosilicate system. A detailed time-series EMT-type zeolite crystallization study in the model hydrogel system is performed in order to elucidate the topological and temporal aspects of zeolite nucleation. A comprehensive set of analytical tools and methods is employed to analyze the gel evolution complementing the primary methods of transmission electron microscopy (TEM) and nuclear magnetic resonance (NMR) spectroscopy. TEM tomography reveals that the initial gel particles exhibit a core-shell structure. Zeolite nucleation is topologically limited to this shell structure and the kinetics of nucleation is controlled by the shell integrity. The induction period extends to the moment when the shell is consumed and the bulk solution can react with the core of the gel particles. These new findings, in particular the importance of gel particle shell in zeolite nucleation, can be used to control the growth process and properties of zeolites formed in hydrogels.

Introduction

Aluminosilicate zeolites are amongst the most widely used heterogeneous catalysts and molecular sieves in petroleum refining, petrochemistry, fine chemical production and pollutant abatement. Their application in large scale chemical processes and environmental protection is equally important. Hence, the engineering of zeolite materials remains a challenge that motivates academic and industrial researchers. This challenge is particularly important nowadays with the changes in quality and constitution of available fossil hydrocarbons that remain the most important energy sources, as well as the new implemented environment protection regulations.[1] Often the zeolite crystals are subjected to post-synthesis modification in order to face the requirements of a particular chemical process.[2] The successful use of post-synthesis methods, however, strongly depends on the intrinsic characteristics of zeolite crystals, that is, the way the crystals are synthesized. Thus, the fine control of zeolite formation is indispensable for the preparation of high quality materials and their further use.

The general model describing the zeolite formation mechanism was established long time ago.[3] The classical theory used for describing the nucleation under hydrothermal conditions postulates that the system is expected to reach a certain level of supersaturation before the first nuclei are formed.[4] Further, the viable nuclei grow at the expense of nutrient dissolved and transported via the supernatant to growing crystal. However, contemporary growth models agree that zeolite formation does not follow the classical model of crystallization in supersaturated systems.[5] Something more, the reaction pathway depends on the initial composition and reactants used and may differ even for a particular zeolite.[6] A zeolite framework type can be

synthesized from different initial systems, ranging from optically clear water solutions through hydrogels to very thick gels. Although, structurally the products obtained from such systems are similar, their physical and chemical features usually are different. For instance, the particle size, morphology and the level of aggregation will be different for each of the above described initial systems. Further, the chemical composition and the distribution of framework cations are controlled also by the employed initial systems. Therefore, the control of the nucleation process and the following crystallization steps is indispensable if the goal is the rational control of zeolite properties.

The progress in the molecular understanding of zeolite growth mechanism had advanced substantially during the last decade. The use of very diluted systems containing well defined discrete particles allowed to shed more light in the formation of primary particles and their aggregation into larger units that exhibit long range order.[7-21] Most of these studies were performed on transparent solutions obtained by mixing TPAOH - TEOS - H_2O that yield silicalite-1 (MFI-type). Very recently, again such a solution was employed in an *in situ* AFM study with the goal to discriminate the species participating in the growth process.[22] According to this study both silica molecules and preformed nanoparticles participate in the growth process showing again that the zeolite formation may include both classical and non-classical crystallization pathways.

Hydrogels containing alkali metal cations are used in the industrial mass production of zeolites. Such systems are not uniform; they exhibit distinct solid and liquid parts. Besides their physical appearance, the hydrogels are not uniform in chemical composition, which is due to uncontrolled polymerization of the silica/alumina species after mixing of the reactants.[23-28] The so-called autocatalytic nucleation model was applied by Subotić and co-workers to explain crystal growth in such system.[29] According to their model the nuclei are formed in the gel and liberated in the mother liquor before the growth ensues. Increase in the surface area of the growing nuclei accelerates the reaction rate. Thompson revised this model and postulated that the dormant nuclei are located near the surface of the gel particles.[30] Our studies on very small initial gel particles showed that the nucleation and growth can take place via propagation of crystalline phase through the amorphous network.[31] Nucleation and growth was observed in discrete gel particles that do not change substantially their size during the transformation of amorphous into crystalline material. The system used in the latter case was rich of organic structure directing agent and the crystallization was performed at room temperature. Lately, this crystallization mechanism was extended to organic template-free initial systems.[32,33] The careful preparation of the initial systems allowed stabilization of the discrete gel particles, although the systems contained large amounts of sodium hydroxide. However, such conditions are difficult to be utilized on an industrial scale and the process of nucleation in mass production of zeolites is highly uncontrolled. Consequently, the crystalline products differ in size and level of agglomeration. A better understanding of the mechanism of zeolite nucleation in conventional hydrogel system would allow better control of the growth process and consequently the properties of the final crystalline product.

The objective of the present study is to explore the nucleation process in a conventional hydrogel system. More precisely, the goal is to determine the temporal and spatial aspects of the formation of the first nuclei by following the chemical and physical evolution of the solid phase. In order to reach this goal a system yielding a zeolite with great industrial potential was employed. The crystallization was performed at a temperature close to ambient conditions to

slow down the crystal growth kinetics in order to distinguish between different crystallization steps. Methods commonly used in the characterization of crystalline porous materials were employed. The study was primarily based on complementary TEM methods, as electron tomography (ET), high resolution TEM (HRTEM), and energy filtered TEM (EFTEM). TEM analyses were combined with hyper-polarized ^{129}Xe NMR, which was used to determine the first zeolite cages formed in the solid. Thus, a complete picture of physical and chemical changes in gel precursor was obtained.

Results

General characterization

The crystal growth kinetics was studied by XRD analysis. The obtained solids appeared amorphous up to 18 h of hydrothermal treatment (See Figure S1). Distinct diffraction peaks associated with EMT-type zeolite emerged after 24 h of hydrothermal treatment (Figure S1). The crystallinity increased gradually to 36 h of synthesis. Further extension of crystallization time did not result in a product with higher X-ray crystallinity. The XRD peaks were relatively large phenomenon, which was attributed to the small size of the crystalline domains. The Si/Al ratio of the highly crystalline EMT-type zeolite obtained after 36 h, determined by ICP analysis, was 1.18.

The SEM analysis of the samples confirmed that the gel and zeolite particles are very small and it was difficult to distinguish their detailed morphology. The zeolite crystals from longer run durations form complex aggregates with random shapes (Figure S2).

N_2 sorption measurements corroborated the XRD data. The isotherms of the sample taken between 0 and 18 h are typical of non porous materials with negligible micropore volume. The specific surface area of these samples was also low. The initial gel exhibited a S_{BET} of 12 $m^2 g^{-1}$ that corresponds to spherical particles with diameter of about 350 nm. The specific surface area slowly increased during the induction period from 16 to 48 cm^2g^{-1} for the samples synthesized for 6 and 18 h, respectively. Substantially different surface and porous characteristics could be observed after the formation of crystalline phase. The sample from run duration of 24 h exhibits type I isotherm (Figure S3). After rapid uptake at low relative pressure a slight inclination of the curve and a second uptake at high relative pressure could be observed. These particularities of the isotherm, which are not typical of crystalline microporous materials, revealed the presence of some mesopores. The samples synthesized for 30 and 36 h showed a slight increase of micropore volume, but the differences with the sample from the 24 h experiment were not significant. Therefore it could be concluded that the mass transformation from amorphous into crystalline EMT-type material took place between 18 and 24 h of treatment. The sample obtained after 24 h of hydrothermal treatment exhibits a S_{BET} of 478 cm^2g^{-1} and micropore volume of 0.19 cm^3g^{-1}.

TEM study

The crystal growth kinetics of the system yielding EMT-type zeolite was followed by means of transmission electron microscopy. A collection of representative TEM images of amorphous precursors and crystalline product is shown in Figure 1.

Through conventional TEM imaging we were able to follow the morphological changes of the solid phase. The initial gel (Figure 1a) is built of oval gel particles creating more complex aggregates. The mesopores appear as “white spots” inside the gel network.[34] These mesopores

are filled with liquor from the mother solution as shown in the Movie 1 (Supplementary information). To verify this interpretation the high energy electron beam was focused in a probe with small diameter and high beam current on a nanometric gel particle causing rapid increase in the temperature of the irradiated zone. This led to disappearance of most of the mesopores by forcing the liquid outside the pores and inducing secondary phase growth (see Movie 1, Supplementary information).

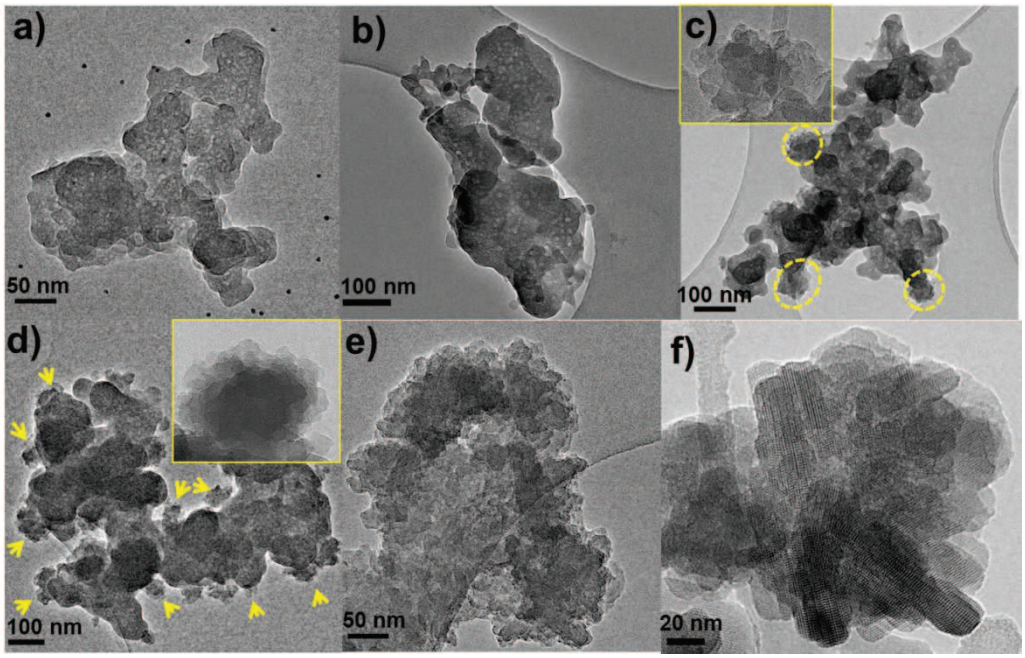

Figure 1. TEM images of the solid phase obtained in the system yielding EMT-type zeolite at 40 °C: a) initial gel (0 h), b) 6 h, c) 12 h, d) 18 h, e) 24 h, f) 36 h. The yellow ellipsoids and arrows from c) and d) highlight the presence of crystalline non-porous areas (see the insets).

The morphology of the gel changed after 6 h of hydrothermal treatment (Figure 1b). The individual gel particles could be distinguished more easily and the presence of straight edges points towards development of certain order within the solid. The "white spots" attributed to mesopores were observed as well. Crystalline particles aggregates with size of about 50 nm built up by very small crystallites were clearly identified after 12 h of crystallization (Figure 1c-yellow ellipsoids). Very few crystalline particles could be identified in the solid, while the amorphous particles did not change substantially their physical appearance in respect to the 6 h sample. The area occupied by the crystalline regions and their abundance continued to increase for the 18 h sample (Figure 1d-yellow arrows). It is worth recalling that the XRD pattern of the sample did not reveal presence of crystalline phase at this stage (Figure S1). The mass of crystalline phase and the size of the crystallized domains are obviously below the detection limit of XRD technique, which is between 3 and 5 wt.%. The product obtained after 24 h consisted mostly of crystalline zeolite (Figure 1e). Porous amorphous particles were replaced completely by apparently non-porous crystalline aggregates. An image of the completely crystallized zeolite obtained after 36 h of treatment is presented in Figure 1f.

The data above provides only a macro-morphological description of the solid phase without offering an insight into the nanoscale features (molecular level). Since conventional TEM

imaging provides essentially a 2D projection of 3D objects and features, it offers limited information about the topology, size distribution, and spatial connectivity in the case of a complex porous network inside aggregates such as we have in the studied samples. We have attempted to resolve this limitation by utilizing the capabilities of electron tomography (ET). Further to ensure that the porous structure is preserved intact and not modified by electron beam interaction, cryo-TEM at -70 °C was utilized to collect TEM images for tomography reconstruction.

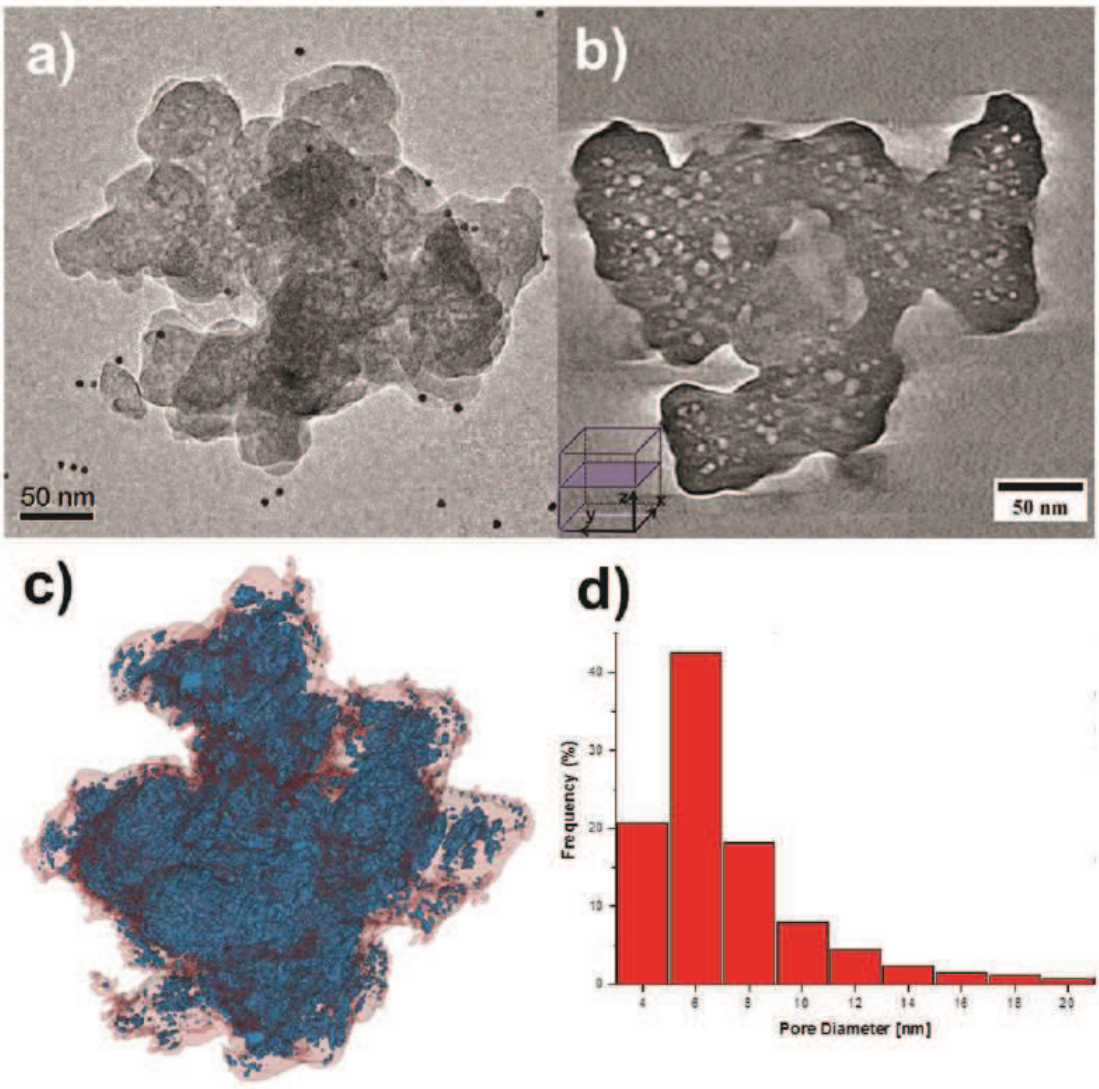

Figure 2. a) Conventional TEM image of a gel particle form the initial run (0 h) used for cryo-ET; b) XY slice through the reconstructed volume of the gel particle; c) general view after segmentation of the gel particle (pores are represented in blue and the gel body in semi-transparent red); d) pore size distribution in the gel particle extracted from the cryo-ET segmented data.

A conventional TEM image at 0° tilt of the specimen from the initial run (0 h) is shown in Figure 2a. The existence of the porous structure can be observed clearly. However, useful

information is difficult to extract due to the 2D nature of the TEM images and the overlap of features positioned at different depth along the electron beam direction. Figure 2b shows a XY slice (thickness of 0.25 nm normal to the plane of view) extracted digitally from a cryo-tomogram created by acquiring tilt-series of images from the gel particle shown in Figure 2a. It can be observed easily that the pores, between 3 and 20 nm in diameter are uniformly distributed throughout the gel particle volume. It is important to note, that the pores do not communicate directly with the external surface of the gel particle. A non-porous zone with a thickness of about 7 to 15 nm covers the entire gel particle and seals the pores inside. To assess the detailed 3D topology of the pore structure the gel particle volume was reconstructed from the tilt-series images. Figure 2c represents an image of the reconstructed gel particle, obtained after segmentation, where the pores are represented in blue and non-porous part in semi-transparent red. The generated model (see Movie 2, Supplementary information) shows clearly that the surface of the gel particle is depleted of pores, which tend to be concentrated in the particle center. A quantitative porosity analysis (see Materials and Methods) reveals an overall porosity of about 22%. The pore size distribution (represented as a function of the frequency of abundance) extracted from the reconstructed volume is centered on ~6 nm with more than 40% of the pores having a diameter between 5 and 7 nm.

The gel treated hydrothermally for 6 h showed the same porous features as the initial gel obtained at room temperature (Figure 3a). However, the appearance of small faceted non-porous regions (red rectangles) with straight edges reveals that the crystallization process had already started. The extreme instability of these crystalline-appearing features under the electron beam even under cryo-TEM conditions precluded direct confirmation by electron diffraction or lattice imaging of a long-range order for the sample treated for 6 h. However, analysis of the subsequent evolution stages of the crystallization process showed clearly that the zeolite's crystallization starts within these faceted regions. The regions with faceted morphology did not contain any pores (Figure 3a). At the 6 h stage a few of these crystalline particles were observed. They form 10-20 nm aggregates situated in the peripheral part of much larger amorphous aggregates. It is difficult to determine whether the crystalline particles are isolated or a continuous part of the amorphous aggregate they are attached to. Most of them are isometric suggesting that crystallization most probably took part around a single crystallization center. The size and abundance of these faceted non-porous regions increased for the sample treated for 12 h suggesting a more extensive process of reorganization and condensation of the aluminosilicate species. Figure 3b presents a particle from the 12 h experiment with such a dual morphology. A HR-TEM confirmed unambiguously the crystalline order and the presence of zeolite micropores (Figure 3c inset). The regions comprising these primary zeolite crystals are localized exclusively in areas free of pores and in the shell of the original gel particles (Figure 2c).

The XY slices (Figure 3c and d) through the reconstructed volume of a particle clearly show the difference in morphology between porous and non-porous regions in the sample treated for 12 h. Furthermore, the morphology of the non-porous regions had changed by developing rough faceted exterior surfaces with an acicular aspect and the abundance and relative volume of these regions had increased compared with the 6 h sample. Interestingly, a small particle is situated inside each mesopore (from the amorphous area) close to its center. Evidently these particles were formed in the process of gel evolution in the time interval between 6 and 12 h. It can be inferred that the mother liquor imprisoned during the initial gel formation has reacted with the aluminosilicate network and has yielded these particles. The attempts to obtain high resolution images or selected area electron diffraction (SAED) of such particles were not

successful due to their instability under the electron beam. It was not possible to determine their chemical composition either. Therefore, it was not possible to prove whether the mesopores/mesocavities have served as micro-reactors yielding zeolite proto-nuclei. The solid particles observed inside the mesopore space could be a metastable phase that disappears in the process of zeolite formation.

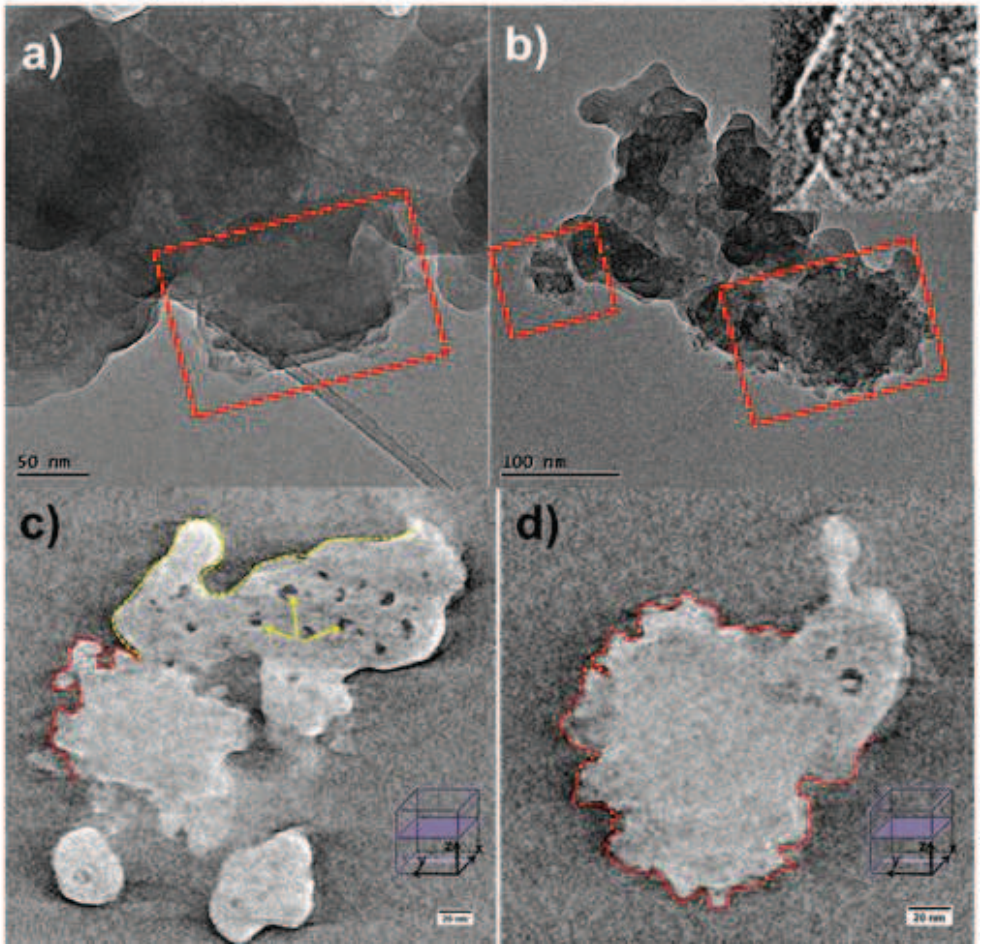

Figure 3. a) TEM image of a 6 h zeolite particles with a dual morphology: porous and non-porous (red rectangles); b) 12 h zeolite sample with a dual morphology (the inset is a HRTEM image of the microporous cages formed in the non-porous regions –in red); c) and d) XY slices through the reconstructed volume of a 12 h zeolite sample.

Cryo-electron tomography (cryo-ET) was performed on the 12 h sample in order to obtain quantitative information about the morphology, topology, distribution, and size of the mesopores. Figure 4a shows a conventional TEM image of a gel particle at 0° tilt, while Figure 4b shows a XY slice through its reconstructed volume. The pore distribution inside the 12 h hydrothermally treated particle is similar to the initial gel particle (0 h). The cavities are isolated and do not communicate with the external surface of the gel particle (see Figure 4c and Movie 3, Supplementary information). Moreover, the pore size distribution is also centered around 6 nm but with a small (5%) decrease in number for the 5-7 nm region and a 10% increase for the 3-5 nm region. The porosity of the core part for the 12 h sample is lower (~17%) than the initial gel

porosity (~22%). The overall porosity, including the non-porous crystalline regions, is about 14%. The pore size distribution is centered around 5 nm.

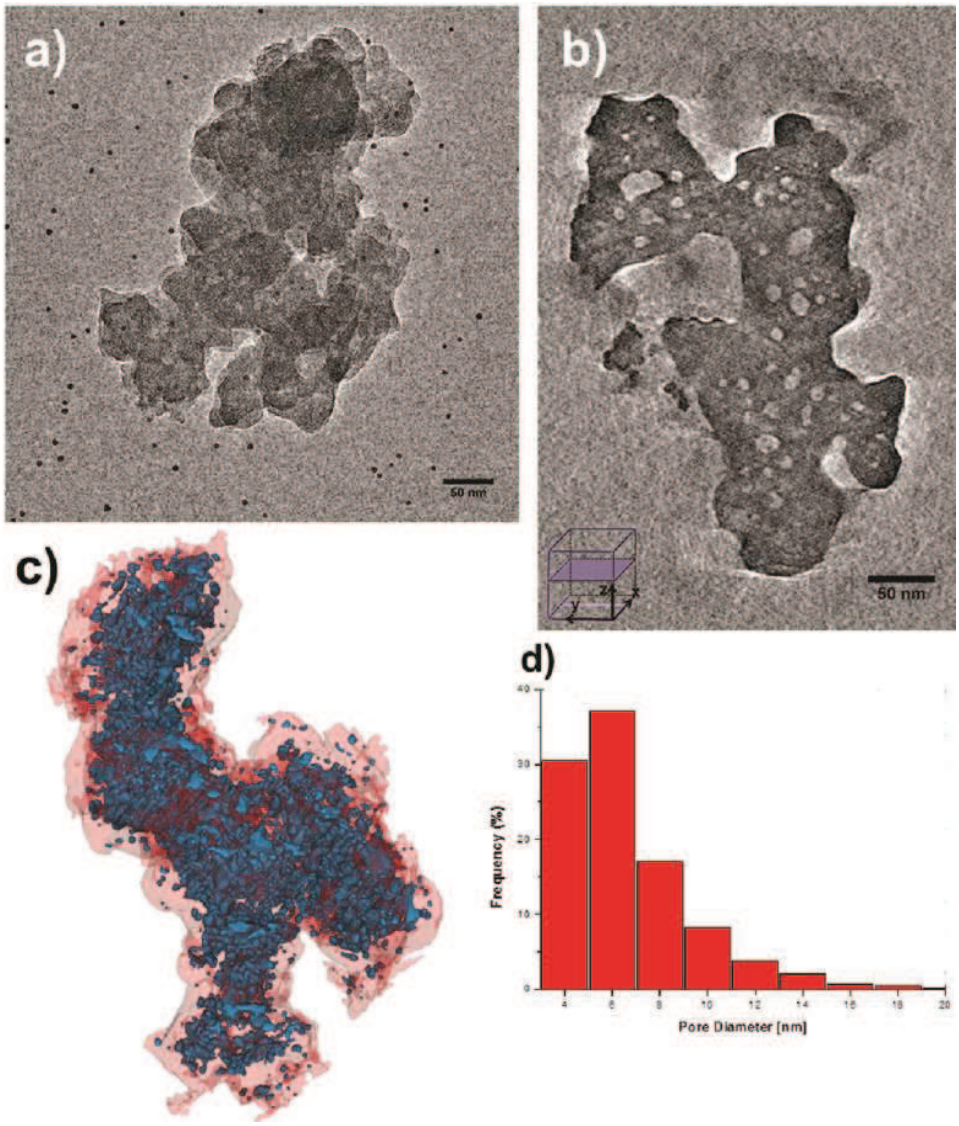

Figure 4. a) Conventional TEM image at 0° tilt of a gel particle from the sample treated hydrothermally for 12 h; b) XY slice through the reconstructed volume of the particle in Figure 4a obtained by cryo-ET; c) digitally reconstructed gel particle after segmentation: pores are represented in blue and the gel body in semi-transparent red; d) pore size distribution of the 12 h sample extracted from the cryo-ET data.

The solid particles exhibit the same dual morphology after 18 h of hydrothermal treatment (Figure 1d). However, the volume fraction of the non-porous regions has increased at the expense of porous ones. The mass transformation of amorphous into crystalline type material took place between 18 and 24 h. As can be seen in Figure 5a, the solid particles of the 24 h sample are aggregates of nanosized crystallites. In the core of aggregates the crystals are smaller (10 – 20 nm) and do not exhibit a defined morphology, while at the periphery the typical for EMT-type zeolite hexagons with platy morphology can be seen. The surface of aggregates has jagged outlines due to the well developed faces of individual crystals. Figure 5b shows a XY slice through a zeolite aggregate particle from the 24 h sample reconstructed digitally from cryo-ET data. It highlights the exterior surface roughness and the complete disappearance of mesopores abundant in the amorphous precursor. The morphology of the zeolite aggregates obtained after 30 h of treatment resembles those from the 24 h sample. However, the formation of prismatic elongated nanostructure (highlighted by yellow dotted lines) on their surface can be observed easily (Figure 5c). As the HR-TEM images in Figure 5d shows, the zeolite crystallization seems to have been completed after 30 h.

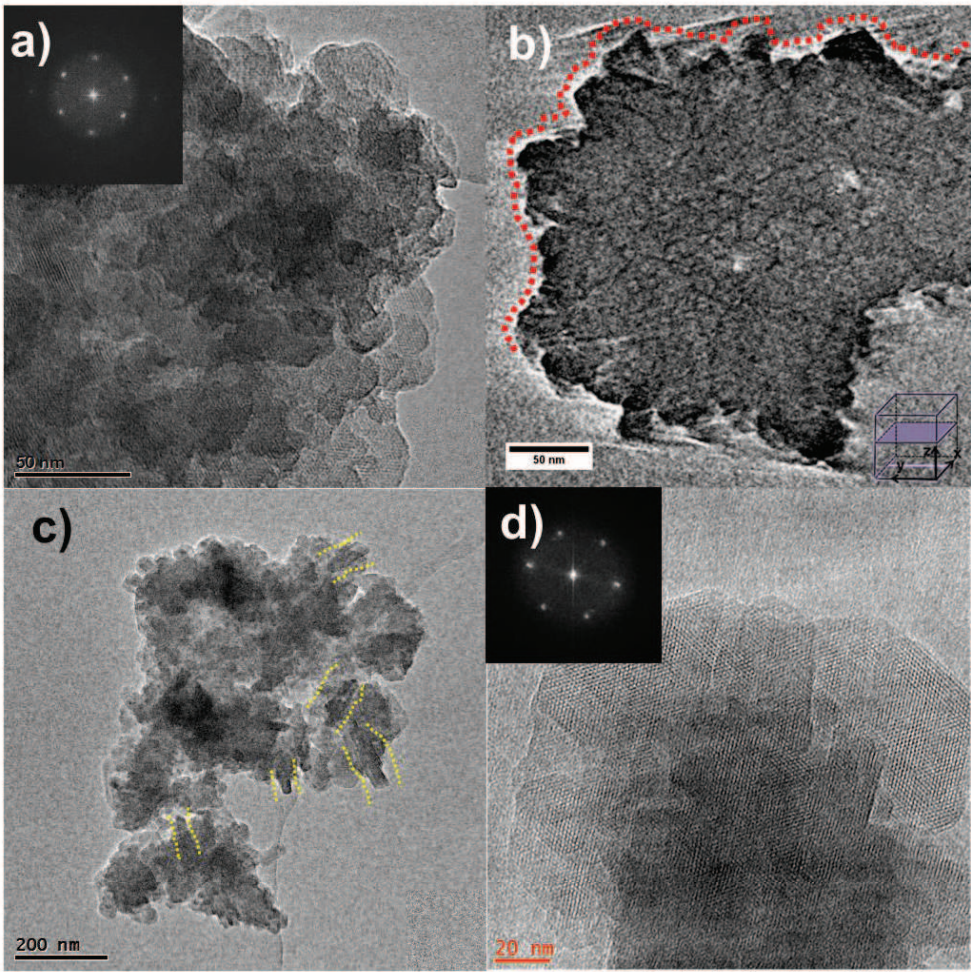

Figure 5. a) TEM image of a 24 h zeolite sample with its FFT inset; b) XY slice through the reconstructed volume of a 24 h zeolite sample, red dotted line outlines the jagged outer edges of the aggregate particle; c) conventional TEM image of a 30 h zeolite sample with the prismatic structure highlighted with yellow dotted lines; d) ABSF filtered HRTEM image of a 30 h sample with its FFT inset.

Analytical TEM investigations

The spatial distribution of the Si and Al was investigated using energy filtered TEM (EFTEM). The instability of the specimens under the high energy electron beam, especially for the amorphous particles, limited the analysis to Si and Al. Oxygen and sodium maps were not acquired. The statistical analysis of the Si and Al distributions (between 5 and 10 grains selected for each sample) showed that both elements are homogeneously distributed in the individual gel particles and crystalline aggregates throughout the entire hydrothermal treatment. Supplementary Figure S4a shows elemental maps of a gel particle while in Figure S4b the maps of a 12 h sample with a dual porous and non-porous morphology is presented. As can be observed there is no difference in the elemental distribution between the porous region (amorphous) and the non-porous one (crystalline). The almost fully crystalline 24 h zeolite grain (Figure S4c) shows the same homogeneity. Nevertheless, a small increasing in the Al concentration on the grains edges is occasionally observed. The energy dispersive X-ray spectroscopy (EDS) showed a small change in the concentration of the alumina and silica species between the initial gel and the final zeolite sample. The average anhydrous composition normalized to 100% and excluding Na_2O is Al_2O_3 43.6 wt.% and SiO_2 56.4 wt% for the particles in the initial gel, while after 30 h of treatment the composition is 45.7% Al_2O_3 and 54.3% SiO_2

Raman study

Raman spectroscopy is used often to study the extent of polymerization of the SiO_4 tetrahedra, their connectivity and the formation of different ring structures in zeolite materials. We have employed Raman analysis to examine the changes in the solid during the induction period (from 0 to 24 h treatment). During the first 12 h no substantial changes in the gel structures were detected (Figure S5). Only a broad peak at about 500 cm^{-1} was observed which is characteristic for four member rings (4MRs) in tectosilicate structures formed by four $Si(Al)O_4$ tetrahedral sharing two common oxygen atom.[35] Obviously these are the units that dominate the amorphous material. The intensity of the peak at 500 cm^{-1} is increased significantly for the 18 h sample suggesting that the 4MRs have become more rigid, statistically more prominently present and they are most probably integrated in larger structures. The broad character of the peak is preserved confirming that there is still significant degree of disorder and randomness in the polymerization among the aluminosilicate tetrahedra. Two additional new weak peaks can be distinguished in the spectrum of this sample. The one at 380 cm^{-1} could be attributed to 6-member rings typically present in sodalite cages.[36] The second peak, at 290 cm^{-1}, is characteristic for rings formed by more than 6 tetrahedra. In the present case this peak could be attributed to 12-member ring pore opening typical for the EMT-type structure.[36] The appearance of these two peaks suggests that a certain number of EMT-cages have been formed in the solid after 18 h of treatment. The XRD pattern of this material (Figure S1) lacks any peaks indicating that the polymerization of the aluminosilicate tetrahedra has mostly short range extent and it lacks the extended long range periodicity typical for crystalline matter. Based on these results, one can conclude that, the starting gel has undergone significant reorganization after 18 h of treatment and EMT-type units are formed and stably present in the amorphous gel particles but the connectivity between the individual units is limited and no long-range order exists. The fast crystalline growth between 18 and 24 h of hydrothermal treatment supports this interpretation.

^{129}Xe NMR study

Unlike conventional or thermal ^{129}Xe NMR in which the nuclear spin polarization is governed by Boltzmann equilibrium, laser-polarized ^{129}Xe NMR is based on magnetic nuclear hyperpolarization obtained by magnetization transfer from Rb alkali-metal electronic spins optically pumped. The ^{129}Xe signal sensitivity is enhanced by 10^3–10^5 fold even at diluted Xe loading. Thus, the hyperpolarized (HP) ^{129}Xe NMR technique is particularly useful for systems with low surface areas and/or long spin–lattice relaxation times (T_1), and has found widespread applications, for example, in characterization of surfaces, nanocrystals or thin films, porous materials, magnetic resonance imaging and medical imaging, sensors, etc.[37-41]

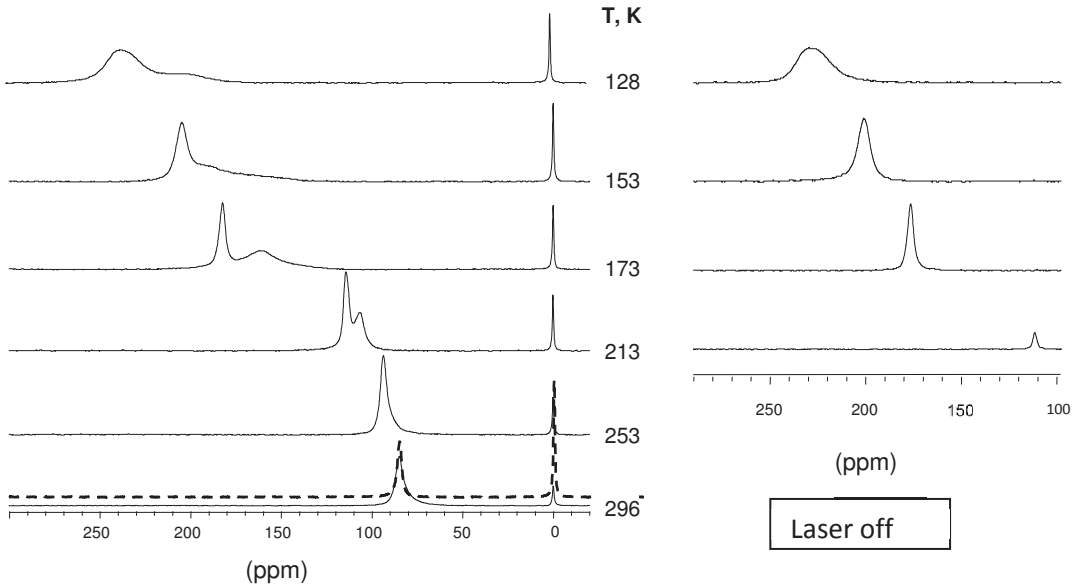

Figure 6. ^{129}Xe NMR spectra versus temperature of xenon adsorbed in the sample from the 36 h run duration. On the right hand side, spectra recorded with the lasers off (for $T \leq 213$ K). A spectrum of EMT sample synthesized with 18-crown-6 ether is shown by a dashed line. The intensity of the spectra is arbitrary.

The characterization of the synthesis run products in this study by XRD and TEM showed that after 24 h of hydrothermal treatment the samples are crystalline. Although the 30 h sample is highly crystalline we have used the 36 h synthesized sample for ^{129}Xe NMR study in order to further minimize any possible interference by amorphous material. Variable-temperature (between 296 and 128 K) spectra of the sample measured with hyperpolarized xenon are presented in Figure 6. At 296 K, in addition to the gas phase line at 0 ppm, the spectrum exhibits a single line, at 85 ppm, corresponding to adsorbed xenon. This shift is completely consistent with the ^{129}Xe NMR spectrum that we recorded with a reference EMT-type sample synthesized with 18-crown-6 ether as templating agent.[42] As temperature decreases, its chemical shift in the NMR spectrum increases and the signal splits into two components which become broader. Spectra were also recorded with the lasers off at temperatures below 213 K. Under such conditions one peak is present corresponding to the high chemical shift line of the HP spectra. This peak is due to purely thermally-polarized Xe below 193 K proving that the HP Xe nuclei

lose their polarization rapidly in the zeolite pores and are not exchanged by HP Xe during the time delay between two subsequent radiofrequency pulses. The low-chemical-shift peak, appearing when temperature is decreased, can be attributed to the fraction of Xe atoms exchanging between the gas phase and adsorbed phase. This shift is temperature independent and characteristic for HP Xe, since it disappears when the laser is switched off. The presence of such an exchange is not surprising since the crystals have nanometric size and the Xe atoms may diffuse in and out of the crystallites during the NMR measurement timescale. If the pore space or gaps between the crystalline particles are reduced, for example when the powder sample is compressed, then the intensity of this peak decreases and ultimately disappears at $T < 173$ K (Figure S6).

At room temperature, the two peaks cannot be distinguished because all the adsorbed Xe atoms are in exchange with the gas phase. Taking the formalism of Jameson et al.[43] the crystals can be divided into two parts: a peripheral shell (called reservoir III) in which the adsorbed Xe atoms can exchange with the gas phase surrounding the crystals and an inner part (called reservoir IV) in which the adsorbed Xe atoms cannot exchange with the gas phase. Xe diffusion depends on multitude of factors. Of primary importance are pore size of the materials, pore connectivity and temperature. This means that the relative importance of these two reservoirs varies with the crystal size. The crystals in the samples of the present study have nanometric dimensions and, at room temperature, they can be considered essentially as reservoirs of type III. As the temperature decreases, the mobility of Xe atoms decreases and the inner part of the crystals becomes a reservoir of type IV. Therefore, two signals are detected; the most shifted corresponds to reservoir IV and the other, mostly hyperpolarized, even at low temperature, to reservoir III. This is consistent with the fact that the most shifted signal becomes a "thermal" signal (vide supra). We can also notice that, when the signal splits as the temperature decreases, below 233 K, the chemical shift of the reservoir IV signal increases rapidly (Figure S7). This is also consistent with the fact that there is no longer exchange with the gas phase therefore the chemical shift of adsorbed Xe is no longer averaged by that of the Xe gas (0 ppm).

Large channels are present in the alumosilicate framework in the EMT structure, which are expected to provide a rapid diffusion of Xe atoms and respectively an exchange with the gas phase within the acquisition time (few ms). Despite the open channel structure only two peaks were observed at temperatures substantially below room temperature that could be attributed to Xe in reservoirs III and IV. We interpret this observation as a consequence of the high Na^+ content in the synthesized low silica EMT zeolite. Most probably the Na cations are blocking the access and movement of Xe inside the crystals.

The chemical shift variation of the characteristic NMR peaks of EMT is plotted versus temperature for the series of experimental samples prepared for different synthesis time and the reference sample synthesized with 18-crown-6 ether (Figure 7). The shape of the curves is generally normal and within the expected behavior and the low-field signal can be attributed to the EMT structure. The increase in chemical shift with decreasing temperature, occurring essentially at temperatures below 220 K, is due to the increase in the residence time of the Xe atoms on the surface and the increase in the Xe-Xe interactions on the surface as well. The variable-temperature experiments are performed with HP ^{129}Xe under continuous loss of flow, which means that the sample remains at adsorption equilibrium at any temperature and the amount of adsorbed Xe becomes rather large when the temperature approaches the temperature of phase transformation of the bulk phase (about 115 K at 8 Torr Xe pressure).

There are some small deviations from the expected behavior in the high-temperature region, for instance the curves for all experimental samples are at higher ppm values than the reference EMT sample. The differences could be attributed to reduction in the average size of the channels possibly due to structural distortions or/and to difference in the permeability of the cages due to the interference of the increased Na^+ content. In the low-temperature region, the chemical shifts of the run products are smaller than that of the reference. This might be a consequence of slightly reduced volume of the EMT cages caused by distortions or intereference by the Na^+ cations.

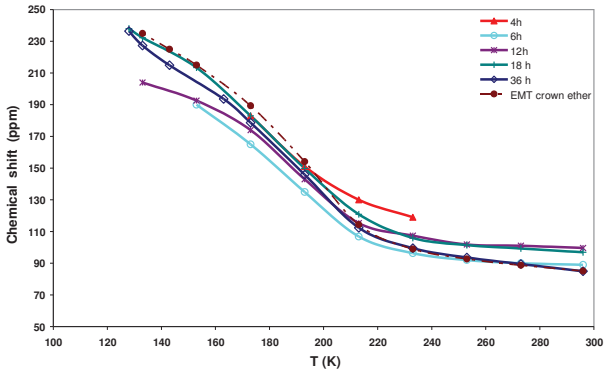

Figure 7. Chemical shift variation of the NMR peaks versus temperature for the experimental samples obtained in different synthesis run duration compared to the reference EMT sample synthesized with 18-crown-6 ether.

The intensity of the NMR peaks from the EMT structure was fairly intense after 6 h of hydrothermal treatment. In order to determine when the first EMT cages appear in the solid phase we have studied the samples subjected to 2 and 4 h hydrothermal treatment. First traces of EMT-like cages were detected for the 4 h sample at $T \leq 233$ K. At higher temperature, the amount of Xe adsorbed in the EMT phase is smaller and the signal is too weak to be observed.

Figure 8 shows the spectra recorded at 193 K of samples synthesized at different synthesis times. The signal characteristic of EMT-type material, around 145 ppm, is highlighted by a yellow square. For the samples synthesized between 4 and 18 h the signal is broad, possibly due to the exchange of Xe between the EMT cages and larger cavities, the latter could be the intrinsic gel mesopores or the textural mesopores between the gel particles.

The other signals, at lower chemical shifts, differ drastically from one sample to another. They are due to Xe atoms interacting with an amorphous phase having a more or less structured mesoporosity and exchanging between various environments and the gas phase. One cannot derive precise information from this part of the spectra because it depends on many parameters including the morphology of the voids, their relative amount, their connectivity and the degree of polarization of the Xe nuclei. The presence of a narrow and intense signal observed in the fully amorphous sample reveals the existence of well-defined meso-voids in the initial gel. The average size of these voids can be estimated from the chemical shift of the signal measured at 296 K (22 ppm) and using the relationship between the chemical shift, □, and the mean pore size, *D*,

established by Terskikh et al.[44] for silica gels: □=118/(1+*D*/122). A value of 5.3 nm is obtained. We attribute this signal to the mesocavities in the rim of gel particles. This suggestion is

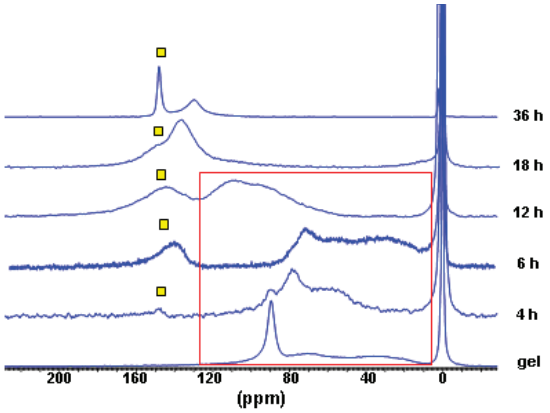

Figure 8. ^{129}Xe NMR spectra recorded at 193 K of xenon adsorbed in the initial gel and samples obtained after various synthesis times. The signal characteristic of the EMT structure is highlighted with a yellow square and the lines corresponding to amorphous phase not well structurally organized are surrounded by a red rectangle. The intensity of the spectra is arbitrary.

supported by the fact that this signal decreases for the 4 h sample, when first zeolite cages are detected. Hence, one may speculate that the mesopore cages close to the surface might be a preferential place for the zeolite nucleation. In any case, the process of reorganization is limited to the shell of gel particles and includes negligible part of the mass of the solid because the other methods employed, that is, XRD for long range order and Raman spectroscopy for short range order, did not detect any changes in this stage of gel evolution.

After 4 h of hydrothermal treatment a low-field shift and broadening of the mesopore peak is observed (Figure 8). This trend is much pronounced in the 6 h sample. These are clearly indications that some changes in the solid phase take place that change the structure of mesoporous voids and their accessibility by gas phase Xe. After 18 h of hydrothermal treatment the peaks corresponding to Xe exchange with mesopores are not observed in the spectra, although still amorphous phase containing mesopores is present as shown by TEM tomography analysis. This fact is due to increased mass of microporous phase (EMT), where the Xe atoms are preferentially adsorbed.

Discussion

It is common knowledge at present that zeolite nucleation is a heterogeneous reaction, which is supported by both theoretical [45,46] and experimental[31,47] studies. All zeolite yielding systems are heterogeneous in nature, comprising a solid and liquid phase. The nucleation process is a consequence of the reactions between these parts of the system. Chemical concentration and potential gradients between solid and liquid phase are the driving force for the exchange of species that leads to certain degree of homogenisation of the system. Ultimately the dissolution, transport and precipitation of the reactive species produce supersaturation that induces nucleation. Such intense exchange between the solid and liquid parts of one hydrogel continues

during the crystal growth process until complete exhaustion of nutrients in the system. Thus, the solid and liquid parts in a zeolite yielding system are equally important, as each part has a specific function. Investigating the reactions in the liquid part is difficult, even by in-situ methods, because of the heterogeneity of the zeolite precursors and the numerous metastable equilibrium steps that a system passes through. The evolution of the gel leading to crystalline final products can be tracked more easily by studying the solid part of the gel. Furthermore, up till now direct observation of the process of birth of the first zeolite cages has been observed only in a solid phase, although in a very particular zeolite yielding system.[31] The main objective of the present study as motivated by the preceding considerations was to study in depth the changes in the solid phase pertinent to zeolite nucleation. The polymerization reaction between the two initial solutions was designed as a way to form aggregated zeolite particles, which are easy to separate from the mother liquor. Certainly sub-colloidal particles remained in the liquid phase, but their impact on the overall process of zeolite formation is considered negligible.

The TEM investigation revealed that the initial mixing of the two starting solutions produced relatively large gel aggregates although the mixing was performed under vigorous stirring. The internal part of the gel aggregates comprised abundant mesopores and mesocavities. Mother liquor was imprisoned in these meso-voids. Considering the initial gel composition and the fact that most of the aluminosilicate precursors polymerize almost instantly, the liquid in voids must be rich in Na^+ and OH^- and low-weight silica/alumina species. Each particle has a shell, which contains only a few mesocavities. This shell built of densely polymerized aluminosilicates is not permeable to fluids. The high stability of the shell structure is proven by the fact that it survives the purification procedure, the drying, and even the N_2 adsorption experiments. The low specific surface area of the initial gel supports further the latter statement. Only under focused high energy electron beam the shell was destroyed liberating the imprisoned fluid. This new finding reveals that in the beginning of the nucleation process only the external surface of the gel particles is accessible for the bulk liquid. Therefore, the relative fraction of solid surface reacting with the mother liquor is limited considerably in the beginning of the process. This is the most probable reason for the long induction period and limited crystallization during the first 18 h of hydrothermal treatment. Progressively, the non-porous domains of the gel were converted in zeolite type crystals, decreasing the thickness of the impermeable gel shell. After 18 h of hydrothermal treatment most of the particles shell is dissolved and the access to the core rich in mesocavities is opened. This is the exact temporal location in the sequence of reaction events that the mass transformation from amorphous into crystalline zeolite-type material takes place. After 24 h the major part of the solid has been converted into EMT-type zeolite.

Two crystallization mechanisms were observed in this study. The first one includes the propagation of crystalline phase through the gel network, which is confined spatially in the peripheral part of the gel particle. The second mechanism proceeds via aggregation around a crystallization center resulting in crystalline aggregates with isometric shape. This latter type of growth is considered a result of autocatalytic nucleation, where the viable nuclei liberated in the solution continue growing into crystals. This seems to be the governing crystallization mechanism in the system under investigation. We base this conclusion on the morphological features of the crystalline aggregates, which are dominated by round isometric aggregates. The fact that the aggregates are formed by small polycrystalline particles is due most probably to the low temperature of the system that favors nucleation over the growth.

The physical evolution of the solid yielding EMT-type zeolite was investigated in details by a combination of electron microscopy techniques. Even this powerful technique could not identify the location and reveal the structure of the first zeolite cages. The appearance of the latter is a proof that particular zeolite structure has been formed and that most likely it will continue to grow into crystals. In order to correlate the spatial analysis by TEM with the temporal analysis of zeolite nucleation, we employed spectroscopic techniques that provided information on the formation of the first zeolite units. However, the Raman study did not provide valuable information for the induction period. The formation of larger ring structures that could be related to the formation of sodalite and EMT cages was detected only after 18 h of hydrothermal treatment.

In contrast, the hyperpolarized ^{129}Xe NMR analysis revealed important changes in the pore structure of the solid in the very early stages of gel evolution. It was established that the first EMT cages are formed after 4 h of hydrothermal treatment. The amount of crystalline material in the solid remains very low up to 18 h of synthesis. The slow nucleation in the system is a consequence most probably to the limited total volume of the shell, where initial nucleation takes place and the large particle size that hampers fast access of the reactant species to the core of the gel. The initial gel particles have a rim, built of heavily polymerized aluminosilicate, during the induction period this shell starts to get dissolved slowly as in certain areas the conditions for nucleation are attained. These areas, however, are limited in number because of the limited accessible surface of the gel. The interpretation that the nucleation takes place preferentially in the dense shell of gel particles is further supported by the changes of the mesopores in this part of the gel revealed by HP ^{129}Xe NMR.

We have observed the formation of particles in the voids deep inside the gel core (Figure 3c). These particles, which are most probably metastable sodium aluminate/silicates, are not likely to play key role in zeolite nucleation. Moreover, these particles are confined to the gel core and there is no communication between the mesopores and mother liquor. Thus, again our conclusion is that the nucleation was limited to the shell of the gel particles that in the present system was between 10 and 40 nm thick.

The applied value of this finding is that nucleation is a function of the size and morphology of initial gel particles. More precisely, by varying the conditions of preparation initial gel particles different in size and aggregation could be designed. This is supported strongly by a recent study based on a system similar to the one employed in the present one.[32] Slow mixing of the sodium-silicate and sodium-aluminate solutions at 4°C resulted in colloidal suspension of discrete gel particles; upon moderate heating the gel particles were converted in ultra small (15 x 2 nm) EMT crystals. The crystals were single, non-aggregated with well-defined crystal morphology. In the present study the instant mixing of the two starting solutions at room temperature resulted in the large core-shell particles as described here. The ultimate product is heavily aggregated as the particles are much larger in size. The importance of initial gel preparation was further confirmed by the synthesis of ultra small FAU-type in Na-rich organic template-free free system.[33] Again a suspension of very small gel precursor particles was stabilized by careful preparation of initial gel. The small discrete gel particles provide large accessible surface that leads to abundant nucleation in the system. The aggregation is also limited in such a system since each individual particle yields a single crystal.

Conclusions

The formation of EMT-type zeolite from an organic-template-free Na-rich gel system was studied. Complementary methods providing information on the long- and short-range structural order of the solid phase as well on the textural properties were employed. The crystal growth kinetics of EMT type was subjected to a detailed analysis. First zeolite cages were detected by HP ^{129}Xe NMR analysis as early as 4 h of hydrothermal treatment. The induction period was relatively long (18 h), which is attributed to the small reaction surface area between the solid and mother liqueur. The mass transformation of amorphous into crystalline material took place between 18 and 24 h of treatment.

An important finding that has critical implications on the kinetics and mechanism of both nucleation and growth is that the initial gel particles exhibit a core-shell structure. The core is rich of mesopores containing trapped mother liquor. The aluminosilicate shell is dense, impermeable for fluids and contains very limited number of mesocavities. This shell seems to be relatively stable and inert because after 18 h of hydrothermal treatment the core-shell structure is still preserved for most of the gel particles. The progressive erosion of the shell during the induction period opens access to mesopore volume of the gel. It was established that the moment when reactive species in the liquid part of the gel gain access to the core marks the moment of a radical surge in the rate of crystallization.

The time-series synthesis experiments in this study complemented by detailed characterization allowed to reveal the dynamics and kinetics of the process of zeolite nucleation and to localize spatially and temporally the formation of first nuclei. Our results prove unambiguously that inception of zeolite nucleation is localized in the shell of gel particles. The extremely thin surface zone is the place where the first nuclei are formed on. Thus the external surface area of the primary gel particles plays important role in the nucleation process and determines the kinetics of zeolite nucleation. Ensuing major implication of this study is that important zeolite properties such as size and level of aggregation can be controlled by proper design of the initial gel particles.

References

[1] C. Martinez, A. Corma, *Coord. Chem. Rev.* **2011**, *255*, 1558-1580.
[2] V. Valtchev, G. Majano, S. Mintova, J. Perez-Ramirez, *Chem. Soc. Rev.* **2013**, *42*, 263-290.
[3] D. Breck, *Zeolite Molecular Sieves*, John Wiley and Sons, New York, **1974**.
[4] J. W. Mullin, *Crystallization*, 4th Edition, Butterworth –Heinemann, Oxford, **2001**.
[5] F. Schüth, *Cur. Opin. Solid State Mater. Sci.* **2001**, *5*, 389-395.
[6] H. F. Greer, *Mater. Sci. Tech.* **2014**, *6*, 611-626.
[7] A. Corma, M. E. Davis, *ChemPhysChem* **2004**, *5*, 304-313.
[8] D. D. Kragten, J. M. Fedeyko, K. R. Sawant, J. D. Rimer, D. G. Vlachos, R. F. Lobo, M. Tsapatsis, *J. Phys. Chem. B* **2003**, *107*, 10006-10016.
[9] S. L. Burkett, M. EDavis, *Chem. Mater.* **1995**, *7*, 1639-1650.
[10] W. H. Dokter, H. F. Van Garderen, T. P. MBeelen, R. AVan Santen, W. Bras, *Angew. Chem., Int. Ed.* **1995**, *34*, 73-75.
[11] B. J. Schoeman, J. Sterte, J. E. Otterstedt, *Stud. Surf. Sci. Catal.* **1994**, *83*, 49-56.
[12] B. J. Schoeman, O. Regev, *Zeolites* **1996**, *17*, 447-456.
[13] J. D. Rimer, J. M. Fedeyko, D. G. Vlachos, R. F. Lobo, *Chem. Eur. J.* **2006**, *12*, 2926-2934.
[14] S. A. Pelster, R. Kalamajka, W. Schrader, F. Schüth, *Angew. Chem., Int. Ed.* **2007**, *46*, 2299-2302.
[15] L. Tosheva, B. Mihailova, L. H. Wee, B. Gasharova, K. Garbev, A. M. Doyle, *Angew. Chem., Int. Ed.* **2008**, *47*, 8650-8653.

[16] C. E. A. Kirschhock, R. Ravishankar, P. A. Jacobs, J. A. Martens, *J. Phys. Chem. B* **1999**, *103*, 11021-11027.
[17] T. Wakihara, S. Kohara, G. Sankar, S. Saito, M. Sanchez-Sanchez, A. R. Overwag, W. Fan, M. Ogura, T. Okubo, *Phys. Chem. Chem. Phys.* **2006**, *8*, 224-227.
[18] F. Wei, M. Ogura, G. Sankar, T. Okubo, *Chem. Mater.* **2007**, *19*, 1906-1917.
[19] T. M. Davis, T. O. Drews, H. Ramanan, C. He, J. Dong, H. Schnablegger, M. A. Katsoulakis, E. Kokkoli, A. V. McCormick, R. L. Penn, M. Tsapatsis, *Nat. Mater*. **2006**, *5*, 400-408.
[20] S. R. Bajpe, C. E. A. Kirschhock, A. Aerts, E. Breynaert, G. Absillis, T. N. Parac-Vogt L. Giebeler, *Chem. Eur. J*. **2010**; *16,* 3926-3932.
[21] S. Bals, K. J. Batenburg, D. Liang, O. Lebedev, G. Van Tendeloo, A. Aerts, J. A. Martens, C. E. A. Kirschhock, *J. Am. Chem. Soc*. **2009**; *131*, 4769-4773.
[22] R. Szostak, *Molecular Sieves: Principles of Synthesis and Identification*, Van Nostrand-Reinhold, New York, 1989.
[23] A. V. McCormick, A. T. Bell, C. J. Radke, *J. Phys. Chem.* **1989**, *93*, 1741-1744.
[24] A. Katović, B. Subotić, I. Šmit, Lj. A. Despotović, *Zeolites* **1990**, *10*, 634-641.
[25] M. Smaihi, O. Barida, V. Valtchev, *Eur. J. Inorg. Chem.* **2003**, *2003*, 4370-4377.
[26] V. Valtchev, S. Rigolet, K. N. Bozhilov, *Microporous Mesoporous Mater.* **2007**, *101*, 73-82.
[27] D. P. Serrano, M. A. Uguina, G. Ovejero, R. Van Grieken, M. Camacho, *Microporous Mesoporous Mater.* **1996**, *7*, 309-321.
[28] P. K. Dutta, J. Twu, *J. Phys. Chem.* **1991**, *95*, 2498-2501.
[29] B. Subotić, A. Graovac, *Stud. Surf. Sci. Catal.* **1985**, *24*, 199-206.
[30] R. W. Thompson, *Zeolites* **1992**, *12*, 837-840.
[31] S. Mintova, N. H. Olson, V. Valtchev, T. Bein, *Science* **1999**, *283*, 958-960.
[32] E.-P. Ng, D. Chateigner, T. Bein, V. Valtchev, S. Mintova, *Science* **2012**, *335*, 70-73.
[33] H. Awala, J.-P. Gilson, R. Retoux, P. Boullay, J.-M. Goupil, V. Valtchev, S. Mintova, *Nat. Mater.* **2015**, *14*, 447-451.
[34] V. Valtchev, K. N. Bozhilov, *J. Phys. Chem. B* **2004**, *108*, 15587-15598.
[35] P. K. Dutta, D. C. Shieh, M. Puri, *Zeolites* **1988**, *8*, 306-309.
[36] C. Li, Z. Wu, in *Handbook of Zeolite Science and Technology* (Eds.: S. M. Auerbach, K. A. Carrado, P. K. Dutta,), Marcel Dekker Inc., New York, **2003**.
[37] M.-A. Springuel-Huet, A. Nossov, Z. Adem, F. Guenneau, C. Volkringer, T. Loiseau, G. Férey, A. Gédéon, *J. Am. Chem. Soc.* **2010**, *132*, 11599-11607.
[38] M.-A. Springuel-Huet, A. Nossov, F. Guenneau, A. Gédéon, *Chem. Commun.* **2013**, 49, 7403-7405.
[39] T. Brotin, J. P. Dutasta, *Chem. Rev.* **2009**, *109*, 88-130.
[40] A. Nossov, E. Haddad, F. Guenneau, C. Mignon, A. Gédéon, D. Grosso, F. Babonneau, C. Bonhomme, C. Sanchez, *Chem. Commun.* **2002**, 2476-2477.
[41] A. Nossov, F. Guenneau, M.-A. Springuel-Huet, E. Haddad, V. Montouillout, B. Knott, F. Engelke, C. Fernandez, A. Gedeon, *Phys. Chem. Chem. Phys.* **2003**, *5*, 4479-4483.
[42] F. Dougnier, J.-L. Guth, *J. Chem. Soc., Chem. Commun.* **1995**, 951-952.
[43] C. J. Jameson, A. K. Jameson, R. E. Gerald, H.-M. Lim, *J. Phys.Chem. B* **1997***, 101*, 8418-8437.
[44] V. V. Terskikh, I. L. Moudrakovski, S. R. Breeze, S. Lang, C. I. Ratcliffe, J. A. Ripmeester, A. Sayari, *Langmuir* **2002**, *18*, 5653-5656.
[45] B. Subotić, J. Bronić, T. Antonić-Jelić, in *Ordered Porous Materials* (Eds.: V. Valtchev, S. Mintova, M. Tsapatsis), Elsevier, Amsterdam, **2009**.
[46] V. Nikolakis, D. G. Vlachos, M. Tsapatsis, *Microporous Mesoporous Mater.* **1998**, *21*, 337-346.
[47] D. P. Serano, R. van Grieken, *J. Mater. Chem.* **2001**, *11*, 2391-2407.
[48] A. Nossov, E. Haddad, F. Guenneau, A. Galarneau, F. Di Renzo, F. Fajula, A. Gedeon, *J. Phys. Chem. B* **2003**, *107*, 12456-12460.
[49] J. R. Kremer, D. N. Mastronarde, J. R. McIntosh, *J. Struct. Biol.* **1996**, *116*, 71-76.
[50] J. I. Agulleiro, J. J Fernandez, *Bioinformatics* **2011**, *27*, 582-583.

List of publications

Accepted

1. G. Melinte, I. Florea, S. Moldovan, I. Janowska, W. Baaziz, R. Arenal, A. Wisnet, C. Scheu, S. Begin-Colin, D. Begin, C. Pham-Huu, O. Ersen, *A 3D insight on the catalytic nanostructuration of few-layer graphen,* Nature Communications, 5, **2014**.

2. G. Melinte, S. Moldovan, C. Hirlimann, X. Liu, S. Bégin-Colin, D. Bégin, F. Banhart, C. Pham-Huu, O. Ersen, Toward *nanoprinting with metals on graphene,* Nature Communication, accepted*,* **2015**.

3. G. Melinte, V. Georgieva, M.A. Springuel, A. Nossov, O. Ersen, A. Gedeone, A. Palcic, K. Bozhilov, C. Pham-Huu, S. Mintova, V.Valtchev, *3D study of morphology and dynamics of zeolite nucleation,* Chemistry—A European Journal, accepted, **2015**.

4. C. E. Bertrand-Drira, X.W. Cheng, T. Cacciaguerra, P. Trens, G. Melinte, O. Ersen, D. Minoux, A. Finiels, F. Fajula, C. Gerardin, *Mesoporous mordenites obtained by desilication: Mechanistic considerations and evaluation in catalytic oligomerization of pentene*, Microporous and Mesoporous Materials, **2015**.

5. X. Liu, I. Marangon, G. Melinte, C. Wilhelm, C. Ménard-Moyon, B. P. Pichon, O. Ersen, K. Aubertin, W. Baaziz, C. Pham-Huu, S. Begin-Colin, A. Bianco, F. Gazeau, D. Begin, *Design of Covalently Functionalized Carbon Nanotubes Filled with Metal Oxide Nanoparticles for Imaging, Therapy and Magnetic Manipulation,* ACS Nano, 8 (11) **2014**.

6. A. Ciesielski, S. Haar, M. El Gemayel, H. Yang, J. Clough, G. Melinte, M. Gobbi, E. Orgiu, M. V. Nardi, G. Ligorio, V. Palermo, N. Koch, O. Ersen, C. Casiraghi, P. Samorì: *Harnessing the Liquid-Phase Exfoliation of Graphene Using Aliphatic Compounds: A Supramolecular Approach*, Angewandte Chemie International, 53 (39), **2014**.

7. M. El Gemayel, S. Haar, F. Liscio, A. Schlierf, G. Melinte, S. Milita, O. Ersen, A. Ciesielski, V. Palermo, P. Samori, *Leveraging the Ambipolar Transport in Polymeric Field-Effect Transistors via Blending with Liquid-Phase Exfoliated Graphene*, Advanced Materials, 26 (28), **2014**.

8. W. Baaziz, G. Melinte, O. Ersen, C. Pham-Huu, I. Janowska, *Effect of nitriding / nanostructuration of few layer graphene supported iron-based particles; catalyst in graphene etching and carbon nanofilament growth*, Physical Chemistry Chemical Physics, 16 (30), **2014**.

9. W. Baaziz, L. Truong-Phuoc, C. Duong-Viet, G. Melinte, I. Janowska, V. Papaefthymiou, O. Ersen, S. Zafeiratos, D. Begin, S. Begin-Colin, C. Pham-Huu, *Few-Layer Graphene Decorated*

with Homogeneous Magnetic Fe_3O_4 Nanoparticles with Tunable Covering Densities, Journal of Materials Chemistry 2 (8), **2013**.

Submitted and manuscripts in progress

10. S. Haar, M. El Gemayel, Y. Shin, G. Melinte, M. A. Squillaci, O. Ersen, C. Casiraghi, A. Ciesielski, P. Samorì, *Enhancing the liquid-phase exfoliation of graphene in organic solvents upon addition of n-octylbenzene*, submitted to Carbon, **2015.**

11. G. Melinte et al., *Environmental TEM investigation of the graphene nanopatterning*, manuscript in progress